October 2021

A Search for Exotic Higgs Decays or: How I Learned to Stop Worrying and Love Long-lived Particles

Jackson Burzynski
University of Massachusetts Amherst

A SEARCH FOR EXOTIC HIGGS DECAYS OR: HOW I LEARNED TO STOP WORRYING AND LOVE LONG-LIVED PARTICLES

A Dissertation Presented

by

JACKSON CARL BURZYNSKI

Submitted to the Graduate School of the
University of Massachusetts Amherst in partial fulfillment
of the requirements for the degree of

DOCTOR OF PHILOSOPHY

September 2021

Physics

A SEARCH FOR EXOTIC HIGGS DECAYS OR: HOW I LEARNED TO STOP WORRYING AND LOVE LONG-LIVED PARTICLES

Dissertation Presented

by

JACKSON CARL BURZYNSKI

Approved as to style and content by:

_____

B. Brau, Chair

_____

C. Dallapiccola, Member

_____

J. De Vries, Member

_____

A. Pope, Member

_____

Narayanan Menon, Department Chair

Physics

ABSTRACT

A SEARCH FOR EXOTIC HIGGS DECAYS OR: HOW I LEARNED TO STOP WORRYING AND LOVE LONG-LIVED PARTICLES

SEPTEMBER 2021

JACKSON CARL BURZYNSKI

B.Sc., TUFTS UNIVERSITY

M.Sc., UNIVERSITY OF MASSACHUSETTS AMHERST

Ph.D., UNIVERSITY OF MASSACHUSSETTS AMHERST

Directed by: Professor B. Brau

A novel search for exotic decays of the Higgs boson to pairs of long-lived neutral particles, each decaying to a bottom quark pair, is performed using 139 fb^{-1} of $\sqrt{s} = 13$ TeV proton-proton collision data collected with the ATLAS detector at the LHC. Events consistent with the production of a Higgs boson in association with a leptonically-decaying Z boson are analyzed. Long-lived particle (LLP) decays are reconstructed from inner detector tracks as displaced vertices with high mass and track multiplicity relative to Standard Model processes. The analysis selection requires the presence of at least two displaced vertices, effectively suppressing Standard Model backgrounds. The residual background contribution is estimated using a data driven technique. No excess over Standard Model predictions is observed, therefore upper limits are set on the branching ratio of the Higgs boson to LLPs. Branching ratios of 10% are excluded for LLP mean proper lifetimes as small as 4 mm and as large as 110 mm. For LLP masses below 40 GeV, these results represent the most stringent constraint in this lifetime regime.

Acknowledgements

Like many first year graduate students, when I first arrived at UMass Amherst I was overcome with feelings of doubt, from concerns about having made the right choice of program to the familiar phenomenon of imposter syndrome. But over the three years I spent in Western Massachusetts I found an incredible community of people both in and outside of the physics department that showed me that I both belonged and could thrive there. I was lucky to find a close-knit group in my cohort to work through demanding problem sets and prepare for the grueling qualification exam. I would specifically like to thank Dario for conversations over beers at the Moan and Dove, and Sachin for the good-sprited debates over problem sets. But most importantly, I owe a tremendous debt of gratitude to Maggie Ng, my partner throughout the majority of my PhD who provided unending love and support to get me through the most difficult periods. I truly would not be where I am today without them ♥.

Despite moving to CERN right before the COVID-19 pandemic began, I was fortunate enough to find a group of people with whom to share a very unusual year. Our daily Zoom lunches were a much needed source of human interaction in an otherwise isolated work week, and the excursions to explore the mountain huts of Switzerland are memories that I will cherish forever. In particular I would like to thank Brendan, for discussions about statistics over good French wines, and most importantly for forcing me to go skiing when it was clear I was in need of a respite from thesis- and conference-related stress. Will, for invaluable reminders of the importance of work-life balance and for his hospitality in providing an alpine refuge wherein several sections of this thesis were written. And Grace, for always having my back when conversations turned political ☺.

On a professional level, I would like to thank my incredible analysis team, without whom the results presented in this thesis would not be possible. In particular, I thank John Stupak for spearheading the $VH(4b)$ search effort, Amber Roepe for their significant contribution to developing and optimizing the filter used to collect our data and Bingxuan Liu, whose idea for a background estimation strategy tied the analysis together and significantly accelerated our timeline. It has been an honor to serve as the team's analysis contact, and I am looking forward to continuing this collaboration in my future research

endeavors. Additionally, I owe my success in part to Verena Martinez Outschoorn for connecting me with the $VH(4b)$ effort, and of course my advisor Ben Brau for introducing me to the incredible ATLAS long-lived particle community and guiding me through two fascinating searches.

Finally, this thesis would not have been possible without the efforts of the entire ATLAS collaboration. Each of the over 3000 current scientific authors has contributed in some way to the success of each and every ATLAS result. I would also like to thank CERN for the very successful operation of the LHC, as well as the support staff without whom ATLAS could not be operated efficiently.

Contents

List of Figures

List of Tables

To Maggie

Introduction

What we know is a drop, what we don't know is an ocean.

-Isaac Newton

Seeking what is true is not seeking what is desirable.

-Albert Camus, *The Myth of Sisyphus and other essays*

The discovery of a new particle consistent with the Higgs boson at the Large Hadron Collider in 2012 constituted the final missing piece of the puzzle of the Standard Model of particle physics [1], [2]. Since then, a new physics program has emerged which aims to scrutinize the nature of this elusive particle and understand its properties. While the Standard Model has been enormously successful in predicting the results of every major collider experiment, it is known to not be the ultimate theory of the universe. Many theories which aim to address the limitations of the Standard Model point to the Higgs boson as a possible portal to new physics, with exotic Higgs decays being the primary phenomenological consequence and means of discovery. It is well motivated both from theory and experimental constraints to consider the scenario in which the particles produced in these exotic decays have macroscopic proper lifetimes and give rise to unique detector signatures.

This work describes a search for exotic decays of the Higgs boson to two long-lived, neutral, spin-0 particles which subsequently decay to pairs of b quarks, giving the signature $H \to aa \to 4b$. The search uses 139 fb^{-1} of $\sqrt{s} = 13$ TeV pp data collected with the ATLAS detector between 2015 and 2018 and focuses on Higgs production in association with a Z boson. The signature of interest comprises two leptons from the Z boson decay and two displaced hadronic vertices in the ATLAS inner detector from the decays of the

long-lived particles. The analysis uses a data-driven method to predict the number of expected events from background and novel discriminating variables which were optimized to reduce the background to $\mathcal{O}(1)$ events while maximizing the signal sensitivity. The work presented in this thesis has led to the paper "Search for exotic decays of the Higgs boson to long-lived particles in pp collisions at $\sqrt{s} = 13$ TeV using displaced vertices in the ATLAS inner detector" [3], and was first presented at the 55$^{\text{th}}$ Rencontres de Moriond session on Electroweak Interactions and Unified Theories in a talk titled "Probing the dark sector with b-quarks with the ATLAS detector" [4].

This thesis organized in three parts. Part I contains a discussion of the Standard Model, its successes and shortcomings, and an overview of several beyond Standard Model scenarios which aim to address these limitations. The motivation for searches for long-lived particles is presented, along with a discussion of previous searches that have set constraints on this signature. Part II describes the experimental apparatus used in this work. An overview of the ATLAS experiment at the Large Hadron Collider is given, along with details about the reconstruction of the physics objects used in this analysis. A chapter is then dedicated to a discussion of the specialized reconstruction methods needed to identify the decays of long-lived particles. Finally, Part III outlines a search for Higgs boson decays to long-lived particles. The results of this search are presented along with a discussion of the statistical methods used to perform the interpretation.

Part I

Theoretical Motivation

Chapter 1

The Standard Model

There is no exquisite beauty...without some strangeness in the proportion.

-Edgar Allan Poe

Why should things be easy to understand?

-Thomas Pynchon

The **Standard Model (SM)** of particle physics constitutes one of the greatest scientific achievements in modern history. Based on empirical evidence gathered by experiments over the course of more than 100 years, the SM provides a single elegant theoretical framework which describes the interactions between all known elementary particles to astonishing levels of precision. Starting with the discovery of the electron by J.J. Thomson in 1897 [5] and developed over the course of much of the 20$^{\text{th}}$ century, this theory represents the culmination of a decades long effort to understand the dynamics of elementary particles at ever-increasing energies. The discovery of the Higgs boson at the Large Hadron Collider in 2012 [1], [2] completed our current picture of the SM and underlined the predictive power of the theory, cementing its place in scientific history as one of the most successful models of all time.

As of the writing of this thesis, there are four known fundamental forces at work the universe: electromagnetism, the strong interaction, the weak interaction, and gravity. These forces are responsible for the interactions between the fundamental, point-like particles that make up the matter in the universe. Of these four, the SM describes all but

gravity, which is too weak in relation to the other three forces to play a role in high-energy physics experiments. While the gravitational force is attributed to the curvature of space-time as described by Einstein's general theory of relativity, the SM describes the other three forces as being mediated by elementary particles. The electromagnetic force (Section 1.2) is carried by the photon, γ, and is responsible for the attraction between the electrons and protons which holds atoms together. The strong interaction (Section 1.3) is carried by the gluon, g, and is responsible for binding quarks together to form hadrons such as protons and neutrons. Finally, the weak interaction (Section 1.4) is carried by the W and Z bosons, and gives rise to the radioactive decay of atomic nuclei. In this chapter, we will give an overview of how the SM describes each of these forces, which will lead us to a discussion of the role of the Higgs boson in the SM and its phenomenology (Section 1.5), and allow us to understand the motivation for a more complete theory beyond the SM (Section 1.6).

1.1 Quantum Field Theory and Gauge Theory

The particles described by the SM come in two general classes:

- **fermions** are characterized by having half-integral spin. The two types of fermions, **leptons** (such as the electron), and **quarks** (which group together to form baryons such as protons and neutrons) combine to form the atoms which comprise all visible matter in the universe.

- **bosons** are characterized by having integral spin. The three fundamental interactions described by the SM are mediated by spin-1 bosons ($W^{\pm}, Z, \gamma$), and the spin-0 Higgs boson h is responsible for giving mass to other elementary particles.

Mathematically, these elementary particles are described as the quanta of **fields** in the language of **Quantum Field Theory (QFT)**. This section will discuss several basic concepts of QFT that are essential for understanding the theoretical motivation for the search presented in this thesis and will serve as a reference for later discussions.

1.1.1 Cross sections and decay widths

QFT provides a framework within which various observables that are measured in high energy physics experiments can be predicted. First, the decay rate, Γ, is the probability per unit time that a particle will decay. For an ensemble of N identical particles, the decay rate satisfies $dN = -\Gamma N dt$. Thus, given an initial population of N_0 particles, we have

$$N(t) = N_0 e^{-\Gamma t} \tag{1.1}$$

In most scenarios, several decay modes are possible. The total decay rate is then given as a sum over the rates of the individual modes, which allows us to compute the **proper lifetime** of the particle, given by the reciprocal of the total rate:

$$\tau = \frac{1}{\Gamma_{\text{total}}}, \quad \Gamma_{\text{total}} = \sum_{i=1}^{n} \Gamma_i. \tag{1.2}$$

It is conventional to write the lifetime multiplied by the speed of light, so that the product $c\tau$ has units of distance. From this, we may compute the **branching ratio** of an individual decay mode $A \to ii$, defined as

$$\text{Br}(A \to ii) = \frac{\Gamma_i}{\Gamma_{\text{total}}}. \tag{1.3}$$

When measuring the mass of an elementary particle, the total decay rate appears as the irreducible "width" of the Gaussian distribution. For this reason the decay rate is often called the **width** of the particle[1].

The decay rate is computed from **Fermi's golden rule**, which separates the rate as a product of dynamic and kinematic factors:

$$d\Gamma = |\mathcal{M}|^2 \times (\text{phase space}) \tag{1.4}$$

where $\mathcal{M}$ is the **amplitude** or **matrix element** of the decay process and the phase space factors consist of differential forms over 4-momentum space and energy and momentum

---

[1] Γ has dimensions of inverse time, which in natural units is the same as mass.

conserving δ-functions. The amplitude encodes information regarding the underlying pro-
cess and will depend on the coupling constants, masses of intermediate particles, etc. More
concretely, for an n-body decay $A \to f_k$ ($k = 1, \ldots, n$), Fermi's Golden rule for the differ-
ential decay rate is given by

$$d\Gamma = |\mathcal{M}|^2 \frac{S}{2m_A} \left(\prod_{k=1}^{n} \frac{d^3\vec{p}_k}{(2\pi)^3 2E_k} \right) \times (2\pi)^4 \delta^4 \left(p_A - \sum_{k=1}^{n} p_k \right) \tag{1.5}$$

where p_k is the 4-momentum of the kth particle, and S is a statistical factor corresponding
to the permutations of identical particle families in the final state.

In collider experiments, one must also compute the $2 \to n$ *scattering* process $AB \to f_k$.
The likelihood for a scattering process to occur is measured in terms of the scattering **cross
section**, σ. The cross section may be thought of as the constant of proportionality that
relates the number of scatterings, N_S, to the numbers of incoming particles N_A and N_B,
divided by the overlap area A. More concretely,

$$N_S = \sigma \frac{N_A N_B}{A} \tag{1.6}$$

Thus, the cross section has units of area. Cross sections are typically measured in units of
barns (b), where $1 \text{ b} = 10^{-24} \text{ cm}^2$. At the LHC, interesting processes have cross sections
that are much smaller than 1 b, so in practice units of picobarns (pb) and femtobarns (fb)
are more common. In analogy with Equation 1.5, we may right down the "golden rule of
scattering" which gives the differential cross section for the $2 \to n$ process:

$$d\sigma = |\mathcal{M}|^2 \frac{S}{4\sqrt{(p_A \cdot p_B)^2 - (m_A m_B)^2}} \left(\prod_{k=i}^{n} \frac{d^3\vec{p}_k}{(2\pi)^3 2E_k} \right) \times (2\pi)^4 \delta^4 \left(p_A + p_B - \sum_{k=1}^{n} p_k \right) \tag{1.7}$$

For a given Lagrangian density $\mathcal{L}$, the formalism of QFT gives a prescription for how to
compute $\mathcal{M}$ for a given decay or scattering process. The Lagrangian density of the SM will
be introduced in the next several sections.

1.1.2   Symmetries and Representations

Symmetry plays a crucial role in quantum field theory. In 1918, German mathematician Emmy Noether published a pioneering result which related global symmetries of a Lagrangian to conservation laws [6]. The result showed that if the Lagrangian of a physical system is invariant under a continuous infinitesimal transformation

$$\phi(x) \to \phi'(x) = \phi(x) + \alpha\Delta\phi(x) \tag{1.8}$$

then the quantity

$$j_\mu(x) \equiv \frac{\partial\mathcal{L}}{\partial(\partial^\mu\phi)}\Delta\phi \tag{1.9}$$

has vanishing divergence, $\partial_\mu j^\mu(x) = 0$. This quantity $j_\mu(x)$ is called the **Noether current**. From this we may define

$$Q \equiv \int_{\text{all space}} j^0 d^3x \tag{1.10}$$

which will satisfy $\frac{d}{dt}Q = 0$, meaning that it is conserved in time. To reiterate this important result, for every continuous symmetry transformation which leaves the Lagrangian invariant, there is a corresponding Noether current with vanishing divergence, and therefore a conserved charge. These currents and charges will appear throughout our discussion of the SM.

In the SM, particles are classified based on how their fields transform under the operations of various symmetry transformations. These sets of transformations are known as **Lie groups**, and their action on the fields of the SM is formalized using the language of representation theory. Given a Lie group G and a vector space V, we define a **representation** of G to be a map $\Pi : G \to \text{GL}(V)$ from the group G to the group of linear operators on V $\text{GL}(V)$ satisfying

$$\Pi(g \cdot h)v = \Pi(g) \cdot \Pi(h)v$$

for all $g, h \in G$ and $v \in V$. We write the representation as a pair (Π, V). The multiplication on the left is taking place in G, whereas the multiplication on the right is taking place in $\text{GL}(V)$. We can similarly define a representation of the Lie algebra $\mathfrak{g}$ which is related to Π via the Lie group-Lie algebra correspondence. In QFT when we refer to representations,

we usually are referring to representations of the Lie algebra.

In the SM, there are two important types of symmetries to consider: spacetime symmetries such as translations, rotations and boosts, and gauge symmetries which act on internal degrees of freedom in a quantum system.

Symmetries of Spacetime

Perhaps the most familiar symmetry of nature is that the speed of light has the same value in all reference frames. Originally stated axiomatically in Albert Einstein's *annus mirabilis* paper on what is now called special relativity [7], this symmetry now provides the foundation for all quantum field theories which describe elementary particles. The set of transformations that respect this symmetry, the **Poincaré group**, is described mathematically as the semi-direct product of the group of spacetime translations $\mathbb{R}^{3,1}$, and the set of Lorentz transformations, $O(3,1)^2$. From Noether's theorem, the translational symmetries give rise to energy and momentum conservation, whereas the Lorentz symmetry gives conservation of angular momentum.

To understand how different types of particles transform under Poincaré transformations, it is necessary to classify the different representations of the group. In practice, this is done by studying the representation theory of the Lie algebra of the Lorentz group, $\mathfrak{so}(3,1)$. With a bit of algebra, one can show that this Lie algebra is isomorphic to $\mathfrak{su}(2) \times \mathfrak{su}(2)$ and we see the connection between spin and relativistic transformation properties. Borrowing from what we know from the theory of non-relativistic spin, the representations of $\mathfrak{so}(3,1)$ must then be characterized by pairs of numbers (j_1, j_2) where j_1, j_2 are either integer or half-integer. The particles that make up the SM may then be classified based on their transformation properties using these two values. A table of these representations is given in Table 1.1.

---

[2]The set of Lorentz transformations is defined as the set of isometries of Minkowski space. That is, it is the group of transformations $\mathbf{\Lambda}$ satisfying $g_{\lambda\sigma} = \Lambda^\mu{}_\lambda \Lambda^\nu{}_\sigma g_{\mu\nu}$.

Representation	Spin	Name
$(0,0)$	0	scalar
$(\frac{1}{2},0)$	$\frac{1}{2}$	left-handed Weyl spinor
$(0,\frac{1}{2})$	$\frac{1}{2}$	right-handed Weyl spinor
$(\frac{1}{2},0) \oplus (0,\frac{1}{2})$	$\frac{1}{2}$	Dirac spinor/bispinor
$(\frac{1}{2},\frac{1}{2})$	1	vector

Table 1.1: The representations of the Lorentz group.

The massive fermions in the SM transform in the $(\frac{1}{2},0)\oplus(0,\frac{1}{2})$ representation. We write their 4-component fields as a combination of two Weyl spinors

$$\psi = \begin{pmatrix} \psi_L \\ \psi_R \end{pmatrix} \tag{1.11}$$

where ψ_L and ψ_R transform under $(\frac{1}{2},0)$ and $(0,\frac{1}{2})$, respectively. We can project out the left- and right-handed components of a fermion using the projection operators

$$\psi_L = P_L\psi = \frac{1}{2}(1-\gamma_5)\psi, \quad \psi_R = P_R\psi = \frac{1}{2}(1+\gamma_5)\psi \tag{1.12}$$

where $\gamma^5 = i\gamma^0\gamma^1\gamma^2\gamma^3$ is the **chirality** operator. The distinction between left-handed and right-handed representations will be crucial for understanding the electroweak force in the SM (Section 1.4).

Gauge Theory

The core idea underpinning the SM is **gauge theory**. A gauge theory with gauge group G is a quantum field theory with a Lagrangian that is invariant under local transformations of a Lie group G. The most notable example of a gauge theory is quantum electrodynamics (Section 1.2) which is based on the abelian $U(1)$ group. In the 1950's, Chen Ning Yang and Robert Mills extended the concept of gauge theory to nonabelian groups in an attempt to provide an explanation for strong interactions [8]. This sparked the so-called "gauge theory revolution" and would turn out to be one of the most crucial developments in the

history of the making of the SM. For this reason, non-abelian gauge theory is also referred
to as **Yang-Mills theory**.

To appreciate the subtleties of Yang-Mills theory, we begin with a complex-valued
Dirac field $\psi(x)$, and require that our theory should be invariant under the transforma-
tion

$$\psi(x) \rightarrow e^{i\alpha(x)^a T^a} \psi(x) \tag{1.13}$$

where the set $T^a \in \mathfrak{g}$, often referred to as the **generators** of the transformation, form a
basis of the Lie algebra of G. The transformation property in Equation 1.13 is that of the
fundamental or **defining** representation because the operators T^a are represented by the
matrices that define the Lie group structure. The fermionic fields in a gauge theory always
belong to either the fundamental representation or the trivial representation where $\psi \rightarrow \psi$.

In order to describe a dynamical theory, the Lagrangian must also contain terms in-
volving derivatives of the fields $\partial_\mu \psi$. Local gauge invariance complicates this, because the
definition of the derivative (in a given direction specified by n^μ)

$$n^\mu \partial_\mu \psi = \lim_{\epsilon \to 0} \frac{1}{\epsilon} \left[\psi(x + \epsilon n) - \psi(x) \right] \tag{1.14}$$

requires a comparison of fields at different points in spacetime which will have *different
transformation properties* in our local gauge theory. To include derivative terms in our La-
grangian, we then need a systematic and consistent way to "connect" or identify the gauge
transformation properties of our field ψ over nearby points in spacetime. In other words,
how can we transport our field $\psi(x)$ along a path in a gauge covariant way?

To do this, we introduce an additional mathematical structure A_μ known as a **connec-
tion** which is a Lie algebra valued 1-form: $A_\mu \equiv A_\mu^a T^a$. The role of the connection is to
compensate for the difference in gauge transformations from one point to the next:

$$n^\mu D_\mu \psi = \lim_{\epsilon \to 0} \frac{1}{\epsilon} \left[\psi(x + \epsilon n) - ig\epsilon n^\mu A_\mu(x)\psi(x) \right] \tag{1.15}$$

This operator D_μ in Equation 1.15 is called the **gauge covariant derivative** and will take the
place of the usual $\partial_\mu \psi$ terms in our Lagrangian. More succinctly, the covariant derivative

takes the form

$$D_\mu \psi(x) = \partial_\mu \psi(x) + ig A_\mu \psi(x) \tag{1.16}$$

In gauge theories, the connection is called a **gauge field** as it may be identified with the gauge bosons that carry the forces between particles. The gauge fields transform under the **adjoint representation**, defined by

$$A_\mu \to A'_\mu = U A_\mu U^\dagger + \frac{i}{g}(\partial_\mu U) U^\dagger \tag{1.17}$$

Mathematically, the adjoint representation of a Lie group is the representation of the group on its own Lie algebra. To build a gauge-invariant kinetic term for the gauge fields, we define the **field strength tensor** as[3]

$$F^a_{\mu\nu} = \partial_\mu A^a_\nu - \partial_\nu A^a_\mu + g f^{abc} A^b_\mu A^c_\nu \tag{1.18}$$

where f^{abc} are the structure constants of the Lie algebra $\mathfrak{g}$

$$[T^a, T^b] = i f^{abc} T^c, \quad \text{for } T^a \in \mathfrak{g} \tag{1.19}$$

With the covariant derivative in hand, we can now write down the Lagrangian. The Lagrangian density for a free, massless non-Abelian gauge theory with gauge group G is given by

$$\mathcal{L} = -\frac{1}{4} F^a_{\mu\nu} F^{a,\mu\nu} \tag{1.20}$$

This allows us to define the SM as a non-abelian gauge theory with a gauge group that is a direct product of the QCD gauge group and the electroweak gauge group

$$G_{\text{SM}} \cong \underbrace{SU(3)_C}_{\text{QCD}} \times \underbrace{SU(2)_L \times U(1)_Y}_{\text{EW}}. \tag{1.21}$$

These two pieces will be described in detail in the following sections.

---

[3]For the reader who prefers coordinate free notation, the field strength tensor may be expressed as $\mathbf{F} = d\mathbf{A} + \mathbf{A} \wedge \mathbf{A}$, where $\mathbf{A} \wedge \mathbf{A}$ does not vanish because $\mathbf{A}$ takes values in the Lie algebra.

1.2 Quantum Electrodynamics

In the late 1920's, Paul Dirac introduced the first relativistic treatment of quantum mechanics, solving a problem that had eluded physicists since the early days of the quantum theory [9], [10]. This breakthrough was the first of many in the development of the SM and laid the groundwork for relativistic quantum field theory. However, it was the work of Dyson, Feynman, Schwinger, and Tomanaga that finally formulated electrodynamics in the language of relativistic quantum field theory in a consistent manner [11]–[17]. Their theory, known as **Quantum Electrodynamics (QED)** was the first such relativistic quantum field theory and marked the first major development in the making of the SM.

Formally, QED is an abelian gauge theory with $G = U(1)_{\text{em}}$. The covariant derivative (Equation 1.16) is given by

$$D_\mu \psi = \partial_\mu \psi + ieA_\mu \psi \tag{1.22}$$

where ψ is a Dirac spinor, and e, the coupling constant of the theory, is the familiar electric charge. From this, we may construct the QED Lagrangian for a single Dirac fermion ψ:

$$\mathcal{L}_{\text{QED}} = -\frac{1}{4}F_{\mu\nu}F^{\mu\nu} + \overline{\psi}(i\gamma^\mu D_\mu - m)\psi \tag{1.23}$$

This Lagrangian is invariant under a $U(1)$ gauge transformation acting as

$$A_\mu \to A_\mu + \partial_\mu \lambda, \quad \psi \to e^{-ie\lambda}\psi \tag{1.24}$$

for an arbitrary function $\lambda(x)$. The Noether current associated with this symmetry may then be computed using Equation 1.9

$$j^\mu = e\overline{\psi}\gamma^\mu\psi. \tag{1.25}$$

After quantizing the theory, we may write down the expression for the conserved charge corresponding to the Noether current,

$$Q = e \int \frac{d^3p}{(2\pi)^3} \sum_{s=1}^{2} \left(b_{\vec{p}}^{s\dagger}b_{\vec{p}}^s - c_{\vec{p}}^{s\dagger}c_{\vec{p}}^s\right) \tag{1.26}$$

which is equal to the electric charge times number of particles $(b_{\vec{p}}^{s\dagger} b_{\vec{p}}^{s})$, minus the number of antiparticles $(c_{\vec{p}}^{s\dagger} c_{\vec{p}}^{s})$. Thus, we observe the motivation for defining the coupling constant to be the electric charge. The electric charge is usually expressed in terms of the dimensionless ratio α, known as the **fine structure constant**:

$$\alpha = \frac{e^2}{4\pi\hbar c} \approx \frac{1}{137} \tag{1.27}$$

As alluded to in the first paragraph of this section, in the late 1940's it was shown that the divergent contributions to physical quantities such as the self-energy of the electron could be removed in a systematic fashion through the procedure of **renormalization**. This cemented QED as a robust description of the interaction between light and matter. QED is still most accurate physical theory ever formulated and serves as a prototype for a successful quantum field theory.

1.3 Quantum Chromodynamics

Much before the development of the modern understanding of the SM it was known that a "strong nuclear interaction" must exist to overcome electrostatic repulsion in atomic nuclei. In the 1950s and 1960s, a large number of stable hadrons and hadronic resonances were discovered that were thought to interact via this strong interaction, but little was understood about their dynamics. To make sense of the mass spectrum of this so-called "particle zoo", Murray Gell-Mann [18] and Yuval Ne'eman [19] posited that the observed hadrons are members of specific representations of a new approximate $SU(3)$ symmetry that was an extension to the $SU(2)$ description of isospin put in place by Werner Heisenberg in 1932 to relate protons to neutrons [20]. Due to the fact that certain mesonic (spin-0) and baryonic (spin-1/2) states could be neatly classified by the **8** representation of $SU(3)$, this model was deemed the **Eightfold way**. Then in 1963, the **quark model** was introduced independently by Murray Gell-Mann [21] and George Zweig [22], [23] as a way to explain the origins of this $SU(3)$ symmetry. The model proposed the existence of a new type of fundamental particle called the quark which came in three different **flavors**, and

an approximate $SU(3)_f$ symmetry that related them[4]. After the experimental findings of James Bjorken showed that hadrons behave as collections of point-like constituents when probed at high energies [24], the quark model was cemented as a fundamental aspect of the SM and our understanding of strong nuclear force.

Despite the great successes of the $SU(3)_f$ quark model, there were several phenomenon that it could not explain. In particular, the model could not explain the fact that the spin $S = 3/2$ baryon, the Δ^{++}, was comprised of three up quarks with parallel spins and vanishing orbital angular momentum, thereby having a symmetric wavefunction and seemingly violating Fermi-Dirac statistics. To solve this dilemma, Gell-Mann and others hypothesized that quarks carry an additional quantum number called **color** [25]–[27]. The Fermi–Dirac problem is then solved if the baryon wavefunctions are antisymmetric under this new color charge, giving rise to a totally antisymmetric wavefunction. For this mechanism to work, three color indices were needed for the quarks with an internal symmetry group $SU(3)_C$ to relate them, building on the earlier work of Yang and Mills.

This theory, known as **Quantum chromodynamics (QCD)**, is a non-nonabelian gauge theory with $G = SU(3)_C$ which describes the strong nuclear force. The Lie algebra $\mathfrak{su}(3)$ has dimension $3^2 - 1 = 8$, and is spanned by a set of 3×3 hermitian matrices T^a with $a = 1, \ldots, 8$. As usual, the $T^a \in \mathfrak{su}(3)$ are used to generate the local $SU(3)$ gauge transformations $\psi(x) \rightarrow U(x)\psi(x)$ where $U(x) = e^{iw^a(x)T^a}$. We can then write down the covariant derivative, defined by its action on a field ψ in the fundamental representation.

$$D_\mu \psi(x) = (\partial_\mu - ig_s T^a A^a_\mu)\psi(x) \tag{1.28}$$

where the gauge fields A^a_μ are the **gluon** fields, and g_s is the QCD coupling constant. The QCD Lagrangian is then deceptively simple:

$$\mathcal{L}_{\text{QCD}} = -\frac{1}{4}F^a_{\mu\nu}F^{a\mu\nu} + \overline{\psi}^j(i\displaystyle{\not}D^k_j - m\delta^k_j)\psi_k \tag{1.29}$$

with $F^a_{\mu\nu}$ as defined in Equation 1.18. Aside from the masses of the quarks (whose origin will be discussed in Section 1.4.3), the QCD coupling constant g_s is the only fundamental

---

[4]"f" for flavor, of course

parameter of QCD. In analogy with the fine-structure constant of QED, this coupling is usually written in terms of $\alpha_s = \frac{g_s^2}{4\pi}$.

Despite the simplicity of the QCD Lagrangian, there are many intricacies lurking beneath which make QCD a complex and fascinating theory. Like all QFTs, predictions for QCD observables are expressed in terms of the renormalized coupling constant $\alpha_s(\mu_R^2)$, where μ_R is the renormalization scale. The exact value of μ_R is unphysical, but when taken to be the scale of the momentum transfer Q of a given process, $\alpha_s(Q^2)$ is representative of the effective strength of the interaction in that process. The evolution of the coupling constant as the scale changes is called the **running** of the coupling. This running is described by the **renormalization group equation (RGE)**

$$\mu_R^2 \frac{d\alpha_s}{d\mu_R^2} = \beta(\alpha_s) = -(b_0 \alpha_s^2 + b_1 \alpha_s^3 + b_2 \alpha_s^4 + \cdots). \tag{1.30}$$

For a nonabelian gauge theory with $G = SU(N)$, the 1-loop β-function b_0 is given by

$$b_0 = \frac{1}{12\pi}\left(11N - 2n_f\right) \tag{1.31}$$

For QCD, we have $N = 3$ and $n_f = 6$. Thus,

$$\beta_{\text{QCD}}(\alpha_s) = -(\frac{7}{4\pi}\alpha_s^2 + \cdots) \tag{1.32}$$

The negative sign on the 1 loop β-function implies that the strength of the coupling constant *decreases* as the renormalization scale increases. For momentum transfers on the order of 100 GeV–1 TeV, $\alpha_s \approx 0.1$, meaning that the quarks inside hadrons behave more or less as free particles when probed at large enough energies. This property of QCD is known as **asymptotic freedom**, and was first discovered in 1973 by David Gross, Frank Wilczek [28] and David Politzer [29], earning the trio the 2004 Nobel Prize. In this so-called "perturbative regime", analytic computations using perturbation theory allow for quantitative predictions for hadronic interaction cross sections.

At one loop, we may solve the RGE for $\alpha_s(Q^2)$:

$$\alpha_s(Q^2) = \frac{\alpha_s(\mu^2)}{1 + b_0 \alpha_s(\mu^2) \ln(Q^2/\mu^2)} \tag{1.33}$$

This may be simplified by introducing the **QCD scale parameter** Λ as

$$\frac{1}{\alpha_s(Q^2)} = \frac{1}{\alpha_s(\mu^2)} + b_0 \ln\left(\frac{Q^2}{\mu^2}\right) \equiv b_0 \ln\left(\frac{Q^2}{\Lambda^2}\right). \tag{1.34}$$

The scale Λ corresponds to the scale where $\alpha_s(\mu^2)$ becomes infinite. Equation 1.33 may then be written as

$$\alpha_s(Q^2) = \frac{1}{b_0 \ln(Q^2/\Lambda^2)}. \tag{1.35}$$

The value of Λ has been derived experimentally and is roughly 300 MeV [30]. For Q^2 values close to Λ, the coupling constant becomes large and perturbative QCD breaks down. For large distances (small Q), the coupling then becomes so large that is impossible to isolate a quark from a bound hadronic state. In fact, it becomes energetically favorable for a *new* quark-antiquark pair to be created, forming a new bound state. This property, known as **color confinement**, is observed experimentally and in lattice simulations but cannot be derived from first principles due to the failing of perturbation theory in this regime. Thus, the only stable QCD states are color-neutral groupings of quarks and gluons such as mesons and baryons. In collider experiments, color confinement manifests in the formation of **jets**, collimated sprays of hadrons and other particles initiated from the production of a single quark or gluon. When a quark or gluon is produced in isolation, quark/anti-quark pairs are spontaneously created from the vacuum to form color neutral bound states. This process is known as **hadronization**. Figure 1.1 shows a simplified diagram of jet formation, in which two free quarks are produced which subsequently hadronize, each forming an isolated jet. The simulation of this phenomena will be described in Section 6.1.1.

1.4 Electroweak Unification

The story of the SM gets particularly interesting when we begin to consider the weak nuclear force. Perhaps the most important realization during the entire development of
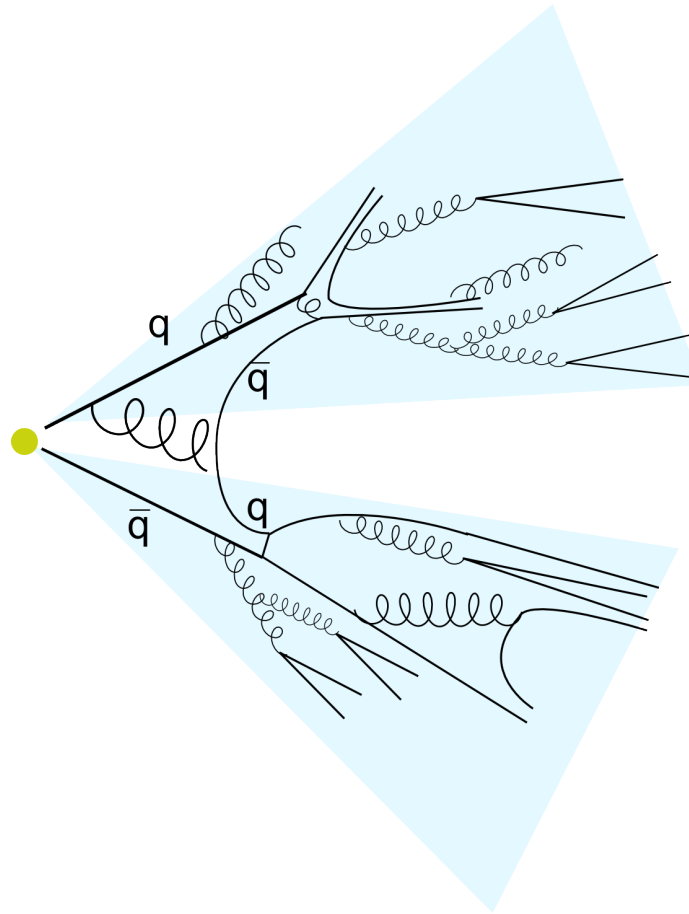
Figure 1.1: The formation of two jets from a quark-antiquark pair [31].

the SM was the discovery that the weak force and the electromagnetic force were two sides of the same coin. The discovery of this so-called "electroweak unification" (and the subsequent symmetry breaking mechanism that breaks it down) in many ways *defines* the SM, and radically redefined our current understanding of high-energy physics. In this Section, we will discuss this development in depth, starting with a brief overview of the weak force (Section 1.4.1) before diving into electroweak unification (Section 1.4.2).

1.4.1 The Weak Force

Following the tremendous success of QED, 20th century physicists were motivated to provide a quantum field theoretic description of the experimentally observed weak nuclear force responsible for β-decay. In 1933, Enrico Fermi proposed a theory of β-decay which posited a four-fermion interaction between the neutron, electron, neutrino, and proton

known as the **Fermi interaction**. This theory was expanded to further explain the decay of the muon [32], and incorporate the parity violation observed in the famous 1958 experiment conducted by Chien-Shiung Wu [33]. Then in 1958, Richard Feynman and Murray Gell-Mann determined that the tensor structure of the four fermion interaction was that of a vector minus axial vector, or $V - A$ [34], and it seemed that the fundamental nature of the weak nuclear force was slowly being uncovered.

However, despite its success as a low energy description of the weak force, there were several fundamental issues with the Fermi theory. For one, computations resulted in irremovable infinities when pushed to higher order in perturbation theory, indicating that the Fermi theory was not as robust as QED which by that time had been shown to be renormalizable. Perhaps even more distressing was the fact that there was little rational for the structure of the Fermi interaction. Physicists at the time viewed the model as a theory that was "cobbled together" to fit experimental data [35]. This eventually led to the replacement of the four-fermion contact interaction by a more complete theory describing a short-range non-contact force mediated by the W and Z bosons, once again taking advantage of the work of Yang and Mills. But as we will see, in order to apply Yang-Mills theory to the weak force, it must be viewed as a manifestation of a unified theory of electroweak interactions.

1.4.2 Glashow-Weinberg-Salam Theory

In the 1960's, Sheldon Glashow, Steven Weinberg, and Abdus Salam developed a groundbreaking model for the unification of the weak force and electromagnetism [36]–[38]. The theory, known as the **GWS model** or **electroweak model**, was a major milestone in the development of the Standard Model and earned its three founders the Nobel prize in 1979. The GWS theory is a non-abelian gauge theory with gauge group $SU(2)_L \times U(1)_Y$. The subscript Y is used to differentiate the $U(1)$ of the GWS model from the more familiar $U(1)_{\text{em}}$ of QED. The relationship between the two will be described in Section 1.4.3.

In the GWS model, fermions are grouped into $SU(2)_L$ doublets

$$\underbrace{\begin{pmatrix} \nu_e \\ e^- \end{pmatrix}, \begin{pmatrix} \nu_\mu \\ \mu^- \end{pmatrix}, \begin{pmatrix} \nu_\tau \\ \tau^- \end{pmatrix}}_{\text{leptons}}; \quad \underbrace{\begin{pmatrix} u \\ d \end{pmatrix}, \begin{pmatrix} s \\ c \end{pmatrix}, \begin{pmatrix} b \\ t \end{pmatrix}}_{\text{quarks}} \tag{1.36}$$

This is motivated by the experimentally observed properties of the weak force which show that the interactions induce a transition between fermions of different charges. The other important property of the weak interaction is that it is a **chiral** theory, meaning that it treats left-handed and right-handed fermion representations differently. The subscript L in the $SU(2)_L$ group refers to the fact that only the *left-handed* fermions transform under a non-trivial representation of the $SU(2)_L$ group whereas the right-handed fermions transform as singlets. Hence, the doublets in Equation 1.36 are further decomposed into their left- and right-handed Weyl spinor components. The left-handed fields form $SU(2)_L$ doublets

$$E_L = \begin{pmatrix} \nu_{e,L} \\ e_L \end{pmatrix}, \cdots ; \quad Q_L = \begin{pmatrix} u_L \\ d_L \end{pmatrix}, \cdots \tag{1.37}$$

while the right-handed components are singlets $\psi_{e_R} = e_R, \cdots, \psi_{q_R} = u_R, \cdots$. The fields transform under local gauge transformations as

$$\Psi_L \to \Psi'_L = e^{iY_L\beta(x)} e^{i\alpha(x)^a T^a} \Psi_L \tag{1.38}$$

$$\psi_R \to \psi'_R = e^{iY_R\beta(x)} \psi_R \tag{1.39}$$

where the charge $Y_{L,R}$ is called the **weak hypercharge** (hence the subscript Y on $U(1)_Y$) and $T^a = \sigma^a/2$ are the familiar $SU(2)$ generators in the spinor representation. These charges are related to the familiar electric charge Q via the **Gell-Mann-Nishijima relation**:

$$Q = T_3 + Y/2 \tag{1.40}$$

Like all gauge theories, local gauge invariance gives rise to connection forms. For the $SU(2)_L$ group, there are three gauge bosons W_μ^a ($a = 1, 2,$ or 3) which form the adjoint

representation. Like the familiar $U(1)$ of QED, the $U(1)_Y$ gauge group has only a single gauge boson B_μ in the adjoint representation. The action of the covariant derivative on $SU(2)_L$ doublets and singlets Ψ_L and ψ_R is given by

$$D_\mu \Psi_L = \left(\partial_\mu + igW_\mu^a T^a + ig'Y_L B_\mu\right) \Psi_L, \quad D_\mu \psi_R = \left(\partial_\mu + ig'Y_R B_\mu\right) \psi_R \tag{1.41}$$

It is convenient to re-parameterize the gauge fields as

$$W_\mu^\pm = \frac{1}{\sqrt{2}} \left(W_\mu^1 \mp iW_\mu^2\right) \tag{1.42}$$

$$A_\mu = \cos\theta_W B_\mu + \sin\theta_W W_\mu^3 \tag{1.43}$$

$$Z_\mu = -\sin\theta_W B_\mu + \cos\theta_W W_\mu^3 \tag{1.44}$$

where θ_W is the **weak mixing angle**

$$\sin\theta_W = \frac{g'}{\sqrt{g^2 + g'^2}}, \quad \cos\theta_W = \frac{g}{\sqrt{g^2 + g'^2}} \tag{1.45}$$

This angle quantifies the degree of **gauge mixing** that occurs between the $SU(2)_L$ and $U(1)_Y$ groups.

Using this re-parameterization, we can now write down the fermion portion of $\mathcal{L}_{\text{EW}}$ starting with the general form

$$\mathcal{L}_{\text{fermion}} = \sum_j \overline{\Psi}_{jL}\gamma^\mu D_\mu \Psi_{jL} + \sum_f \overline{\psi}_{jR}\gamma^\mu D_\mu \psi_{jR} \tag{1.46}$$

where the index j runs over the three fermion generations, the index f runs over the 9 charged fermions. Plugging in the covariant derivative expressed in terms of the fields $W_\mu^\pm, Z_\mu$ and A_μ, we obtain terms corresponding to both charged and neutral currents. The charged current is given by

$$\mathcal{L}_{\text{CC}} = \frac{g}{\sqrt{2}} \left[(\overline{u}_L\gamma^\mu d_L + \overline{\nu}_{e,L}\gamma^\mu e_L)W_\mu^+ + \text{h.c.}\right] \tag{1.47}$$

The charged current has several notable properties. First, only left-handed fermions and

right-handed antifermions couple to the $W^\pm$ bosons. This means there is a maximal break-ing of both parity P (left $\leftrightarrow$ right) and charge conjugation C (particle $\leftrightarrow$ antiparticle) sym-metries in this interaction. Also, the charged current couples the W to $SU(2)_L$ fermion doublets which differ by one unit of electric charge. We may use the chiral projection operator (Equation 1.12) to rewrite these couplings as

$$\bar{\nu}_{e,L}\gamma^\mu e_L = \frac{1}{2}\bar{\nu}_e\gamma^\mu(1-\gamma_5)e. \tag{1.48}$$

In this form, we observe that the charged current has the form of a vector (γ^μ) minus axial vector ($\gamma^\mu\gamma_5$), making the connection with the $V-A$ Fermi interaction manifest.

The neutral current has two components:

$$\mathcal{L}_{\text{NC}} = \mathcal{L}_{\text{QED}} + \mathcal{L}_{\text{NC}}^Z \tag{1.49}$$

Using the Gell-Mann-Nishijima relation (Equation 1.40) and letting $e = g\sin\theta_W$ we obtain the interaction term from the familiar QED Lagrangian

$$\mathcal{L}_{\text{QED}} = eA_\mu \sum_j \bar{\psi}_j\gamma^\mu Q_j\psi_j \tag{1.50}$$

The neutral weak interaction is given by

$$\mathcal{L}_{\text{NC}}^Z = \frac{g}{\cos\theta_W}\sum_j \left[\bar{\psi}_{jL}\gamma^\mu\left(T_j^3 - Q_j\sin^2\theta_W\right)\psi_{jL} + \bar{\psi}_{jR}\gamma^\mu\left(-Q_j\sin^2\theta_W\right)\psi_{jR}\right]Z_\mu \tag{1.51}$$

The neutral current differs from the charged current in several ways. First, all interaction vertices are flavor conserving: both the γ and Z boson couple to fermions and their own antiparticles. Second, both the QED and weak neutral currents interact with both fermion chiralities due to the $SU(2)_L \times U(1)_Y$ gauge mixing. However, only the QED current respects P symmetry because the neutrino coupling to the Z only exists for left-handed chiralities.

As is stands, we have accomplished the goal of constructing a theory which combines QED and both the neutral and charged weak interactions. However, there is an important

piece missing from the theory which is known to be true from experimental results: the fermion and gauge boson mass terms. This is where the Higgs mechanism comes into play.

1.4.3 Symmetry Breaking and the Higgs Mechanism

In 1964, three landmark papers were submitted to Physical Review Letters by separate teams in close succession which proposed related mechanisms to introduce mass terms to a gauge theory in a way that respected the symmetry of the theory [39]–[41]. This mechanism, now known as the **Brout–Englert–Higgs mechanism**, or simply the **Higgs mechanism**, showed that by introducing an additional field that spontaneously breaks the gauge symmetry, the gauge bosons can acquire mass terms in a consistent manner. To illustrate the mechanism, we begin with a simple example of an abelian gauge theory with gauge group $U(1)$. Consider the gauge field portion of the Lagrangian:

$$\mathcal{L}_{\text{gauge}} = -\frac{1}{4} F_{\mu\nu} F^{\mu\nu} \tag{1.52}$$

This Lagrangian is invariant under the usual local $U(1)$ gauge transformation of a field in the adjoint representation: $A_\mu(x) \to A_\mu(x) - \frac{1}{e} \partial_\mu \eta(x)$. If we were to naively add a mass term for the gauge field

$$\mathcal{L}_{\text{gauge}} = -\frac{1}{4} F_{\mu\nu} F^{\mu\nu} + \frac{1}{2} m A_\mu A^\mu \tag{1.53}$$

it would spoil the $U(1)$ gauge symmetry of the Lagrangian. Instead, we may extend the gauge field Lagrangian in Equation 1.52 by introducing a complex scalar field ϕ:

$$\mathcal{L} = -\frac{1}{4} F_{\mu\nu} F^{\mu\nu} + (D_\mu \phi)^\dagger (D_\mu \phi) - V(\phi) \tag{1.54}$$

with the usual covariant derivative $D_\mu = \partial_\mu + ie A_\mu$ and scalar field potential

$$V(\phi) = -\mu^2 \phi^\dagger \phi + \frac{\lambda}{2} \left(\phi^\dagger \phi \right)^2 \tag{1.55}$$

The Lagrangian in Equation 1.54 is invariant under the local $U(1)$ gauge transformation

$$A_\mu(x) \to A_\mu(x) - \frac{1}{e} \partial_\mu \alpha(x), \quad \phi(x) \to e^{i\alpha(x)} \phi(x). \tag{1.56}$$

(a) $\mu^2 < 0$ (b) $\mu^2 > 0$
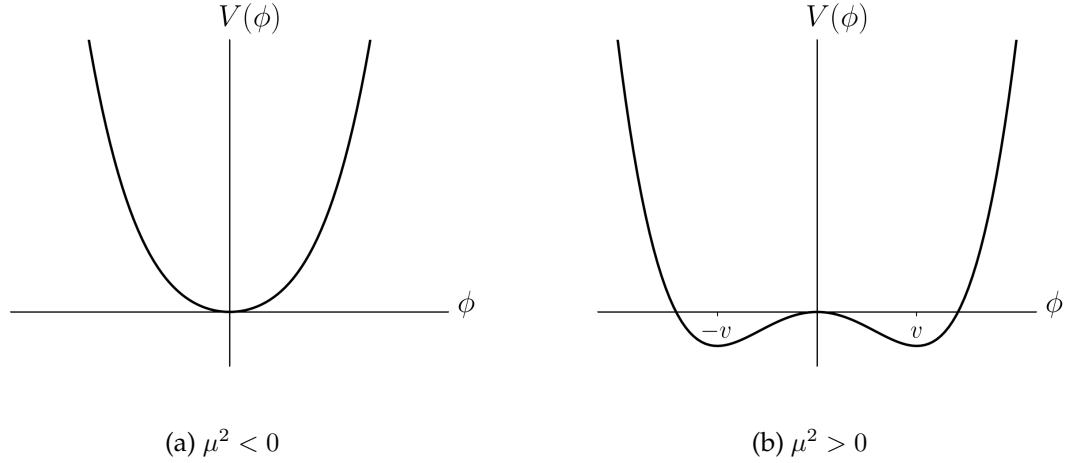
Figure 1.2: The Higgs potential $V(\phi)$. For $\mu^2 < 0$ (a), the minimum energy configuration of the fields will be that with $\phi = 0$, and the global $U(1)$ symmetry of the Lagrangian is preserved. For $\mu^2 > 0$ (b), the potential will obtain local minima at $\phi = \pm\sqrt{\mu^2/\lambda} \equiv \pm v$, and the $U(1)$ symmetry is broken.

If $\mu^2 < 0$, the classical minimum energy configuration of the fields will be that with $\phi = 0$.
In this case, the global $U(1)$ symmetry of the Lagrangian is preserved, and our Lagrangian
simply describes a massless gauge boson coupled to a charged scalar field ϕ with mass μ.
However, if $\mu^2 > 0$, then the extremum at $\phi = 0$ is unstable, and two global minima appear
in the potential at $v = \pm\sqrt{\mu^2/\lambda}$. In this case, the field ϕ will acquire a **vacuum expectation value**, or **vev**. In this configuration of the fields, the global $U(1)$ symmetry is said to have
been spontaneously broken. This is shown graphically in Figure 1.2.

To observe the consequences of this **spontaneous symmetry breaking (SSB)**, we can
expand the field ϕ about the minimum v:

$$\phi(x) = (v + h(x))e^{i\xi(x)} \tag{1.57}$$

for small $h(x), \xi(x)$. Plugging this expansion into the Lagrangian, we have to lowest non-trivial order in the fields $h(x), \xi(x)$,

$$\mathcal{L} = (\partial_\mu h)^2 + e^2(v+h)^2(A_\mu + \frac{1}{e}\partial_\mu\xi)^2 - \frac{1}{4}F_{\mu\nu}F^{\mu\nu} + \frac{\mu^4}{2\lambda} - 2\mu^2 h^2 \tag{1.58}$$

Thus, after SSB we have a field h with mass $m_h = 2\mu$, and a massless field ξ called the

Goldstone boson. This is a specific example of a more general principal known as **Goldstone's theorem** which states that for every spontaneously broken continuous symmetry, there must arise a new massless scalar particle [42].

Despite having broken the global $U(1)$ symmetry, we can still exploit the *local $U(1)$* gauge symmetry to choose A_μ in such a way as to eliminate $\xi(x)$ from the Lagrangian. This choice of gauge is called the **unitary gauge**, and is given by fixing $A'_\mu = A_\mu + \frac{1}{e}\partial_\mu\xi$. We can now write down the Lagrangian after SSB and unitary gauge transformation:

$$\mathcal{L} = -\frac{1}{4}F'_{\mu\nu}F'^{\mu\nu} + (\partial_\mu h)^2 + e^2 v^2 (A'_\mu)^2 + \frac{\mu^4}{2\lambda} - 2\mu^2 h^2 + \cdots \tag{1.59}$$

where we have omitted terms that are cubic or quartic in the fields A_μ, and h. From this, we see that we now have a *massive* gauge boson with mass $m_A = \sqrt{2}ev$ which depends on the vev of the original scalar field ϕ. But what happened to the Goldstone mode ξ? It is useful now to consider the number of degrees of freedom before and after SSB. We began with a massless gauge boson with two longitudinal degrees of freedom, and a complex scalar with two additional degrees of freedom for a total of four degrees of freedom. After SSB, we have a *massive* gauge boson with two longitudinal degrees of freedom and one transverse degree of freedom, and a real scalar field with one degree of freedom, once again for a total of four degrees of freedom. Hence, the complex degree of freedom of our original scalar field has gone into the new longitudinal mode of the gauge boson. Because of this, it is often said that the Goldstone mode is *eaten* by the gauge boson to give it its mass.

Generation of W/Z masses

We can now apply the Higgs mechanism to the GWS model. It was Weinberg and Salam who incorporated the Higgs mechanism to Glashow's model of electroweak unification, giving the theory its modern form. Consider a complex scalar Φ which is an $SU(2)_L$ doublet

$$\Phi = \begin{pmatrix} \phi^+ \\ \phi^0 \end{pmatrix} \tag{1.60}$$

with a Lagrangian

$$\mathcal{L}_\Phi = (D^\mu\Phi)^\dagger(D_\mu\Phi) - V(\Phi) = (D^\mu\Phi)^\dagger(D_\mu\Phi) + \mu^2\Phi^\dagger\Phi - \lambda\left(\Phi^\dagger\Phi\right)^2 \tag{1.61}$$

The minimum of $V(\Phi)$ in Eq. 1.61 occurs for

$$\Phi^\dagger\Phi = \frac{\mu^2}{2\lambda} \equiv \frac{v^2}{2} \tag{1.62}$$

Expanding about this minimum [5], we obtain

$$\Phi = \frac{1}{\sqrt{2}}\begin{pmatrix} 0 \\ v + h(x) \end{pmatrix} \tag{1.63}$$

where $h(x)$ is a real scalar field. Evaluating the electroweak Lagrangian $\mathcal{L}_{\text{EW}}$ for this particular value of Φ, we observe that the covariant derivative term generates terms quadratic in the gauge boson fields

$$(D^\mu\Phi)^\dagger(D_\mu\Phi) = \left|\left(\partial_\mu + \frac{ig'}{2}B_\mu + \frac{ig}{2}\tau^i W^i_\mu\right)\frac{1}{\sqrt{2}}\begin{pmatrix}0\\v\end{pmatrix}\right|^2 + \ldots \tag{1.64}$$

$$= \frac{v^2}{8}\left|(g'B_\mu + g\tau^i W^i_\mu)\begin{pmatrix}0\\v\end{pmatrix}\right|^2 + \ldots \tag{1.65}$$

$$= \frac{v^2}{8}\left|\begin{pmatrix}gW^1_\mu - igW^2_\mu \\ g'B_\mu - gW^3_\mu\end{pmatrix}\right|^2 + \ldots \tag{1.66}$$

$$= \frac{v^2}{8}\left[g^2\left((W^1_\mu)^2 + (W^2_\mu)^2\right) + (g'B_\mu - gW^3_\mu)^2\right] + \ldots \tag{1.67}$$

Using the redefinition of the fields from Eq. 1.44, this first term becomes

$$\frac{v^2}{8}\left[g^2\left((W^1_\mu)^2 + (W^2_\mu)^2\right) + (g'B_\mu - gW^3_\mu)^2\right] = \frac{g^2v^2}{8}W^+_\mu W^{-\mu} + \frac{(g'^2 + g^2)v^2}{8}Z_\mu Z^\mu \tag{1.68}$$

---

[5]To obtain this form a gauge transformation to the unitary gauge is also necessary.

yielding mass terms for three of the four gauge fields:

$$m_W = \frac{gv}{2}, \quad m_Z = \frac{v}{2}\sqrt{g'^2 + g^2}, \quad m_A = 0 \tag{1.69}$$

The mass terms for the W and Z bosons break the global $SU(2)_L \times U(1)_Y$ symmetry, but the massless photon preserves a residual global $U(1)_{em}$ symmetry subgroup. Thus, the field Φ acquiring a vev has broken the EW symmetry $SU(2)_L \times U(1)_Y \to U(1)_{em}$.

Fermion Masses

In the Dirac Lagrangian, the fermion mass terms appear as Dirac bilinears, $m\overline{\psi}\psi$. Expanding this in terms of the Weyl spinor components, we have

$$m\left(\overline{\psi}_L\psi_R + \overline{\psi}_R\psi_L\right) \tag{1.70}$$

Because this term contains couplings between left and right handed fields, it will no longer be gauge invariant due to the fact that these fields have different transformation properties under $SU(2)_L$. Luckily, the introduction of the scalar field Φ allows us to formulate fermion mass terms in a gauge invariant way. First, consider the lepton $SU(2)_L$ doublet terms. Without loss of generality, we specialize to the electron term. We have

$$\mathcal{L}^e_{\text{Yukawa}} = -\lambda_e \overline{E}_{La}\Phi^a e_R + \text{h.c.} \tag{1.71}$$

where a is the $SU(2)_L$ index, and λ_e is a new dimensionless coupling constant. This is of course gauge invariant because combinations of the form $\overline{L}\Phi R$ are $SU(2)_L$ singlets. After SSB, we may replace Φ in the above equation with Equation 1.63 to obtain

$$\mathcal{L}^e_{\text{Yukawa}} = -\frac{1}{\sqrt{2}}\lambda_e v \overline{e}_L e_R + \text{h.c.} + \cdots . \tag{1.72}$$

Thus, we have generated a mass term for the electron which is proportional to the vev of the Higgs field:

$$m_e = \frac{1}{\sqrt{2}}\lambda_e v. \tag{1.73}$$

The same procedure may be applied to the quark families. For simplicity, we only consider the first generation. We have

$$\mathcal{L}^q_{\text{Yukawa}} = -\lambda_d \overline{Q}_{La} \Phi^a d_R - \lambda_u \epsilon^{ab} \overline{Q}_{La} \Phi_b u_R + \text{h.c.} \tag{1.74}$$

Substituting the vev of Φ once again, we have

$$\mathcal{L}^q_{\text{Yukawa}} = -\frac{1}{\sqrt{2}} \lambda_d \overline{d}_L v d_R - \frac{1}{\sqrt{2}} \lambda_u \overline{u}_L u_R + \text{h.c.} \tag{1.75}$$

which gives us mass terms for the d and u quarks:

$$m_d = \frac{1}{\sqrt{2}} \lambda_d v, \quad m_u = \frac{1}{\sqrt{2}} \lambda_u v \tag{1.76}$$

These additions to the Lagrangian are known as **Yukawa interactions**, and will henceforth be referred to as $\mathcal{L}_{\text{Yukawa}}$. Note that there is no corresponding mass term for the neutrino. Because there is no right-handed neutrino in the SM, it cannot obtain its mass through the Yukawa interaction.

So far, the way we have written the electroweak Lagrangian points to only interactions between fermion pairs in the same generation. This is true for particles in their weak eigenstates. However, a freely propagating particle will always be in a mass eigenstate. The difference between the two bases is encoded in a unitary matrix V known as the **Cabibbo-Kobayashi-Maskawa (CKM) matrix**:

$$\begin{pmatrix} \psi'_d \\ \psi'_s \\ \psi'_b \end{pmatrix} = \begin{pmatrix} V_{ud} & V_{us} & V_{ub} \\ V_{cd} & V_{cs} & V_{cb} \\ V_{td} & V_{ts} & V_{tb} \end{pmatrix} \begin{pmatrix} \psi_d \\ \psi_s \\ \psi_b \end{pmatrix} \tag{1.77}$$

The off-diagonal terms in V allow for non-zero transition amplitudes between different quark generations. This allows for weak flavor changing currents involving the $W^\pm$ bosons. There are no flavor changing neutral currents in the SM because the Z boson is neutral and can hence only couple to quarks of the same charge. For leptons, all experimental evidence is consistent with the mass eigenstates being equal to the weak eigenstates. Thus, there are

no weak processes that are capable of changing lepton flavor in the SM.

1.5 The Higgs Boson

We have seen how introducing an additional scalar doublet Φ with an appropriate potential can spontaneously break the $SU(2)_L \times U(1)_Y$ and give rise to mass terms for the vector bosons. We have also see how the field Φ can be used to give mass terms to the fermions of the SM in a gauge invariant way. However, our discussion has yet to consider terms involving the new scalar field $h(x)$ from Equation 1.63. Let us first combine the pieces of our previous discussion to write down the complete electroweak Lagrangian:

$$\mathcal{L}_{\text{EW}} = \mathcal{L}_{\text{gauge}} + \mathcal{L}_{\text{fermion}} + \mathcal{L}_{\Phi} + \mathcal{L}_{\text{Yukawa}} \tag{1.78}$$

The field Φ appears in both $\mathcal{L}_{\Phi}$ and $\mathcal{L}_{\text{Yukawa}}$. After SSB, we can plug the expression in Equation 1.63 into the above Lagrangian. This gives kinetic terms for the field $h(x)$ as well as terms which couple the field $h(x)$ to itself, fermions, and electroweak gauge bosons. We obtain a mass term for the $h(x)$ field, as well as cubic and quartic self interaction terms.

$$\mathcal{L}_h = \frac{1}{2}(\partial^{\mu} h)(\partial_{\mu} h) - \mu^2 h^2 - \lambda v h^3 - \frac{1}{4}\lambda h^4 \tag{1.79}$$

We can thus interpret the quantum of the field $h(x)$ as a scalar particle with mass

$$m_h = \sqrt{2}\mu^2 = \sqrt{\frac{\lambda}{2}}v. \tag{1.80}$$

This particle is known as the **Higgs boson**, and the field $h(x)$ is the **Higgs field**. The interactions between the Higgs field and the gauge vector bosons are

$$\mathcal{L}_{hV} = \left(\frac{h^2}{2v^2} + \frac{h}{v}\right)\left(2m_W^2 W_{\mu}^+ W^{-\mu} + m_Z^2 Z_{\mu} Z^{\mu}\right) \tag{1.81}$$

This gives rise to 3-point and 4-point interactions between the Higgs boson and the massive vector bosons. Finally, the interactions between the Higgs boson and the fermion

sector is given by

$$\mathcal{L}_{hf} = -\sum_f \frac{m_f}{v}\overline{f}fh \tag{1.82}$$

To summarize, we see that in order to explain the masses of the vector gauge bosons and fermions, we must have a new massive scalar particle that couples to the SM fields.

In 1973 the weak neutral current was observed for the first time in a bubble chamber at CERN, providing clear evidence of the existence of a new neutral boson consistent with the Z [43]. Then, in 1983, unambiguous evidence of direct production of the W and Z bosons was observed at the Super Proton Synchotron at CERN [44]–[47]. However, for nearly 50 years, the Higgs boson eluded experimental evidence. But in 2012, a new particle was observed by the ATLAS and CMS experiments at the Large Hadron Collider that was consistent with the SM Higgs boson [1], [2]. By fitting the mass distribution of dipho-
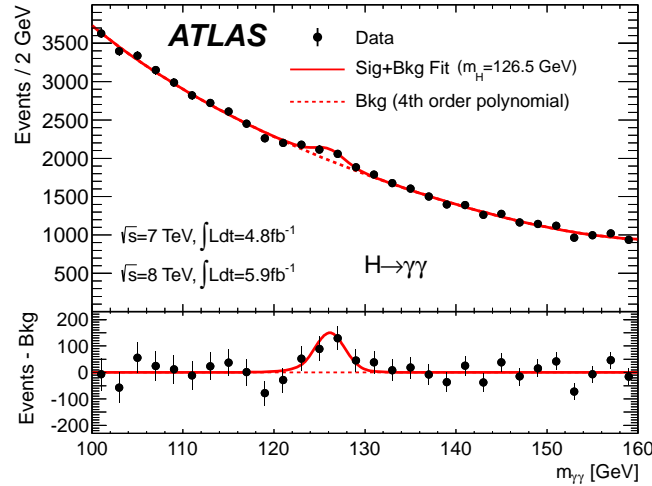
Figure 1.3: The invariant mass distribution of diphoton candidates observed using ATLAS data at $\sqrt{s} = 7$ TeV and $\sqrt{s} = 8$ TeV. The resonant structure in the distribution at 125 GeV constituted the first observation of the Higgs boson decaying to two photons. Image taken from [1].

ton and ZZ pairs as shown in Figure 1.3, the new particle was found to have a mass of roughly 125 GeV. The observation of the diphoton decay mode indicated that the new particle was not a vector boson, providing further evidence that was consistent with it being the SM scalar Higgs. This all but confirmed that the Higgs mechanism applied to the electroweak theory is an accurate description of Nature, and in 2013, François Englert and Peter Higgs were jointly awarded the Nobel Prize in Physics for their contributions to this
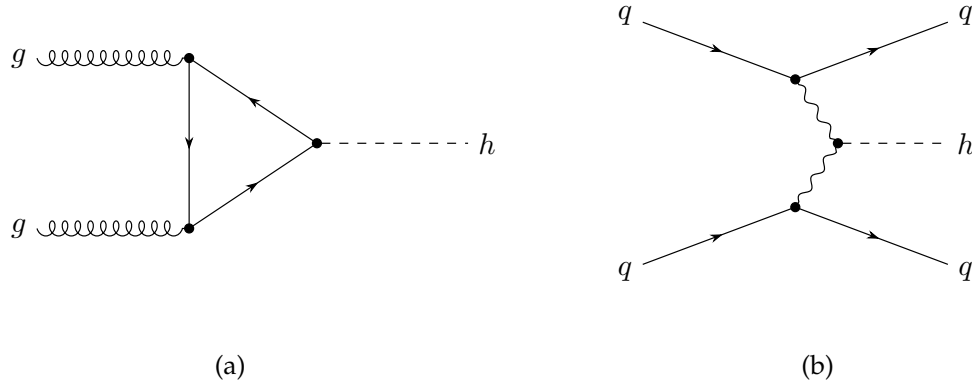
Figure 1.4: Leading order Higgs production modes via the (a) ggF and (b) VBF processes. Diagrams created using the T*ik*Z-Feynman package [48].

groundbreaking achievement.

Since the initial observation of the Higgs boson, a rigorous program has been under-way to study this new particle and better understand its properties. At proton-proton col-liders such as the Large Hadron Collider, the Higgs boson can be produced through several different interactions. Feynman diagrams of several leading-order production modes are shown in Figures 1.4 and 1.5, and the corresponding cross sections are given in Table 1.2.

As described above, the Higgs boson couples to all massive SM particles allowing for a

$\sqrt{s}$ (TeV)	Production cross section (in pb) for $m_h = 125$ GeV				
	ggF	VBF	WH	ZH	total
7	$16.9^{+4.4\%}_{-7.0\%}$	$1.24^{+2.1\%}_{-2.1\%}$	$0.58^{+2.2\%}_{-2.3\%}$	$0.34^{+3.1\%}_{-3.0\%}$	19.1
8	$21.4^{+4.4\%}_{-6.9\%}$	$1.60^{+2.3\%}_{-2.1\%}$	$0.70^{+2.1\%}_{-2.2\%}$	$0.42^{+3.4\%}_{-2.9\%}$	24.2
13	$48.6^{+4.6\%}_{-6.7\%}$	$3.78^{+2.2\%}_{-2.2\%}$	$1.37^{+2.6\%}_{-2.6\%}$	$0.88^{+4.1\%}_{-3.5\%}$	55.1
14	$54.7^{+4.6\%}_{-6.7\%}$	$4.28^{+2.2\%}_{-2.2\%}$	$1.51^{+1.9\%}_{-2.0\%}$	$0.99^{+4.1\%}_{-3.7\%}$	62.1

Table 1.2: The SM Higgs boson production cross sections for $m_h = 125$ GeV in pp collisions as a function of the center of mass energy [49].

wide range of potential decay modes. Figure 1.6 shows the predicted branching ratio of the Higgs to various final states as a function of m_h. For $m_h = 125$ GeV, the most favorable decay mode is $h \to b\bar{b}$ with Br($H \to b\bar{b}$) = 58%.
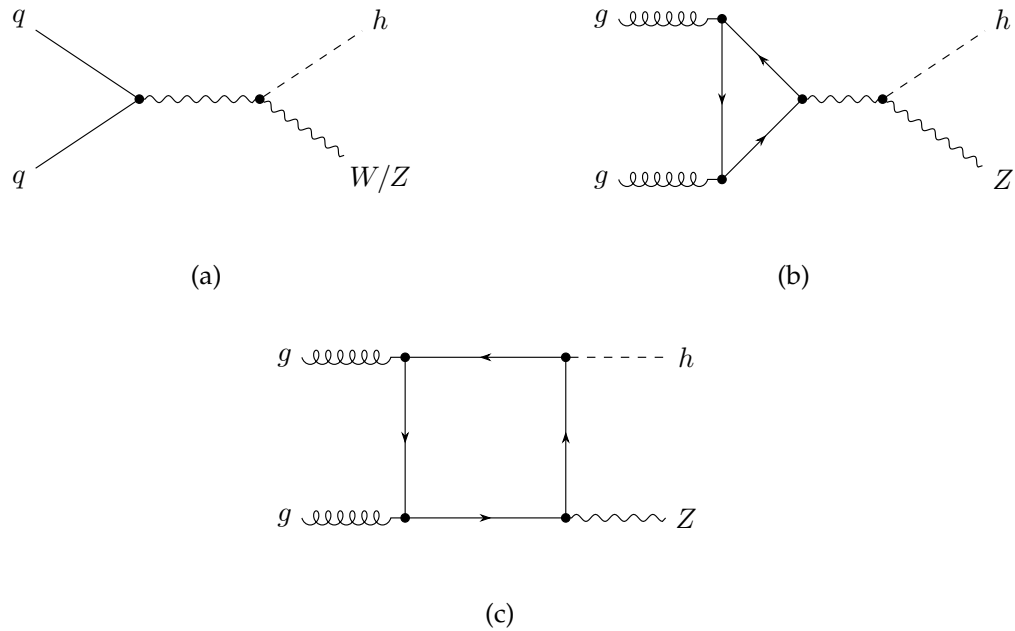
Figure 1.5: Leading order VH production modes via the (a) $qq \to VH$ and (b,c) $gg \to ZH$ processes. Diagrams created using the Ti*k*Z-Feynman package [48].
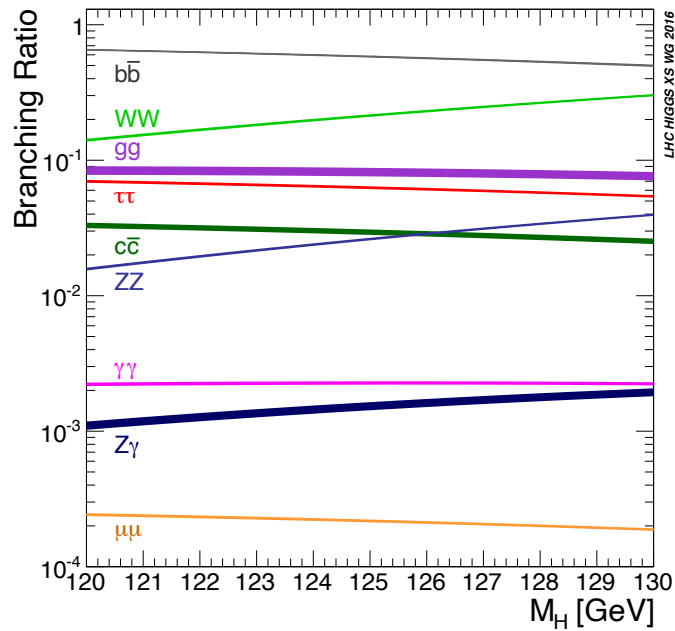
Figure 1.6: The branching ratios for the dominant decay modes of the SM Higgs boson as a function of m_h. Image taken from Ref [50].

1.6 Summary

Putting the pieces together, the complete SM Lagrangian is simply the sum of the QCD and EW Lagrangians (Equations 1.29 and 1.78)

$$\mathcal{L}_{\text{SM}} = \mathcal{L}_{\text{QCD}} + \mathcal{L}_{\text{EW}} \tag{1.83}$$

The complete particle content of the SM is summarized in Figure 1.7. In total, there are three generations of lepton doublets, three generations of quark doublets, four gauge bosons, and the Higgs boson.
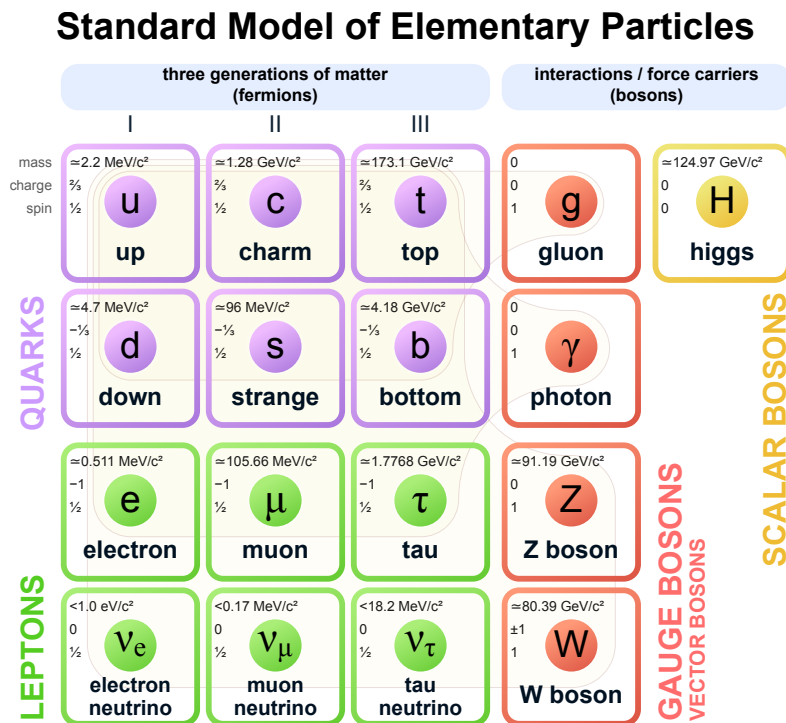
Figure 1.7: The particle content of the Standard Model.

The SM has been overwhelmingly successful at predicting the results of every collider experiment conducted thus far and to date, there has been no statistically significant evidence suggesting that any of the Standard Model's predictions are inconsistent with nature. This makes the SM unequivocally the most successful theory of physics of all time. This may be summarized by comparing the predicted and observed cross sections for a

range of SM processes. The total and fiducial production cross sections for several SM processes observed by the ATLAS experiment are shown in Figure 1.8, along with the most precise theoretical expectations currently available. Each measurement is found to agree with the theoretical expectation within uncertainties, underscoring the profound prediction power of the SM.
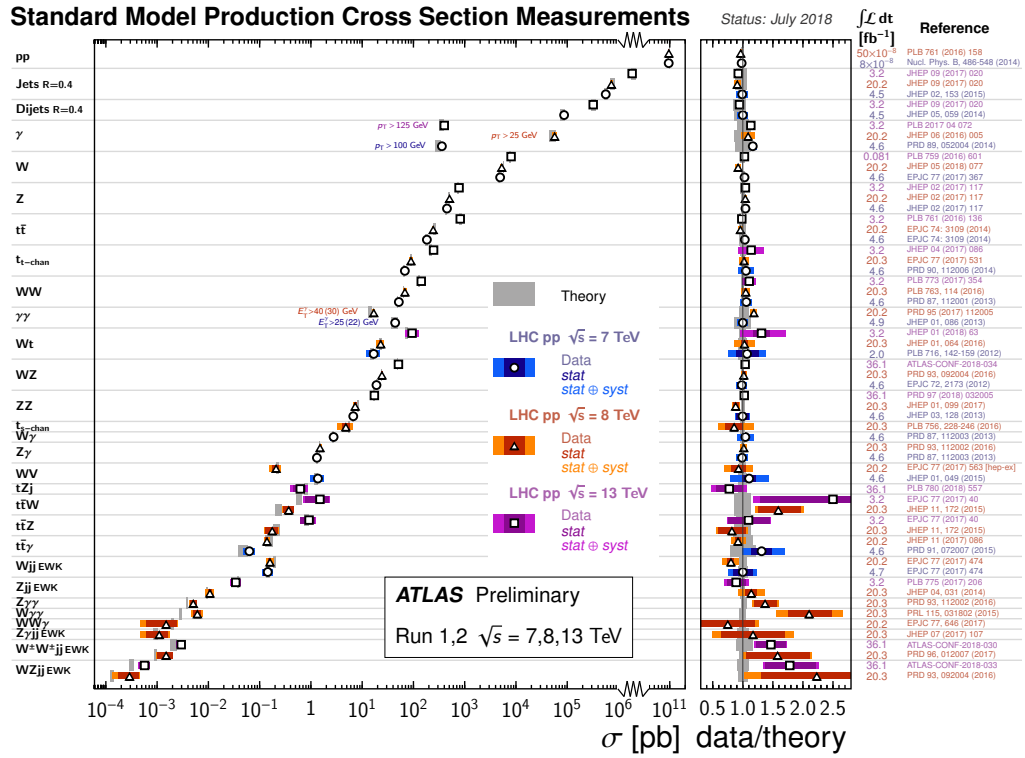
Figure 1.8: Summary of several Standard Model total and fiducial production cross section measurements, corrected for leptonic branching fractions, compared to the corresponding theoretical expectations. All theoretical expectations were calculated at NLO or higher. The dark-color error bar represents the statistical uncertainty. The lighter-color error bar represents the full uncertainty, including systematics and luminosity uncertainties. The data/theory ratio, luminosity used and reference for each measurement are also shown. Image taken from Ref [51].

Furthermore, the Higgs boson has now been observed in all of its dominant production modes, and the experimentally measured cross sections for each process have been found to be in perfect agreement with the SM predictions, as shown in Figure 1.9a. By measuring the cross section of the various decay modes, the strength of the interactions between the Higgs boson and SM particles can be tested (Equations 1.81 1.82). Figure 1.9b shows the coupling strength as a function of particle mass. All data points agree perfectly with the

SM predictions. At the time of writing, there has yet to be any indications of a discrepancy between the SM description of the Higgs boson and the observed properties of the particle observed at the LHC in 2012.

(a)   (b)
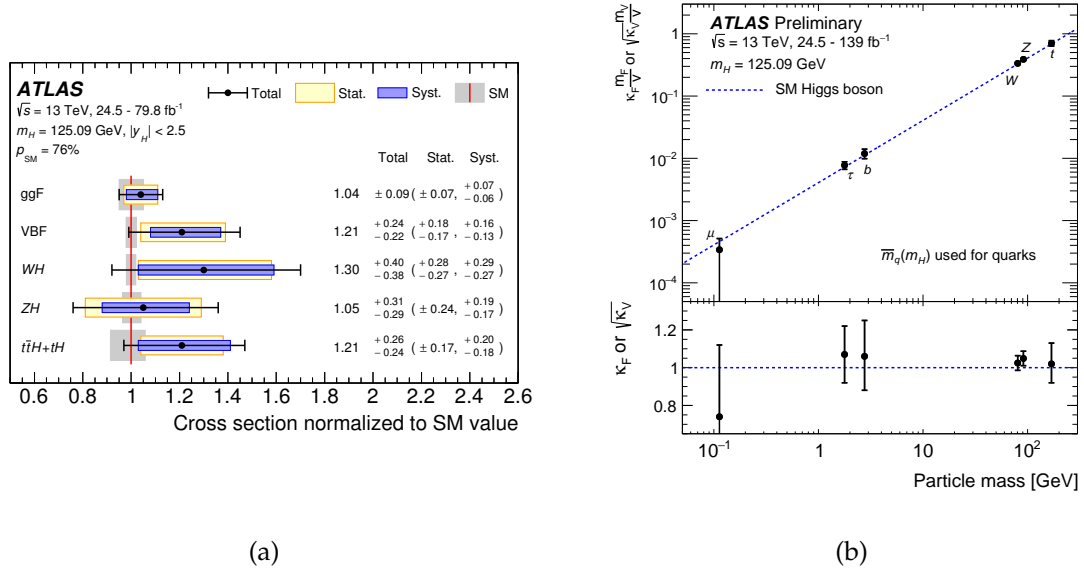
Figure 1.9: Experimental measurements of the properties of the Higgs boson compared to theoretical predictions by the Standard Model. (a) Cross sections for ggF, VBF, WH, ZH and $t\bar{t}H + tH$ normalized to their SM predictions. Image taken from Ref [52]. (b) Reduced coupling strength modifiers $\kappa_F \frac{m_F}{b}$ for fermions ($F = t, b, \tau, \mu$) and $\sqrt{\kappa_V} \frac{m_V}{v}$ for weak gauge bosons ($V = W, Z$) as a function of their masses m_F and m_V, respectively, and the vacuum expectation value of the Higgs field $v = 246$ GeV. The SM prediction for both cases is shown as a dotted line. Image taken from Ref [53].

1.6.1   Shortcomings of the Standard Model

In spite of the overwhelming successes of the SM, there are several glaring issues with the SM which remain unresolved. First and foremost, there are many fundamental phenomena observed in nature that are not predicted or explained by the SM. These include gravity, the nature of dark matter, neutrino masses, and the matter-antimatter asymmetry observed in the universe, among others. Second, there are theoretical problems with the SM which imply a lack of complete understanding of underlying phenomena. Examples include the hierarchy problem and the strong CP problem.
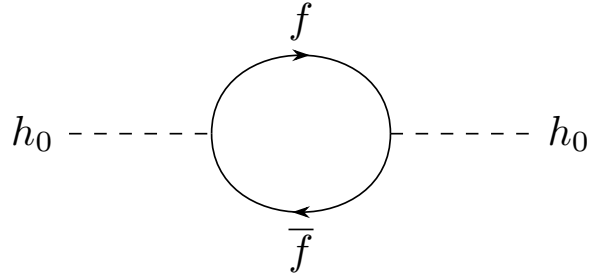
Figure 1.10: The contribution to the Higgs self energy due to a heavy fermion. Diagram created using the Ti*k*Z-Feynman package [48].

The Hierarchy Problem

When computing the mass of the Higgs boson at one-loop level, self-interactions, gauge loops, and fermion loops provide corrections to the bare mass:

$$m_h^2 = m_{h,0}^2 + \delta m_h^2$$

Consider the contribution to the self energy of the Higgs boson from the diagram in Figure 1.10. Let the $Hf\overline{f}$ coupling be λ_f. Computing this correction gives

$$
\begin{aligned}
\Sigma_{hh}^f(0) &= -N(f) \int \frac{d^4k}{(2\pi)^4} \mathrm{tr}\left[\left(i\frac{\lambda_f}{\sqrt{2}}\right) \frac{i}{\not{k}-m_f} \left(i\frac{\lambda_f}{\sqrt{2}}\right) \frac{i}{\not{k}-m_f}\right] \\
&= -2N(f)\lambda_f^2 \int \frac{d^4k}{(2\pi)^4} \frac{k^2 + m_f^2}{\left(k^2 - m_f^2\right)^2} \\
&= -2N(f)\lambda_f^2 \int \frac{d^4k}{(2\pi)^4} \left[\frac{1}{k^2 - m_f^2} + \frac{2m_f^2}{\left(k^2 - m_f^2\right)^2}\right]
\end{aligned}
\tag{1.84}
$$

where $N(f)$ is a multiplicity factor equal to the number of color indices of the fermion ($N(f) = 3$ for the SM quarks). The first term in the last expression of Equation 1.84 is quadratically divergent. This means that in order to explain the observed mass of the 125 GeV Higgs boson, its bare mass $m_{h,0}$ must be **fine-tuned** in order to almost perfectly counteract this divergent term. While this is not a physical dilemma, it is conceptually worrisome because it is at odds with the guiding aesthetic principal of **naturalness** which

posits that there should not be a hierarchy of scales among free parameters in a theory. This is what is known as the **hierarchy problem**.

Dark Matter

A range of astrophysical measurements point to the existence of a non-baryonic type of matter that is not described by the SM [54]–[56]. As early as the 1930s it was observed that the rotation curves of spiral galaxies could not be explained by their visible matter content alone. This phenomenon can be explained by the existence of **dark matter** (DM) which interacts gravitationally with visible baryonic matter but not electromagnetically. A representative distribution is shown in Figure 1.11 for the NGC 6503 galaxy. While
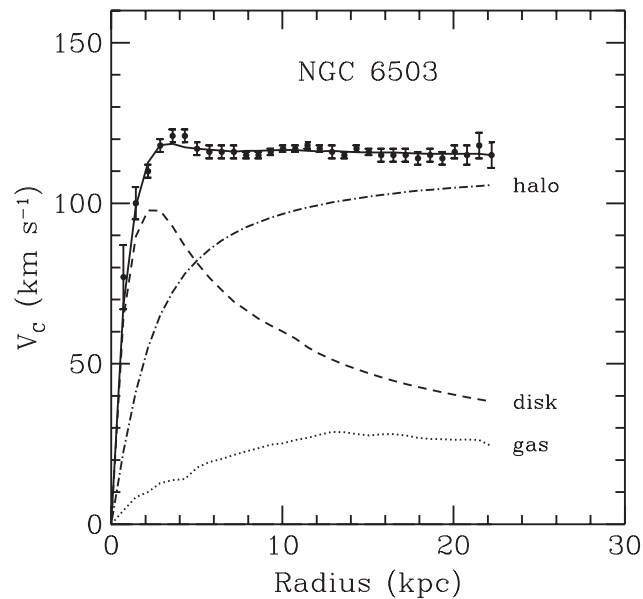
Figure 1.11: Rotation curve of the NGC 6503 galaxy. The dotted, dashed and dash–dotted lines are the contributions of gas, disk and dark matter, respectively. Image taken from Ref [57].

there are several ways of explaining these measurements, the most natural explanation is that DM comprised of **weakly interacting massive particles (WIMPs)**. It is now believed that as much as 27% of the matter content of the universe is comprised of dark matter, and yet there is currently no explanation as to what is it or how it fits into out current understanding of elementary particles. The fact that the SM does not provide a dark matter

candidate is one of the most compelling arguments for the existence of a more universal theory of particles beyond the SM.

Chapter 2

Physics Beyond the Standard Model

If you think this Universe is bad, you should see some of the others.

-Philip K. Dick

Reality is not always probable, or likely.

-Jorge Luis Borges

Given the shortcomings of the SM described in Section 1.6.1, there have been many efforts to develop a more complete theory which gives rise to the same predictions as the SM at low energies, but incorporates **Beyond Standard Model (BSM)** physics at higher scales. These range from "Theories of Everything" such as string theory, to "Grand Unified Theories" which unify the three gauge symmetries of the SM in one single gauge symmetry such as $SU(5)$ [58], to simple extensions to the SM gauge group via the inclusion of additional gauge symmetries. In this chapter, we will discuss some of these theories with an emphasis on phenomenology and prospect for discovery at hadron colliders. Section 2.1 introduces the concept of supersymmetry, which posits an additional symmetry of spacetime that can be used to simultaneously solve both the hierarchy problem as well as provide potential dark matter candidates. Section 2.2 then considers alternative scenarios that share similarities with supersymmetric models while evading certain experimental constraints. The phenomenology of these models is described in Section 2.3, which leads us to a general overview of long-lived particles in Section 2.4. Section 2.5 introduces a simplified class of models that can be used to search for new physics in a model independent way, and a

summary of existing constraints on these simplified models is summarized in Section 2.6 which provides further motivation for the search presented in this thesis.

2.1 Supersymmetry

In a famous "no-go" theorem published by Coleman and Mandula in 1967, the authors prove that the most general symmetry of the S-matrix takes the form of a direct product of Poincaré symmetry and internal symmetry [59]. That is to say, there can be no transformations acting on the fields which cannot be factorized into the product of two terms, one acting only on the particle type indices and the other acting only on the space-time indices. As written, this theorem seems to preclude symmetries which mix particles of different spins while still preserving non-trivial interactions. However, as is the case with most "no-go" theorems, it was only a matter of time before further symmetries of the S-matrix were discovered.

Supersymmetry (SUSY) is a principle of several notable BSM theories which posits the existence of a symmetry relating fermions and bosons [60]–[65]. At its core, SUSY is a feature of spacetime which extends the Poincaré algebra into a **super-Poincaré algebra**. The simplest supersymmetric extension of the Poincaré algebra adds a 2-component (Weyl) spinor Q and its conjugate $\overline{Q}$ with the anti-commutation relation

$$\{Q_\alpha, \overline{Q}_{\dot{\beta}}\} = 2\left(\sigma^\mu\right)_{\alpha\dot{\beta}} P_\mu \tag{2.1}$$

These operators generate the SUSY transformations, and acts on states as follows:

$$Q\left|\text{boson}\right\rangle = \left|\text{fermion}\right\rangle \tag{2.2}$$

$$Q\left|\text{fermion}\right\rangle = \left|\text{boson}\right\rangle \tag{2.3}$$

While this may seem to violate the Coleman and Mandula Theorem, a key assumption in the 1967 proof required that the generators of the spacetime symmetry be *bosonic* operators, that is, that they obey commutation relations and not anticommutation relations. In 1975, Haag, Lopuszanski and Sohnius generalized the Coleman Mandula theorem to show

that the only non-trivial quantum field theories have a symmetry group which is a direct product of a *super*-Poincaré group and internal symmetries [66]. This spurred a revolution in theoretical physics and paved the way for deriving the current understanding of SUSY.
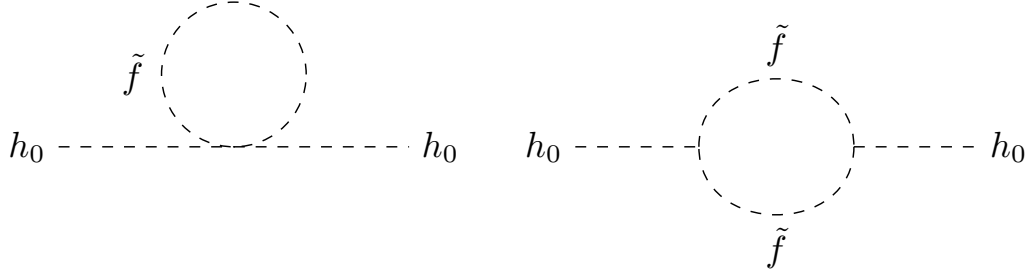
Figure 2.1: The contribution to the Higgs self energy due to a heavy sfermion $\tilde{f}$. Diagrams created using the Ti*k*Z-Feynman package [48].

The simplest extension to the SM which realizes SUSY is known as the **Minimal Supersymmetric Standard Model (MSSM)**. The MSSM essentially doubles the number of particles in the SM, but with the addition of an extended Higgs sector needed to cancel a gauge anomaly. In the MSSM, the gauge structure of the theory commutes with supersymmetry, implying that particles and their superpartners carry identical gauge charges. To see how the MSSM can resolve the hierarchy problem, consider a simplified example in which two complex scalars $\tilde{f}_L$ and $\tilde{f}_R$ are added to the SM which couple to the Higgs field as follows:

$$\mathcal{L}_{h\tilde{f}} = \frac{1}{2}\tilde{\lambda}_f h^2 \left(|\tilde{f}_L|^2 + |\tilde{f}_R|^2 \right) + v\tilde{\lambda}_f h \left(|\tilde{f}_L|^2 + |\tilde{f}_R|^2 \right) + \left(\frac{\lambda_f}{\sqrt{2}} A_f h \tilde{f}_L \tilde{f}_R^* + h.c. \right) \tag{2.4}$$

This Lagrangian gives additional contributions to Σ_{hh} (shown in Figure 2.1) which are computed as [67]:

$$\Sigma_{hh}^{\tilde{f}}(0) = -\tilde{\lambda}_f N(\tilde{f}) \int \frac{d^4k}{(2\pi)^4} \left[\frac{1}{k^2 - m_{\tilde{f}_L}^2} + \frac{1}{k^2 - m_{\tilde{f}_R}^2} \right] \qquad (2.5)$$

$$+ \left(\tilde{\lambda}_f v\right)^2 N(\tilde{f}) \int \frac{d^4k}{(2\pi)^4} \left[\frac{1}{\left(k^2 - m_{\tilde{f}_L}^2\right)^2} + \frac{1}{\left(k^2 - m_{\tilde{f}_R}^2\right)^2} \right]$$

$$+ |\lambda_f A_f|^2 N(\tilde{f}) \int \frac{d^4k}{(2\pi)^4} \left[\frac{1}{\left(k^2 - m_{\tilde{f}_L}^2\right)\left(k^2 - m_{\tilde{f}_R}^2\right)} \right]$$

where we have assumed $N(\tilde{f}_L) = N(\tilde{f}_R) = N(\tilde{f})$. The first term in Equation 2.5, which corresponds to the left diagram in Figure 2.1, is quadratically divergent. Comparing with Equation 1.84, one finds that these two terms can be made to cancel if the following properties are satisfied:

$$N(\tilde{f}) = N(f)$$

$$\tilde{\lambda}_f = -\lambda_f^2$$

While this may seem like trading one fine tuning for another, the remarkable thing is that in the MSSM this relation is *precisely satisfied* naturally from the symmetries of the theory[1]. Note that this cancellation does not rely on any particular values of the masses $m_{\tilde{f}_L}$, $m_{\tilde{f}_R}$ or the coupling A_f.

In addition to providing a solution to the hierarchy problem, SUSY is further motivated due to the fact that it can easily incorporate dark matter. **R-parity** is a $\mathbb{Z}_2$ symmetry acting on the fields of the MSSM defined as

$$P_R = (-1)^{3(B-L)+2s} \qquad (2.6)$$

All Standard Model particles have R-parity of $+1$ while supersymmetric particles have R-parity of -1. If R-parity is a conserved quantity, then the lightest supersymmetric particle (LSP) of the MSSM would be forbidden from decaying into any SM particle. This means

---

[1]For a full proof, see Ref [68], for example.

that the LSP is a stable, weakly interacting massive particle (WIMP), making it a prime dark matter candidate. Thus, the MSSM is an extremely promising theory that can simultaneously restore naturalness to the SM as well as potentially explain the nature of dark matter.

Finally, supersymmetry is also a necessary feature of all formulations of string theory which give a realistic description of low energy physics [2]. As a self-consistent formulation of quantum gravity, string theory is widely considered the most promising candidate for a Theory of Everything. Hence, SUSY is even further motivated as a potentially experimentally probeable manifestation of Plank scale physics.

2.2 Models of uncolored naturalness

Despite providing a compelling solution to the hierarchy problem, the top partners of the MSSM carry SM color, and are therefore expected to be produced abundantly at the LHC. In the absence of a discovery at collider experiments, the MSSM and other theories with colored top partners are becoming increasingly constrained. However, it is also possible for extensions of the SM to address the hierarchy problem while introducing top partners which *do not carry SM color*, due to the fact that the cancellation mechanism in Equation 2.5 works independently of the color of the particles in the loop. That is to say that color in this context is nothing but a dummy index that is summed over, and it is logically consistent for top partner states to be SM color-neutral. Because the production cross-section of the uncolored top partners is significantly reduced, these models of **neutral naturalness (NN)** can help resolve the hierarchy problem while evading constraints imposed by experiment. In this section we will briefly review the most notable examples of NN: Folded SUSY, Twin Higgs, and Quirky Little Higgs models.

2.2.1 Folded SUSY

Folded SUSY (FS) theories [69], [70] address the question: can we have SUSY with colorless stops? In FS theories, at low energies the Lagrangian for the top sector has the same

---

[2]Bosonic string theory exists without supersymmetry, but since we know fermions to exist, it should not be considered a theory with a realistic description of low energy physics.

form as in in MSSM, however the scalars are not charged under SM color, but rather a new hidden color group. To realize this, FS theories turn to 5D constructions with the extra dimension compactified on $S_1/\mathbb{Z}_2$. In these extra dimensional models, the five dimensional space is called the *bulk*, and the surfaces at the points $y = 0$ and $y = \pi R$ are called *branes*, where y is the coordinate of the fifth dimension. These models rely on the parent/daughter *orbifold correspondence*, which is a relationship that exists between the correlation functions of supersymmetric "parent" theories and those of their non-supersymmetric "orbifold daughters" which are created by projecting out states of the parent theory by a discrete symmetry. Using this correspondence, it is possible to build non-SUSY daughter models that cancel the quadratic divergences of the Higgs mass due to the SUSY of the parent theory.

The gauge structure of FS models is

$$SU(3)_A \times SU(3)_B \times SU(2)_L \times U(1)_Y \tag{2.7}$$

i.e. the gauge structure of the SM with an additional $SU(3)_B$. Despite not having SM color, the stops charged under $SU(3)_B$ must couple to the SM-like Higgs identically to the stops in the MSSM in order to protect the Higgs mass through the mechanism described in Section 2.1. However, the stops in Folded SUSY still carry EW charge, which implies that they must not be lighter than 100 GeV due to LEP-era constraints [71]. The lightest states in the mirror sector will therefore be pure gauge $SU(3)_B$ states known as **mirror glueballs**.

2.2.2   Twin Higgs

Twin Higgs models posit the existence of an additional copy of the SM called the Twin (or mirror) sector, along with a discrete $\mathbb{Z}_2$ symmetry that exchanges the two sectors [72]. In these models, the Higgs is identified as a **pseudo-Nambu Goldstone boson (pNGB)** of an additional global symmetry that is spontaneously broken by one of the two fields acquiring a vev $f/\sqrt{2}$. The amount of this vev contained in each sector is given by

$$v_A \equiv f \sin\left(\frac{v}{f}\right) = f \sin\vartheta, \, v_B \equiv f \cos\left(\frac{v}{f}\right) = f \cos\vartheta \tag{2.8}$$

where $v_A = 246$ GeV.

The $\mathbb{Z}_2$ symmetry between the SM and twin sectors ensures that the quadratic correc-
tions to the Higgs mass due to gauge and fermion loops are canceled. Unlike Folded SUSY,
light fermions charged under the mirror $SU(3)_B$ will be EW singlets and are therefore not
excluded from existing constraints. However in the absence of light mirror QCD matter,
the low energy limit of the Twin Higgs model can be described similarly to Folded SUSY
as a pure gauge $SU(3)_B$ theory giving rise once again to glueballs of $SU(3)_B$.

2.2.3 Quirky Little Higgs

Finally, there are several BSM models which posit the existence of "quirks", or quark-like
fermions that are charged under a different $SU(3)_B$ group than the SM quarks. One might
naively suspect that a theory could be devised in such a way that the "top quirk" cancels
the divergence caused by the top quark loop in the Higgs mass calculation. However,
without a symmetry argument requiring the cancellation of the divergence, this would not
amount to a solution of the hierarchy problem, but rather an additional instance of unnat-
ural fine-tuning. The **Quirky Little Higgs (QLH)** model [73] ensures this cancellation by
embedding the $SU(3)_A$ and $SU(3)_B$ groups in a larger gauge symmetry.

Similar to FS, QLH is a 5D construction which is compactified over an $S_1/\mathbb{Z}_2$ orbifold
with branes at $y = 0$ and $y = \pi R$. The gauge structure of the bulk is $SU(6) \times SU(3)_W \times U(1)_X$, but boundary conditions on the brane at $y = 0$ break the gauge symmetry to
$SU(3)_A \times SU(3)_B \times SU(2)_L \times U(1)_Y$. Thus, the gauge structure of QLH is identical to
that of FS. The most notable difference between QLH and FS constructions is that the
top-partners in QLH are *fermions*, but the low-energy phenomenology of QLH models is
largely identical to FS. Like FS, the fermionic top-partner in QLH carries EW charge and
therefore the bottom of the $SU(3)_B$ spectrum will consist of pure gauge states.

2.3 Neutral naturalness phenomenology

As described above, models of uncolored naturalness generally involve a mirror sector that
can be described as a pure $SU(3)_B$ gauge theory in the low energy limit with pure gauge

mirror glueballs comprising the bottom of the mirror $SU(3)_B$ spectrum. The spectrum of pure QCD glueball states has been computed using lattice methods and provides a description of 12 stable eigenstates [74]. The mirror glueball masses are entirely determined by the running of the $SU(3)_B$ coupling constant α_s^B and are given as multiples of m_0, the mass of the scalar glueball state at the bottom of the spectrum, denoted 0^{++}. The value of m_0 is thus highly dependent on the choice of model and relevant model parameters, but has been shown to be preferred in the range of 12 - 55 GeV [75].

2.3.1 Exotic Higgs decays

Just as the SM Higgs boson couples to gluons through a top quark loop, the corresponding top-partner loop provides a coupling between the Higgs and the mirror glueballs of NN. Assuming that the mass of the top partner is sufficiently heavy, this interaction may be described in an effective field theory through the addition of a dimension-6 operator to the SM:

$$\delta\mathcal{L}^{(6)} = \frac{\alpha_s^B}{3\pi}\left[\frac{y^2}{M^2}\right]|H|^2 G_{\mu\nu}^{(B)}G^{(B)\mu\nu} \tag{2.9}$$

where H is the SM-like Higgs doublet, $G_{\mu\nu}^{(B)}$ is the $SU(3)_B$ field strength tensor, and $\left[y^2/M^2\right]$ is a coefficient that depends on the specific UV-complete theory being considered. For Folded SUSY, this coefficient is given by

$$\frac{y^2}{M^2} = \frac{1}{8v^2}\frac{m_t^2}{m_{\tilde{t}}^2} \tag{2.10}$$

where $m_{\tilde{t}}$ is the FS stop mass. For certain Twin Higgs models, it is found to be

$$\frac{y^2}{M^2} = \frac{1}{4v_A^2}\frac{m_t^2}{m_T^2}\cos\vartheta \tag{2.11}$$

where m_T is the mass of the top partner.

Given that the preferred mass of the lightest glueball state satisfies $m_0 < m_h/2$, this coupling gives rise to the possibility of exotic Higgs decays to pairs of mirror glueballs. This decay is therefore regarded as a "smoking gun" signature of NN models. For a simplified scenario assuming symmetric two-body Higgs decays only, the branching ratio of
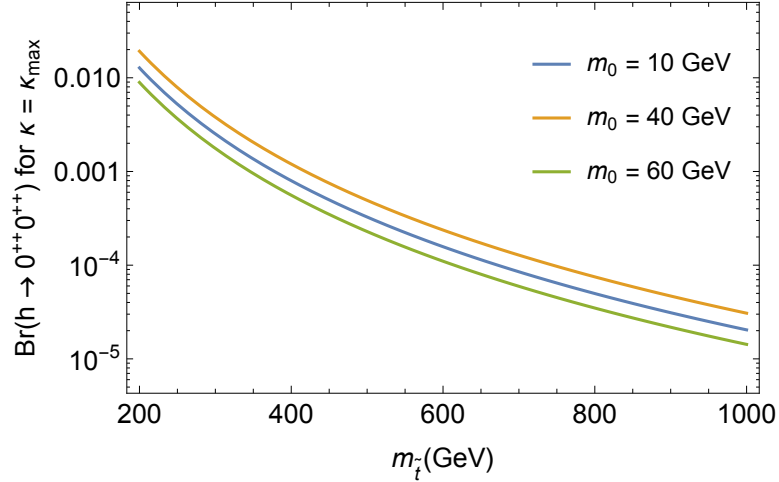
Figure 2.2: The branching ratios of the Higgs boson to pairs of light glueball states 0^{++} as a function of top-partner mass $m_{\tilde{t}}$. Image taken from Ref [75].

the Higgs to pairs of mirror glueball states 0^{++} is given by

$$\text{Br}(h \rightarrow 0^{++}0^{++}) \approx \text{Br}(h \rightarrow gg)_{\text{SM}} \cdot \left(\frac{\alpha_s^B(m_h)}{\alpha_s^A(m_h)} 4v^2 \left[\frac{y^2}{M^2} \right] \right)^2 \cdot \sqrt{1 - \frac{4m_0^2}{m_h^2}} \cdot \kappa(m_0) \quad (2.12)$$

where $\kappa(m_0)$ is a parameter which represents potential effects from glueball hadronization that are not taken into account [75]. The branching ratios are shown as a function of $m_{\tilde{t}}$ for Folded SUSY in Figure 2.2 assuming $\kappa(m_0) = 1$. Depending on the values of m_0 and $m_{\tilde{t}}$, the branching ratio $\text{Br}(h \rightarrow 0^{++}0^{++})$ can be on the order of 1%, making this decay mode easily probeable by current LHC experiments and well within the current experimental constraints on Higgs decays to exotic states (see Section 2.6).

2.3.2 Glueball decays

The dimension-6 operator in Equation 2.9 also provides a mechanism for glueballs to decay back to SM particles through an off-shell Higgs. For the lightest glueball decaying to two SM particles ξ, the decay width is given by [76]:

$$\Gamma(0^{++} \rightarrow \xi\xi) = \left(\frac{1}{12\pi^2} \left[\frac{y^2}{M^2} \right] \frac{v}{m_h^2 - m_0^2} \right)^2 (4\pi\alpha_s^B \mathbf{F_{0^{++}}^S})^2 \Gamma_{h \rightarrow \xi\xi}^{\text{SM}}(m_0^2), \quad (2.13)$$
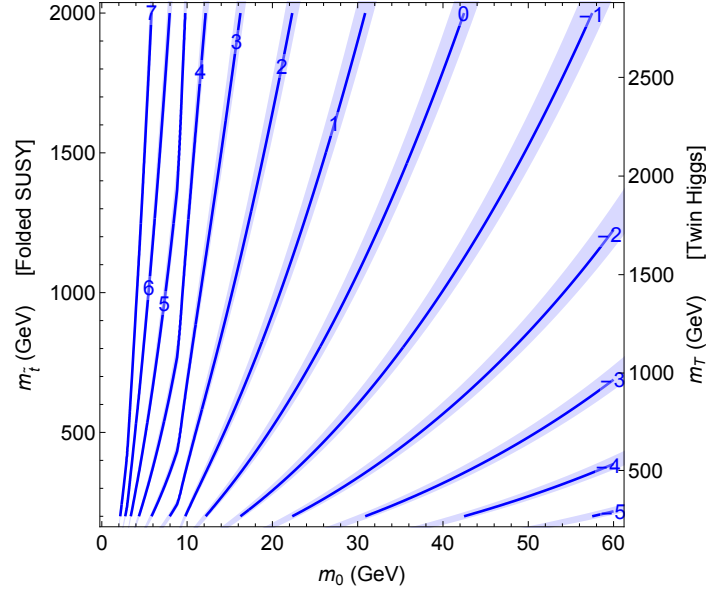
Figure 2.3: Contours of $\log_{10} c\tau/m$, where $c\tau$ is the mean proper lifetime of the lightest glueball state 0^{++}. Image taken from Ref [75].

where $\mathbf{F}^{\mathbf{S}}_{\mathbf{0}^{++}} = \langle 0| \operatorname{Tr} G^{(B)}_{\mu\nu} G^{(B)\mu\nu} |0\rangle$, and $\Gamma^{\mathrm{SM}}_{h\to\xi\xi}(m_0^2)$ is the partial decay width of a SM-like Higgs boson with mass m_0. Thus, the branching ratios of mirror glueballs are identical to those of a SM-like Higgs boson of the same mass. From the discussion in Section 1.5, we know that the dominant mirror glueball decay mode will thus be to $b\bar{b}$, giving rise to a $4b$ final state.

From Equation 2.13, we may compute the proper lifetime of the glueballs using Equation 1.2. The glueball lifetimes are shown as contours of $\log_{10} c\tau/m$ in Figure 2.3 as functions of m_0 and both $m_{\tilde{t}}$ and m_T for the Folded SUSY and Twin Higgs scenarios, respectively. For masses in the preferred mass range of $12-55$ GeV, the lifetime of the lightest glueball state spans nine orders of magnitude, ranging from microns to kilometers. Particles with such macroscopic proper lifetimes are referred to as **long-lived particles (LLPs)** due to the fact they will travel sizeable distances from the primary interaction point prior to decaying. Thus, we arrive at an important conclusion: models of uncolored naturalness give rise to the signature of exotic decays of the Higgs boson to pairs of long-lived scalar particles with masses in the $12-15$ GeV range. Such decays would provide striking detector signatures and would likely be missed without dedicated searches. This signature will

be further motivated in the next section.

2.4 Long-lived particles

In addition to strong motivation from top-down theories of Neutral Naturalness, LLPs are becoming increasingly well motivated from an experimental point of view. As we approach the beginning of the third run of the LHC, the absence of new physics observed at the LHC is becoming more and more perplexing: we know that it must exist, yet we still have as many unanswered questions as we did before the beginning of the LHC era. While it may well be the case that new physics is above the scale accessible by the LHC, or requires a much larger dataset to observe, we must consider the possibility that we are looking for new physics in the wrong places. Nature may not necessarily be kind to the experimentalist, and within the vast theory space available there are many scenarios that give rise to more challenging detector signatures that may be extremely difficult to observe. While the general approach at the beginning of the LHC era was to start with the simplest search scenarios, the plethora of null search results has led experimentalists to begin focusing their efforts on well-motivated but significantly more challenging searches. These include low-mass, low cross section signals, very soft final states, and most notably, non-prompt BSM decays. From the detector perspective, LLPs are of particular interest due to their ability to elude the majority of searches which rely on the assumption that the BSM particles will decay close to the primary interaction point. However, if the lifetime of the LLPs is such that they decay within the fiducial volume of the LHC experiments they can provide striking detector signatures with little to no SM backgrounds. Figure 2.4 shows an overlay of several different long-lived signatures that are being pursued at the LHC, including disappearing tracks, emerging jets, and various displaced jet scenarios. Each of these signatures requires a dedicated search with non-standard analysis strategies.

Despite giving rise to unconventional detector signatures, long-lived particles are not an intrinsically exotic phenomena that should be discounted as a fringe corner of phase space. From Fermi's golden rule (Equation 1.5) we know that there are many possible mechanisms which may give a particle a long lifetime, such as small couplings, heavy
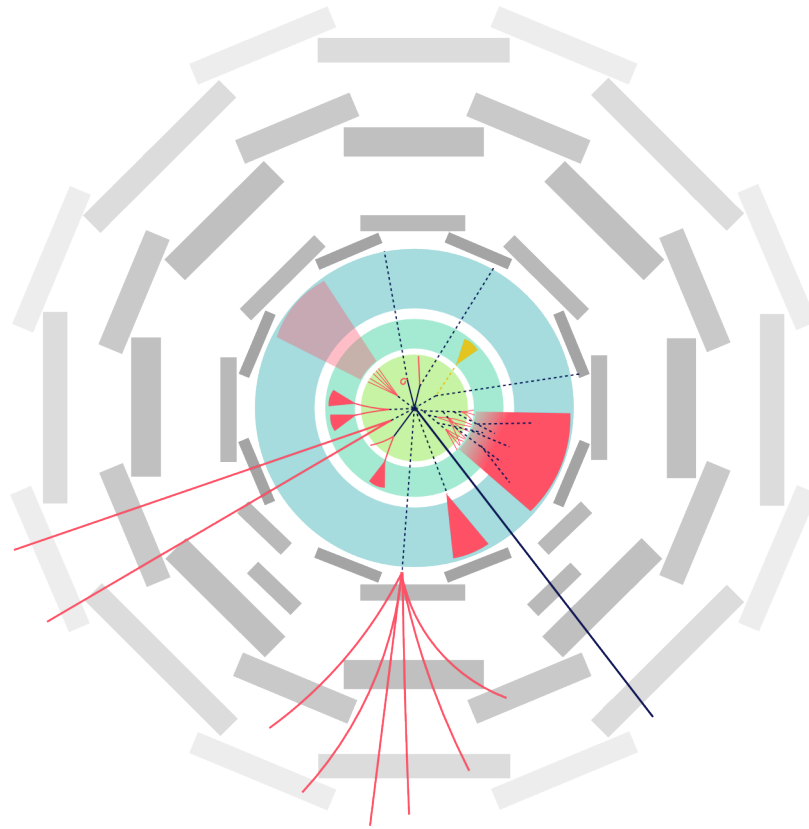
Figure 2.4: An overlay of several different LLP signatures in the ATLAS detector [77].
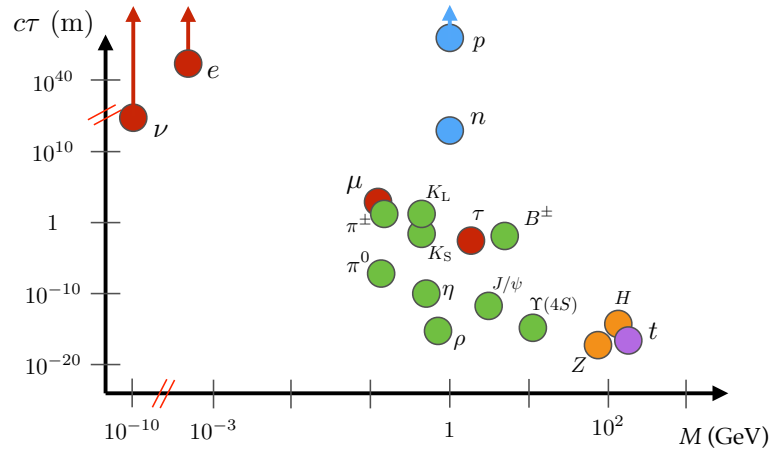
Figure 2.5: The lifetime $c\tau$ as a function of particle mass for a variety of particles in the Standard Model. Image taken from Ref [78].

mediators, and phase space suppressions from small mass splittings. Figure 2.5 shows the lifetime as a function of particle mass for several SM particles. There are many particles in the SM that have very macroscopic lifetimes, ranging from metastable particles like Kaons and b-hadrons with lifetimes on the order of a few cm, to the muon with it's nearly 1 km lifetime. Thus, given the existence of LLPs in the Standard Model, it is perfectly reasonable to consider the scenario in which BSM particles may also have macroscopic lifetimes. Any model with small couplings, small mass splittings, or decays via off-shell particles can similarly give rise to long lived particles.

Due to the exponential nature of particle decays (Section 1.1.1), the highest density of decays per-unit volume will always occur close to the LLP production point. This means that searches for LLP decays in the innermost tracking subsystems of particle detectors at the LHC have sensitivity for wide ranges of proper lifetimes and are among the most promising strategies for observing LLP signatures. In particular, if the LLPs decay within the volume of the silicon tracking detectors of the ATLAS and CMS experiment, their decay position may be precisely reconstructed as a **displaced vertex (DV)** from the reconstructed trajectories of its charged decay products. Example diagrams of this signature are shown in Figure 2.6. Depending on the angular separation of the decay products, a hadronically decaying LLP can give rise to either a single merged jet (Figure 2.6a) or a pair of well-separated jets (Figure 2.6b) that originate from a common vertex. Searches for this

(a)   (b)
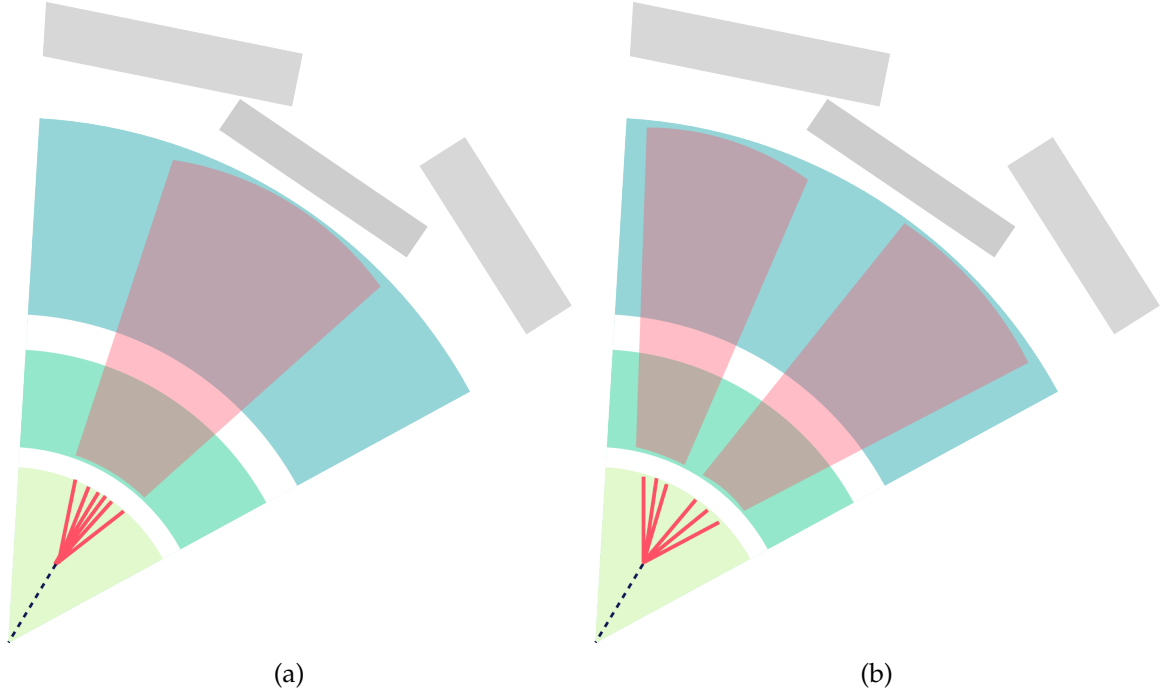
Figure 2.6: A long-lived particle hadronically decaying in the inner detector to (a) a single reconstructable jet [79] and (b) two reconstructable jets in the calorimeters [80].

signature are thus sensitive to a wide range of potential BSM scenarios with LLPs.

2.5 Bottom-up considerations

We have now seen that LLP signatures are well-motivated both from top-down theories of Neutral Naturalness described Section 2.2, as well as from a generic detector perspective as constraints on strongly-interacting theories with traditional detector signatures grow ever more stringent. Throughout the past several years prior to the writing of this thesis, the focus of much of the theory community has shifted away from specific UV-complete models of new physics toward more phenomena-driven approaches to hopefully identify such signatures. This so-called "bottom-up" approach attempts to build simplified models that give rise to unique signatures. Considering these simplified models allows signature-driven searches to proceed in a largely model-independent way and remain sensitive to a wide range of top-down BSM scenarios. These models should not necessarily be considered "toy models", but rather potential scenarios that arise naturally in the IR limits of

more complete theories of Neutral Naturalness. These models simplify the task of simulating BSM physics while still containing the relevant phenomenological signatures needed to probe UV complete scenarios. Two such scenarios are described in the remainder of this section.

2.5.1 The hidden sector

Hidden Valleys (HVs), also known as Hidden or "Dark" Sectors, are a generic class of models in which a new confining gauge group is added to the SM [81]. Unlike the pure gauge scenarios discussed in Section 2.2, HV models consider light "v-particles" that are charged under the new gauge group but neutral under the SM. Due to the confining nature of the HV gauge group the v-particles will assemble into neutral bound states called **v-hadrons**. In these models, v-hadrons masses are predicted to be much smaller than 1 TeV but can only be observed by passing over a barrier separating the hidden sector from the Standard Model sector creating a so-called "valley" of states.

To explore the phenomenology of HV models further, let us consider a concrete example[3]. We begin by extending the SM gauge group with an additional $U(1)' \times SU(n_v)$ symmetry, where $n_v > 2$. If the $U(1)$ symmetry is broken via a scalar vev $\langle \phi \rangle$, we obtain a massive gauge boson labeled Z'. The $U(1)$ breaking is also responsible for giving mass to the v-particles via the usual Higgs mechanism. For values of the HV confinement scale Λ_v between 1 GeV and 1 TeV, we expect Z' masses on the order of 1–6 TeV [81]. Both Standard Model fermions and v-particles will carry $U(1)'$ charge, allowing the Z' to serve as a mediator between the HV and the SM. The TeV-scale mass of the Z' gives rise to the aforementioned "barrier" between the two sectors.

If the SM-like Higgs boson mixes with ϕ, then this model predicts exotic Higgs decays to pairs of v-hadrons. The v-hadrons may be unstable, decaying back to SM particles via their mutual interaction with the Z'. In some scenarios, v-hadrons decay preferentially to heavy flavor giving rise to the same $H \to b\bar{b}b\bar{b}$ final state observed in the Neutral Naturalness models considered previously. Given the large Z' mass, the lifetime of the v-hadrons may be sizeable. A diagram of the $H \to b\bar{b}b\bar{b}$ process as predicted by the HV scenario is

---

[3]It should be noted that this is just one example of a large set of possible models.

shown in Figure 2.7. Thus, in this example we have constructed a simplified model with
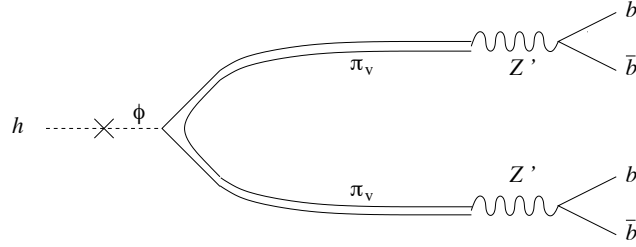
Figure 2.7: Diagram of Higgs decays to v-pions, each of which decay to $b\bar{b}$. The mixing with the scalar ϕ provides the mechanism for the coupling between the Higgs boson and the hidden sector. Image taken from Ref [82].

similar phenomenology to the top-down Neutral Naturalness models but from an entirely bottom-up approach that does not rely on a specific UV-completion.

2.5.2 A simplified model

To maximize the discovery potential of a search for BSM physics, it is useful to conduct the search in a way which is as model-independent as possible. Thus, rather than focusing on a particular model, the search described in this thesis instead considers an even simpler model to the HV scenarios in which a single additional scalar field is added to the SM which couples to the Higgs field via the renormalizable Higgs portal interaction $\epsilon S^2 H^\dagger H$. A simple model can be constructed with the scalar Lagrangian

$$\mathcal{L}_{\text{scalar}} = \mathcal{L}_{\text{kin}} - \frac{1}{2}\epsilon S^2 H^\dagger H + \frac{1}{2}\mu_S S^2 - \frac{\lambda_s}{4!}S^4 + \mu_H^2 H^\dagger H - \lambda_H \left(H^\dagger H\right)^2 \tag{2.14}$$

where a discrete Z_2 symmetry $S \to -S$ has been imposed to prevent all terms cubic and linear in S^4. Depending on the choice of couplings, the value of the scalar potential may have a minimum at $S = 0$ in which case the Z_2 symmetry will be unbroken and there will be no mixing between the H and S fields. Thus, the scalar S will not decay and the coupling ϵ induces the invisible Higgs boson decay mode $h \to ss$. If the minimum instead has $S \neq 0$, then the two fields acquire nonzero vevs, $S = s + v_s$ and $H = (h + v_h)/\sqrt{2}$, and the two scalar states will mix. One of the mass eigenstates may be identified with

---

[4]These terms complicate the model but do not drastically change the phenomenology. Thus, for the sake of this discussion the simplified model is sufficient.

the observed Higgs boson mass $m_h = 125$ GeV, and v_h may be identified as the usual Higgs vev, $v_H = 246$ GeV. The remaining free parameters in the Lagrangian written in Equation 2.14 may be identified with the mass of the new scalar, the mixing angle,

$$\sin \theta = \frac{\epsilon v_h v_s}{m_h^2 - m_s^2} + \mathcal{O}(\epsilon^3) \tag{2.15}$$

and the hss coupling constant. After symmetry breaking, the effective Lagrangian contains the term

$$\mathcal{L} \ni \frac{\kappa}{2} h s^2 = \frac{1}{2} \sqrt{\frac{\lambda_s}{3}} \sin \theta \left(\frac{m_h^2 + 2m_s^2}{m_s} \right) h s^2 \tag{2.16}$$

which governs the interaction of the Higgs with two BSM scalar particles.

The partial width for decays of the Higgs boson to these new scalars is then given by

$$\Gamma(h \to ss) = \frac{1}{16\pi} \frac{\kappa^2 v_h^2}{m_h} \beta_f \tag{2.17}$$

where $\beta_f = \sqrt{1 - 4m_f^2/m_s^2}$. At lowest order, the partial decay width of the scalar to pairs of fermions is given by

$$\Gamma(s \to f\bar{f}) = \sin^2 \theta_S \frac{N_c}{8\pi} \frac{m_s m_f^2}{v_h^2} \beta_f^3 \tag{2.18}$$

where N_c is the number of colors (3 for quarks, 1 for leptons). This width is equivalent to the Standard Model-like Higgs of the same mass reduced by a factor of $\sin^2 \theta$, i.e. $\Gamma_s = \Gamma_{h,\text{SM}}(m_s) \sin^2 \theta$. The branching ratios $B(s \to \text{SM})$ and $B(h \to ss \to \text{SM})$ may then be computed from Equations 2.17 and 2.18, and are shown in Figure 2.8 as functions of the scalar mass m_s. Assuming that s cannot decay to other non-SM fields, the mixing angle then determines the lifetime $c\tau$ of the scalar s. For sufficiently small values of the mixing angle ($\theta \lesssim 10^{-5}$), the lifetime of s is macroscopic, giving us a model of Higgs boson decays to pairs of LLPs.

Although this is a simplified model, is has been used to describe a wide range of phenomena such as dark matter and naturalness and appears in the IR limit of more complete models such as Folded SUSY and Quirky Little Higgs. Thus, targeting this model allows for constraints to be placed on a wide range of top-down BSM scenarios. In this thesis, this SM+scalar model will be referred to as the **signal model**, and the specific $h \to ss \to b\bar{b}b\bar{b}$
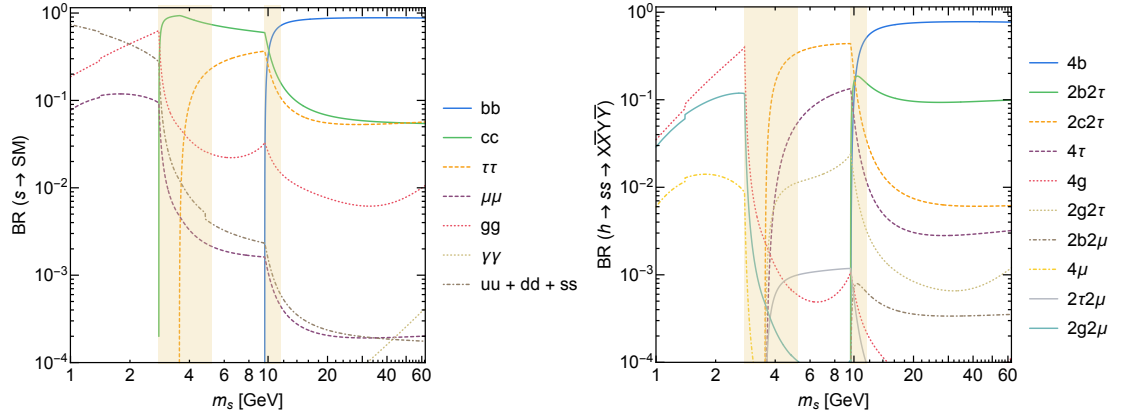
Figure 2.8: Branching ratios of (left) a CP-even scalar singlet to SM particles, as a function of m_s, and (right) exotic decays of the Higgs boson to as a function of m_s. Image taken from Ref [83].

process is the **signal process**. All non-signal processes will be referred to as **background**.

2.6   Existing constraints on $\mathbf{Br}(H \to ss)$

Under the assumption that new physics does not increase the magnitude of the couplings of the Higgs boson to W/Z bosons, current experimental constraints allow for branching ratios of the Higgs boson to BSM states of up to 21% [52], [84]. As shown in Figure 2.2, the predicted branching ratios of the Higgs to pairs Folded SUSY mirror glueballs range from $10^{-5} - 0.01$, meaning that indirect probes through SM Higgs measurements are currently insensitive to this signature. Thus, dedicated searches for exotic Higgs decays are necessary.

Several searches for $h \to ss \to b\bar{b}b\bar{b}$ decays have been performed at the LHC, optimized for different regimes of $c\tau_s$. To identify LLP decays in the hadronic calorimeter, the ATLAS experiment uses a dedicated trigger algorithm to select jets with anomalously high ratios of energy deposited in the hadronic and electromagnetic calorimeters, providing sensitivity for 0.1 m $\lesssim c\tau_s \lesssim$ 10 m [85], [86]. ATLAS extends this sensitivity up to $c\tau_s \lesssim$ 100 m with searches for LLPs decaying within the muon spectrometer. These searches make use of a dedicated trigger algorithm which identifies clusters of regions of interest in the muon spectrometer [85]. Offline, these searches reconstruct DVs from muon spectrometer tracks

and further require large missing transverse energy or a second displaced vertex in the ATLAS inner detector, providing sensitivity to a wide range of LLP lifetimes [87], [88]. All of these searches rely on dedicated triggers designed to select events with LLPs decaying in the ATLAS calorimeter or muon spectrometer. The lack of an equivalent trigger for LLP decays in the ATLAS inner detector has been a limiting factor in probing LLP lifetimes less than 10^{-2} m.

Other LHC experiments have developed searches targeting this lifetime regime. The LHCb experiment performed a search for DVs resulting from LLP decays with sensitivity in the range 1 mm $\lesssim c\tau_s \lesssim$ 0.1 m [89]. The CMS experiment also has a robust LLP search program, and has placed limits on Higgs decays to LLPs in the range 1 mm $\lesssim c\tau_s \lesssim$ 1 m for $m_s \geq$ 40 GeV using a DV signature [90]. These results are shown in Figure 2.9.
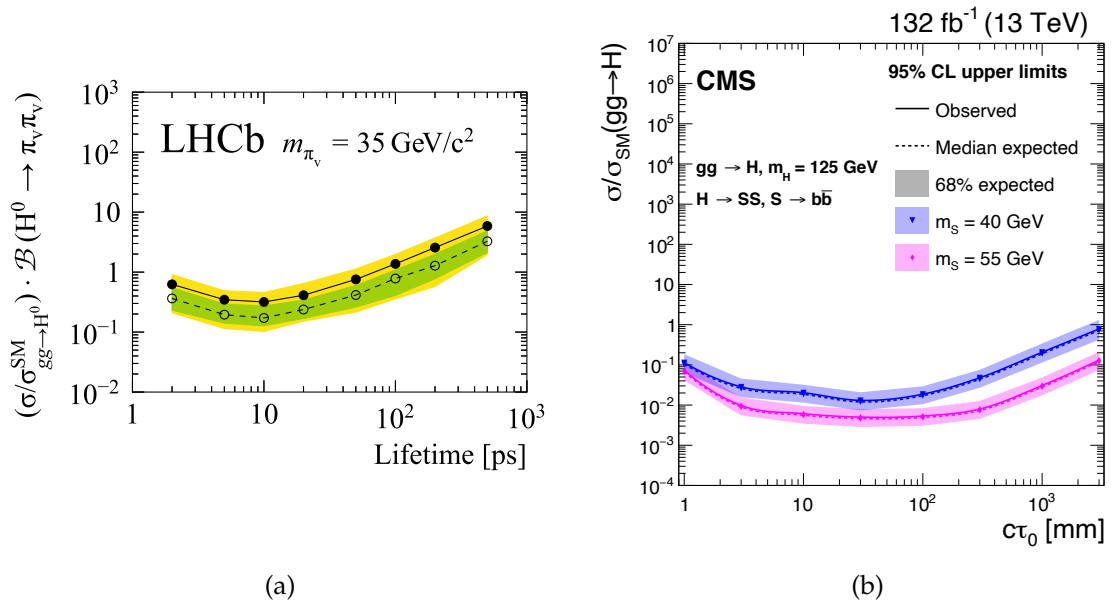
Figure 2.9: Existing limits on the Higgs branching ratio to pairs of long-lived particles derived by (a) the LHCb experiment [89] and (b) the CMS experiment [90].

To circumvent the difficulty of triggering on LLP decays, other ATLAS searches have exploited the VH associated production mode and relied on leptonic trigger signatures. Searches based on standard b-tagging techniques were performed by ATLAS, with sensitivity for $c\tau_s \lesssim$ 1 mm [91], [92]. However, for longer lifetimes, standard reconstruction algorithms become inefficient for identifying displaced decays and specialized reconstruction algorithms are needed. The current exclusion limits on Higgs boson decays to pairs of
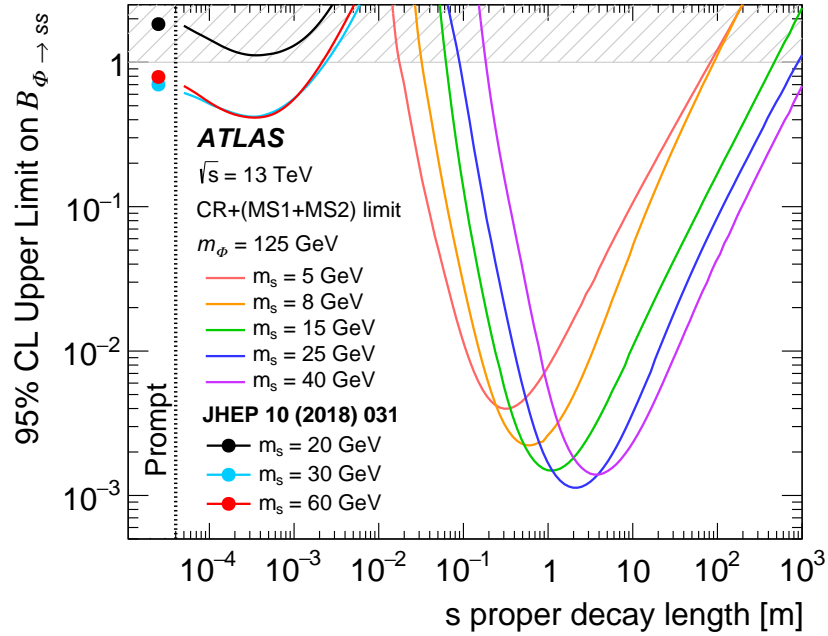
Figure 2.10: Summary of current exclusion limits for Higgs boson decays to long-lived scalar particles s. Figure taken from Ref [86].

scalar particles are shown in Figure 2.10 as a function of the proper lifetime of the scalar. For values of $c\tau_s \lesssim 100$ mm, the branching ratio of the Higgs boson to pairs of LLPs is largely unconstrained by current ATLAS searches. The search presented in this thesis is optimized for this range of proper lifetimes and aims to close the gap in coverage left by previous ATLAS searches.

Part II

Experimental Apparatus

Chapter 3

The Large Hadron Collider and the ATLAS Detector

Gee, I wish we had one of them doomsday machines.

-Stanley Kubrick, *Dr. Strangelove*

Machines take me by surprise with great frequency.

-Alan Turing

This thesis describes a search performed using data collected by the ATLAS detector at the Large Hadron Collider. In this chapter, we provide an overview of these two machines and describe how the data were obtained. Section 3.1 describes the mechanics and operation of the Large Hadron Collider. An overview of the machine design is given which outlines how the protons are accelerated to their final collision energies within the ATLAS detector, and the metrics of the accelerator's performance are defined. Section 3.2 then gives an overview the ATLAS detector. The operation and performance of the three ATLAS subdetectors are detailed, along with a discussion of how ATLAS collects the data that is used for physics analysis. The goal of this chapter is to provide the reader with adequate background information so as to understand the discussions in Chapters 4, 5, and 7. As such, the discussion is focused on the aspects of the LHC and ATLAS detector that are most relevant to the search presented in this thesis.

3.1 The Large Hadron Collider

The **Large Hadron Collider (LHC)** [93] is a multi-purpose particle accelerator located at the European Organization for Nuclear Research (CERN) in Geneva, Switzerland. The accelerator inhabits a tunnel approximately 100 m under the French-Swiss border extending from the CERN site in Meyrin to the foothills of the Jura mountains. The 3.8 m wide concrete-lined tunnel was originally built for the Large Electron–Positron Collider (LEP) [94], [95], and the LHC is the natural successor to that machine. At 27 km in circumference, the LHC is the largest and most complex machine in the world. The LHC is a particle-particle collider [1], meaning that it accelerates beams of identical particles in opposite directions through two separate beampipes. While primarily a proton-proton collider, it is capable of accelerating both protons as well as heavy ions in each of its beams. This allows the various LHC experiments to study proton-proton (pp), proton-lead (p-Pb), or lead-lead (Pb-Pb) collisions. The LHC was designed to achieve a maximal pp center of mass energy of $\sqrt{s} = 14$ TeV, corresponding to a beam energy of 7 TeV per beam.

Situated at different points along the ring are the four main LHC experiments: ATLAS [96], CMS [97], LHCb [98], and ALICE [99]. The ATLAS and CMS experiments are general purpose particle detectors designed to be sensitive to a wide range of final states. The two experiments have similar design, sensitivity, and physics goals, and were built to ensure reproducibility of results. The LHCb experiment was designed to study flavor physics and CP-violation, and the ALICE experiment primarily uses heavy ion collisions to study quark-gluon plasma. A map of the LHC and surrounding area is given in Figure 3.1 which shows the location of the four main experiments along the ring.

3.1.1 Machine design

Injection chain

Before being injected into the main LHC ring, particles are accelerated to increasingly high energies by a series of smaller accelerators known together as the **injection chain** [101]. The protons used in pp collisions begin their journey as hydrogen gas [102]. After being

---

[1] as opposed to a particle-antiparticle collider, for example
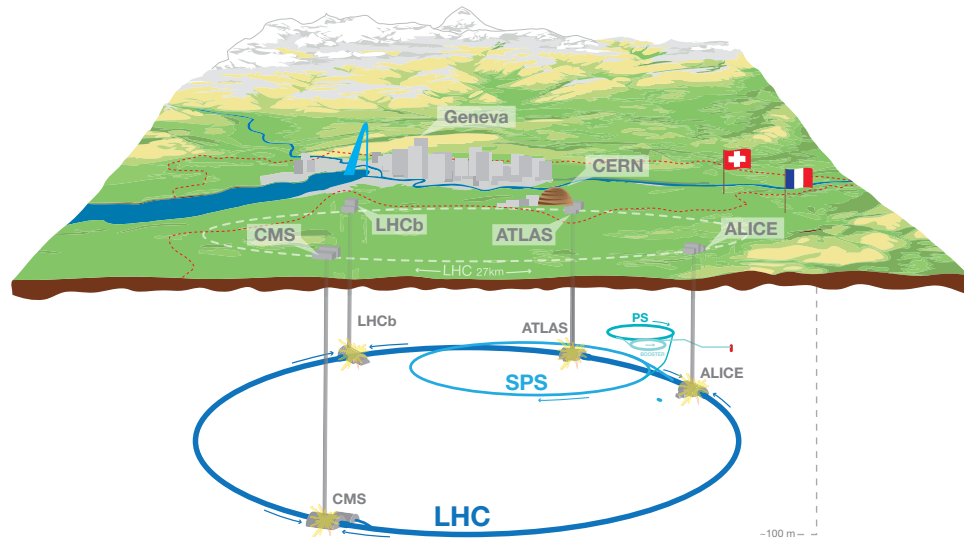
Figure 3.1: Overall view of the LHC, including the ALICE, ATLAS, CMS and LHCb experiments. Image taken from Ref. [100]

stripped of their electrons, they are fed into the first step of the injection chain which is a linear accelerator named **Linac2**. Here, the protons are accelerated from rest to an energy of 50 MeV. They are then transferred to the **Proton Synchrotron Booster (PSB)**, a circular accelerator of radius 25 m, where their energy is increased from 50 MeV to 1.4 GeV. Next, the protons are injected into the **Proton Synchotron (PS)** and further accelerated to 25 GeV before being transferred to the aptly named **Super Proton Synchotron (SPS)**. As the final step of the injection chain, the SPS brings the protons up to an energy of 450 GeV at which point they are ready to be injected into the main LHC ring. A schematic of the various stages of the injection chain is shown in Figure 3.2.

The LHC machine

After the protons are accelerated through the injection chain, they are fed into the LHC through two 2 km-long tunnels. The LHC ring consists of eight octants, with straight
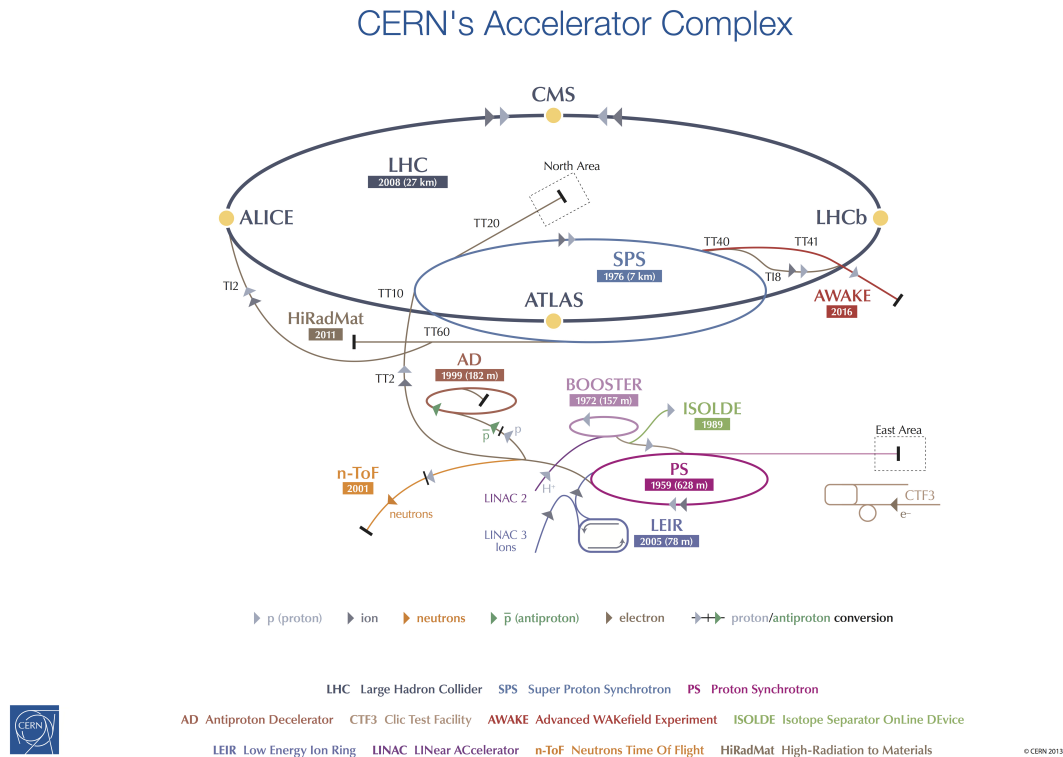
Figure 3.2: The CERN accelerator complex. Image taken from Ref. [103].

sections at their centers that are connected by arcs, as shown in Figure 3.3. The straight sections are referred to as "Points" and house the main experimental and service facilities of the LHC. The ATLAS, ALICE, CMS, and LHCb experiments are located at Points 1, 2, 5, and 8, respectively. At these points the two counterrotating beams are brought together to yield collisions, and are therefore referred to as the **interaction points (IPs)**. The other points accommodate various beam service facilities that are needed to maintain the integrity of the beam. The LHC beam cleaning services are located at Points 3 and 7. These facilities are used to collimate the beams to protect the accelerator from particles straying away from the main beam path. Point 4 hosts the superconducting radio-frequency (RF) cavities which are used to increase the energy of the beam from 450 GeV to 6.5 TeV [104]. There are eight RF cavities per beam which oscillate at a frequency of 400 MHz and provide an accelerating field of 5 MV/m. This corresponds to an increase in energy of 16 MeV per LHC revolution, allowing the desired beam energy of 6.5 TeV to be reached after about 20 minutes. Point 6 is the location of the "beam dump" facility. Here, so called "kicker"
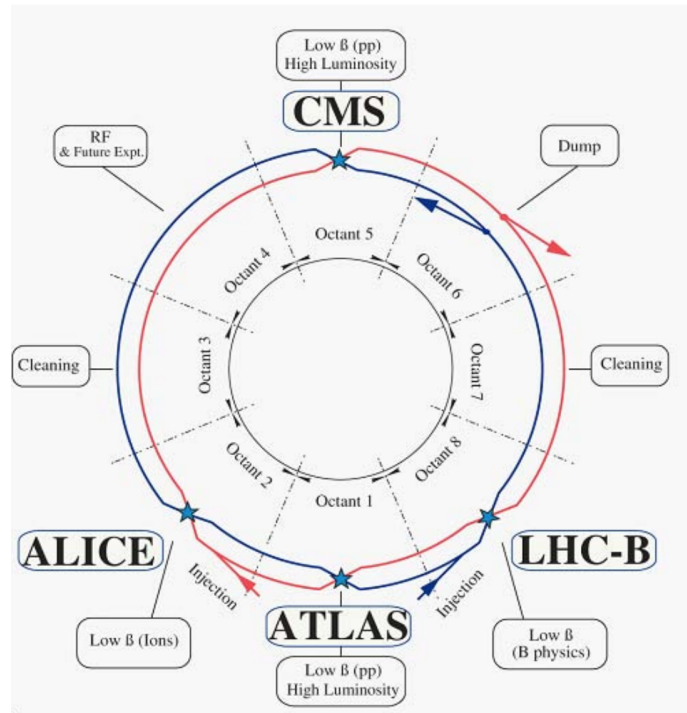
Figure 3.3: Schematic layout of the LHC. Beam 1 travels clockwise and Beam 2 travels counterclockwise. Image taken from [93].

magnets are used to quickly re-direct the beams vertically out of the LHC ring and into an external absorber [105]. This allows for the emptying of the LHC beams in a safe and controlled way in case of malfunctions or to prepare the beam for a new fill.

The LHC magnet system consists of coils of superconducting Niobium-Titanium (NbTi) cooled by superfluid helium to an operating temperature of 1.4 K. The bending of the beam through the arc sections of the LHC ring is provided by 1232 dipole magnets. Each dipole magnet is 15 m long and produces a magnetic field of 8.33 T which constrains the beam to a circular orbit. Given the limited space in the tunnel, the two LHC beams are housed in the same cryostat and coupled magnetic fields of opposite polarity allow for the bending of the counter-rotating beams. A cross sectional diagram of an LHC dipole magnet is shown in Figure 3.4. A combination of dipole, quadrupole, sextupole, and octopole magnets are used to focus the beam and further control the beam optics. This includes the squeezing of the beam that occurs prior to collisions at the various IPs as well as maintaining a fixed beam radius as the energy increases.

LHC DIPOLE : STANDARD CROSS-SECTION

CERN AC/DI/MM - HE107 - 30 04 1999

ALIGNMENT TARGET

MAIN QUADRIPOLE BUS-BARS

HEAT EXCHANGER PIPE

SUPERINSULATION

SUPERCONDUCTING COILS

BEAM PIPE

VACUUM VESSEL

BEAM SCREEN

AUXILIARY BUS-BARS

SHRINKING CYLINDER / HE I-VESSEL

THERMAL SHIELD (55 to 75K)

NON-MAGNETIC COLLARS

IRON YOKE (COLD MASS, 1.9K)

DIPOLE BUS-BARS

SUPPORT POST
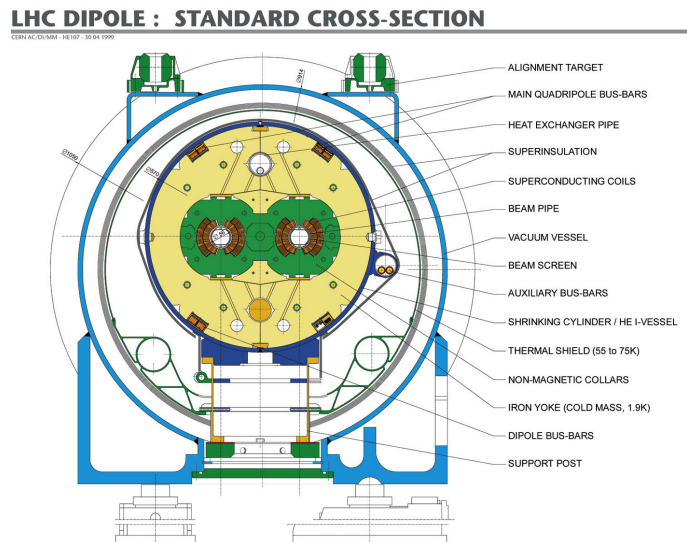
Figure 3.4: Cross-section of an LHC dipole magnet. Image taken from Ref [106].

3.1.2 Performance and operation

The LHC began stable operation in 2009, with the main research program commencing in March 2010 after a center of mass energy of $\sqrt{s} = 7$ TeV was reached for the first time. The first data taking period of the LHC (Run 1) took place between 2010 and 2012, with a brief shutdown at the end of 2011 to allow for an increase in beam energy from 3.5 to 4 TeV per beam. In 2013, the LHC was shut down for a two year period known as Long Shutdown 1 (LS1). During this time various upgrades were performed to the detectors, injection chain (the PS and SPS), and bending magnets to prepare for beam energies of 7 TeV.

The second data taking period (Run 2) began in 2015 with a beam energy of 6.5 TeV and continued though 2018. The full Run 2 dataset comprises the data used in this thesis. At the time of writing, the LHC is currently in the Long Shutdown 2 (LS2) period. During this time, the first phase of upgrades are being performed to the ATLAS and CMS experiments to prepare for the High-Luminosity LHC (HL-LHC) era. A diagram of the operational timeline of the LHC is shown in Figure 3.5.

The LHC beam

The protons that comprise the LHC beam are not uniformly distributed, but rather divided into **bunches** which are shaped by the RF cavities. As mentioned previously, the
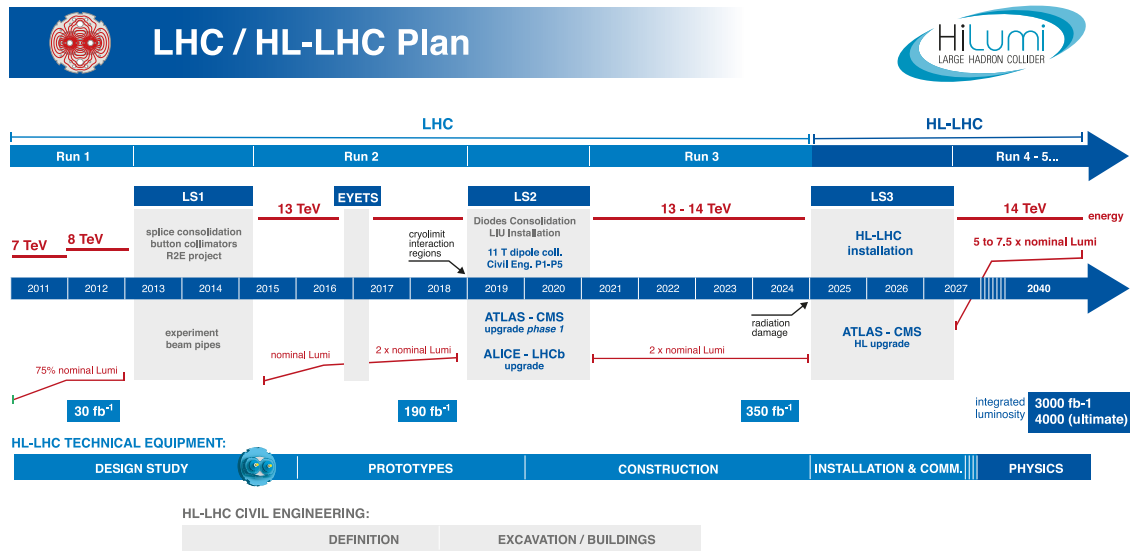
Figure 3.5: The planned run schedule of the LHC.

electromagnetic field in the RF cavities oscillates at a frequency 400 MHz. A proton that is perfectly synchronised with the RF frequency is called a **synchronous particle** and will not receive any further acceleration. However, any protons that arrive before or after the synchronous particle will be accelerated or decelerated so as to match the RF frequency. This results in the protons in the LHC clustering around the synchronous particle in bunches. The number of protons per bunch is on the order of 10^{11}.
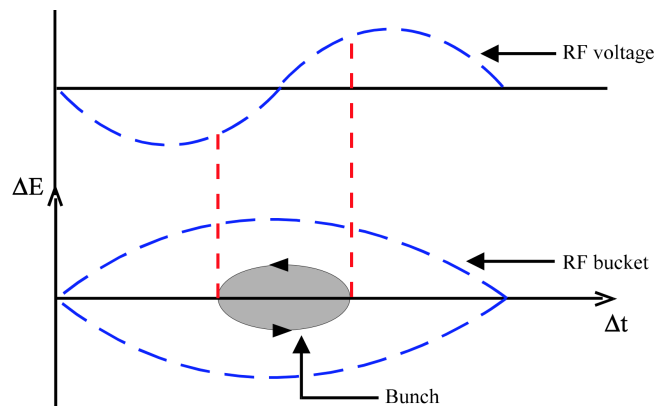
Figure 3.6: Schematic of how a proton bunch is constrained inside of an RF bucket. Image taken from [107].

The oscillation of the RF cavities defines an envelope of allowed positions for the proton bunch known as an RF bucket, shown in Figure 3.6. The operating conditions of the LHC determine the number of buckets to be approximately 35640, meaning that a maximum of 35640 bunches can occupy the LHC ring. However, not all RF buckets can be filled with bunches as this would overwhelm the experimental capabilities of the detectors at the various IPs. Instead, only 1 out of every 10 RF buckets are filled with a proton bunch. This corresponds to 2808 total bunches with a bunch spacing of 25 ns [108] and a bunch collision rate of 40 MHz at the IPs.

Luminosity

The amount of potential collisions in a detector per unit time is characterized by a quantity known as **instantaneous luminosity**, or $\mathcal{L}$. The luminosity is the proportionality factor between the number of events per second dN/dt and the interaction cross section of the colliding particles

$$\frac{dN}{dt} = \mathcal{L} \cdot \sigma_{pp} \tag{3.1}$$

Thus, the instantaneous luminosity is measured in $\mathrm{cm}^{-2}\mathrm{s}^{-1}$. The luminosity is a characteristic of the accelerator. Assuming the particles in the beam are Gaussian distributed in the transverse plane, the instantaneous luminosity is given by

$$\mathcal{L} = \frac{N_1 N_2 n_b f_{\mathrm{rev}} \gamma_r}{4\pi \epsilon_n \beta^*} F, \tag{3.2}$$

where N_i is the number of particles in each bunch, n_b is the number of bunches per beam, f_{rev} is the frequency of revolution, γ_r is the Lorentz factor, ϵ_n is the emittance of the beams, β^* is the beta function of the beam which quantifies how narrow the beam is, and F is a geometric factor due to the crossing angle of the beams [109]. The total amount of luminosity delivered is then simply the integral of the instantaneous luminosity with respect to time:

$$\mathcal{L}_{\mathrm{int}} = \int \mathcal{L} dt \tag{3.3}$$

The LHC is designed to deliver collisions to ATLAS and CMS with an instantaneous luminosity of $\mathcal{L} = 10^{34}$ cm^{-2}s^{-1}. The total integrated luminosity delivered and recorded by the ATLAS experiment are shown as a function of time in Figure 3.7. During Run 2, the peak instantaneous luminosity recorded at ATLAS was 2.1×10^{34} cm^{-2}s^{-1}, far exceeding the design luminosity.
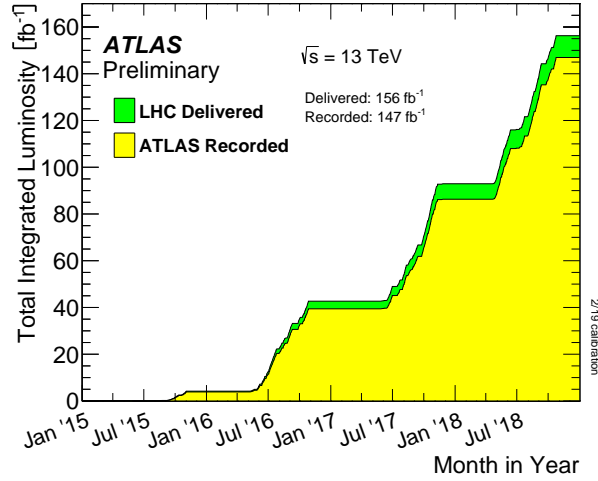
Figure 3.7: The integrated luminosity versus time delivered to (green) and recorded by ATLAS (yellow) during stable beam conditions for *pp* collisions at $\sqrt{s} = 13$ TeV. Image taken from [110].

Pileup

As described previously, the bunches in the LHC consist of roughly 100 billion protons each, which is necessary to achieve the desired luminosity (Equation 3.2). A consequence of this is that each time a pair of bunches cross paths at one of the interaction points, there will be multiple distinct *pp* interactions. The interaction vertex with the highest $\sum p_\text{T}^2$ of associated tracks is known as the **hard-scatter vertex**, and is the most promising candidate for producing interesting physics. The *pp* interactions that occur in addition to the hard scatter are known as **pileup** and mostly consist of soft, inelastic scattering events. When the pileup interactions occur in the same bunch crossing as the hard scatter vertex it is called **in-time** pileup, and if the collisions originate from a previous or subsequent bunch crossing it is called **out-of-time** pileup. Pileup presents a challenge to detector experiments because the additional energy deposits complicate the identification of the physics objects

originating from the hard scatter. The amount of pileup interactions is characterized by computing the time averaged number of interactions per bunch crossing $\langle\mu\rangle$. During Run 2, the average value of $\langle\mu\rangle$ in ATLAS was $\langle\mu\rangle = 33.7$ with peak values of $\langle\mu\rangle$ reaching 70. The luminosity-weighted distribution of $\langle\mu\rangle$ is shown in Figure 3.8 for each data taking year.
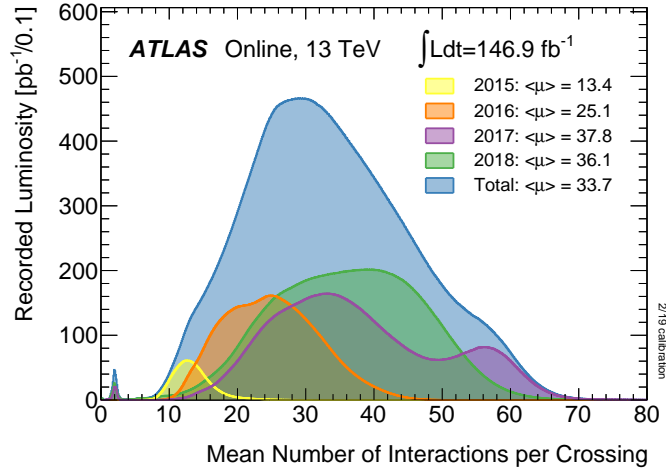
Figure 3.8: The luminosity-weighted distribution of the mean number of interactions per bunch crossing for the 2015-2018 pp collision data at $\sqrt{s} = 13$ TeV. Image taken from [110].

3.2 The ATLAS Detector

ATLAS (A Toroidal LHC ApparatuS) is a cylindrical multi-purpose particle detector located at Point 1 of the LHC ring (Figure 3.2). Spanning 44m in length and 25m in height, ATLAS is the largest particle detector ever constructed and one of the most complex scientific experiments in existence. The detector spans nearly 4π radians in solid angle coverage with respect to the pp interaction point. The ATLAS detector is composed of three subsystems known as **subdetectors**, each of which are specialized for the identification of specific types of particles produced in pp collisions. The subdetectors are the inner tracking detector, the electromagnetic and hadronic calorimeters, and the muon spectrometer. The combination of these three systems makes ATLAS extremely versatile and capable of reconstructing a wide range of potential interactions and final states. The ATLAS cylinder is divided into the **barrel** region and two **endcap** regions. Each subdetector is designed

around this geometry with each system forming a coaxial layer around a central beam pipe. Figure 3.9 shows the layout of the ATLAS detector and its subdetector systems. In this section we will provide an overview of each subdetector, after some brief preliminaries.
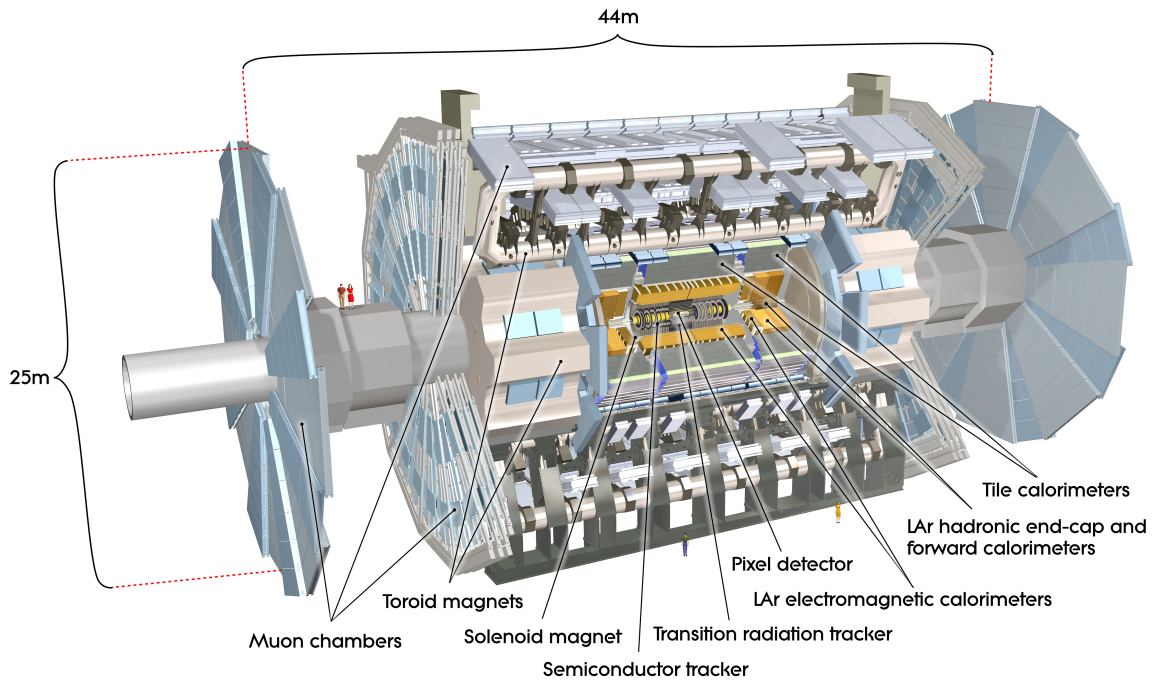
Figure 3.9: A cutaway of the ATLAS detector. Two people are shown for scale on the left side of the figure next to the Muon chambers. Image taken from Ref. [96].

Magnet System

A defining feature of the ATLAS detector is its unique magnet system. The system is composed of two parts: the central solenoid, and the toroidal magnet system[2]. Both systems use a superconducting Niobium-Titanium alloy which is cooled to a temperature of less than 5 K using liquid helium. A schematic of the magnet system is shown in Figure 3.10. The central solenoid is 5.3 m long, 2.4 m in diameter, and only 4.5 cm thick. The layout of the solenoid was designed to minimize the radiative thickness in front of the electromagnetic calorimeter with the entire solenoid assembly contributing a total of ~ 0.66 radiation lengths at normal incidence [111]. The solenoid is responsible for providing a 2 T axial

---

[2]Hence the "T" in ATLAS

magnetic field for the inner detector. The toroid system consists of three separate magnets: one in the barrel and one in each endcap. The barrel toroid is 25.3 m in length, with inner and outer diameters of 9.4 m and 20.1 m, respectively. Each endcap toroid is 10.7 m in diameter with an axial length of 5 m. The toroids use 8 air-core coils each and are responsible for providing the field in the muon spectrometer which allows for the determination of muon momenta. The magnetic field has a magnitude of approximately 0.5 T and 1.0 T in the central and endcap regions, respectively.
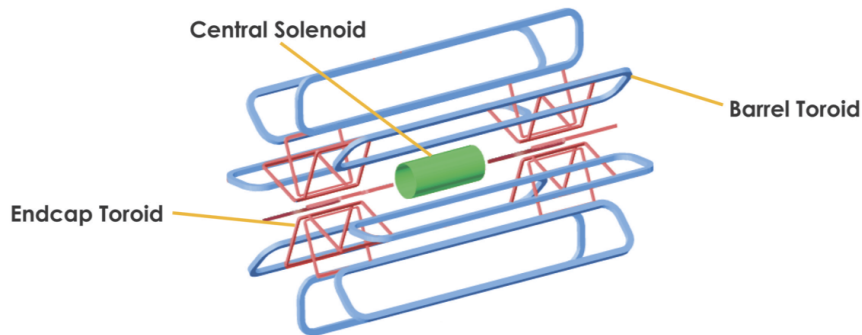
Figure 3.10: Schematic representation of the ATLAS magnets. Image taken from [112].

Coordinate System

The ATLAS detector uses a right-handed coordinate system with its origin at the nominal interaction point in the center of the detector. The positive x-axis points to the center of the LHC ring, the positive y-axis points up toward the surface, and the positive z-axis points along the counter clockwise direction of the beam. Cylindrical coordinates (r, ϕ, z) are used, where the azimuthal angle around the z-axis ϕ is defined such that $\phi = 0$ corresponds to the direction pointing toward the center of the LHC ring. The spherical polar angle θ is measured with respect to the beamline, with $\theta = 0$ in the plane of the LHC ring and $\theta = \pi/2$ in the transverse plane. Momentum vectors are described in terms of the momentum in the transverse plane, p_T, and the momentum in the direction of the beam, p_z. The energy in the transverse plane is labeled $E_T = E \sin \theta$. Transverse quantities are useful because the initial energy in the transverse plane is known to be zero for the colliding system.

The **rapidity** of an object is defined as

$$y = \frac{1}{2} \ln \frac{E + p_z}{E - p_z} \tag{3.4}$$

In the massless or ultrarelativistic limit, the rapidity can be approximated by the **pseudo-rapidity**, defined in terms of the polar angle θ as

$$\eta = -\ln \tan(\theta/2). \tag{3.5}$$

A pseudorapidity of $\eta = 0$ corresponds to a vector in the transverse plane, whereas $\eta = \infty$ corresponds to a vector along the axis of the beam. Pseudorapidity is used as a measure of polar angle rather than θ because it is Lorentz invariant under boosts for massless particles. The coordinate system used to describe a particle or system of particles is usually given in terms of (p_T, η, ϕ). Angular distance is measured in terms of the pseudorapidity using the metric $\Delta R \equiv \sqrt{(\Delta\eta)^2 + (\Delta\phi)^2}$. This is a purely geometric quantity and is Lorentz invariant if the involved particles are massless.

3.2.1 The Inner Detector

The innermost ATLAS subdetector is aptly named the **Inner Detector (ID)** and is the first system to encounter the particles produced in the pp collision. The ID covers the region $|\eta| < 2.5$ and the volume $0.03 \text{ m} < r < 1.1 \text{ m}$ and $|z| < 3.5 \text{ m}$. As a charged particle traverses the ID, it deposits energy in various detector elements. These energy deposits are called **hits** and are used to reconstruct the trajectories of charged particles. The ID is immersed in a 2 T axial magnetic field produced from a superconducting solenoid magnet which bends a particle's trajectory in the azimuthal direction. This allows the detector to measure the direction, momentum, and charge of electrically-charged particles based on their reconstructed trajectory when traveling through the magnetic field. These trajectories are known as tracks, and the algorithms used to reconstruct them will be described in detail in Section 4.1.

The ID is itself composed of three subsystems: the silicon pixel detector, the silicon-strip semiconductor tracker (SCT), and the transition radiation tracker (TRT). Each subsystem is dividing into a barrel region consisting of concentric cylindrical layers surrounding the beam pipe, and two end cap regions on either side of the barrel. A rendering of the ATLAS ID showing these systems is shown in Figure 3.11, and a more detailed schematic is given in Figure 3.12.
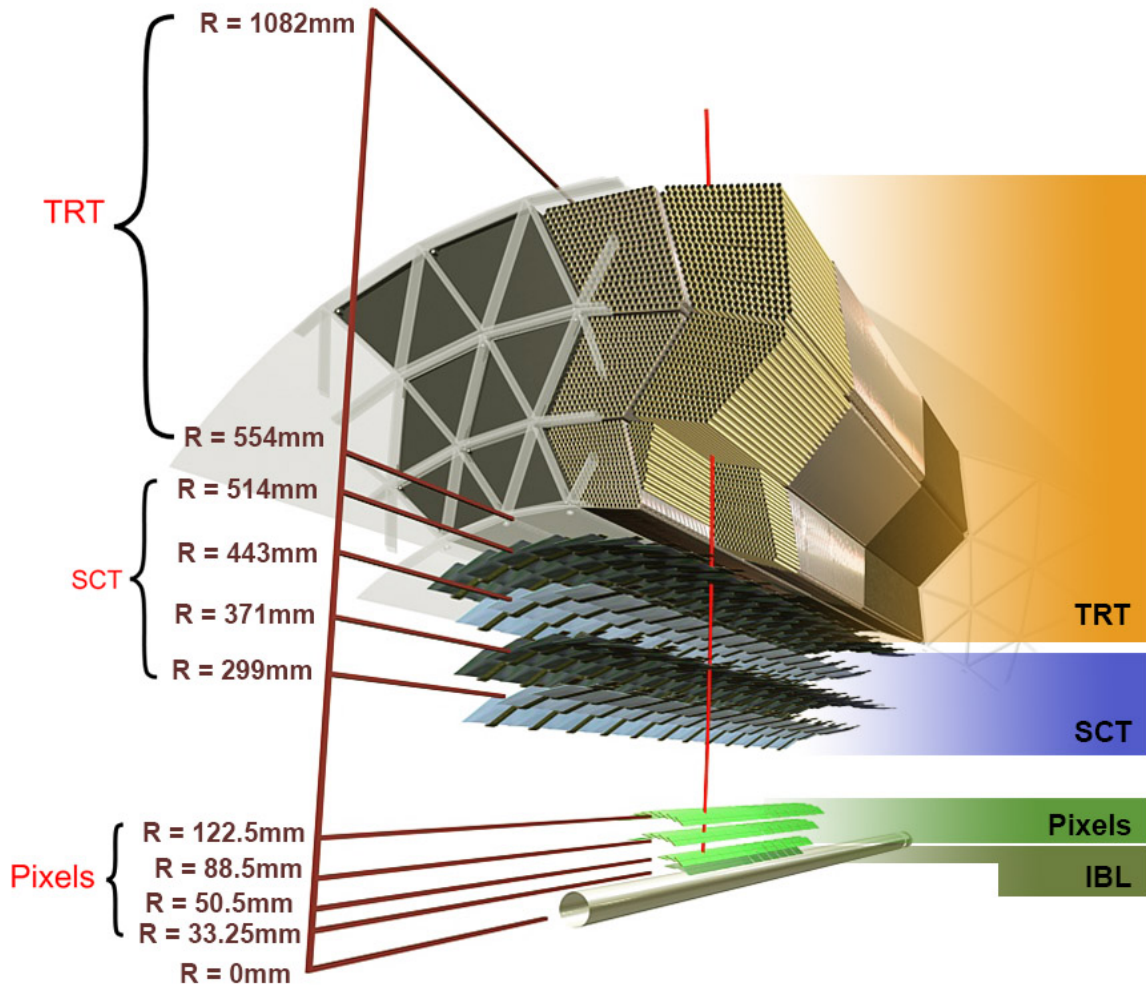
Figure 3.11: A cutaway of the ATLAS inner detector. Image taken from Ref. [113].

Pixel

The innermost subsystem of the ATLAS ID is the **pixel detector** [114]. It is composed of a barrel section and two endcap regions and covers the pseudorapidity range $|\eta| < 2.5$.
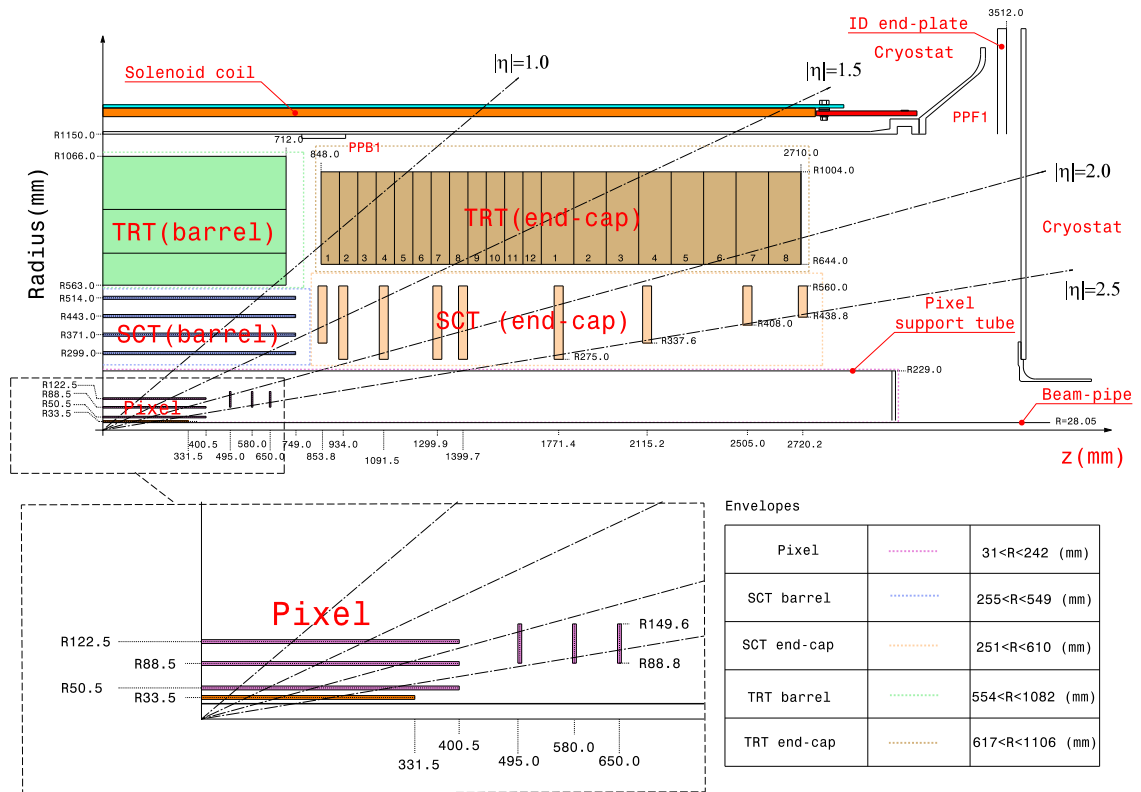
Figure 3.12: The layout of the ATLAS Inner Detector shown as an $R - z$ cross-section. The inlet on the lower left shows the pixel system in more detail including the IBL in orange. The inlet on the lower right describes the fiducial regions defined by the three detector subsystems. Image taken from Ref. [113].

The basic detector element of the pixel system is a module composed of silicon sensors and electronics for readout and control. The sensing material is 250 μm thick and is constructed from an n-type silicon semiconductor. When a charged particle passes through a semiconductor detector such as a pixel sensor, it excites electrons to the conduction band leaving behind holes in the valence band. Under the influence of an electric field, electrons and holes travel to electrodes where they result in a pulse that can be read out by dedicated electronics and registered as a hit. In the pixel detector, this electric field is provided by a bias voltage that is applied over the module.

In the barrel region, the pixel modules are distributed among three concentric 4 m long layers positioned at radii of 50.5 mm, 88.5 mm, and 122.5 mm. In each endcap there are three disks positioned at $|z| = 495, 580, 650$ mm. Each module in these layers is identical and consists of 47232 sensing elements called **pixels** which are 50 μm $\times$ 400 μm in area and

provides a spacial resolution of 10 μm in the $x - y$ plane and 115 μm in z. Thus, each hit in the pixel detector provides a precise three-dimensional measurement for a point along the trajectory of a charged particle. The three barrel layers have 1456 modules for a total of 67M pixels, and the endcap disks have 13M pixels across 288 modules.

Prior to the Run 2 data-taking period, an additional pixel layer was installed between the beam pipe and the B-Layer called the Insertable B-Layer (IBL). The purpose of this upgrade was to improve impact parameter and vertex resolution as well as protect the B-Layer from excessive radiation damage. The IBL consists of 12 million pixels of area 50×200 μm which give a spacial hit resolution of 8 μm in $x - y$ and 40 μm in z. The improvements provided by the IBL are crucial for the reconstruction of secondary vertices such as those originating from b-hadrons or exotic LLPs.

SCT

The pixel detector is surrounded by the **semiconductor tracker (SCT)**. Like the pixel detector, the SCT uses silicon sensors to detect incident ionizing particles but instead of pixels, the SCT uses silicon microstrips. The SCT consists of 61 m^2 of silicon sensors divided between 4088 modules with 1536 channels per module separated by an approximately 80 μm pitch. Each SCT module consists of two 12 cm long layers which are glued back-to-back at a 40 mrad stereo angle in order to provide a two-dimensional position measurement, as shown in Figure 3.13. This configuration provides a hit resolution of 17 μm in the $x - y$ plane and 580 μm in z. In the barrel region, the SCT is composed of four cylindrical layers positioned at radii of 299, 371, 443, and 514 mm. In each endcap there are nine SCT disks, ranging from $|z| = 854$ to 2720 mm. In total, the SCT contains approximately 6.3M readout channels.

TRT

The outermost system of the ID is the **transition radiation tracker (TRT)** which provides tracking information out to $|\eta| < 2.0$. Unlike the silicon-based pixel and SCT detectors, the TRT is a gaseous drift tube detector. The basic detector element of the TRT is a straw tube with 4 mm diameter which surrounds a 0.03 mm diameter gold-plated tungsten wire.
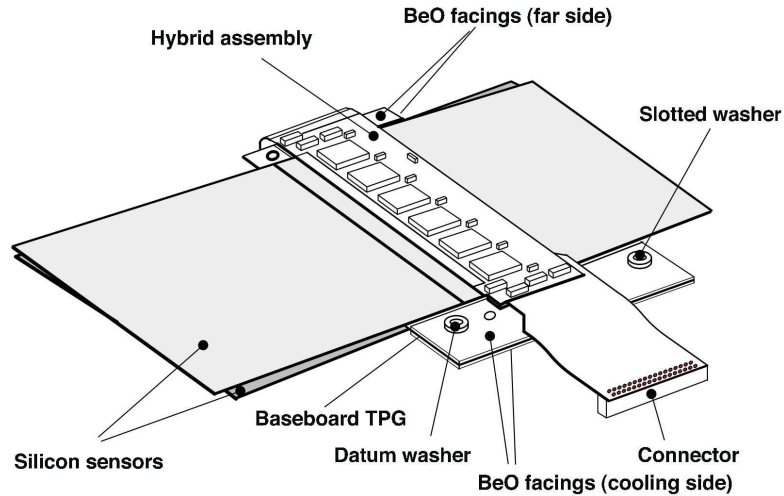
Figure 3.13: Diagram of an SCT barrel module, showing the stereo angle offset between the two silicon layers. Image taken from Ref [96].

Each tube is filled with a mixture of 70% Xe, 27% CO_2, and 3% O_2 which is ionized by charged particles as they move through the detector. The central wire is grounded, while the straw wall is kept at a voltage of -1.5 kV. When a charged particle passes through the gaseous mixture, it ionizes the gas, and the resulting free electrons drift towards the central wire, where they are amplified and read out. The barrel region of the TRT covers the pseudorapidity range $|\eta| < 1$ and contains 52544 straw tubes of 144 cm length parallel to the beam axis which extend radially from 554 mm to 1082 mm from the beam center. The endcap region extends from $1 < |\eta| < 2$ and 0.8 m $< |z| < 2.7$ m and contains 122880 tubes of 39 cm length which are arranged radially perpendicular to the beam pipe.

On average, a charged particle leaves 36 hits in the TRT with a resolution of 130 μm per hit. Despite only providing two dimensional ($r - \phi$ in the barrel, $z - \phi$ in the endcap) information with relatively poor position resolution in comparison to silicon detectors, the large number of TRT hits improves the overall momentum resolution of tracks because the curvature can be constrained over a larger path length. Additionally, the straws are interlaced with polypropylene fibres to induce transition radiation as charged particles traverse the material boundaries. The photons emitted are reabsorbed by the Xe atoms in the gas resulting in significantly higher readout signals. This effect is dependent on both the relativistic Lorentz factor of the particle as well as its mass. Thus, the TRT provides additional discrimination power between electrons and charged hadrons such as the pion.

3.2.2 Calorimeter

The ATLAS calorimetry system [115] is designed to measure and absorb the energy of both electrically charged and neutral particles. The calorimeter surrounds the ID and covers the range $|\eta| < 4.9$. It is comprised of two distinct subsystems: the electromagnetic and hadronic calorimeters. The electromagnetic calorimeter is designed to measure the energy of electrons and photons, while the hadronic calorimeter is designed to measure the energy of hadrons such as protons and neutrons. The calorimeter system measures the energy of particles by absorbing their kinetic energy as they interact with the detector material. All particles except muons and neutrinos are stopped by the calorimeter, thereby depositing all of their energy within the system. An overview of the calorimeter is shown in Figure 3.14

Both the electromagnetic and hadronic calorimeters are **sampling calorimeters** which use alternating layers of "passive" and "active" materials. The passive, or absorbing, layers are constructed from a dense material which initiates electromagnetic or hadronic showers as incident particles pass through and interact with the detector material. The active layers then measure the energy produced in the shower and give a detectable signal. Because a portion of the energy of the incident particle is lost to the absorber medium, these calorimeters are only capable of "sampling" the energy of the particle. The design and specifications of the two calorimeter systems are described below.

Electromagnetic calorimeter

The electromagnetic calorimeter (ECal) [117] is divided into a barrel section ($|\eta| < 1.475$) and two endcap components ($1.375 < |\eta| < 3.2$). The barrel region is composed of two identical half-barrels, separated by a 4 mm gap at $z = 0$ and extends from $1250 < r < 2050$ mm and $|z| < 3100$ mm. Each half-barrel is divided into 16 modules, each covering a $\Delta\phi = 22.5°$. Each endcap is composed of two coaxial wheels which are divided into 8 modules. The outer wheel covers the region $1.375 < |\eta| < 2.5$ and the inner wheel covers the region $2.5 < |\eta| < 3.2$. The ECal is called the **Liquid Argon calorimeter (LAr)** because it uses liquid argon as its active material. Lead is used as the absorbing material and is responsible for inducing electromagnetic showers as incident electrons and photons
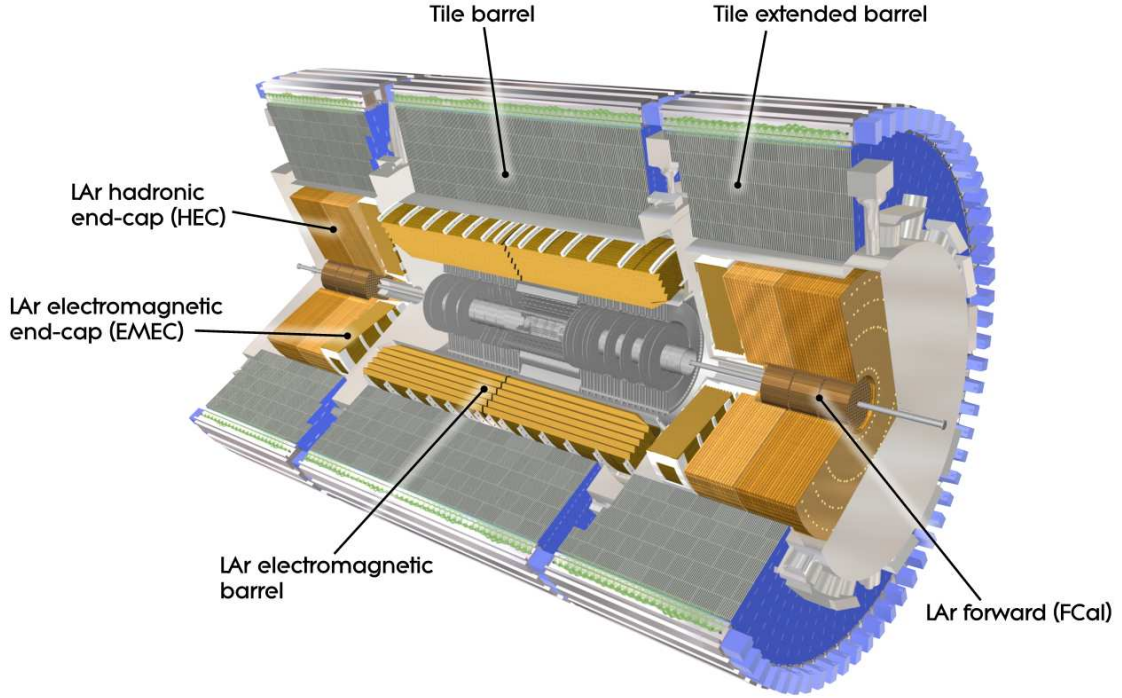
Figure 3.14: A cutaway of the ATLAS calorimeter system showing the electromagnetic and hadronic subsystems. Image taken from Ref. [116].

interact with its heavy nucleus. In the region $|\eta| < 1.8$ a presampler detector is used to correct for the energy lost by electrons and photons upstream of the calorimeter.

The LAr modules are constructed with an accordion geometry which allows for complete symmetry in ϕ without any gaps in acceptance. Each module consists of three layers. The first layer is finely segmented in η with a resolution $\Delta\eta \times \Delta\phi = 0.003 \times 0.1$ in the region $|\eta| < 1.4$ This provides precise position measurements of photons which, unlike electrons, do not have a corresponding ID track. It also allows the ECal to differentiate individual photons from photon pairs which is important in identifying $\pi_0 \rightarrow \gamma\gamma$ decays. This layer is approximately 4 radiation lengths (X_0) thick. The second layer has a resolution of $\Delta\eta \times \Delta\phi = 0.025 \times 0.025$ and a length of at least 16 X_0. The vast majority of the shower energy is deposited in this layer. A coarse third layer with resolution $\Delta\eta \times \Delta\phi = 0.05 \times 0.025$ and length of $2X_0$ is used to collect the tail of the electromagnetic shower and estimate the amount of leakage outside of the ECal. Depending on the location in η, the thickness of each module ranges from 22 X_0 to 33 X_0, ensuring that the vast majority of electrons and

photons are completely stopped by the ECal. A schematic of an LAr module is shown in Figure 3.15.
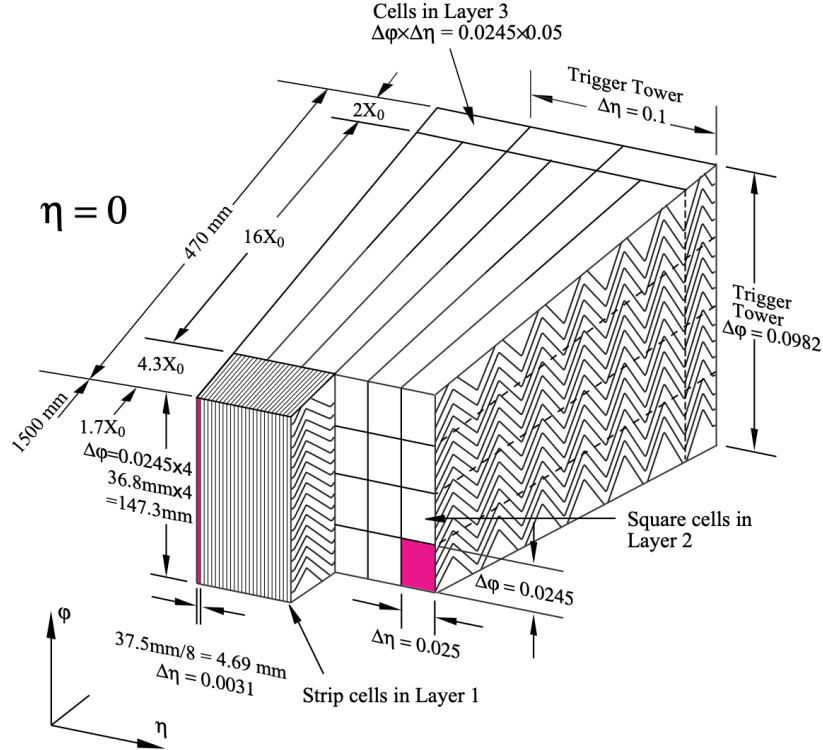
Figure 3.15: Sketch of a barrel LAr module which shows the accordion geometry. The granularity in η and ϕ are shown in the figure for each layer. Image taken from Ref. [96].

Hadronic calorimeter

Hadronic calorimetry is provided by the tile calorimeter, the hadronic end-cap calorimeter (HEC) and the forward calorimeter (FCal) [118]. The combined system covers the range $|\eta| < 4.9$. Like the ECal, the hadronic calorimeters are sampling calorimeters which use active layers to measure showers produced when hadrons interact with the absorbing material.

The tile calorimeter covers the range $|\eta| < 1.7$ and uses plastic scintillator as the active medium with steel tiles as the absorber. It is comprised of a 5.8 m long central barrel ($|\eta| < 1.0$) and two 2.6 m long endcaps, or "extended barrels" ($0.8 < |\eta| < 1.7$). and extends radially from $r = 2.28$ m to $r = 4.25$ m. Each of the three barrel regions of the

tile calorimeter consists of 64 wedge-shaped modules and are segmented in three layers. The barrel layers are approximately 1.5, 4.1, and 1.8 interaction lengths (λ) thick, and the extended barrel layers are 1.5, 2.6, and 3.3 λ thick. As hadrons interact with the steel absorber, showers are produced consisting primarily of pions. These showers interact with the plastic tiles producing scintillation light which is read out through wavelength-shifting fibers and into photomultiplier tubes. A schematic of the modules is given in Figure 3.16 which shows how the readout is integrated with the mechanical structure. In the barrel, the first two layers have a granularity of $\Delta\eta \times \Delta\phi = 0.1 \times 0.1$ while the third layer has a granularity of 0.2×0.1. In the extended barrel, the first layer has a granularity of $\Delta\eta \times \Delta\phi = 0.1 \times 0.1$ and the second two layers have a granularity of approximately $\Delta\eta \times \Delta\phi = 0.2 \times 0.2$.
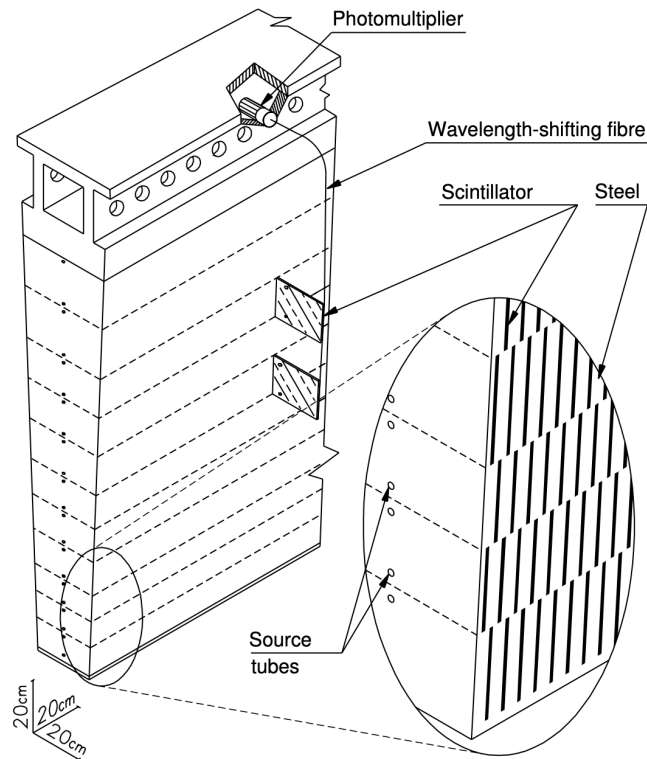
Figure 3.16: Schematic of a tile calorimeter module showing how the optical readout is integrated with the alternating active and passive layers. The "source tubes" labeled in the diagram are used for the radioactive source calibration system. Image taken from Ref. [96].

The HEC extends the coverage of the tile calorimeter to the range $1.5 < |\eta| < 3.2$. Like the ECal, the HEC uses liquid-argon as the active material, but uses copper instead of lead as the absorber. The HEC consists of two wheels per endcap, with each wheel

consisting of 32 wedge-shaped modules. Finally, the FCal further extends the range of the HCal by providing coverage in the region $3.2 < |\eta| < 4.9$. The FCal consists of three layers, each of which use liquid argon as their active medium. The first layer is an electromagnetic module which uses copper as an absorber, while the outer two layers are hadronic modules and use tungsten. The total thickness of the hadronic calorimeter is 9.7λ in the barrel and 10λ in the forward region.

3.2.3 The Muon Spectrometer

The outermost ATLAS subdetector is the **Muon Spectrometer (MS)** [119] which consists of separate trigger and high-precision tracking subsystems. The MS uses large superconducting air-core toroid magnets to bend the tracks of muons after they exit the calorimeter. In the range $|\eta| < 1.4$, the magnetic field is provided by the large barrel toroid and for $1.6 < |\eta| < 2.7$, muon tracks are bent by two smaller toroids inserted into each endcap. This configuration of magnets provides a field that is mostly orthogonal to the trajectories of muons originating from the IP.

The MS is comprised of four gaseous subdetector systems, as shown in Figure 3.17. The tracking system consists of the **Monitored Drift Tubes (MDT)** [120] and the **Cathode Strip Chambers (CSC)** [121]. These systems provide measurements of the coordinate in the bending direction of muons as they traverse the detector allowing for precise momentum measurements determined through the track curvature. The trigger system covers the pseudorapidity range $|\eta| < 2.4$ and uses **Resistive Plate Chambers (RPC)** [122] in the barrel and **Thin Gap Chambers (TGC)** [123] in the endcap. The trigger chambers serve several purposes, including coarse measurement of muon transverse momentum, bunch crossing identification, and second coordinate measurements in the direction orthogonal to those determined by the precision-tracking chambers. A more detailed diagram of the subdetector systems is shown in Figure 3.18, and an overview of the main parameters of each system is provided in Table 3.1. A brief overview of the four subsystems is provided in the remainder of this section.
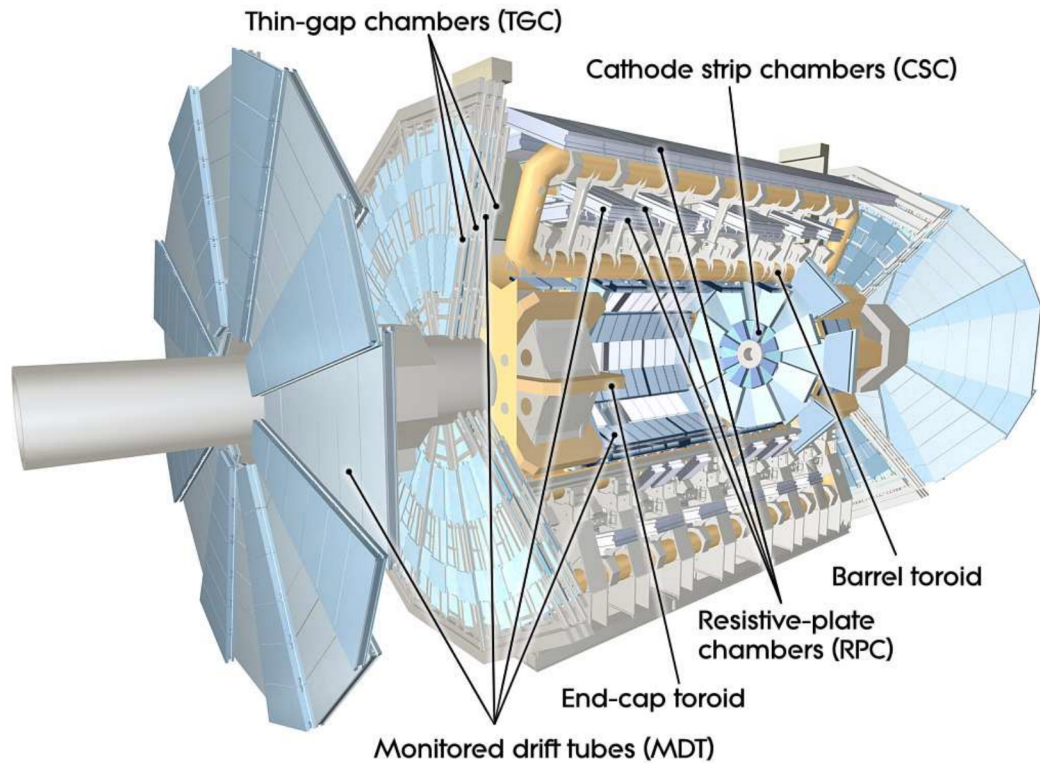
Figure 3.17: A cutaway of the ATLAS muon spectrometer system showing the tracking and triggering subsystems. Image taken from Ref. [96].

Monitored drift tubes

In the range $\eta < 2.0$, muon tracks are measured using monitored drift tube chambers (MDTs). The MDT chambers are arranged in three cylindrical layers at radii of 5 m, 7.5 m, and 10.0 m in the barrel and three endcap layers at $|z|$ positions of 7.4 m, 14.0 m and 21.5 m. The three layers allow for a determination of the muon's momenta based on the sagitta of the track as the trajectory of the muon is bent by the magnetic field. The basic unit of the MDT is a 30 mm in diameter drift tube filled with a 93%/7% mixture of Ar/CO_2 gas. A single tungsten-rhenium anode wire sits at the center of each tube and is kept at a potential of 3 kV. As a charged particle passes through the tube it will ionize the argon, and the resulting electrons will be collected by the central wire and read out as a signal. The time it takes for the electrons to drift to the anode is measured and used to determine the distance between the path of the incident particle and the center of the tube at a precision of 80 μm. In each chamber, the MDT tubes are arranged in two "multilayers" consisting of 3
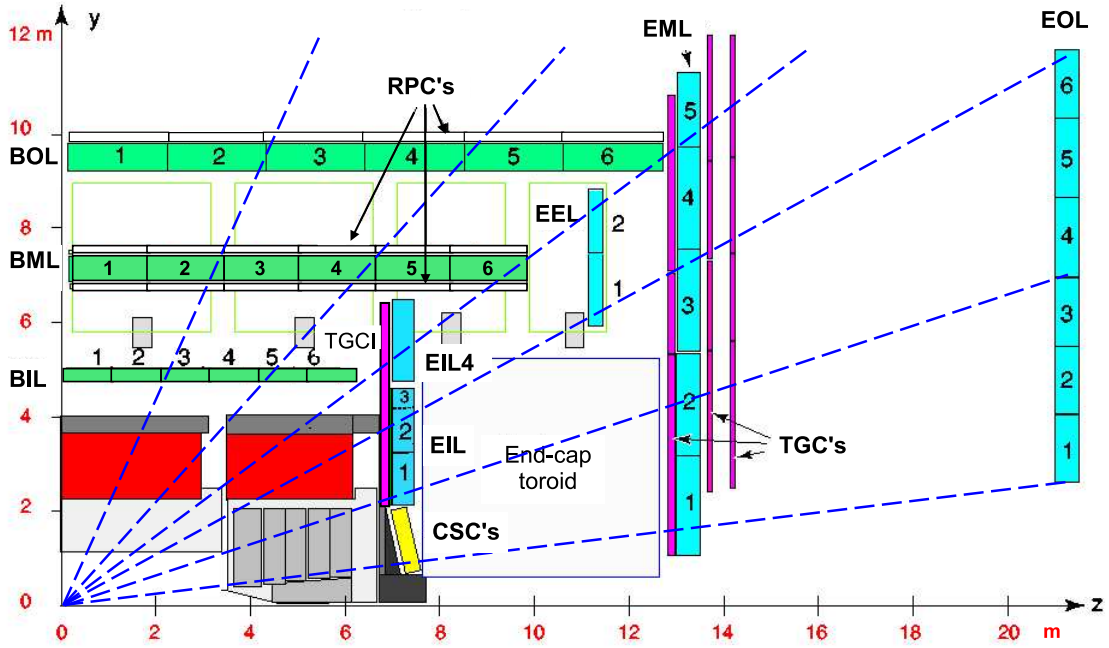
Figure 3.18: Detailed diagram of the muon spectrometer subsystems. Image taken from Ref. [96].

Detector	Function	Coverage	Chambers	Channels
MDT	Precision tracking	$|\eta| < 2.0$	1150	354000
CSC	Precision tracking	$2.0 < |\eta| < 2.7$	32	31000
RPC	Triggering	$|\eta| < 1.05$	606	373000
TGC	Triggering	$1.05 < |\eta| < 2.4$	3588	318000

Table 3.1: Main parameters of the muon spectrometer

or 4 layers of tubes which are used to form the tracklets used in muon track building. This is shown schematically in Figure 3.19. The MDT chambers are arranged into 16 sectors in ϕ and are oriented such that the center points of the tubes are tangential to circles around the beam axis. The entire MDT detector system consists of 1,150 chambers and a total of 354 000 individual drift tube channels.

Cathode strip chambers

In the region $2.0 < \eta < 2.7$, particle fluxes exceed the design capabilities of the MDT chambers of 150 Hz/cm^2. To accommodate this harsh environment, Cathode Strip Chambers
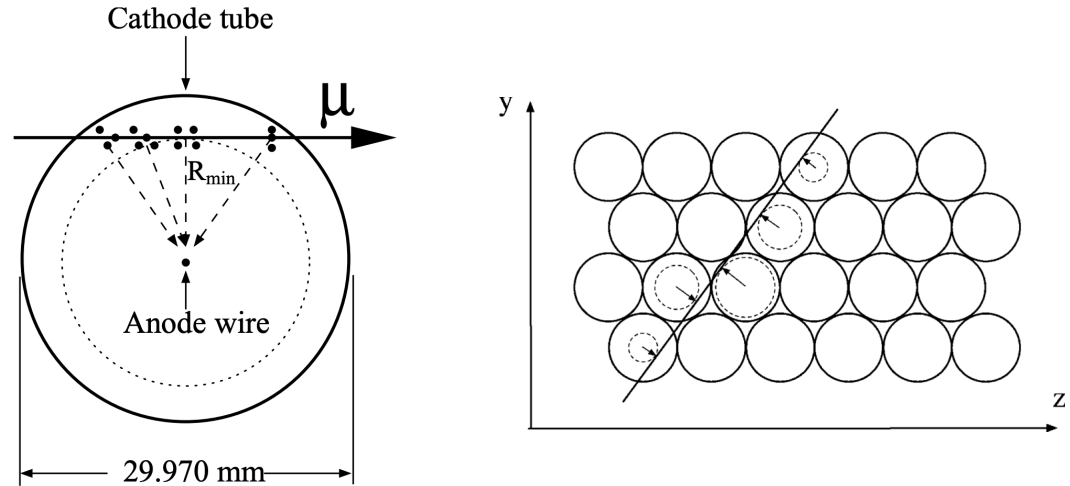
Figure 3.19: (a) MDT tube cross section showing ionization clusters along a muon track. Image taken from Ref. [124]. (b) Track fit in a MDT multilayer. Image taken from Ref. [125]

(CSC) are used which can sustain hit rates as high as 1 kHz/cm^2. The CSCs are multiwire proportional chambers with cathodes segmented into strips, as shown in Figure 3.20. The chambers use a 80%/20% mixture of Ar/CO_2 gas and operate at a voltage of 1900 V. The anode-cathode distance is $d = 2.54$ mm which corresponds to a maximum drift time of about 30 ns. Like the MDTs the CSCs are segmented into large and small chambers in ϕ. Each endcap consists of eight small chambers and eight large chambers, each of which contain four CSC planes providing four independent (η, ϕ) measurements along each track with resolutions of 60 μm $\times 5$ mm. The CSC system consists of 32 chambers in total and 31 000 individual readout channels.
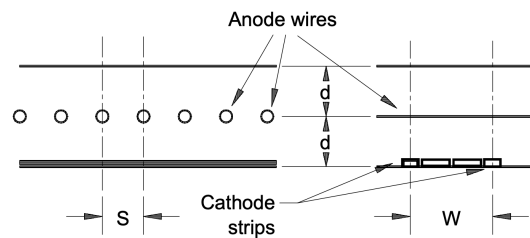
Figure 3.20: Schematic diagram of the cathode strip chamber. The anode-cathode distance, d, and the wire spacing, S, are both 2.54 mm. The Cathode readout pitch, W is 5.08 mm. Image taken from [119].

Resistive plate chambers

In the pseudorapidity range $|\eta| < 1.05$, trigger signals are provided by a system of resistive-plate chambers (RPCs). RPCs are gaseous parallel-plate detectors filled with tetrafluorethane ($C_2H_2F_4$). Each chamber consists of two resistive plates separated by a 2 mm gap and kept at a potential difference of 9.8 kV. This configuration allows for trigger timing resolutions of less than 2 ns. Each side of the chamber has a readout strip, with one side providing a measurement in z and the other in ϕ. Each RPC unit consists of two of the above described detector layers and four readout strip panels. Like the MDTs, the RPCs chambers are distributed among 16 sectors in ϕ and are positioned on either side of the MDT chambers as shown in Figure 3.18.

Thin gap chambers

In the region $1.05 < |\eta| < 2.4$, the trigger system is comprised of thin-gap chambers (TGCs). The CSCs provide both trigger capabilities as well as a second, azimuthal coordinate to complement the MDT measurement in the radial bending direction. Like the CSCs, the TGCs are multiwire proportional chambers with a 55%/45% gas mixture of CO_2/n-C_5H_{12}. The anode wires are kept at a nominal potential of 2.9 kV and run perpendicular to the cathode strips to allow for two-dimensional spacial coordinate measurements, The TGC wires provide a measurement of the radial, bending coordinate and the azimuthal coordinate is measured by the strips. The layout of the TCG chamber is shown in Figure 3.21. The distance between the wires is 1.8 mm and the anode-cathode distance is 1.4 mm. This potential and cell geometry allows for a trigger timing resolution of 4 ns. The TGC chambers are organized in 12 sectors per endcap, with each sector containing an inner and outer part, as shown in Figure 3.18. In total the TGC system consists of 3588 chambers and 318 000 individual readout channels.

3.2.4 Trigger

During Run 2, the LHC delivered pairs of proton bunches to the ATLAS detector every 25 ns, corresponding to a crossing rate of 40 MHz. The amount of memory needed to write
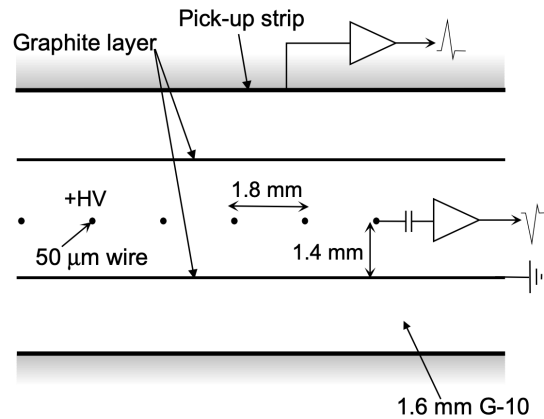
Figure 3.21: Schematic diagram of the thin gap chamber. Image taken from [119].

out the data from all detector subsystems is approximately 1.5 Mb per collision, meaning that if ATLAS were to record every single event it would generate over 60 Tb of data *per second*! It would be both unfeasible as well as unnecessary to store all of this data, as most *pp* collisions are soft parton scattering events which are absent of noteworthy physics. To reduce the data rate to a manageable level, ATLAS uses a combined hardware and software system known as the **trigger** to identify and save potentially interesting events for further analysis.

The ATLAS trigger system consists of two levels, or tiers. The **Level 1 (L1)** trigger is a hardware based system which uses coarse data collected from the calorimeters (L1Calo) and MS (L1Muon) to perform an initial loose event filtering decision within 2.5 μs of the bunch crossing. It tries to identify events with high p_T leptons, photons, jets, and large total or missing transverse energy. The L1 trigger also defines Regions-of-Interest (RoI's) in η and ϕ where the system has identified interesting features. The trigger decision is performed by the central trigger processor (CTP). The CTP can also perform prescaling which reduces the rate of events passing a nominal L1 decision by a constant factor. The L1 trigger reduces the event rate from the LHC crossing frequency of 40 MHz to a design value of 100 kHz.

Events which are selected by the L1 trigger are then passed to a software-based system known as the **High-Level Trigger (HLT)** which performs a more refined filtering of

the data by roughly reconstructing physics objects. The HLT uses all of the available detector data within the RoI's identified by the L1 system at full granularity and precision. The HLT reduces the rate of events which are written out to approximately 1 kHz, which corresponds to roughly one out of every 40000 collision events being saved. The events selected by the HLT are then transferred to the Tier-0 computing facility at CERN for offline reconstruction.
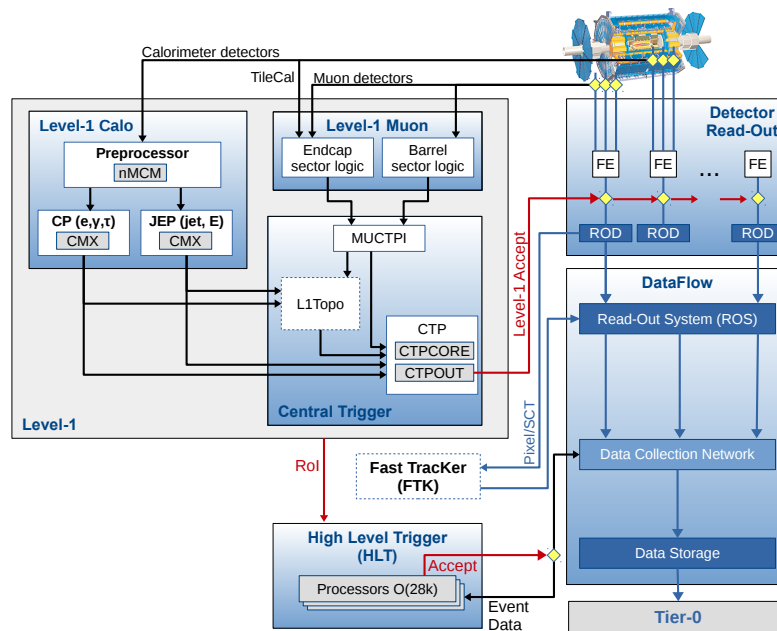
Figure 3.22: A schematic overview of the ATLAS TDAQ system in Run 2 with the L1 and HLT trigger systems shown on the left. The Fast TracKer (FTK) shown in this figure was being commissioned during Run 2 but was canceled. Image taken from Ref. [126].

Chapter 4

Event Reconstruction

It has been my philosophy of life that difficulties vanish when faced boldly.

- Isaac Asimov

In order to translate the raw data read out from the various ATLAS subsystems described in Chapter 3.2 into actual representations of the final state particles usable for physics analysis, a multitude of **reconstruction algorithms** are performed. Figure 4.1 shows how various particles interact with the ATLAS subdetectors. After the event is recorded by the online trigger system, the information from all subdetectors is combined to reconstruct so-called "physics objects" like electrons, muons, jets, etc. These objects are the closest representation available to the actual particles produced in the underlying physics process, but should always be considered candidates rather than true particles due to the imperfection of the reconstruction process[1]. This chapter describes the "standard" physics objects used in this thesis, which consist of electrons, muons, photons, and jets. A separate discussion is dedicated to the reconstruction of non-standard physics objects associated with the decays of LLPs in Chapter 5. First, Section 4.1 describes how inner detector tracks and primary vertices are reconstructed. These tracks are used as input to various physics object reconstruction algorithms, and the primary vertex is used to define the reference point for the downstream reconstruction algorithms. Section 4.2 then describes the algorithms used to reconstruct and identify jets, muons, electrons, and photons.

---

[1]Photons can be misreconstructed as electrons, for example.
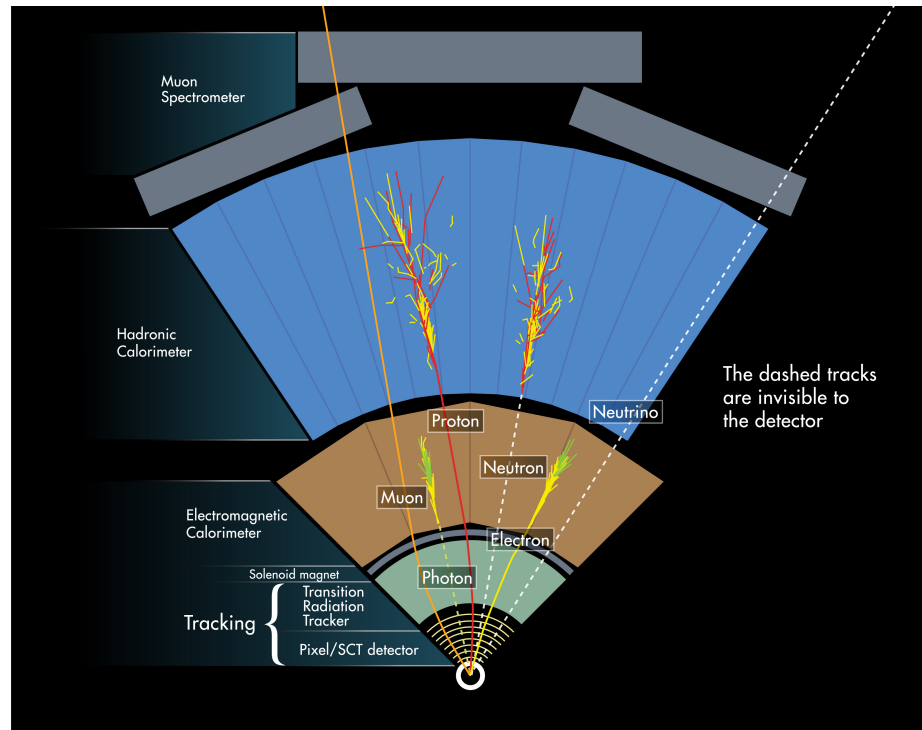
Figure 4.1: Diagram of how ATLAS detects various particles [127].

4.1 Track and vertex reconstruction

The first step in reconstructing a collision event in the ATLAS detector is the reconstruction of charged particle trajectories and identifying the proton-proton interaction vertex from which they originate.

4.1.1 Track reconstruction

As described in Section 3.2.1, a charged particle will leave energy deposits, or hits, in the active material of the ID as it traverses the detector. The trajectory, or **track**, of this charged particle may then be reconstructed by "connecting the dots" of the hits left in the various ID subsystems. However, this is much, *much*, easier said than done. To see why, consult Figure 4.2 which shows a representative event display from the view of the inner detector. In this event, 25 proton-proton collision vertices are reconstructed, each of which results in many charged particles which deposit their energy in the ID. Due to this incredibly dense environment, tracking is an exceptionally complex combinatorial problem that requires advanced algorithms to solve.
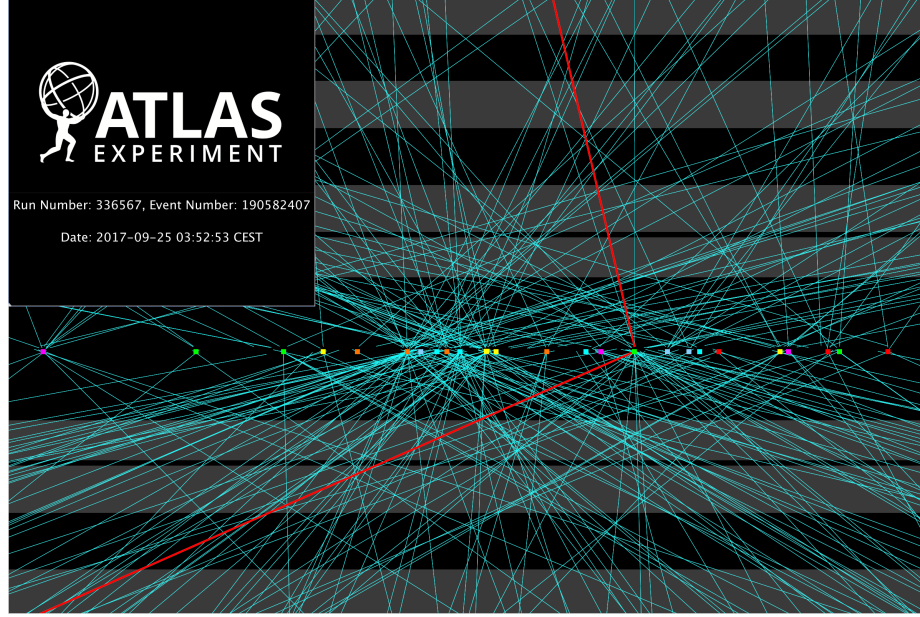
Figure 4.2: A display of a $Z \to \mu\mu$ candidate event from proton-proton collisions recorded by ATLAS with LHC stable beams at a collision energy of 13 TeV on 25$^{\text{th}}$ September 2017 (Run 336567, Event 190582407). The Z candidate is reconstructed in a beam crossing with 24 additionally reconstructed vertices from minimum bias interactions. The display is a zoom into the interaction region and shows a fraction of the 25 reconstructed vertices. The hard interaction vertex is represented by a green square from which the two muons (red tracks) are emerging. Tracks with pT > 500 MeV are displayed. Image and caption taken from [128].

Tracks are described by a set of five parameters, using a perigee representation measured in relation to the primary vertex:

$$\tau = (d_0, z_0, \phi_0, \theta, q/p) \tag{4.1}$$

The transverse and longitudinal impact parameters (d_0 and z_0) are the distances of closest approach between the track and the primary vertex in the transverse and longitudinal plane. The other three parameters are the azimuthal angle ϕ and the polar angle θ of the track momentum, and the ratio q/p of the charge of the reconstructed track divided by the magnitude of its momentum. The principal goal of track reconstruction is then to compute these five parameters for each charged particle trajectory. In this section, we will describe the various algorithms used in the standard ATLAS tracking procedure, and in Section 5.1 we will extend this discussion to the specialized tracking used to reconstruct the decays of

long-lived particles. Track reconstruction in the inner detector primarily uses an **inside-out** tracking algorithm which starts from track seeds in the pixel and SCT detectors that is then extended to a full track. A second tracking pass, referred to as **outside-in**, is then performed starting from information in the TRT and then extending to the pixel and SCT using hits that are unassociated to tracks formed in the inside-out pass. These algorithms are described in detail below.

Inside-out

The inside-out tracking procedure begins with the formation of clusters from raw pixel and SCT measurements. A cluster consists of groups of pixels or strips in a given sensor with energy deposits above threshold that share an edge or corner (Figure 4.3). From
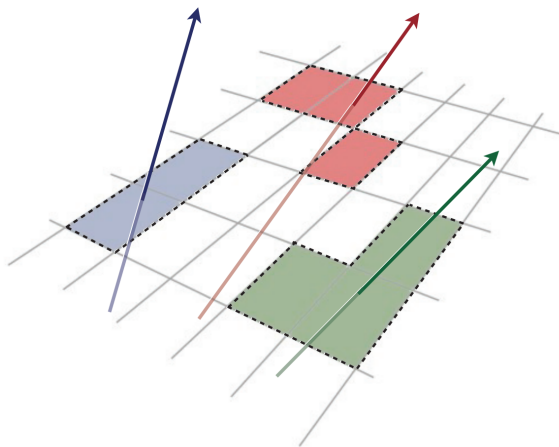
Figure 4.3: The formation of clusters from raw energy deposits in the pixel system. Image taken from Ref [129].

these clusters, three-dimensional position measurements called **space-points** are created. In the pixel detector this is simple, because the pixel modules already provide a three-dimensional local measurement. In the SCT however, the precision measurement is only given in the direction orthogonal to the silicon strip direction. To obtain a three-dimensional point, the stereo angle rotation between the two sides of the SCT layers modules is used (Section 3.2.1).

Tracks are then **seeded** using sets of three space-points [130]. Seeds can be built from three pixel space-points, three SCT space-points, or a combination of space points from

both detectors. The seed provides already a rough estimate of the momentum and impact parameters of the trajectory, and loose selections are placed on the track seeds to remove those which are not compatible with a charged particle originating from the IP. Most notably, seeds are removed if the absolute value of the transverse (longitudinal) impact parameter, d_0 (z_0) is greater than 10 mm (250 mm). The impact of this selection will be discussed in Chapter 5. The combinatorial Kalman filter algorithm [131] is then used to form track candidates from the accepted seeds by incorporating additional space-points which are compatible with the initial seed trajectory. The Kalman filter is an iterative process which alternates between two steps, called the filter and the smoother. The filter performs a prediction about the location of the next hit along the track trajectory. If a compatible hit is found it is added to the track. In the smoothing step, the track fit is updated to reflect the newly added measurement. Each time a new measurement is incorporated the track parameters and error matrix are recomputed. This process increases the accuracy on the track parameter estimate after each new measurement is added, and continues until it reaches the last layer of the silicon detector.

The track finding process results in a very high number of track candidates, many of which have overlapping or incorrectly assigned space points. To resolve this, the track candidates are then fed into ambiguity-solving algorithms which assign each candidate a score based on its momentum, number of hits, number of shared modules, and number of holes[2] [130]. Each additional hit associated with a track increases the score, with the weight of each hit determined by the precision of the corresponding subdetector (pixel clusters are weighted higher than SCT). The presence of holes on the other hand reduces the overall track score. The χ^2 of the track fit is also used to penalize against poor quality candidates. Track candidates with a high score are most likely to correctly represent the trajectory of a charged particle, whereas tracks with a low score are more often purely combinatorial collections of hits, often referred to as **fakes**. Tracks that are assigned a low relative score by the ambiguity solver are rejected.

After the tracks are assigned scores, the ambiguity solver determines how to handle clusters that are assigned to multiple track candidates. When clusters are shared between

---

[2]Holes are defined as intersections of the reconstructed particle trajectory with an active detector module that do not contain a corresponding hit.

multiple tracks, the candidates compete against each other to determine to which track the hit will be associated. Hits are mainly assigned to the track with higher score, and the remaining track is refit without the formerly shared hit and scored again. Track candidates are then rejected by the ambiguity solver if they fail to meet a series of quality criteria given in Table 4.1.

Parameter	Cut value
Min. p_T	400 MeV
Max. $|\eta|$	2.5
Max. $|d_0^{BL}|$	2 mm
Max. $|z_0^{BL} \sin\theta|$	3 mm
Min Si hits	7
Max. shared clusters	1 pixel or 2 SCT
Max. # of pixel holes	1
Max. # of Si holes	2

Table 4.1: Quality criteria used in the ambiguity solver. Si refers to the combined pixel and SCT systems. $|d_0^{BL}|$ and $|z_0^{BL}|$ are the impact parameters calculated with respect to the measured beam-line position [129].

Finally, track candidates that pass the ambiguity solver are extended into the TRT by extrapolating the trajectory of the track and associating TRT hits compatible with the candidate. The track is then refit and the track parameters are recomputed. The quality of the combined track is then evaluated using a similar procedure to that of the ambiguity solver, and the scores of the original silicon-only track are compared to the score computed after the TRT extension. If the extended track is assigned a worse score than the non-extended track, the extension is rejected and the original silicon track is kept. This can happen if there are too many outlier TRT hits or holes (see Figure 4.4). If the inclusion of the TRT hits improves the overall track fit, the TRT extension is marked successful and is incorporated into the final track.

Outside-in

After the inside-out algorithm is run, a second, outside-in, tracking pass is performed. The outside-in algorithm begins by reconstructing standalone TRT track segments in regions seeded by the electromagnetic calorimeter. The resulting TRT segments are then extrapolated into the silicon detectors, and compatible hits that were not used in the inside-out
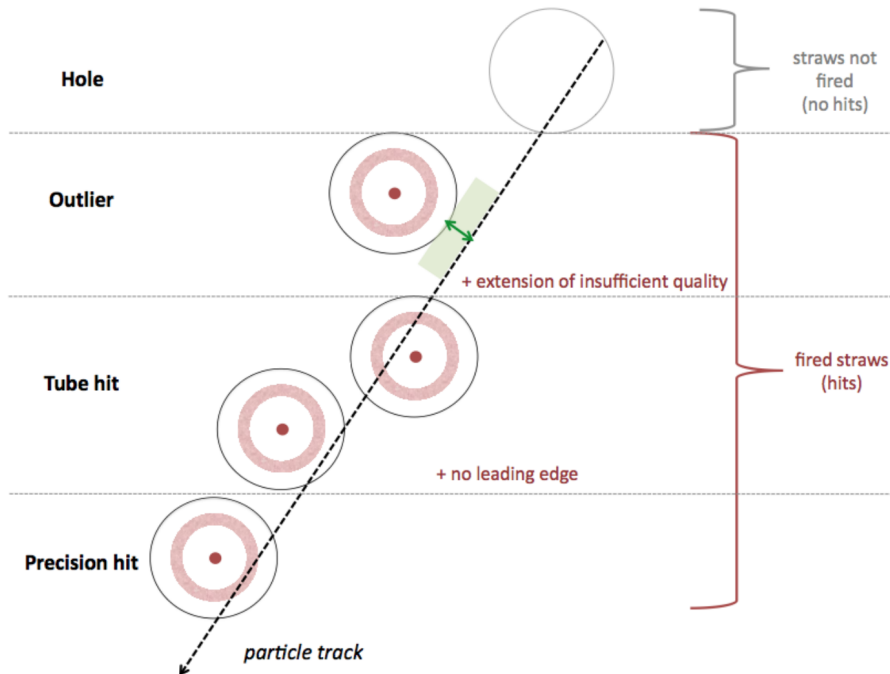
Figure 4.4: Definition of TRT hits. Image taken from [132].

tracking pass are used to extend the segment to a full track. The outside-in algorithm is capable of reconstructing tracks coming from secondary decay vertices (e.g. K_S^0 decays and photon conversions) which may not have a sufficient number of silicon hits to be reconstructed by the inside-out algorithm, but still have small enough impact parameters to survive the quality cuts.

Tracking performance

The resulting tracks from both the inside-out and outside-in tracking passes form the complete collection of standard tracks. After reconstruction, additional selections are placed on tracks to define tight and loose working points. The track reconstruction efficiency as a function of truth p_T is shown in Figure 4.5 for both working points.

It is important to note the limitations of the standard tracking procedure. As mentioned previously, both the inside-out and outside-in algorithms place strict cuts on the transverse and longitudinal impact parameters at 10 mm and 250 mm, respectively. These requirements are put in place to reduce both the number of fake tracks that are reconstructed, as well as the overall CPU time of the tracking algorithm. However, they also severely limit
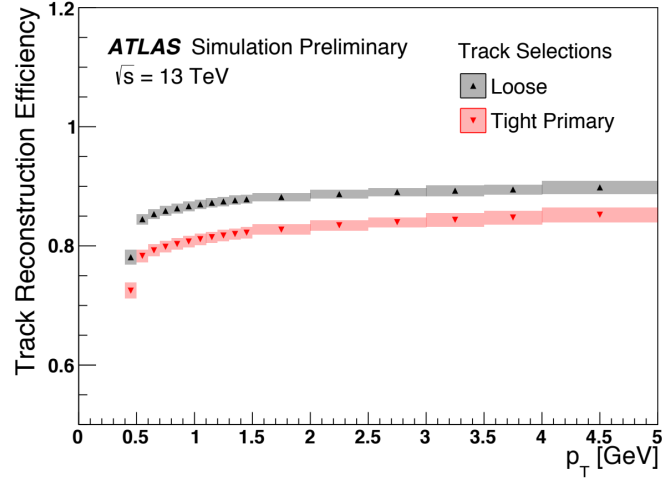
Figure 4.5: The standard track reconstruction efficiency as a function of truth p_T. Image taken from [133].

the ability of the standard tracking procedure to reconstruct tracks that are significantly displaced from the IP such as those originating from the decays of long-lived particles. To reconstruct these decays, an additional tracking pass is needed with loosened impact parameter requirements. This will be described in Section 5.1.

4.1.2   Primary vertex reconstruction

Once the charged particle trajectories have been reconstructed by the tracking algorithm, the next step in reconstructing the full kinematic properties of the event is to determine from which pp interaction each charged particle originated. The process of associating charged particle trajectories to pp interactions is known as **primary vertex reconstruction** and is essential for the reconstruction of hard-scatter interactions. The ATLAS primary vertex reconstruction algorithm [134] consists of two steps: vertex finding, in which vertex candidates are formed from the collection of selected tracks, and vertex fitting which reconstructs the vertex position along with its covariance matrix.

For tracks to be considered in the vertex reconstruction, they are required to satisfy following requirements [134], [135]:

- $p_T > 500$ MeV; $|d_0| < 4$ mm; $\sigma(d_0) < 5$ mm; $\sigma(z_0) < 10$ mm;

- Number of silicon hits ≥ 9 (11) if $|\eta| < 1.65$ ($|\eta| > 1.65$)

- Hits in the first two pixel layers ≥ 1

- A maximum of 1 shared module (1 shared pixel hit or 2 shared SCT hits)

- Pixel holes = 0

- SCT holes ≤ 1

From the collection of selected tracks, an iterative algorithm is used to identify primary vertex candidates. The algorithm proceeds in several steps. First, a seed position for the first vertex is computed using the center of the beam spot to determine the x- and y- coordinates, and the mode of the z-coordinates of tracks at their points of closest approach the beam spot to determine the z-coordinate. Next, the input tracks and the seed position are used to determine the best fit vertex position. The fit uses an iterative annealing procedure, where each input track is assigned a weight corresponding to its compatibility with the vertex estimate. The vertex position is recalculated using the weighted tracks, and then the procedure is repeated, with new track weights computed with respect to the updated vertex position. At first all tracks will have similar weights. But after several iterations, tracks that are not compatible with the vertex will have small weights and therefore a minimal impact on the vertex position. A representative histogram of the distribution of track weights at several points in the iterative process is shown in Figure 4.6. After the vertex
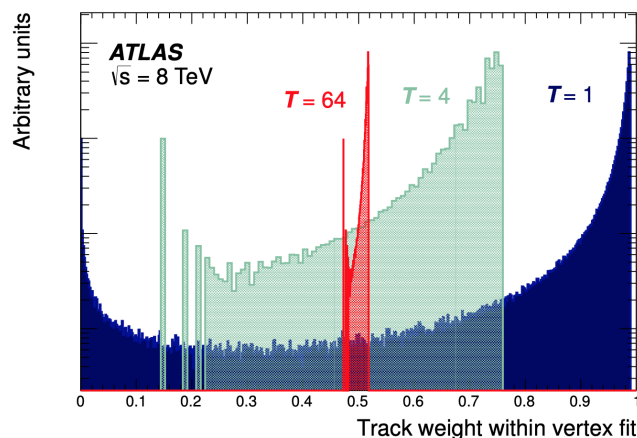
Figure 4.6: Histogram showing the weights applied to tracks in the vertex reconstruction fit. At each iteration, outlier tracks are downweighted so as to have a lesser impact on the vertex position in the fit. Image taken from [135].

position is determined, tracks that are incompatible with the vertex by more than seven

standard deviations are removed, and the rejected tracks are used as input for a new itera-

tion of the vertex finding algorithm. The above procedure is repeated until there are either

no remaining tracks, or no additional vertices can be found.

All vertices with at least two tracks are considered in the collection of reconstructed

vertices. The vertex with the highest $\sum p_{\mathrm{T}}^2$ of associated tracks is taken to be the hard scatter

vertex and is usually referred to as *the* primary vertex. All other vertices are considered to

be pileup interactions.

4.2 Physics object reconstruction

This analysis makes use of a variety of different standard physics objects, including jets,

muons, electrons, and photons. Each object has an associated reconstruction algorithm

which is used to identify candidates, and careful calibration procedures are applied to

ensure good agreement between data and simulation. In some cases, additional identifi-

cation algorithms are applied which help to reduce spurious detector signals that may be

reconstructed as true physics objects. These algorithms are detailed below for each physics

object.

4.2.1 Jets

Jet reconstruction

Jet reconstruction begins with the formation of three-dimensional, massless, topologically

connected EM and hadronic calorimeter cells called **topo-clusters** using a nearest-neighbor

algorithm [116]. The basic observable controlling this cluster formation is the cell signal

significance, $\varsigma_{\mathrm{cell}}^{\mathrm{EM}}$, defined as the ratio of the cell energy to the expected noise in each cell:

$$\varsigma_{\mathrm{cell}}^{\mathrm{EM}} = \frac{E_{\mathrm{cell}}^{\mathrm{EM}}}{\sigma_{\mathrm{noise,cell}}^{\mathrm{EM}}} \tag{4.2}$$

Topo-clusters are formed starting from a calorimeter cell with a highly significant seed

signal satisfying $\varsigma_{\mathrm{cell}}^{\mathrm{EM}} > 4$. Cells neighboring the seed cells in three-dimensions are added to

the topo-cluster using the threshold $\varsigma_{\text{cell}}^{\text{EM}} > 2$ to control its growth. If a particular neighbor is a seed cell passing the threshold $\varsigma_{\text{cell}}^{\text{EM}} > 4$ the two clusters are merged. Finally, cells with $\varsigma_{\text{cell}}^{\text{EM}} \geq 0$ in the perimeter are added to the cluster, to ensure that the tails of showers are not discarded. This set of thresholds is often referred to as '4-2-0' topo-cluster reconstruction. The resulting topo-cluster is characterized by a core of cells with highly significant signals surrounded by an envelope of less significant cells. The resulting energy of the topo-cluster is defined at the electromagnetic (EM) scale, and corrections are applied to the topo-cluster four-vectors to account for the position of the primary vertex.

The jets used in this thesis are reconstructed using only calorimeter-based energy information using the origin-corrected EM scale topo-clusters and are referred to as **EMtopo jets**. Hadronic final-state measurements can be improved by using the information from both the tracking and calorimeter systems using the particle flow (PFlow) algorithm [136]. However, the use of tracking information in jet reconstruction is not suitable for jets originating from the decay of long-lived particles which may not satisfy the assumptions made by the PFlow algorithm.

The topo-cluster four-vectors are then used as input constituents to the **anti-k_t** jet clustering algorithm [137]. The anti-k_t algorithm is a sequential recombination algorithm that is infrared and collinear (IRC) safe and has the property that the boundaries of the final jets are not significantly affected by soft radiation, making it the default jet-finding algorithm used by the experiments at the LHC among the set of IRC-safe jet finding algorithms. The algorithm relies on the distance metrics

$$d_{ij} = \min\left(\frac{1}{k_{T,i}^2}, \frac{1}{k_{T,j}^2}\right)\frac{\Delta R_{ij}^2}{R^2} \tag{4.3}$$

$$d_{iB} = \frac{1}{k_{T,i}^2} \tag{4.4}$$

where $\Delta R_{ij}^2 = (y_i - y_j)^2 + (\phi_i - \phi_j)^2$, R is the **radius parameter**, and $k_{T,i}$ is the transverse momentum of the ith jet constituent. The metric d_{ij} is a measure of the "distance" between the ith and j^{th} constituents, and d_{iB} is the distance between the ith constituent and the beam. The jets used in this thesis are defined using radius parameter $R = 0.4$.

For each input constituent i, the algorithm proceeds by computing d_{iB} and d_{ij} for all

other constituents $j \neq i$. If the minimum distance computed is a d_{ij}, then the two constituents i and j are combined to form a single constituent in the list, and the original constituents are removed. If instead $d_{iB} < \min(d_{ij})$, then the ith constituent is removed from the set of constituents and is considered as a complete jet. The algorithm continues sequentially until there are no more constituents in the input list. The result of this process is a set of jets in the form of recombined constituents, as shown in Figure 4.7. The key
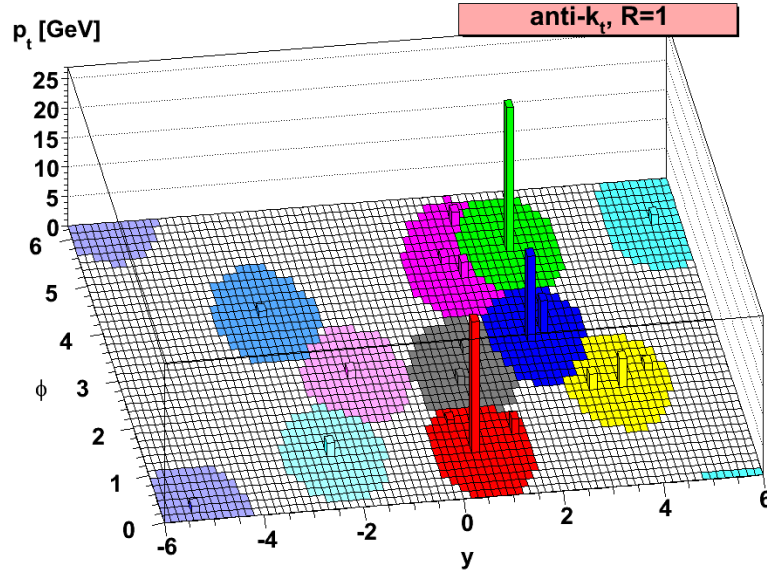
Figure 4.7: A sample parton-level event clustered with the anti-k_t algorithm. Image taken from Ref [137].

feature of the anti-k_t algorithm is that it tends to cluster soft particles with hard ones long before they cluster among themselves. If an energetic constituent has no similarly hard neighbors within a distance $2R$, then the algorithm will simply combine all soft particles within a circle of radius R resulting in a perfectly conical jet. This results in jet boundaries that are resilient with respect to soft radiation, but flexible with respect to hard radiation.

Jet calibration

As mentioned in the previous section, the energy of the topo-clusters is defined at the EM-scale, meaning that energy deposited in the calorimeters by particles produced in electromagnetic showers is correctly measured. However, this does not take into account energy deposited by particles produced in a hadronic shower. To correct for this as well as several

other effects, a series of **jet energy scale (JES)** calibrations are applied to the jet four-vectors to correct the energy of the reconstructed jets in the detector to match that of the truth-level jets. The JES calibration sequence is shown in Figure 4.8 and described in more detail in this section.
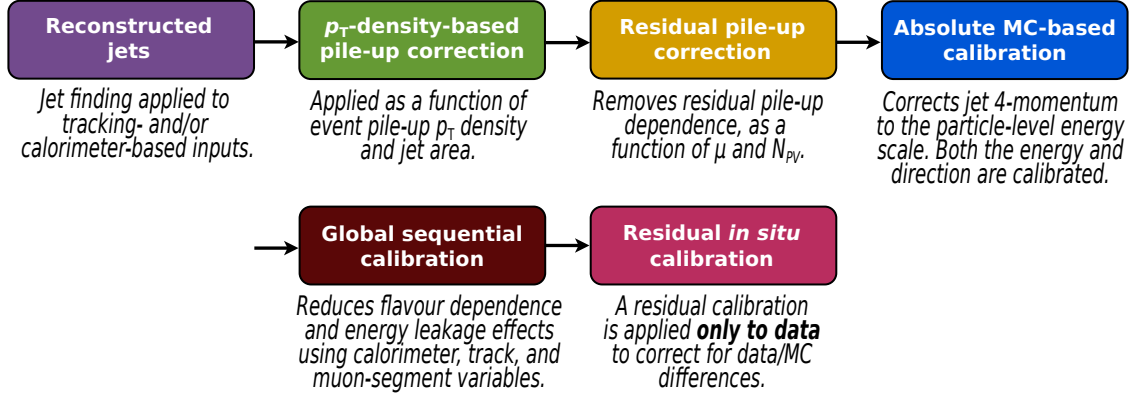
Figure 4.8: The stages of jet energy scale calibrations. Each correction is applied to the four-momentum of the jet. Image taken from Ref [138].

When performing the jet clustering in dense environments, particles originating from pileup interactions are likely to contribute to the measured jet energy. The JES pileup calibrations corrects for this by subtracting off these additional contributions from the reconstructed jet p_T. The first correction is computed from the median p_T density of jets in the $\eta - \phi$ plane, $\rho = \langle p_T/A \rangle$, where the jet area A is a measure of the susceptibility of the jet to pileup and is computed from the relative number of *ghost* particles associated with a jet after clustering [139]. The quantity $\rho \times A$ then gives an estimate of the pileup contribution for a jet of area A. However, due to the fact that the ρ calculation does not fully describe the pileup sensitivity in the forward calorimeter region or in the higher-occupancy core of high-p_T jets, some dependence of the jet p_T remains after the p_T-density based correction. This residual dependence is corrected for by computing the difference between the reconstructed jet p_T and truth jet p_T as a function of both N_{PV} and μ, which are sensitive to in-time and out-of-time pile-up respectively. The jet p_T after all pileup corrections is given by

$$p_T^{\mathrm{corr}} = p_T^{\mathrm{reco}} - \rho \times A - \alpha \times (N_{\mathrm{PV}} - 1) - \beta \times \mu \qquad (4.5)$$
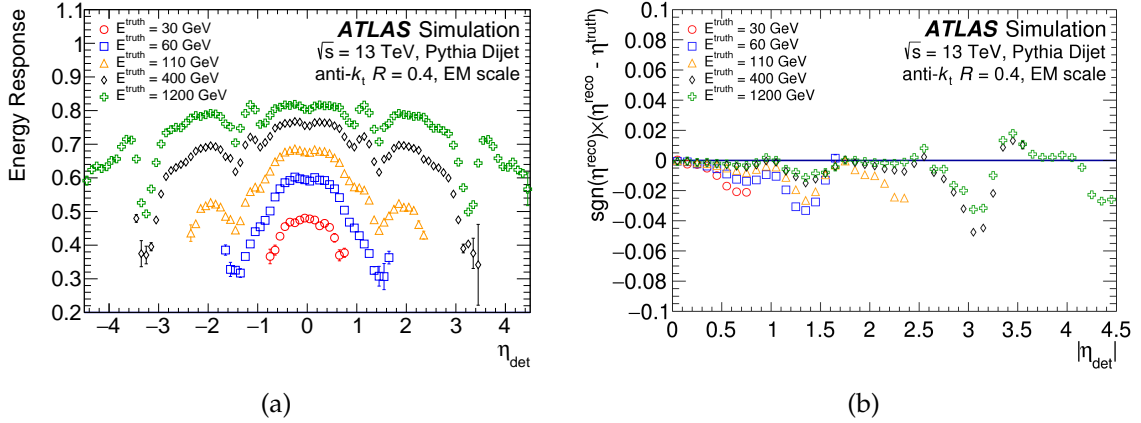
Figure 4.9: (a) The average jet energy response as a function of η_{det} for jets with several difference values of E^{truth}. The energy response is computed after origin and pile-up corrections are applied. (b) The signed difference between the truth jet η^{truth} and the reconstructed jet η^{reco} due to biases in the jet reconstruction. Images taken from Ref [140].

where $\alpha = \frac{\partial p_T}{\partial N_{\text{PV}}}$, and $\beta = \frac{\partial p_T}{\partial \mu}$.

Next, the absolute jet energy scale and η calibrations restore the reconstructed jet four-momenta to the particle-level energy scale. These calibrations account for differences between the measured and true jet energies due to detector effects such as non-compensating calorimeter response, mismodeling of the inactive material within the detector, and biases in the jet η reconstruction caused by the transition between different calorimeter technologies and regions with different calorimeter granularity. The JES calibration is derived from MC simulation by calculating the **jet response**, $\mathcal{R}$, defined as the ratio $E^{\text{reco}}/E^{\text{truth}}$. The average jet response is shown in Figure 4.9a for several different values of E^{truth}. The inverse of the jet response is applied as a correction to the EM scale jets, after which the response is consistent with unity [140]. A bias in the reconstructed jet η is also observed, as shown in Figure 4.9b. This bias artificially increases the energy of one side of the jet with respect to the other, thereby distorting the reconstructed four-momentum. An additional correction is then applied to η to account for this effect as a function of $|\eta_{\text{det}}|$. EMtopo jets calibrated with the full JES and η calibrations are considered to be at the **EM+JES scale**.

After applying the previous jet calibrations, residual dependencies of the JES on several jet properties remain. These include the flavor and energy distribution of the jet's constituent particles, their transverse distribution within the jet, and effects due to the initiating particle (i.e. quark- vs. gluon-initiated jets) such as the average particle composition

and shower shape. In a given $(p_\mathrm{T}^\mathrm{true}, |\eta_\mathrm{det}|)$ bin, fluctuations in these properties can impact the JES from jet to jet. To account for these effects, a series of multiplicative corrections known as the **Global Sequential Calibration (GSC)** are applied. The GSC has five stages[3], each of which consists of an independent jet four-momentum correction derived based on a particular jet observable that has been identified to improve the JES. The corrections are applied sequentially, neglecting correlations between observables. The GSG improves the **Jet Energy Resolution (JER)** without changing the average jet energy response, where the jet resolution is defined as the standard deviation of a Gaussian fit to the jet p_T response distribution[4].

The final JES calibration step accounts for remaining differences in the EM+JES jet response between data and simulation. As opposed to the previously described calibrations, this so-called *in situ* calibration is only applied to data. First, the jet energy scale of forward jets $(0.8 < |\eta_\mathrm{det}| < 4.5)$ is corrected to that of well-measured central jets $(|\eta_\mathrm{det}| < 0.8)$ using dijet events in a process known as η-**intercalibration**. The calibration is derived from the ratio of the jet p_T responses in data and simulation. Three other *in situ* calibrations are derived by balancing the p_T of a jet against other well-measured reference objects including photons, Z bosons, and calibrated jets. A statistical combination of the three methods provides a single smooth calibration which is applicable across the full range of p_T, as shown in Figure 4.10.

The uncertainties corresponding to the full set of JES calibrations will be discussed in Section 7.3.

Flavor tagging

ATLAS uses several different algorithms to identify jets containing b-hadrons (b-jets). These so-called **b-tagging algorithms** are essential tools for both measurements of SM processes as well as searches for new physics. The DL1 b-tagging algorithm quantifies the likelihood that a jet originated from a light- (u, d, s, c, g) versus b-flavor quark [141], [142]. This

---

[3]The GSC for PFlow jets has an additional stage to correct the fraction of the jet p_T measured from ghost-associated tracks [138].

[4]Similarly to the jet energy response, the p_T response is defined as the ratio of $p_\mathrm{T}^\mathrm{reco}$ to $p_\mathrm{T}^\mathrm{truth}$
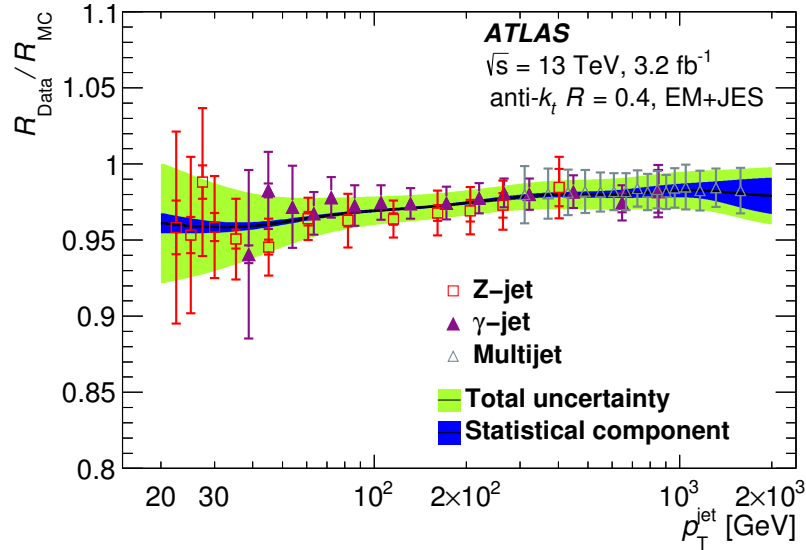
Figure 4.10: Ratio of the EM+JES jet response in data to that in simulation as a function of jet p_T for Z-jet, γ-jet, and multijet *in situ* calibrations. Image taken from Ref [140].

algorithm exploits several features of b-jets, such as the lifetime, mass, and decay kinematics of b-hadrons, within a deep feed-forward neural network to distinguish between these hypotheses. Large values of the DL1 discriminant correspond to b-like jets, while small values correspond to light-like jets. In the search presented in this thesis, the DL1 discriminant is an important ingredient used to classify and predict the number of expected events due to SM backgrounds (Section 7.2).

4.2.2 Muons

The search presented in this thesis utilizes muons to identify the muonic decays of the Z boson. The algorithms used by the ATLAS experiment to reconstruct, identify, and calibrate muons are hence described below.

Muon reconstruction

Muons are reconstructed using independent tracking information from both the ID and the MS detector subsystems [143]. The ID tracks are reconstructed using the same algorithm described in Section 4.1. In the MS, track reconstruction begins by combining hits in each MDT chamber to form muon **segments** by fitting the hits found in each layer to a straight-line. Information from the trigger chambers (RPC and TGC) is used to measure

the coordinate orthogonal to the bending plane. In the region $|\eta| > 2.0$, the CSC chambers provide additional tracking coverage and a separate combinatorial search is used to reconstruct tracklets.

Muon track candidates are then built by combining segments from different layers. First, candidates are seeded in the central layers of the detector where the number of hits in the trigger chambers is greatest. When no further candidates may be seeded, the search is extended to form seeds in the inner and outer layers. At least two segments are required to build a track candidate, except in the transition region between the barrel and endcap where one high quality segment may be used. An overlap removal algorithm is then used to resolve the situation in which one segment is used to build several track candidates by either assigning the segment to the track to which it has the strongest association, or in some situations allowing for the segment to be shared between two tracks. For example, to maintain high efficiency for muons produced with small opening angles, tracks are allowed to share segments in two layers so long as their trajectories diverge in the outermost layers. The hits associated with each track candidate are then fitted using a global χ^2 fit, and candidates are accepted if the χ^2 satisfies the selection criteria. Hits are removed from the track candidate if they are found to negatively impact the fit, and additional hits may be added if they are found to be compatible with the trajectory. The track candidate is refit each time a hit is added or removed.

There are four muon reconstruction algorithms used to combine the information from the various detector subsystems into a fully reconstructed muon:

- **Combined (CB)** muons use the tracking information from both the ID and the MS and are reconstructed by performing a global refit of the hits corresponding to the ID and MS tracks. During the refitting procedure, MS hits may be added or removed from the track to improve the fit quality. In general, combined muons are reconstructed following an outside-in pattern recognition algorithm, in which the muons are first reconstructed in the MS and then extrapolated inward and matched to an ID track.

- **Segment-tagged (ST)** muons consist of a fitted ID track and a single MS segment. ST

muons are used to reconstruct muons which cross only one layer of MS chambers, either because of insufficient p_T or because they fall in a region of reduced acceptance.

- **Calorimeter-tagged (CT)** muons consist of a fitted ID track and an energy deposit in the calorimeters. CT muons have the lowest purity of all the muon types but recover acceptance for muons in regions with low coverage from the MS.

- **Extrapolated (ME)** muons consist of only a MS track and a loose requirement on compatibility with originating from the IP. These muons are required to traverse at least two layers of MS chambers to provide a track measurement, except in the forward region where three layers are required. ME muons are used to extend the acceptance for muon reconstruction into the region $2.5 < |\eta| < 2.7$, which is not covered by the ID.

When two muon types share the same ID track, preference is given first to CB muons, then to ST, and lastly to CT muons. Overlap between ME muons is resolved by selecting the track with the best fit quality and highest number of hits.

Muon identification

Muons are categorized by a set of identification working points (WPs) which applying quality requirements designed to reduce backgrounds from pion and kaon decays. Four muon identification selections (*Medium*, *Loose*, *Tight*, and *High-p_T*) are provided to accommodate the needs of different physics analysis and performance groups [143]. The Medium identification criteria is the default selection for muons in ATLAS, as well as the WP used in this thesis.

Medium muons are required to have either CB or ME tracks. For CB tracks, the variables used in muon identification are:

1. q/p significance, defined as the absolute value of the difference between the ratio of the charge and momentum of the muons measured in the ID and MS divided by the
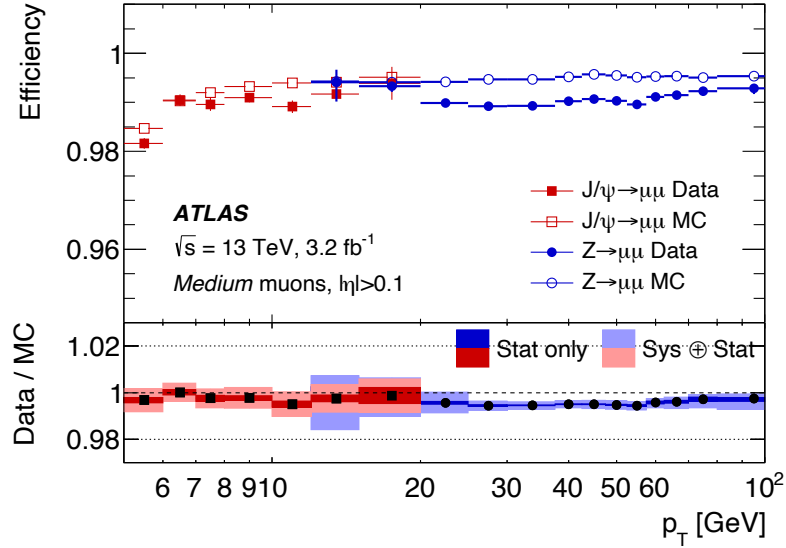
Figure 4.11: Muon reconstruction efficiency for the *Medium* selection as a function of the p_T of the muon in $Z \rightarrow \mu\mu$ and $J/\Psi \rightarrow \mu\mu$ events in both data and MC. Image taken from Ref [143].

sum in quadrature of the corresponding uncertainties:

$$\frac{|(q/p)^{\text{ID}} - (q/p)^{\text{MS}}|}{\sqrt{\sigma(p_T^{\text{MS}})^2 + \sigma(p_T^{\text{MS}})^2}} \tag{4.6}$$

2. ρ', defined as the absolute value of the difference between the transverse momentum measurements in the ID and MS divided by the p_T of the combined track:

$$\frac{|p_T^{\text{MS}} - p_T^{\text{ID}}|}{p_T^{\text{Combined}}} \tag{4.7}$$

3. The normalized χ^2 of the combined track fit

The *Medium* WP requires CB muons to have ≥ 3 hits in at least two MDT layers, except for tracks in the $|\eta| < 0.1$ region where tracks with at least one MDT layer but no more than one MDT hole layer are allowed. ME muons are included to extend the acceptance outside the ID geometrical coverage, and are required to have $2.5 < |\eta| < 2.7$ and hits in at least three MDT/CSC layers. To suppress the contamination due to hadrons misidentified as muons, q/p significance is required to be less than seven to ensure compatibility between the ID and MS momentum measurement. The ID track is required to have at least one

Pixel hit, at least five SCT hits, fewer than three Pixel or SCT holes, and that at least 10% of the TRT hits originally assigned to the track are included in the final fit[5].

The reconstruction efficiency for *Medium* muons is shown in Figure 7.25 for data and simulated samples of $Z \to \mu\mu$ and $J/\Psi \to \mu\mu$ events. As shown in the Data/MC ratio, the measured reconstruction efficiency in data, ϵ^{Data}, differs from that of simulation, ϵ^{MC}. To account for this difference, a scale factor is defined

$$\text{SF} = \frac{\epsilon^{\text{Data}}}{\epsilon^{\text{MC}}} \tag{4.8}$$

which is a function of muon p_{T} and η. The scale factors are applied to each selected muon in an event to correct for systematic differences between data and MC. The systematic uncertainty associated with these scale factors will be discussed in Section 7.3.

Muon calibration

After reconstruction, corrections are applied to muon candidates to achieve better agreement between data and simulation in terms of the muon momentum scale and resolution. To derive these corrections, the transverse momentum of the ID and MS components of a CB track are compared between data and MC in $\eta - \phi$ detector regions that are homogeneous in terms of detector technology and performance [143]. These corrections are applied to MC to account for effects such as magnetic field inhomogeneities that are not properly taken into account in the simulation. The momentum distribution in MC is also smeared such that the relative p_{T} resolution, $\sigma(p_{\text{T}})/p_{\text{T}}$, properly describes that of the data. The invariant mass distributions of $Z \to \mu\mu$ candidates are shown in Figure 4.12 for data as well as uncorrected and corrected simulation. After correction, the distribution in simulation agrees with the data within the systematic uncertainties, demonstrating the overall effectiveness of the muon calibration procedure. The systematic uncertainties associated with this calibration and their impact on the analysis presented in this thesis will be discussed in Section 7.3.

---

[5]The TRT requirement is only employed for $|\eta|$ between 0.1 and 1.9, in the region of full TRT acceptance
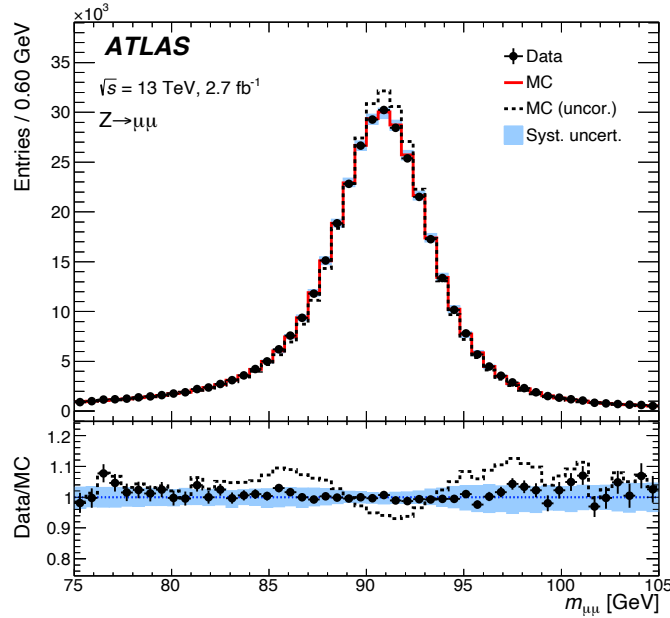
Figure 4.12: Dimuon invariant mass distribution of $Z \to \mu\mu$ events. The solid line corresponds to the simulation with the MC momentum corrections applied while the dashed lines show the simulation when no correction is applied. Image taken from Ref [143].

4.2.3 Electrons

In addition to muons, this search makes use of electrons to identify the $Z \to ee$ decay. The algorithms used by the ATLAS experiment for the reconstruction, identification, and calibration of electrons are described below.

Electron reconstruction

The reconstruction of electron candidates is based on localized clusters of energy deposits in the electromagnetic calorimeter, charged-particle tracks in the inner detector, and a matching in $\eta \times \phi$ space of the tracks to the clusters [144], [145]. A schematic illustrating the path of an electron through the detector is shown in Figure 4.13.

Similar to the jet reconstruction algorithm described in Section 4.2.1, electron reconstruction begins with the formation of topo-clusters from EM and hadronic calorimeter cells using the '4-2-0' set of thresholds on the cell significance. These topo-clusters are then used to identify potential electron tracks using a loose matching criteria in η and ϕ. A subsequent fitting procedure is performed on the matched tracks using a Gaussian Sum Filter

(GSF) [146] method designed to better account for energy loss of charged particles in material than the standard Kalman Filter. The topo-clusters are then grouped into dynamic, variable-size clusters, called **superclusters** which are designed to help recover the energy lost due to the emission of bremsstrahlung photons. The procedure to form superclusters proceeds as follows. First, topo-clusters are tested one by one in order of descending E_T to be seeds for superclustering. For a cluster to be used as an electron supercluster seed, it is required to have $E_T > 1$ GeV and must be matched to a track with at least four Si hits[6]. Once a seed cluster is identified, the algorithm attempts to find satellite clusters based on a $\Delta\eta \times \Delta\phi$ window centered on the seed barycenter to capture energy deposits by secondary showers generated by the original electron. The grouping of seed clusters and their associated satellite clusters are called superclusters.
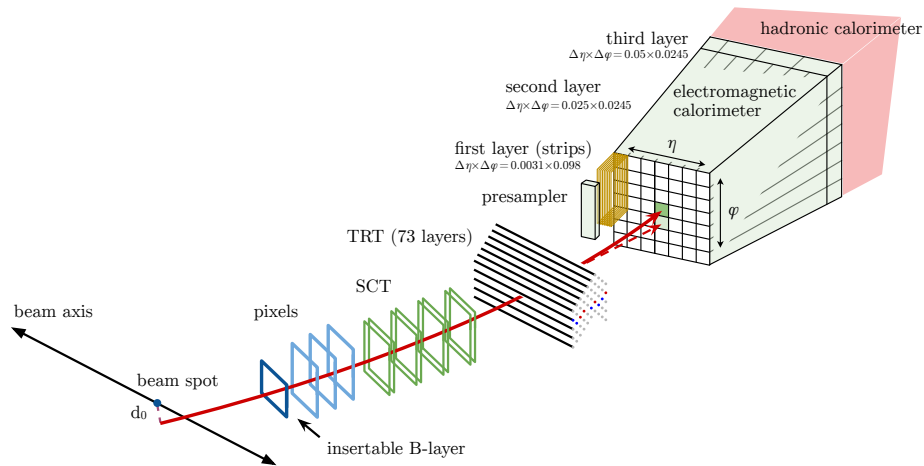
Figure 4.13: A schematic of the path of an electron through the detector. The dashed red trajectory indicates the path of a photon produced by the interaction of the electron with the material in the ID. Image taken from Ref [144].

Electron identification

After reconstruction, electrons are selected using a likelihood based (LH) identification [144] to reject background from jets that mimic the signature of prompt electrons, electrons from photon conversions in the detector material, and non-prompt electrons from the decay of heavy flavor hadrons. The LH is given by the product of probability density functions

---

[6]Outside-in tracks are allowed to have fewer than the requisite 7 Si hits if they are loosely matched to EM clusters.

(PDFs) for a set of input variables chosen based on their ability to discriminate between prompt electrons and various forms of background. The inputs to the LH include measurements from the inner detector, the calorimeter, and quantities that combine both tracking and calorimeter information. The LH is given by

$$L_{S(B)}(\mathbf{x}) = \prod_{i=1}^{n} P_{S(B),i}(x_i) \tag{4.9}$$

where $\mathbf{x}$ is the vector of input quantities, $P_{S,i}(x_i)$ is the PDF of quantity i at value x_i for signal electrons, and $P_{B,i}(x_i)$ is corresponding PDF for background. The signal PDFs are derived from $Z \to ee$ and $J/\Psi \to ee$ events in data, while those for the background are derived from a sample primarily comprised of dijet events. For each electron candidate, a discriminant d_L is formed:

$$d_L = \frac{L_S}{L_S + L_B}, \tag{4.10}$$

which is ultimately transformed to smooth sharp peaks in the distribution using the inverse sigmoid function. The distribution of the transformed LH discriminant is shown in Figure 4.14.
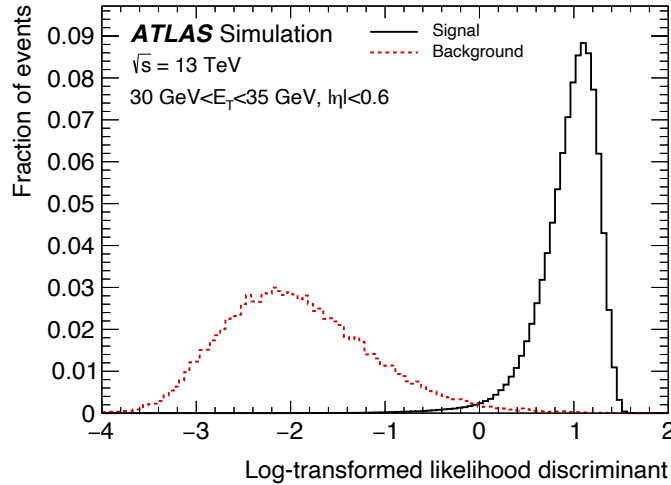
Figure 4.14: The transformed LH discriminant for reconstructed electron candidates with $30 < E_{\mathrm{T}} < 35$ GeV and $|\eta| < 0.6$. Image taken from Ref [144].

Fixed values of the LH discriminant are used to define four operating points corresponding to increasing thresholds of the discriminant. These operating points are referred

to as *VeryLoose*, *Loose*, *Medium*, and *Tight*. The electrons used by the search presented in this thesis are required to pass the *Medium* operating point. The identification efficiency for the *Loose*, *Medium* and *Tight* electron operating points is shown in Figure 4.15 for $Z \rightarrow ee$ events in data. The efficiencies for identifying an electron with $E_\mathrm{T} = 40$ GeV are 93%, 88%, and 80% for the *Loose*, *Medium*, and *Tight* operating points, respectively. As shown in the Data/MC ratio, the measured identification efficiency in data, ϵ^Data, differs from that of simulation, ϵ^MC. For this reason, data-to-simulation scale factors are calculated in the same way as Equation 4.8. The systematic uncertainty associated with these scale factors will be discussed in Section 7.3.
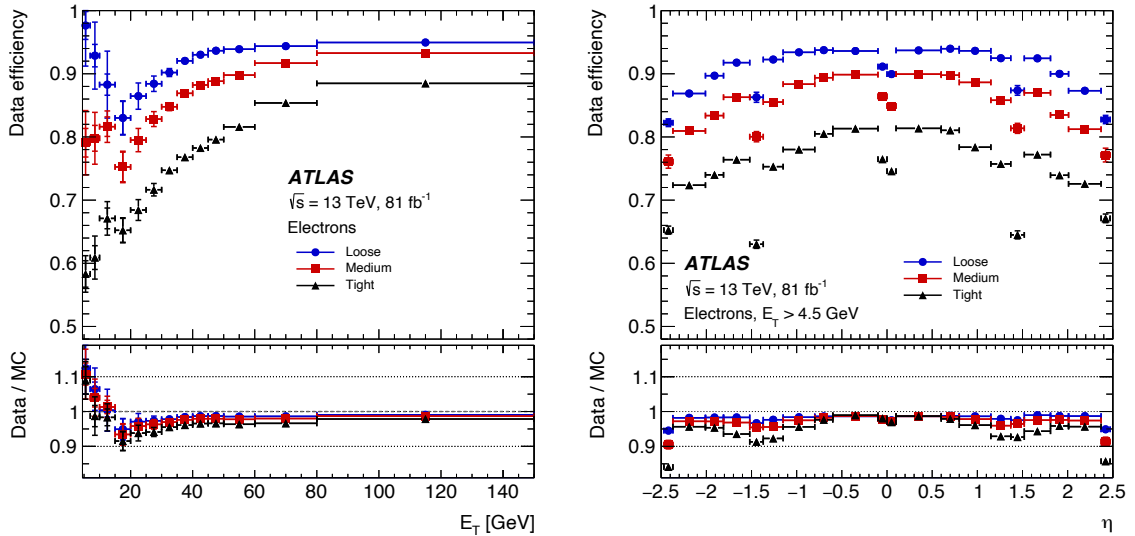
Figure 4.15: The electron identification efficiency in $Z \rightarrow ee$ events in data as a function of E_T (left) and η (right) for the Loose, Medium and Tight operating points. Image taken from Ref [145].

Electron calibration

After reconstruction, electron candidates in data and MC are calibrated to correct for energy losses upstream of the LAr calorimeter and differences between data and simulation. Similar to the jet calibration described in Section 4.2.1, corrections are applied to both data and MC to restore the reconstructed electron four-momenta to the particle-level energy scale [147], [148]. To estimate the energy of the electron from the energy deposits in the calorimeter, a multivariate regression algorithm is used which is trained on samples of

simulated events. The same algorithm is applied to data and simulation. Next, *in situ* corrections are applied to the data to account for residual differences between data and simulation. These include the intercalibration of the different calorimeter layers, pile-up corrections, and corrections to improve the uniformity of the energy response. The overall electron response in data is calibrated so that it agrees with the expectation from simulation, and corrections are derived and applied to simulation such that electron energy resolution matches the data. The invariant mass distributions of dielectron pairs in $Z \to ee$ events are shown in Figure 4.16 for data and simulation after the calibration and resolution corrections are applied. Good agreement is observed indicating the efficacy of the electron calibration procedure.
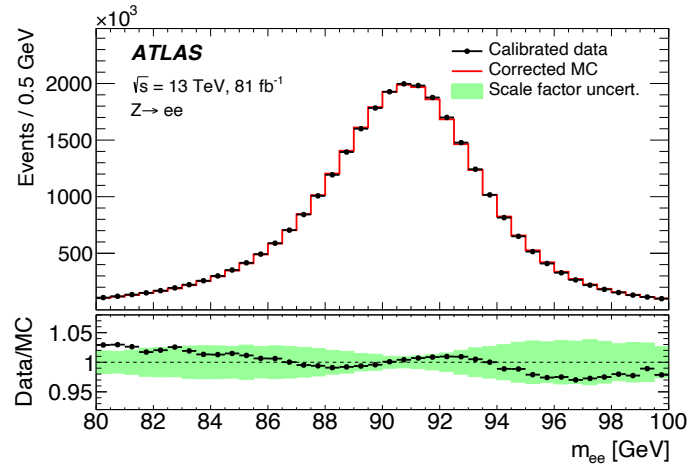
Figure 4.16: Dielectron invariant mass distribution in $Z \to ee$ events after the calibration and resolution corrections are applied. The uncertainty band in the ratio represents the impact of the uncertainties in the calibration and resolution correction factors. Image taken from Ref [145].

4.2.4 Photons

Finally, the search presented in this thesis also makes use of photons in order to define a signal-free region to use to validate the background estimation method (Section 7.2.2). Photon reconstruction follows nearly the same procedure used to reconstruct electrons (Section 4.2.3) but with a few additional complications, due to the fact that as photons travel through the ATLAS detector they will interact nontrivially with the material in the

ID before depositing their energy in the ECal [145]. These interactions can transform photons into e^+e^- pairs in a process known as **photon conversion**. To properly identify photons in the ATLAS detector, it is thus essential to identify these e^+e^- conversion vertices.

First, tracks which are loosely matched to a fixed-size topo-cluster are used to seed the reconstruction of photon conversion vertices. Two-track conversion vertices are reconstructed from pairs of opposite-charge tracks which form a vertex consistent with that of a massless particle. So-called "single-track" vertices are also reconstructed which are individual tracks without hits in the innermost tracking layers. Clusters which are matched to a conversion vertex are then considered as converted photons, while clusters which are matched to neither a track nor a vertex are considered unconverted photons.
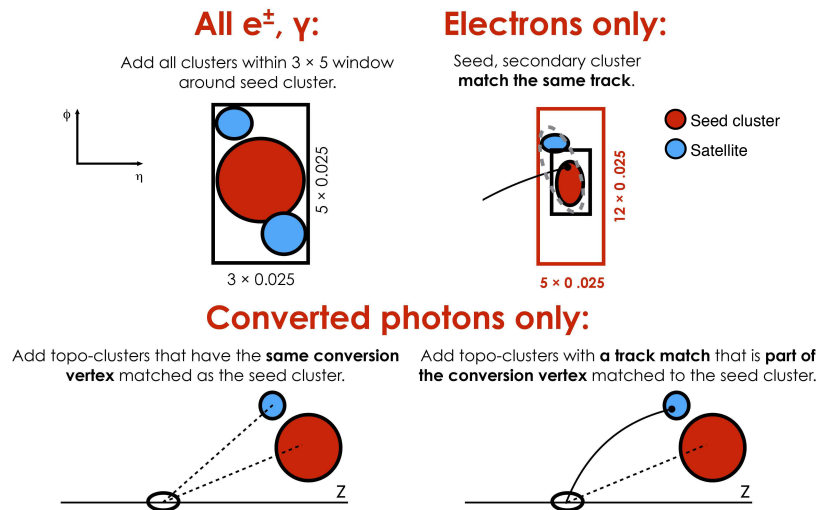
Figure 4.17: Diagram of the superclustering algorithm for electrons and photons. Seed clusters are shown in red, satellite clusters in blue. Image taken from Ref [145].

Superclusters formation then proceeds similarly to the procedure described in Section 4.2.3. As with electrons, the algorithm attempts to find satellite clusters based on a 3×5 window in $\Delta\eta \times \Delta\phi$ space around a seed cluster to capture energy deposits from secondary EM showers. For converted photons, clusters are added to the supercluster if they have the same conversion vertex as the seed cluster, or if their best-matched track belongs to the conversion vertex which is matched to the seed cluster. Figure 4.17 shows a diagram of the superclustering algorithm for electrons and photons to illustrate the differences between the two clustering algorithms.

The photon energy scale is calibrated following a procedure similar to that described in Section 4.2.3 [145]. A rectangular cut-based selection is then used to construct photon identification working points. The search presented in this thesis considers photons which pass the *Loose* identification working point, which does not differentiate between converted and unconverted photons.

Chapter 5

Reconstruction of Long-Lived Particle Decays

You cannot swim for new horizons until you have courage to lose sight of the shore.

-William Faulkner

The ATLAS detector was designed to reconstruct particles originating from close to the primary interaction point. This is sufficient for probing the SM electroweak sector as well as most BSM scenarios because lifetimes of heavy states like the Higgs and W/Z bosons are generally on the order of 10^{-14} m or smaller. The track reconstruction algorithm described in Section 4.1 was developed with these types of signatures in mind and therefore places strict requirements on the transverse and the longitudinal impact parameters. These selections are necessary to maintain high purity of primary charged particle reconstruction and efficient computation times, but at the detriment of sensitivity to long-lived particle signatures. To search for particles with lifetimes greater than a few millimeters, the ATLAS detector must be repurposed and the standard reconstruction chain described in Chapter 4 reimagined.

To reconstruct the decays of long-lived particles in the inner detector, the search described in this thesis uses two dedicated reconstruction algorithms. First, a tertiary tracking pass is run with loosened impact parameter and hit requirements to recover the loss in efficiency of the standard tracking procedure for displaced decays. This algorithm, known

as Large Radius Tracking, was optimized to maximize efficiency for reconstructing the decay products of long-lived particles and is the subject of Section 5.1. Next, a dedicated secondary vertex reconstruction algorithm is performed taking as input the combined collection of standard and large radius tracks. This allows the decay position of the long-lived particles to be identified and for its kinematics to be studied. The vertex reconstruction algorithm and its performance is described in Section 5.2.

5.1 Large Radius Tracking

The **Large Radius Tracking (LRT)** algorithm [132] is used to supplement the standard tracking algorithm described in Section 4.1. The LRT algorithm follows the same reconstruction algorithm as the inside-out tracking procedure, but has loosened quality selections in both the track seeding and ambiguity solving steps. Most importantly, the transverse and longitudinal impact parameter requirements are relaxed to $|d_0| < 300$ mm and $|z_0| < 1500$ mm, and the range of allowed pseudorapidities is increased to $|\eta| < 5$. This allows the LRT algorithm to reconstruct tracks originating in the inner detector far from the IP. Several hit requirements are also loosened slightly to increase efficiency without significantly degrading the track purity. The main differences between LRT and the standard inside-out tracking are summarized in Table 5.1.

	Standard	Large radius
Maximum d_0 (mm)	10	300
Maximum z_0 (mm)	250	1500
Maximum $|\eta|$	2.7	5
Maximum shared silicon modules	1	2
Minimum unshared silicon hits	6	5
Minimum silicon hits	7	7
Seed extension	Combinatorial	Sequential

Table 5.1: Main selections that differ between the standard inside-out tracking and LRT [132].

The algorithm begins by forming space-points from hits that were not used in either the inside-out or outside-in standard tracking passes. The seeds are then extended using the same approach as the standard tracking, but with a sequential instead of a combinatorial Kalman filter to accommodate the increase in the number of possible track candidates for a

given seed as a result of the loosened requirements. Track candidates are then fed into the ambiguity solver with the same loosened selection criteria used in the track seed selection. The candidates that are accepted by the ambiguity solver are then extended to the TRT, and the resulting tracks are merged with the standard track collection to form the final track collection.

5.1.1 LRT performance

The performance of the LRT algorithm is studied in Ref [132]. The main metric used to evaluate the algorithmic performance is the track reconstruction efficiency, defined as the ratio of the number of tracks matched to a signal truth particle and the number of signal truth particles. The track-truth matching is computed from the weighted fraction of hits left by the generated particle that are included in the reconstructed track. For a track to be considered matched to a truth particle, this fraction must be ≥ 0.5. A benchmark SUSY sample is used in which long-lived gluinos decay to a quark and a virtual squark, which subsequently decays to a neutralino and quark. This leads to the final state of displaced hadronic jets. Despite being a different physics process the final state is not dissimilar to the final state being probed in this search, and the studies are therefore representative of the algorithmic performance for the case of Higgs decays to LLPs.

Figure 5.1 shows the track reconstruction efficiency as a function of charge particle production radius r_{prod}[1] for standard tracks, large radius tracks, and the combined collection of standard and large radius tracks. At low r_{prod}, the standard tracking algorithm is very efficient and leaves relatively few hits to be used as input to the LRT algorithm. However, the efficiency quickly drops after $r_{\mathrm{prod}} > 10$ mm, with fewer than 20% of tracks being reconstructed by the standard tracking algorithm after $r_{\mathrm{prod}} > 50$ mm. The addition of large radius tracks significantly increases the reconstruction efficiency for LLP production radii above 50 mm.

The track reconstruction efficiency decreases roughly linearly as a function of r_{prod}.

---

[1]This variable corresponds exactly to the decay radius of the LLP.
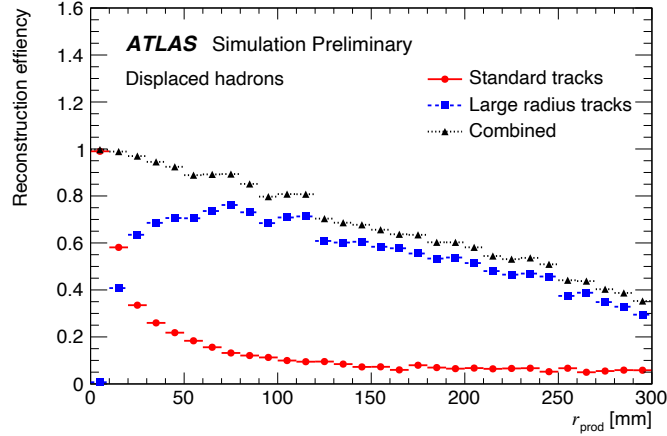
Figure 5.1: Inclusive track reconstruction efficiency for displaced charged particles produced by the decay of long-lived particles as a function of the production radius r_{prod}. The efficiency for standard and large radius tracking is shown, as well as the total efficiency, defined as their sum. Image taken from [132].

This can be a result of both algorithmic inefficiencies as well as the fact that as r_{prod} increases, truth particles are less likely to traverse the necessary number of detector layers to leave at least seven silicon hits. To disentangle these two effects, a **technical efficiency** is defined which places additional requirements on the truth particles entering the efficiency calculation to ensure that the particles are theoretically reconstructible. Figure 5.2 shows the technical efficiency as a function of r_{prod} for the LRT and combined track containers. The total combined track collection has a technical efficiency of $\geq 90\%$ for $r_{\mathrm{prod}} < 300$ mm, with the large radius tracks providing the dominant contribution to the efficiency for $r_{\mathrm{prod}} \gtrsim 20$ mm.

Fiducial selections for technical efficiency
$r_{\mathrm{prod}} < 300$ mm
$|\eta| < 5$
$p_{\mathrm{T}} > 1$ GeV
Number of silicon hits ≥ 7

Table 5.2: Selections on truth particles used to define the technical efficiency [132].

This high reconstruction efficiency is not without its downsides. As a consequence of the loose track selections applied, the LRT algorithm reconstructs many fake tracks that
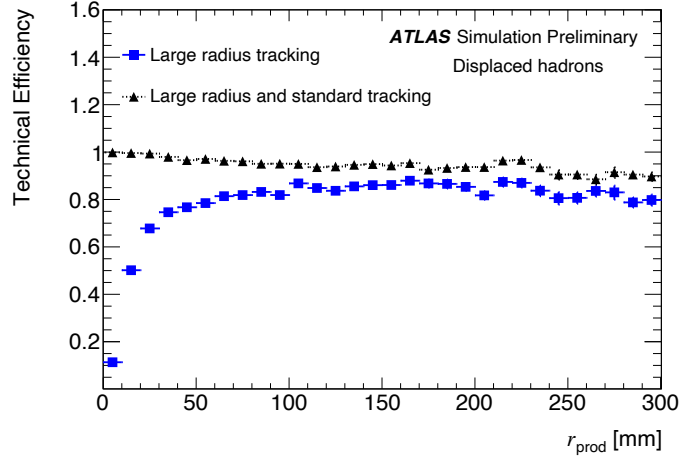
Figure 5.2: Technical reconstruction efficiency for large radius tracking and combined standard plus large radius tracking as a function of production radius r_{prod}. Image taken from [132].

do not correspond to any true charged particle trajectories[2]. The rate of fake tracks reconstructed in the LLP benchmark samples studied in Ref [132] is approximately 80%. This has a significant impact on both the amount of background observed at the analysis level, as well as the computational performance of the algorithm. When large radius tracking is included in the reconstruction chain, the time needed to fully reconstruct each event is increased by a factor of approximately 2.5 with respect to the standard configuration. Not only is the tracking step itself time consuming, but the large number of fake tracks produced as a result of the loose tracking selections complicates downstream reconstruction of physics objects. This precludes LRT from being run by default alongside the standard reconstruction. Instead, approximately a few percent of the data is selected using event-level quantities computed after the standard reconstruction to have the additional reconstruction performed. This process will be described in more detail in Section 6.2.2.

5.2 Displaced Vertex Reconstruction

As we have seen, the LRT algorithm is capable of efficiently reconstructing the charged daughters produced in the decay of a long-lived particle. After reconstructing these displaced tracks, the decay position of the LLP can be identified by reconstructing a **secondary**

---

[2]A track is considered fake if the match score between the reconstructed track and the track created by the hits from a truth particle is less than 50%

vertex from this collection of tracks that may be significantly displaced from the primary *pp* interaction vertex. Reconstructing the decay of the LLP as a secondary vertex is an essential ingredient for studying its kinematics and provides an experimental signature with strong discrimination power between signal and SM backgrounds (see Section 7.1.2).

There are several different algorithms designed to reconstruct secondary vertices used in ATLAS. Use cases for these algorithms range from the reconstruction of *b*-hadron decay vertices inside jets to the mapping of the material inside the inner detector. The search presented in this thesis uses an algorithm known as **VrtSecInclusive (VSI)** [149] which was designed specifically to reconstruct the secondary vertices associated with the LLP decays. A description of the algorithm and an overview of its performance on several LLP signatures is given below.

5.2.1 Description of the algorithm

The VSI algorithm proceeds in several steps. First, vertex reconstruction is seeded by pairs of tracks that are compatible with originating from a long-lived particle decay. The compatibility of each possible pair of preselected tracks is then computed, and those deemed loosely compatible are retained. These two-track seed vertices are then combined to form multi-track vertices using a pairwise compatibility graph. Nearby vertices are then merged, and lower-quality tracks not initially preselected for vertex seeding are attached to compatible vertices. Each step of the algorithm is described in more detail below.

Track selection

Tracks are preselected for vertex reconstruction from the combined collection of standard and large radius tracks using the following selection criteria:

- $p_T > 1\,\text{GeV}$

- the track must not be associated to any primary vertex (hard-scatter or pileup)

- if the track has zero pixel hits, it must have at least six hits in the SCT

- if the track has fewer than two pixel hits, it must have at least one hit in the TRT

- if the track p_{T} is less than 20 GeV, it must have at least seven hits in the SCT

- if the track p_{T} is less than 20 GeV *and* $|\eta|$ is less than 1.7, it must have at least 20 hits in the TRT

The track selections were designed to be as inclusive as possible to allow for sensitivity to a wide range of models while still reducing the number of vertices reconstructed from the random crossing of fake tracks.

Two-track seed finding

Vertex reconstruction begins with the formation of two-track seed vertices. In addition to the track selection criteria listed above, tracks used for vertex seeding must have transverse impact parameter $|d_0| > 2$ mm to reduce the number of vertices formed from SM processes. The algorithm then forms vertices from all possible pairs of preselected tracks. The vertex position is estimated from the track parameters measured with respect to the beam spot, and two-track pairs that have small impact parameters with respect to the estimated secondary vertex position are then fit using a χ^2 minimization [150]. After the fit, vertices are rejected if their radial position r_{vtx} is greater than 563 mm (corresponding to the SCT/TRT boundary) or if the reduced vertex-fitting quality χ^2/n_{DoF} is greater than 5, where n_{DoF} is the number of degrees of freedom in the fit. For vertices this is given by $n_{\mathrm{DoF}} = 2n - 3$ where n is the number of constituent tracks in the vertex.

The tracks in each remaining seed vertex are then required to pass a hit-pattern requirement which checks that the hits associated to each track are compatible with a particle originating from the position of the seed vertex. For example, the tracks in the vertex must not have hits on the layers within the vertex radius and must have hits on the closest layer outside the vertex. The forbidden and allowed hits are shown for two different example seed vertices in Figure 5.3. Silicon layers with disabled modules are treated as if they had produced a hit to ensure that vertices near inactive modules are not spuriously rejected. Seed vertices in which both tracks fulfill the hit-pattern requirement are retained. Otherwise the vertex is rejected.
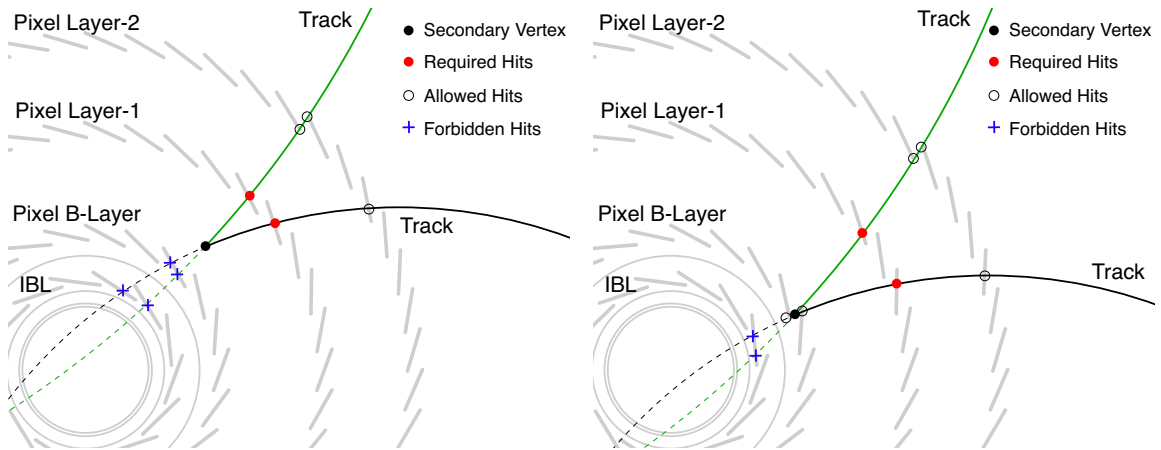
Figure 5.3: Examples of allowed and forbidden hits for tracks associated to seed vertices in the hit-pattern requirement. The tracks must not have hits on the layers within the vertex radius, and must have hits on the closest layer outside the vertex. Image taken from [149].

Multi-track vertex forming

When forming all possible combinations of two-track vertices from the input tracks, it is likely that multiple seed vertices will be formed from the tracks originating from a single LLP decay, as well as individual tracks being associated to multiple vertex seeds. To combine the seeds into multi-track vertices and resolve the sharing of tracks between vertices, a pairwise compatibility graph is constructed by mapping tracks as nodes and two-track vertices as edges between them. The same state can be represented as an **incompatibility graph** where the edges are instead formed between tracks which do not form vertices. The two types of graphs are shown in Figure 5.4. A group of tracks which are fully compati-
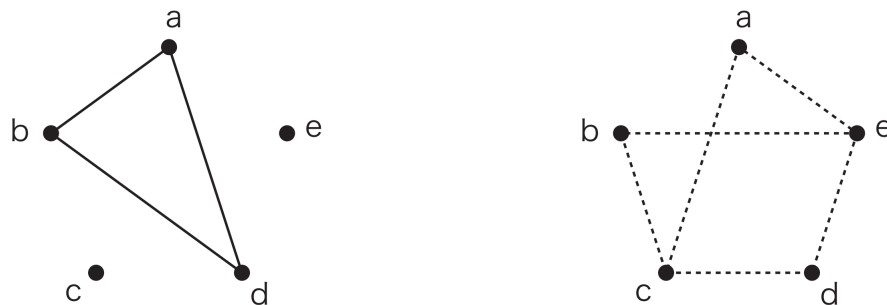
Figure 5.4: Illustration of the (in)compatibility graph for a five-track collection in which three tracks (a, b, d) form a common vertex. Image taken from [149].

ble with each other can then be combined into a single multi-track vertex by removing all irrelevant nodes from the incompatibility graph and performing a new vertex fit.

After the formation of multi-track vertices from the two-track seeds, it is possible for a single track to be associated to multiple vertices. To remedy this, the goodness of fit is evaluated for the track in question between all of its associated vertices, and the track is assigned to the vertex with the best fit. All vertices are then refit with their updated associated track constituents.

Vertex merging

At this point, it is still possible for a single LLP decay to be reconstructed as several distinct multi-track vertices. This leads to a degradation of the vertex track multiplicity which is one of the primary discriminating variables used in searches for displaced vertex signatures (see Section 7.1.2). In order to reconstruct each LLP decay as a single vertex, the algorithm attempts to merge nearby vertices by performing a series of tests as described in Ref [149]. Each pair of vertices are considered for merging if their positions are compatible within 10σ, where σ is the uncertainty on the distance between the two vertex positions calculated from the quadrature sum of the covariance matrices of the vertex fits. Any vertices with a separation of less than 1 mm are forced to merge, and all merged vertices are refit using the combined collection of associated tracks from the two input vertices.

Track attachment

Finally, it is possible that there are tracks that are compatible with the vertices formed in the above algorithm that did not pass the original track selections required for seeding. In order to recover these tracks, a **track attachment** procedure is performed which aims to augment existing vertices with additional tracks to improve the vertex track multiplicity.

Tracks considered for attachment are required to satisfy a loosened set of selection criteria, summarized in Table 5.3. Unlike in the vertex seeding, tracks are considered even

Attached track requirements
$p_{\mathrm{T}} > 1\,\mathrm{GeV}$
$\chi^2/n_{\mathrm{DoF}} < 5$
$|d_{0,\mathrm{SV}}|/\sigma(d_{0,\mathrm{SV}}) < 5$
$|z_{0,\mathrm{SV}}|/\sigma(z_{0,\mathrm{SV}}) < 5$

Table 5.3: The selections applied to tracks during the track attachment procedure.

if they are already associated to a primary pp vertex. In descending order of vertex track multiplicity, an attempt is made to associate a track to each secondary vertex. The impact parameters of the tracks with respect to the target secondary vertex are computed, and tracks with transverse and longitudinal impact parameter significances of less than 5 are attached to the vertex. The vertex position is re-fit for each attempted track association, and the track is accepted if the updated vertex fit has $\chi^2_{\text{vtx}}/n_{\text{DoF}} < 20$. Tracks are limited to be associated to a single secondary vertex, so once a successful vertex fit is performed the track is not considered for further association to other vertices. The philosophy used in the track attachment procedure is to accept as many tracks as possible during reconstruction and for analysis-specific track pruning to be determined downstream[3].

5.2.2 Performance

The performance of the VSI algorithm was studied in Ref [149]. Three different benchmark models containing long-lived particles were used to test the performance on a range of different signatures. The first is an R-parity violating SUSY model that assumes the neutralino is the lightest supersymmetric particle. The neutralino is produced during the cascade decay of a heavier gluino particle in the process $pp \to \tilde{g}\tilde{g}, \tilde{g} \to qq\tilde{\chi}^0_1$ and subsequently decays to light SM quarks via off-shell squarks, $\tilde{\chi}^0_1 \to qqq$. The mass of the squarks and gluino are 3 and 2.4 TeV respectively, and neutralino mass is 2050 GeV with lifetime $c\tau_{\tilde{\chi}^0_1} = 300$ mm. This model probes the performance for heavy LLP decays which produce high-multiplicity hadronic secondary vertices. The second model considers the existence of long-lived heavy neutral leptons (HNL), N. Via a mixing with SM neutrinos the HNL may be produced in decays of the W boson and subsequently decay to $\nu_\ell \ell^+ \ell^-$. HNL masses of 15 GeV are considered with a lifetime of $c\tau_N = 100$ mm. This model probes the secondary vertex reconstruction performance for low-track-multiplicity secondary vertices with leptonic constituents. Finally, the study considered the model probed in this thesis, in which the Higgs boson decays to pairs of pseudoscalar bosons a which subsequently decay to pairs of b quarks. The mass of the a boson was taken to be 55 GeV, with a lifetime $c\tau_a = 100$ mm.

---

[3]It is significantly easier to remove extraneous tracks at the analysis level then to add them in.

To evaluate the vertex reconstruction efficiency on the signal MC samples, a truth matching procedure is used to determine if LLP decays are reconstructed as displaced vertices. LLP decays are considered reconstructed if the tracks associated to a displaced vertex are primarily matched to truth particles originating from the LLP, where the matching of tracks to truth particles uses the same criteria as described in Section 5.1.1. For each pair of a reconstructed vertex v and a truth decay vertex l, a truth-matching score s is computed which uses the magnitude of the track p_T as a weight. The score is given as:

$$s(v, l) \equiv \frac{\sum_{i \in \text{ tracks } \in v} \left(p_T^{(i)} | \text{ descendent of LLP decay } l \right)}{\sum_{i \in \text{ tracks } \in v} p_T^{(i)}}.$$

A vertex is considered matched to a true LLP decay if $s(v, l) > 0.5$.

To decouple the algorithmic performance of the vertex reconstruction algorithm from other effects, the performance of the algorithm is analyzed using several metrics. The **acceptance** ($\mathcal{A}$) of truth LLP vertices is defined as the ratio of reconstructible LLP vertices to all LLP vertices in the MC truth record. A reconstructible LLP decay is defined as one satisfying the following set of requirements:

- the transverse distance from the origin must be $L_{xy} < 563$ mm.

- the z-position must be $|z| < 2720$ mm.

- at least two charged particles with $p_T > 1$ GeV must be produced in the decay chain.

The first two requirements ensure that the LLP decay occurred within the tracking volume of the ID, while the latter ensures that the tracks originating from the decay have large enough momentum to be reconstructed by the tracking algorithms.

In order to reconstruct an LLP decay as a secondary vertex, at least two constituent tracks from the decay must be reconstructed. Furthermore, in order for the LLP decay to be seeded, the tracks must pass the selection criteria detailed in Section 5.2. The **seed efficiency** (ϵ_{seed}) is defined as the ratio of the number of LLP decays with at least two *selected* tracks passing these requirements to the number of LLP decays passing the acceptance criteria.

Finally, the **core efficiency** (ϵ_{core}) is defined as the ratio of the number of LLP decays that are *matched* to a reconstructed vertex (with a match score of at least 0.5) to the number of LLP decays that pass the seeding criteria. The total reconstruction efficiency is then defined as the product of these three terms:

$$\epsilon_{\mathrm{total}} = \mathcal{A} \cdot \epsilon_{\mathrm{seed}} \cdot \epsilon_{\mathrm{core}}. \qquad (5.1)$$

Decomposing the efficiency in this way allows the algorithmic performance to be separated from inefficiencies induced from truth acceptance, track reconstruction, and track selection.

The acceptance, seed, core, and total efficiencies are shown in Figure 5.5 for the three benchmark signal processes. Total reconstruction efficiencies of nearly 60% are observed
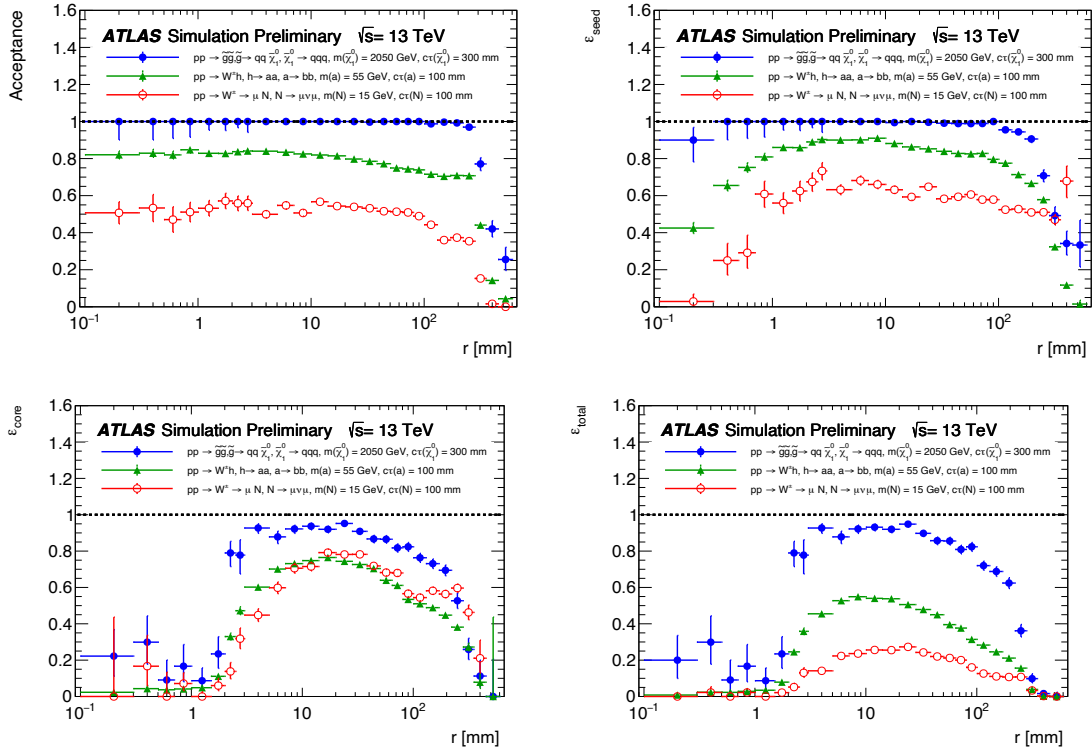
Figure 5.5: Clockwise from upper left: The acceptance, seed, total, and core vertex reconstruction efficiencies as a function of LLP decay radius for all three benchmark models. Image taken from [149].

for the $H \to aa \to b\bar{b}b\bar{b}$ process. The performance of the vertex reconstruction algorithm

was also studied as a function of pileup. As shown in Figure 5.6, the total vertex reconstruction efficiency is observed to decrease as a function of the number of pp interactions, primarily due to a degradation in track quality in high multiplicity environments. However, the algorithm is still found to be robust up to 80 pp interactions per bunch crossing.
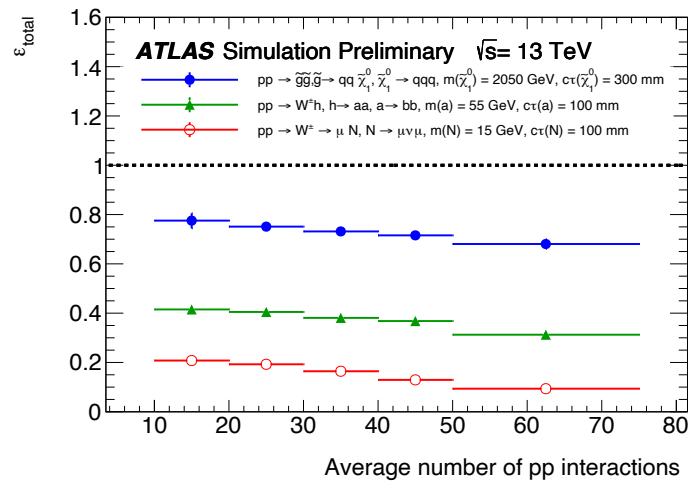
Figure 5.6: The total vertex reconstruction efficiency as a function of the number of pp interactions. Image taken from [149].

Part III

Search for Exotic Higgs Decays

Chapter 6

Data and Simulated Samples

Three quarks for Muster Mark!

-James Joyce

To perform the search for exotic Higgs decays to long-lived particles, simulated and real proton-proton collision data is used. This chapter is dedicated to describing these samples and how they were generated/collected. Section 6.1 describes the simulated signal and background samples that are used to develop the analysis, optimize the event selection criteria, measure the signal selection efficiency, and assess sources of systematic uncertainty. An overview of Monte-Carlo event generation is given with a focus on the simulation of QCD phenomena such as showering and hadronization, and then the procedure for simulating the signal and background processes is detailed. Section 6.2 then describes the dataset used by this search, which was collected by the ATLAS detector between 2015 and 2018 and represents the entirety of the Run-2 dataset.

6.1   Simulation

Accurate simulation of both signal and background processes is a central component of searches for BSM physics. Simulation of the signal process is essential for optimizing the analysis selections to maximize the discovery potential, as well as understanding the efficiency of these selections to determine the total expected number of signal events in the measurement which is needed to perform hypothesis tests on the observed data. Being a rather complicated endeavor, we dedicate a brief discussion to dissecting what goes in to

simulating the physics of high-energy hadron-hadron collisions before detailing the simulation of Higgs boson decays to long-lived particles

6.1.1 Monte-Carlo event generation

The event structure of a hadron-hadron collision is extremely complex, with a description of the full final state involving many multi-particle interactions. To perform the calculations needed to describe these final states, **Monte-Carlo (MC)** methods are the only viable option. Figure 6.1 shows a sketch of a hadron-hadron collision as simulated by a Monte-Carlo event generator. The event consists of many different interactions, from the hard pp collision and subsequent Bremsstrahlung radiation, all the way to the parton-to-hadron transitions and eventual hadron decays. Not to mention the simulation of the dynamics of the remnants of the incoming hadrons that do not participate in the hard scatter! Needless to say, the pp collisions that occur at the LHC are an extremely complicated process to simulate. Due to the complexity of the situation, the simulation of a scattering event such as the one shown in Figure 6.1 is factorized into several stages, which are described below.

The hard scatter

The hard scattering process is the first phase of the event that is simulated. This essentially consists of the evaluation of the cross section for the production of an N-particle final state in a proton-proton interaction. Because the interacting particles are actually constituents of composite hadrons, this cross section relies on the **parton distribution function (PDF)** which describes how the momentum of the incoming proton is distributed among its constituent partons. The cross section is given by

$$\sigma_{pp \to N} = \sum_{a,b} \int dx_1 dx_2 f_a(x_1, \mu_F^2) f_b(x_2, \mu_F^2) \hat{\sigma}_N^{ab} \tag{6.1}$$

where $\hat{\sigma}_N^{ab}$ is the cross-section for a specific partonic initial state (ab), and $f_a(x_1, \mu_F^2)$ is the probability distribution to find a parton a with a fraction x_1 of the energy of the incoming proton evaluated at scale $Q^2 = \mu_F^2$. The scale μ_F is called the **factorization scale** which sets the energy threshold below which radiative effects are absorbed into the PDF and above
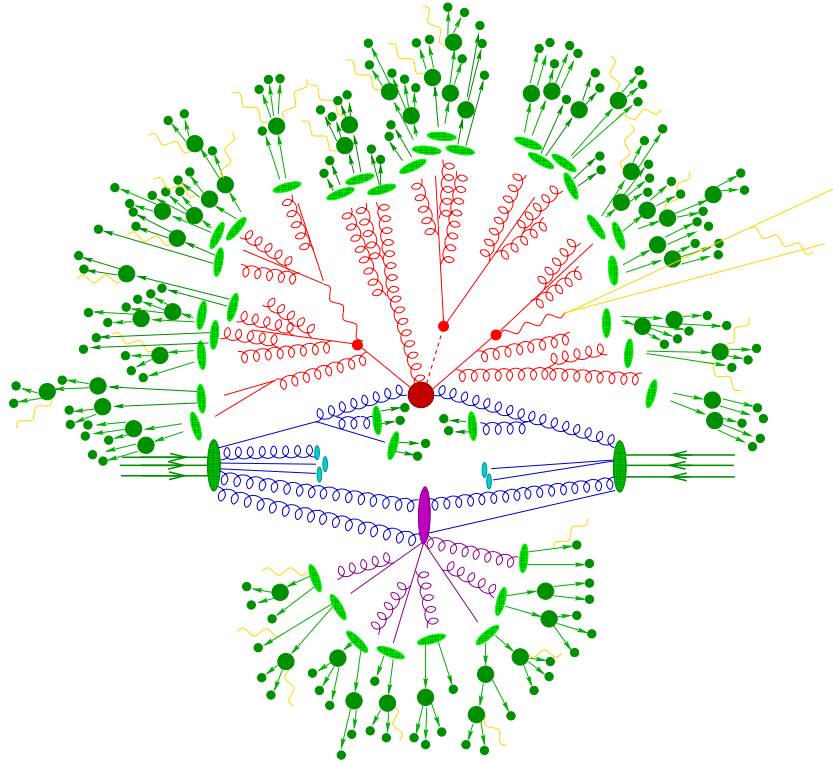
Figure 6.1: Sketch of a hadron-hadron collision as simulated by a Monte-Carlo event generator. The red blob in the center represents the hard collision, surrounded by a tree-like structure representing Bremsstrahlung as simulated by parton showers. The purple blob indicates a secondary hard scattering event. Parton-to-hadron transitions are represented by light green blobs, dark green blobs indicate hadron decays, while yellow lines signal soft photon radiation. Figure and caption from Ref [151].
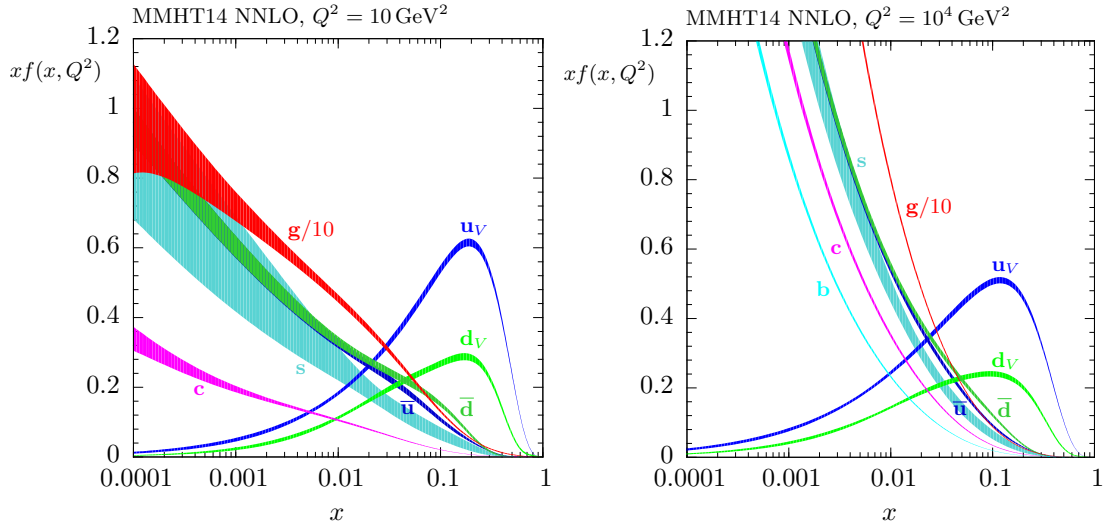
Figure 6.2: The MMHT2014 NNLO PDFs at $Q^2 = 10$ GeV (left) and $Q^2 = 10^4$ GeV (right). The valence quarks are labeled u_V and d_V. Image taken from Ref [152].

which are included directly in the calculation of the hard scatter. The cross section also depends on the **renormalization scale**, μ_R. As usual, this scale is introduced to resolve the logarithmic divergences that appear when computing the loop diagrams representing the amplitude. The QCD coupling constant is then given as a function of the scale, $\alpha_S(\mu_R)$.

Figure 6.2 shows an example PDF derived using data from the LHC at two different values of the scale Q^2. At low energies, the valence quarks u_V and d_V are dominant, whereas at higher energies contributions from virtual partons that form the "quark-sea" become more significant. The PDF shown in Figure 6.2 is the MMHT2014 NNLO PDF [152], which is one of several PDFs used by the experiments at the LHC. The other commonly used PDFs are the NNPDF3.0 [153] and CT14 [154] sets. Several different generators are used for computing the matrix elements of the hard subprocess such as MAD-GRAPH [155] and POWHEGBOX [156]. The generators used to simulate the processes considered in this thesis will be described in Sections 6.1.2 and 6.1.3.

The parton shower

Just as electrically charged particles undergoing acceleration will emit bremstrallung radiation of photons, accelerated partons will emit QCD radiation in the form of gluons.

Unlike QCD, gluons themselves carry color charge and will thus emit their own radiation leading to a so-called **parton shower (PS)**. The parton shower is simulated after the generation of the hard-scatter process and models the emission of both initial- and final-state radiation. Final-state radiation refers to emissions from an outgoing parton of the hard subprocess, and initial-state showers are those that originate from an incoming parton of the hard subprocess. These emissions are in principle higher-order corrections to the hard subprocess, with the dominant contributions originating from collinear parton splitting or soft gluon emission. Consider the almost-collinear splitting of a parton of type i into two partons of type j and k, such as $q \to q + g$. If the n-parton differential cross section before splitting is given by $d\sigma_n$, then at leading order in perturbation theory we have

$$d\sigma_{n+1} \approx d\sigma_n \frac{\alpha_S}{2\pi} \frac{d\theta^2}{\theta^2} dz d\phi P_{ji}(z, \phi) \tag{6.2}$$

where θ and ϕ are the opening angle and azimuthal angle of the splitting, and P_{ji} is the **splitting function** which describes the fraction z of the initial parton (i) energy carried by j [157]. Sequential application of Equation 6.2 using MC methods to generate values of z, θ, and ϕ allows for simulation of the shower for each initial and final state parton. The process is terminated when the energies of the showered partons have fallen to the hadronization scale $Q_0^2 \sim 1$ GeV. The most commonly used of parton-shower MC generators are PYTHIA [158] and HERWIG [159].

Hadronization

To complete the simulation of the event into the final topology as observed by the detector, the quarks and gluons produced in the parton shower must be transformed into color-neutral final states. This process is known as **hadronization**. At the hadronization scale, the coupling α_S is too large for perturbation theory and the dynamics enter a non-perturbative phase. Current analytic methods are unable to describe hadronization from first principles, and thus event generators rely on phenomenological models based on general features of QCD. There are two models currently used to simulate the parton-hadron transition: the string model and the cluster model. The Lund string model [160], depicted

in Figure 6.3a, relies on the observation from QCD lattice simulations that the potential energy between a quark-antiquark pair increases linearly with their separation. When the separation corresponds to a potential energy on the order of hadron masses, it becomes energetically favorable for the gluonic string that stretches between them to break at some point along its length through the creation of a new quark-antiquark pair. This process is then repeated for the new string segments that are formed between the two quark-antiquark pairs, and continues to do so until all of the energy has been converted into quark-antiquark pairs which can be identified with hadrons. The cluster model [161] depicted in Figure 6.3b, is instead based on the *preconfinement* property of QCD [162]. At scales much less than the scale of the hard scatter, the partons in a shower are clustered in colorless groups. It is then natural to identify these clusters at the hadronization scale as *proto-hadrons* that decay into the observed final-state hadrons. In practical implementations of the model, gluons in the shower are forced to split into quark-antiquark pairs which then form clusters with their corresponding color partners. Due to the non-perturbative nature of the hadronization process, the simulation involves many parameters that represent the uncertainty in our understanding of nature. The specific set of parameters that enter the calculation is called a **tune**. Hadronization is usually simulated by the same generators used to produce the PS evolution, with PYTHIA and HERWIG once again being the most commonly used.

The underlying event and pileup

The procedure described above gives a complete picture of how to simulate the final state particles produced from the hard parton-parton subprocess that occurs in the pp collisions at the LHC. However, this is not the full picture of what occurs when two protons collide. Accurate simulation of pp collisions must also consider the dynamics of the partons in the incoming protons that do not directly participate in the hard subprocess. The soft interactions between these "spectator partons" comprise what is known as the **underlying event**, and are highly probably in pp collisions at the LHC [163]. It is also possible to have multiple parton hard-scatterings, i.e. events in which two or more distinct parton interactions occur simultaneously in a single pp collision. Similar to the modeling of

(a)   (b)
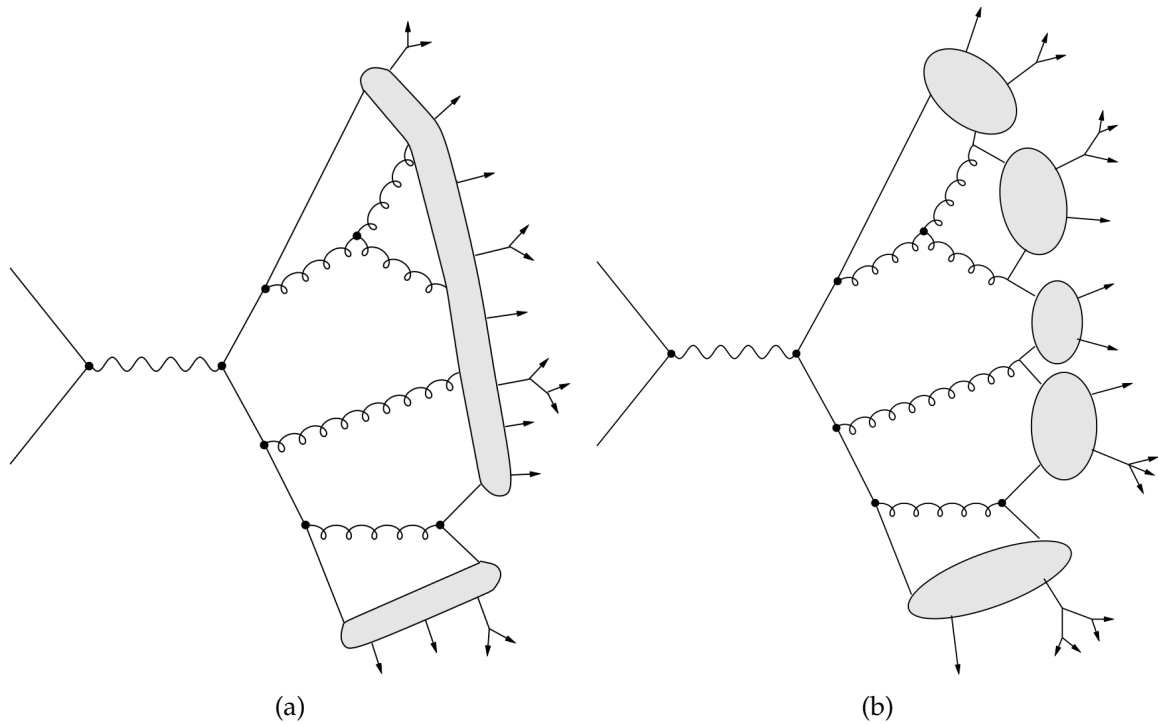
Figure 6.3: The cluster (a) and string (b) hadronization models. Images taken from Ref [157].

hadronization, these interactions are non-perturbative in nature and thus their simulation relies on a large number of free parameters that must be tuned.

The simulation must also take into account the interactions between the other proton-proton interactions in each bunch crossing. Recall from Section 3.1.2 that during Run 2, there were 33.7 interactions per bunch crossing on average. In order to replicated the pileup conditions in data, the generated hard-scatter events are overlayed with simulated **minimum-bias** events, which are soft inelastic collisions that are modeled to represent those observed in data. To account for the fact that the pileup profile used when generating the simulated events may be slightly different than the actual pileup profile observed in data, a reweighting procedure is used known as **pileup reweighting (PRW)**. This procedure (and its associated uncertainties) will be described in more detail in Section 7.3.

Finally, the entire generated event including the hard-scatter, underlying event, and pileup is run through a detailed GEANT4 [164] simulation of the ATLAS detector to simulate the detector response. The result of this simulation is a set of digitized signals which

may be treated in the same way as the data collected by the detector, giving the most accurate possible representation of how the simulated events would be observed.

6.1.2 Simulation of Higgs boson decays to long-lived particles

Simulated events with a Higgs boson produced in association with a Z boson are generated using POWHEG v2 [156], [165]–[167]. The POWHEG prediction is accurate to next-to-leading order for the ZH boson plus one jet production. Virtual amplitudes are constructed through the interface to the GOSAM package [168]. The loop-induced $gg \rightarrow ZH$ process is generated separately at leading order with POWHEG. In all cases, the PDF4LHC15nlo PDF set [169] is used. The simulated prediction is normalized to cross sections calculated at NNLO in QCD with NLO electroweak corrections for $q\bar{q} \rightarrow ZH$ and at NLO and next-to-leading-logarithm accuracy in QCD for $gg \rightarrow ZH$ [170]–[176]. The POWHEG method [166], [167] is used to match the matrix element computation to that of the subsequent parton shower.

The decay of the Higgs boson to two spin-0 a bosons and the subsequent decay of each a boson into a pair of b quarks are simulated with PYTHIA 8.212 [158]. The coupling of the a boson to b quarks is assumed to be that of a pseudoscalar, however, the information about the parity of the a boson assumed in the simulation is lost in the hadronization of the b quarks and thus the results of this search apply equally to scalars and pseudoscalars. A Feynman diagram depicting the leading order production mode for the ZH, $H \rightarrow aa \rightarrow 4b$ process is shown in Figure 6.4. PYTHIA 8.212 is also used for parton showering and hadronization, as well as underlying-event simulation using the AZNLO CTEQ6L1 tune [177]. The samples include weight variations evaluated on-the-fly for the estimation of QCD scale, PDF- and α_S-induced uncertainties. The QCD scales μ_R and μ_F are varied independently by factors of 0.5 and 2.0 to allow for the assessment of their effect on the signal process. Masses of the a boson in the range 15–55 GeV are considered, and statistically-independent samples are produced with mean proper lifetimes of 10 mm, 100 mm, and 1 m for each value of mass. These samples are ultimately reweighted to obtain samples corresponding to alternative lifetimes. This reweighting procedure will be described in Section 8.3.1.
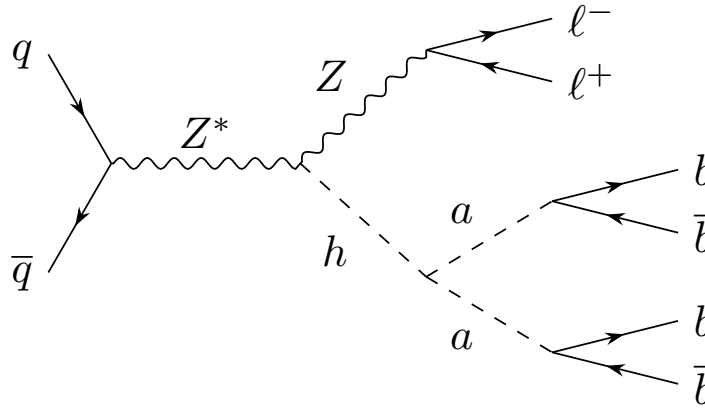
Figure 6.4: Feynman diagram depicting the leading order production mode for the ZH, $H \to aa \to 4b$ process. Diagram created using the Ti*k*Z-Feynman package [48].
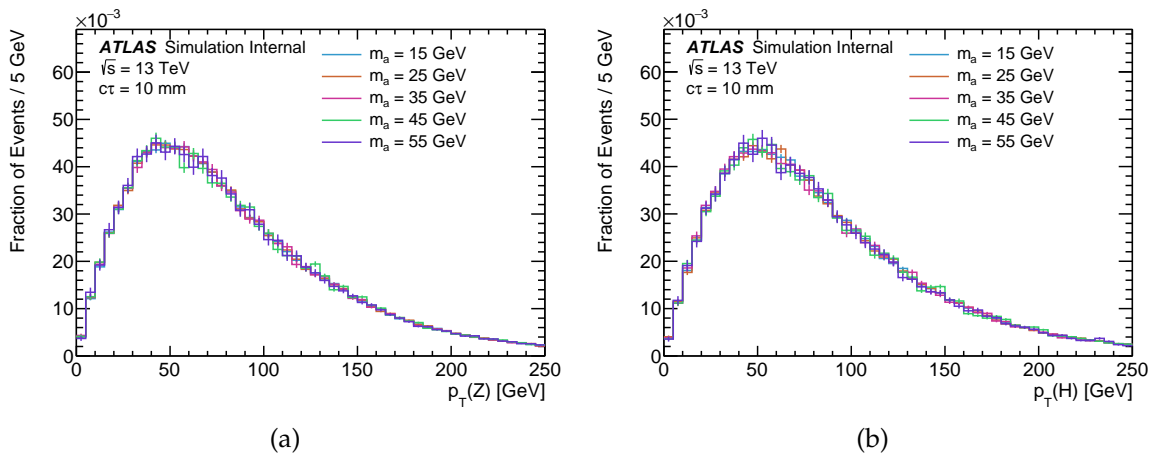
Figure 6.5: Distributions of the p_T of the (a) Z boson and (b) Higgs boson in truth signal MC samples with $c\tau = 10$ mm.
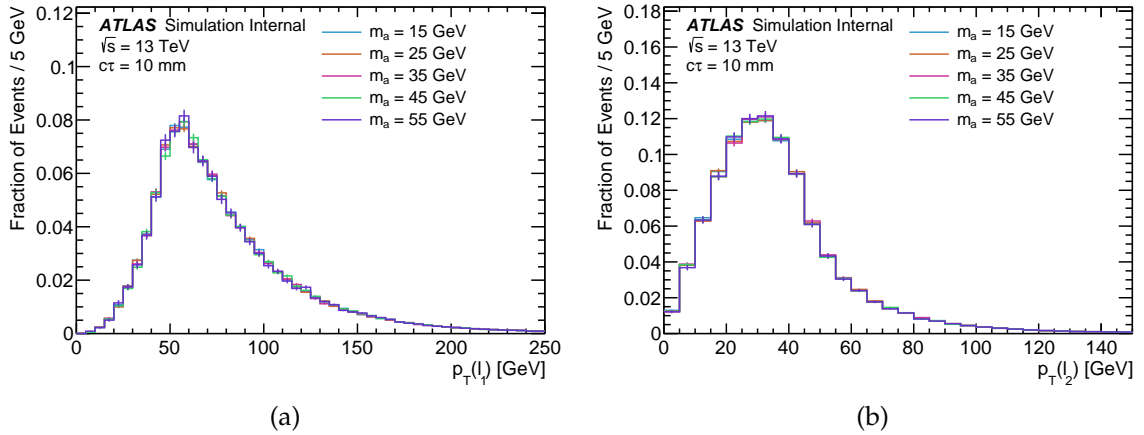
Figure 6.6: Distributions of the p_T of the (a) leading and (b) subleading leptons in truth signal MC samples with $c\tau = 10$ mm.
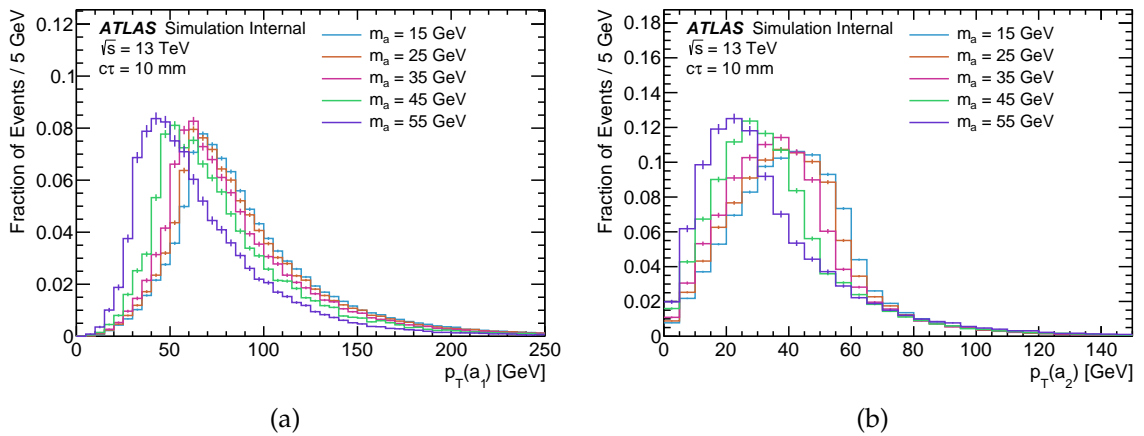
Figure 6.7: Distributions of the p_T of the (a) leading and (b) subleading long-lived a bosons in truth signal MC samples with $c\tau = 10$ mm.
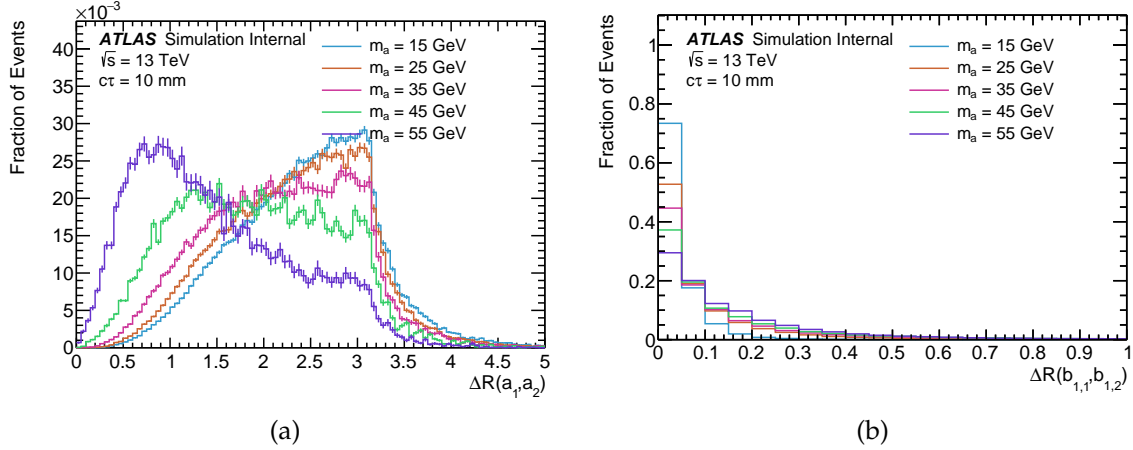
Figure 6.8: Distributions of (a) the ΔR between the two a bosons and (b) ΔR between the decay products of the leading a boson in truth signal MC samples with $c\tau_a = 10$ mm.

The p_T distributions of the Z boson, Higgs, leptons, and the long-lived a bosons are shown in Figures 6.5, 6.6, and 6.7 for signal samples with $c\tau = 10$ mm. The a boson p_T spectra is hardest for small values of m_a due to the larger difference in mass relative to the mass of the Higgs boson. The p_T distributions are independent of the lifetime of the a boson. The ΔR between the two a bosons is shown in Figure 6.8 for signal samples with $c\tau = 10$ mm. The ΔR between the b quarks produced in the leading a boson decay is also shown in Figure 6.8. For large values of m_a, the a bosons tend to have smaller angular separations, but their subsequent decay products are produced with larger separations. The proper lifetime ($c\tau$) of the a bosons are shown in Figure 6.9b for signal samples with $m_a = 15$ GeV and $c\tau = 100$ mm, and the radial decay positions (L_{xy}) of the a bosons are shown in Figure 6.9a.

6.1.3 Simulation of Z+jets events

Simulated samples of the Z+jets process are used to develop the background estimation method and analysis selections, as well as to derive systematic uncertainties (to be described in Section 7.3). These samples are generated with the SHERPA v2.2.1 [178] generator. Matrix elements are calculated for up to two additional partons at NLO and four partons at LO using the Comix [179] and OpenLoops [180] matrix element generators and merged with the Sherpa PS [181] using the ME+PS@NLO prescription [182]. The

(a)　　　　　　　　　　　　　　(b)
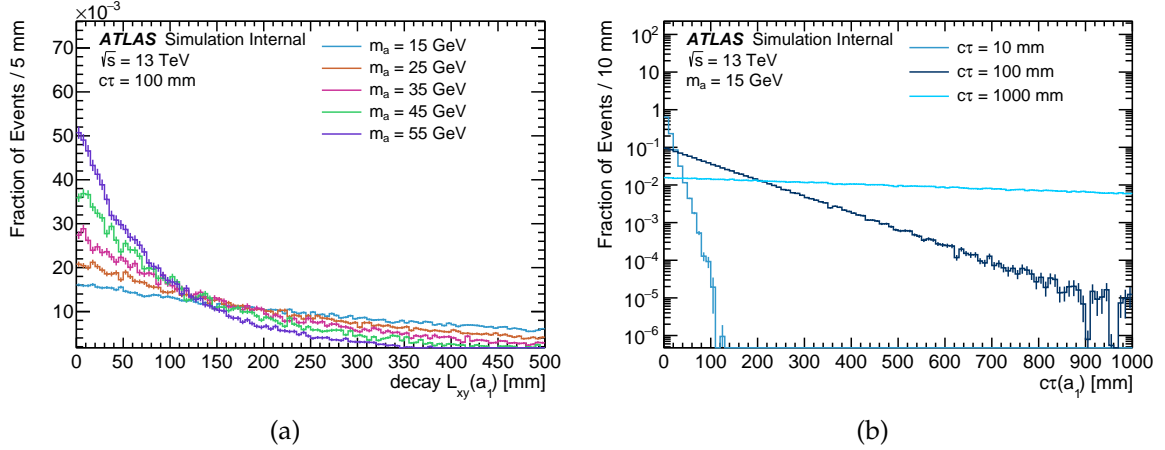
Figure 6.9: Distributions of (a) the radial decay position of the leading a boson with $c\tau = 100$ mm and (b) the proper lifetime of the leading long-lived a boson with $m_a = 15$ GeV.

NNPDF30NNLO PDF set [153] is used in conjunction with a dedicated PS tune developed by the Sherpa authors. The Z+jets events are normalized to their NNLO QCD theoretical cross-sections calculated using FEWZ [183]. Samples are produced in slices of p_T using filters for a b-jet, a c-jet and no b-jet, and with a veto on b and c-jets.

6.2 Data

This analysis uses 139.0 fb^{-1} of $\sqrt{s} = 13$ TeV pp collision data, collected by the ATLAS experiment from 2015–2018. Only data collected during stable beam conditions in which all detector subsystems were operational is considered [184]. The data used in this analysis are preselected with basic event requirements:

- GRL: Events are required to pass the **Good Run List (GRL)** for the corresponding data taking period, which specifies the luminosity blocks from within the data runs (spanning 1-2 minutes of data-taking) which are usable for physics analysis.

- Cleaning: After applying the GRL, there are still some individual events which are affected by detector problems that are not removed. This is because a single luminosity block can be thousands of events, and to remove an entire luminosity block for a single problematic event could lead to a loss of usable data for physics analysis. To remedy this, flags are used to remove problematic events due to errors in the

liquid argon system, tile calorimeter system, SCT inner detector system, or due to incomplete events. Thus, events must not have `LArError`, `TileError`, `SCTError`, or `CoreError`.

- PV: Events are required to have at least one primary vertex reconstructed with two or more associated tracks with $p_T > 500$ MeV.

- Trigger: Events must fire at least one of the triggers described in Section 6.2.1.

- Filter: Events are required to pass the filter described in Section 6.2.2.

The trigger and filter requirements will be described in more detail in the following two subsections.

6.2.1 Trigger

As described in Section 3.2.4, the ATLAS trigger system is used to select interesting events for further processing. To select events consistent with the ZH topology, this analysis uses single lepton triggers which are designed to select isolated electrons and muons with transverse momenta $p_T > 26$ GeV. The lowest threshold unprescaled trigger operating in a given year is used, in addition to higher threshold triggers which have looser restrictions on lepton identification and isolation. Events in both data and simulation are required to fire the trigger. The trigger efficiencies for the most important triggers used in this search are shown in Figure 6.10. The high efficiency of these leptonic triggers and the lack of an explicit trigger for displaced jets is the primary motivating factor for targeting the associated ZH production mode rather than ggF production. The ratios show the difference in trigger efficiencies between data and simulation. These differences are accounted for by applying scale factors to the simulation, which will be described in more detail in Section 7.3. The full list of triggers used, and the years in which they were operation is given in Table 6.1.

This analysis also makes use of a collection of photon triggers in order to define a validation region in which to test the background estimation method (Section 7.2.2). Both
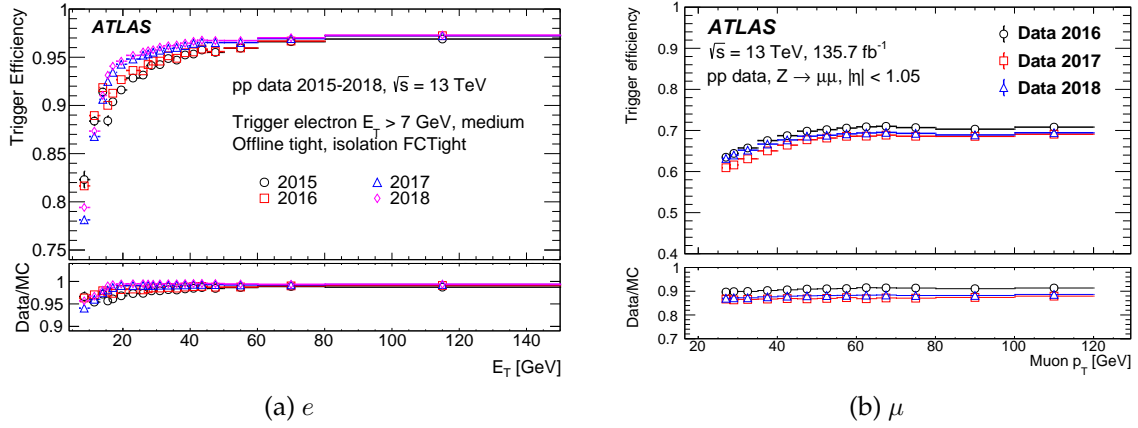
Figure 6.10: Trigger efficiencies for (a) electrons and (b) muons. Images taken from Refs [185], [186].

l	Trigger	2015	2016	2017	2018
e	HLT_e24_lhmedium_L1EM20VH	✓			
	HLT_e24_lhtight_nod0_ivarloose		✓		
	HLT_e26_lhtight_nod0_ivarloose		✓	✓	✓
	HLT_e60_lhmedium	✓	✓		
	HLT_e60_lhmedium_nod0		✓	✓	✓
	HLT_e120_lhloose	✓			
	HLT_e140_lhloose_nod0		✓	✓	✓
μ	HLT_mu20_iloose_L1MU15	✓			
	HLT_mu24_iloose		✓		
	HLT_mu24_ivarloose		✓		
	HLT_mu24_imedium	✓	✓		
	HLT_mu24_ivarmedium		✓		
	HLT_mu26_imedium		✓		
	HLT_mu26_ivarmedium		✓	✓	✓
	HLT_mu40	✓	✓		
	HLT_mu50	✓	✓	✓	✓

Table 6.1: The full list of single lepton triggers used in this search.

single photon and diphoton triggers are used in order to collect a large statistic data sample. The single photon triggers have a p_T threshold of 150 GeV, and the diphoton triggers require at least two photons with $p_T > 60$ GeV.

6.2.2 The `RPVLL` stream

As mentioned in Section 5.1, the LRT algorithm is extremely computationally expensive and can therefore not be run by default on the full dataset[1]. Instead, events are preselected based on a collection of algorithms known as **filters** prior to the LRT reprocessing. The filters can be thought of as an additional trigger-like selection that further reduces the number of events to be processed to a manageable level. Internally to ATLAS, these selections are known as the `DRAW_RPVLL` filter, because they are run in before the `RAW` data format is processed further (`RAW` to `DRAW`) and are used by several analyses targeting R-parity violating SUSY scenarios. The rate of data selected by the `DRAW_RPVLL` filters is shown in Figure 6.11. The combined rate of all filters is less than 50 Hz, which is significantly less than the HLT rate of 1 kHz. Because these events are processed separately from the main data stream, the computational resource quota is increased with respect to the standard ATLAS reconstruction. This allows for the LRT algorithm to be run without having to compromise on performance.

The filter used by this analysis is optimized to select events that match the ZH, $H \rightarrow aa$ topology by requiring the presence of at least one lepton and a jet which is consistent with originating from the decay of an LLP. Displaced jets are defined as the subset of jets that satisfy a logical OR of requirements on two track-based observables, optimized to select jets initiated by LLP decay products and reject those initiated by prompt partons. The first observable [187] exploits the fact that jets with relatively small displacements with respect to the IP will contain tracks that are incompatible with the PV. For each primary vertex PV_i, α_i is defined as

$$\alpha_i = \frac{\left(\sum_{\mathrm{tracks}\in\mathrm{PV}_i} \vec{p}\right)_T}{\left(\sum_{\mathrm{tracks}} \vec{p}\right)_T}, \qquad (6.3)$$

---

[1]In the configuration used in Run 2, that is. The improvements made to LRT to reduce the CPU budget will be discussed in Chapter 9
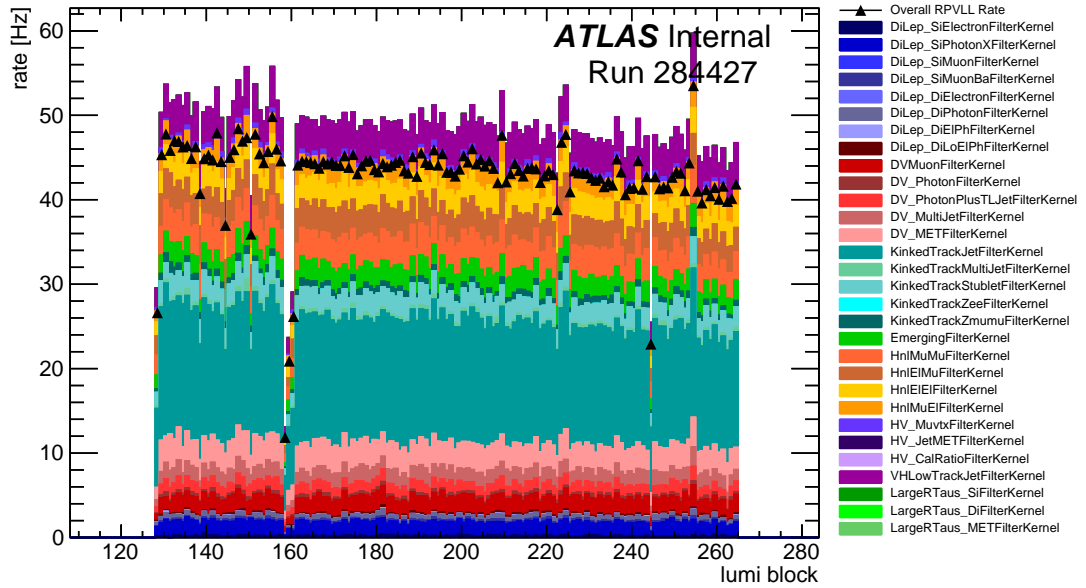
Figure 6.11: Rate of data selected by the collection of `RPVLL` filters for one run during the Run 2 data taking period as a function of luminosity block. The primary filter used by the analysis is labeled "VHLowTrackJetFilterKernel" and is shown in purple. The total rate is shown in black markers, and is less than the sum of the individual filters due to overlapping selections among multiple filter.

where a subscript "T" denotes the component of a vector transverse to the beam direction, the sum in the denominator is over all tracks geometrically-associated to the jet, and the sum in the numerator extends over the subset of tracks that are matched to PV_i. A track is considered matched to a PV if $|d_0| < 0.5$ mm and $|\Delta z_0 \sin \theta| < 0.3$ mm, where Δz_0 is the longitudinal distance between the vertex position and the point of closest approach of the track to the vertex. Standard QCD jets should have a large value of α_i for the vertex in which they were produced, while jets originating from the decay of an LLP should have small values of α_i for all PVs. Therefore, the maximum α_i value for all PVs, $\alpha_{\max} \equiv \max(\alpha_i)$, is used to discriminate between signal and QCD jets and reject jets originating from pileup interactions. The second observable, **charged hadron fraction (CHF)**, exploits the fact that more significantly-displaced jets deposit energy in the calorimeters but contain few reconstructed tracks. CHF is defined as the ratio of the transverse component of the
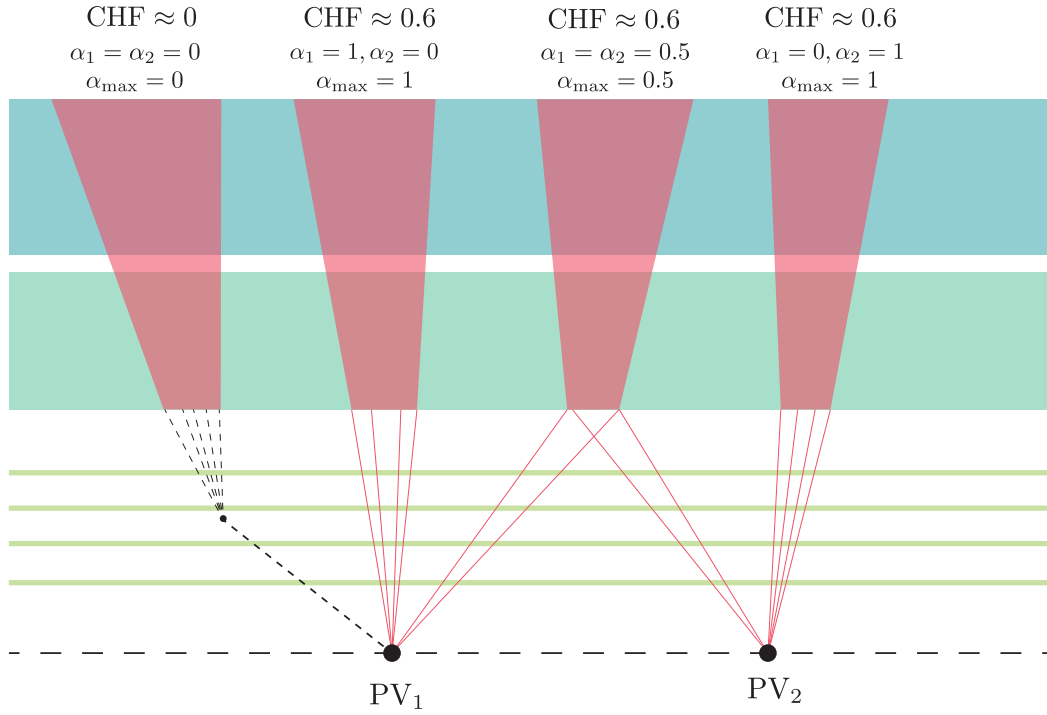
Figure 6.12: Schematic of several types of jets in the ATLAS detector before running the LRT algorithm. The leftmost jet is originating from the decay of an LLP and has few reconstructed tracks. Thus, both CHF and α_{max} take values that are approximately zero. Jets with tracks originating from one or more primary vertices will have larger values of both CHF and α_{max}.

total track momentum to the jet p_{T}, or

$$\text{CHF} = \frac{\left(\sum_{\text{tracks}} \vec{p}\right)_{\text{T}}}{p_{\text{T}}}, \tag{6.4}$$

where the sum in the numerator is over all tracks geometrically-associated to the jet with $|d_0| < 0.5$ mm. These two variables are shown schematically in Figure 6.12. A jet is considered displaced if CHF < 0.045 or $\alpha_{\text{max}} < 0.05$. This selection was optimized to provide high signal efficiency for a wide range of LLP proper lifetimes while maximizing background rejection. For an event to pass the filter, at least one of the leading two jets must satisfy the displaced jet criteria.

In addition to the jet-level observables, the filter also places loose requirements on the

Selection	e	μ
min p_{T}	27 GeV	25 GeV
η	$< 2.47, \not\subset [1.37, 1.52]$	< 2.5
$\|z_0 \sin \theta\|$	< 0.5 mm	< 0.5 mm
$\frac{d_0}{\sigma(d_0)}$	< 5	< 3
Working point	Medium	Medium

Table 6.2: Filter-level lepton selections.

leptons in the event as summarized in Table 6.2. For an event to pass the filter, it is required to have at least one electron or muon passing these selections. This combination of selections efficiently selects events consistent with the signal topology while rejecting SM backgrounds. Events passing the photon triggers described in Section 6.2.1 are also included in a separate filter. The high p_{T} threshold of these triggers gives smaller rates and therefore there is no need for the additional displaced jet requirements.

Chapter 7

Search for Higgs decays to long-lived particles

Your mind will answer most questions if you learn to relax and wait for the answer.

-William S. Burroughs

At this point, we have described all of the prerequisite information needed to develop a search for exotic Higgs decays to pairs of long-lived particles which decay in the ATLAS inner detector. In this chapter, we will describe the methods used to optimize sensitivity for this unique signature, and the procedures used to derive and validate a method to estimate the Standard Model backgrounds which can mimic it. Section 7.1 gives an overview of the event-level and object-level selections applied to identify signal-like events and reject background. These selections are highly effective at reducing the number of SM events, and the residual background is estimated using a data-driven procedure as described in Section 7.2. The validation of the background estimate is presented, and a systematic uncertainty on the prediction is derived. Finally, Section 7.3 describes the various sources of systematic uncertainty on the predicted signal yield that factor into the final results.

7.1 Event Selection

In order to define a region with maximum sensitivity for the $H \rightarrow aa \rightarrow b\bar{b}b\bar{b}$ signature, as well as signal-free regions to derive and validate an estimate for the SM backgrounds in

this region, various event-level selections are applied. These selections will be described in the following section.

7.1.1 Preselection

To define the preliminary selection used to select signal-like events, events are required to contain exactly two opposite-sign, same-flavor leptons. This serves as a baseline selection to identify events containing a Z boson. Electron candidates are required to be within the fiducial region $|\eta| < 2.47$, and not within the calorimeter transition region ($1.37 < |\eta| < 1.52$). To reduce the background from non-prompt electrons and photon conversions, electrons must pass the *Medium* likelihood identification working point (Section 4.2.3). Electron candidates are additionally required to have $|z_0 \sin \theta| < 0.5$ mm and $|\frac{d_0}{\sigma(d_0)}| < 5$. Muon candidates are required to pass the *Medium* reconstruction working point and are further required to have $|\eta| < 2.5$, $|z_0 \sin \theta| < 0.5$, mm and $|\frac{d_0}{\sigma(d_0)}| < 3$ (Section 4.2.2). In both dielectron and dimuon events, the leading lepton is required to have $p_T > 27$ GeV and the sub-leading lepton must have $p_T > 10$ GeV. To further ensure that the selected events are consistent with the presence of a Z boson, the dilepton invariant mass $m_{\ell\ell}$ is required to be in the range $66 < m_{\ell\ell} < 116$ GeV.

Additionally, events are required to contain at least two jets with $p_T > 20$ GeV and $|\eta| < 2.5$. Standard jet cleaning and pileup-rejection cuts are not applied in this analysis as they were found to have a negative impact on jets originating from displaced decays. Instead, a custom jet cleaning working point `LooseBadLLP` is used which has loosened cuts and higher acceptance for displaced decays. In order to avoid double counting of energy deposits in the detector where multiple analysis objects are reconstructed from the same detector signals, an **overlap removal** procedure is used. This algorithm iteratively removes overlapping analysis objects with preference given to different objects at each step. For example, if an electron and a muon are reconstructed using the same inner-detector track, the electron is discarded to suppress contributions from muon bremsstrahlung. For overlapping jets and electrons, jets are first removed if they lie within $\Delta R < 0.2$ of an electrons, then electrons are removed if they lie within $\Delta R < 0.4$ of a remaining jet. The

final-state objects considered in the analysis are those which survive the overlap-removal algorithm.

The trigger, filter, lepton, $m_{\ell\ell}$, and jet requirements comprise the **event preselection**.

7.1.2 Displaced vertex selection

After applying the preselection, the primary discriminating variable between the signal process and SM backgrounds is the presence of multiple displaced vertices. There are several background sources of secondary vertices which mimic the decays of LLPs in the ID. These include QCD decays, interactions between SM particles and detector material, random crossings, and merged vertices. Selections are applied on both the location and kinematics of the vertices which aim to reduce the background contribution to a negligible amount. These selections are described and justified below.

Track pruning

As described in Section 5.2.1, the final step in the vertex reconstruction algorithm attaches lower-quality tracks not initially preselected for vertex seeding to compatible vertices. At the analysis level, a further set of criteria is placed on the tracks associated to existing vertices to remove some of these tracks to improve signal to background discrimination. These cuts are described in Table 7.1. These selections define three different DV working points that were used to investigate and optimize the analysis sensitivity. All DVs considered in the analysis are required to pass the MEDIUM WP, which was optimized using an $S\sqrt{B}$ metric by comparing tracks in signal vertices to those in Z+jets MC. Figure 7.1 shows

Track parameter (w.r.t. DV)	Cut value		
	Loose	Medium	Tight
d_0 (mm)	-	0.8	0.1
z_0 (mm)	-	1.2	0.4
$\sigma(d_0)$ (mm)	-	0.1	0.01
$\sigma(z_0)$ (mm)	-	0.2	0.04

Table 7.1: The track selections applied to vertices at analysis level. Only tracks which pass the given working point selections are used when computing the vertex kinematics.

the L_{xy} distributions of LOOSE and MEDIUM vertices in data and signal MC with $m_a = 15$

GeV and $c\tau_a = 100$ mm. The number of vertices increases substantially after the last pixel layer due to the increased number of fake tracks formed in this region[1]. By placing strict requirements on $\sigma(d_0)$ with respect to the DV, these vertices are largely removed due to the increased track-parameter uncertainties for SCT-only tracks, at the expense of some signal efficiency for samples with longer lifetimes.

(a) Data (b) Signal ($m_a = 15$ GeV and $c\tau_a = 100$ mm)
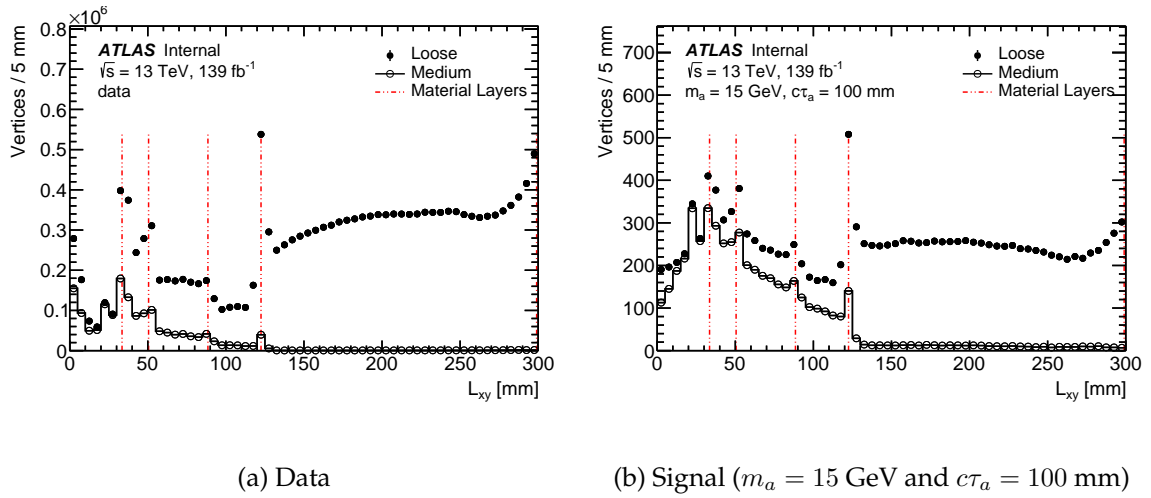
Figure 7.1: The L_{xy} distributions of LOOSE and MEDIUM vertices in (a) data and (b) signal MC with $m_a = 15$ GeV and $c\tau_a = 100$ mm.

Vertex preselection

One of the primary sources of background for secondary vertices in the ID are interactions between SM particles with the detector material. As shown in Figure 7.2, these interactions create secondary vertices concentrated around regions dense in detector material. These vertices may be difficult to distinguish from true exotic decays occurring in the same region of the detector. Figure 7.3 shows the distribution of vertices as a cross-section of the ATLAS detector which clearly shows how the location of vertices closely maps the location of dense detector elements.

To reduce the contribution from hadronic material interactions, a **material veto** is applied which rejects any vertices whose (x, y, z) position coincides with the location of known detector elements. The veto is implemented through the use of two separate 3-dimensional maps of the location of the material in the ID originally developed for a search

---

[1]When not requiring a hit in the pixel detector the number of potential track candidates increases significantly.
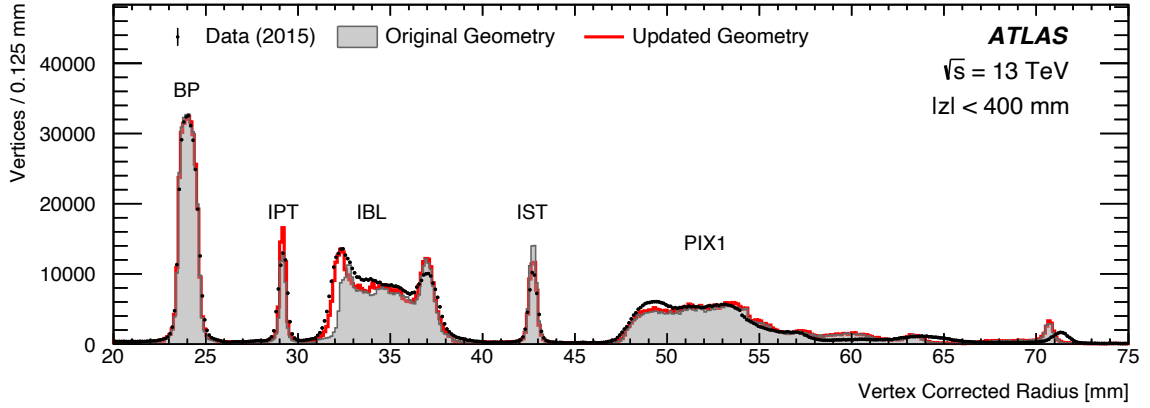
(a) 20 mm $< r <$ 75 mm
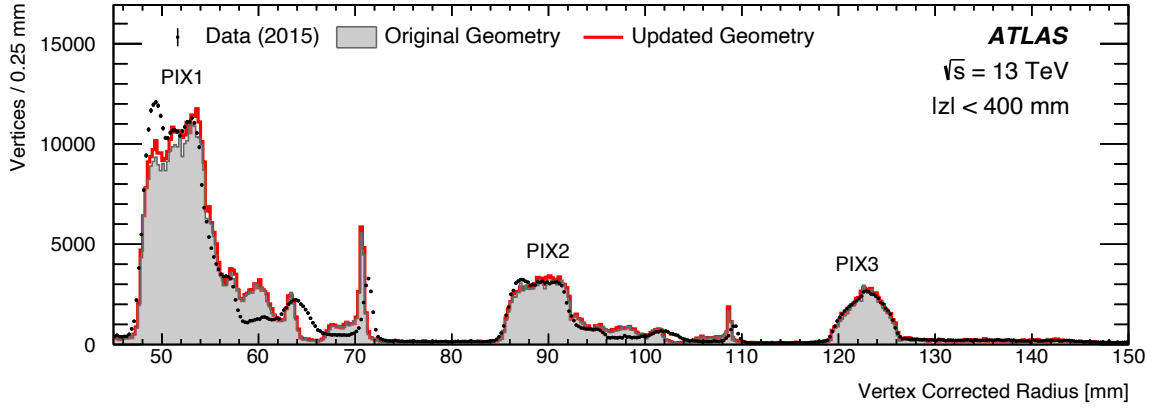
(b) 45 mm $< r <$ 150 mm

Figure 7.2: Comparison of the radial distribution of hadronic interaction candidates between data and simulation. Images from Ref [113].

for R-parity violating SUSY decays [188]. The first map extends to $r < 150$ mm and is constructed from the locations of low-mass, low-track multiplicity vertices in an inclusive data sample using all available Run 2 data. The vertices are required to have $m < 2.5$ GeV to remove potential bias from signal vertices, and vetoes are applied to remove SM LLPs such as K_S^0. Additionally, cuts are placed on the number of pixel hits on each outgoing track, the $\Delta\phi$ between the vertex momentum vector and the vector between the primary and secondary vertex, and the opening angle of the tracks in the vertex in order to reduce vertices reconstructed from fake tracks. To enhance the amount of data in the map a folding technique is used which exploits the periodicity of the detector structures in ϕ. After this folding procedure, the material map is smoothed to avoid the possibility of small regions

[h!]
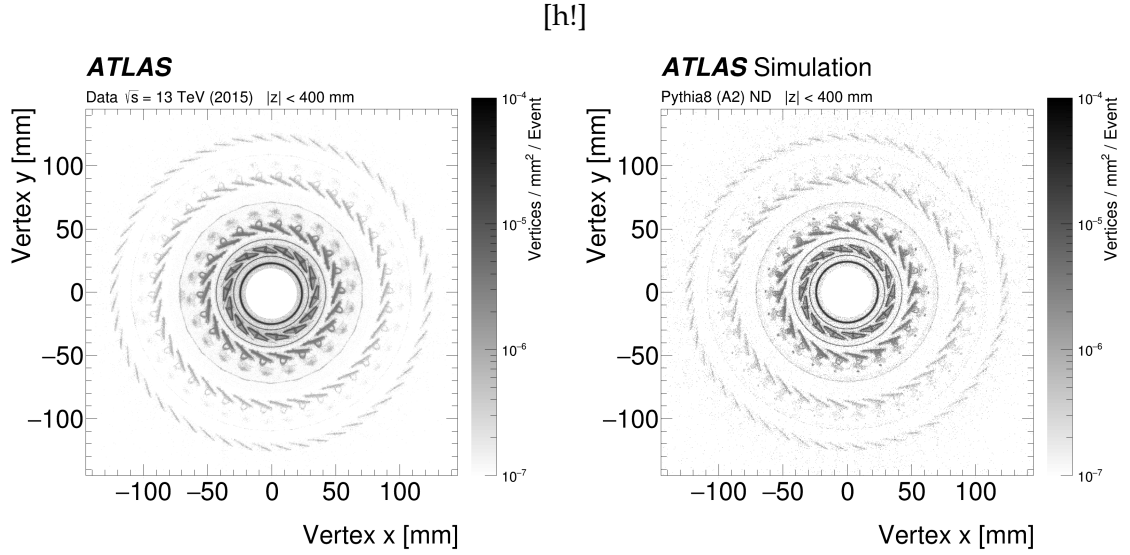
Figure 7.3: Distribution of hadronic-interaction vertex candidates for data and Pythia 8 MC simulation. Image taken from Ref [113].

of detector material being unaccounted for in the map.

The density of vertices found in data starts to decrease sharply after 150 mm due to a lack of statistics. To obtain a robust map of the full fiducial volume, a second map is constructed using simulated data to extend the map in the region $150 < r < 300$ mm. The simulated map is then compared to the data in the region, and modifications are made by hand to improve the agreement between the data and MC. Finally, known regions are added by hand, which is especially necessary in high eta regions at the edge of the preselection criteria.

The material veto is applied by comparing the (x, y, z) position of each vertex to the 3-dimensional map and vetoing vertices in locations where material is present. The impact of the material veto on the radial distribution of secondary vertices is shown in Figure 7.4. The peaks in the distribution of vertices occurring at the pixel layers (shown in red in the figure) are removed by the material veto leaving behind only vertices whose positions do not coincide with regions dense in detector material. Figure 7.5 shows comparisons of the distribution of L_{xy} for vertices in signal samples with $m_a = 15$ GeV and $m_a = 55$ GeV both with and without the material veto applied which illustrate the impact of the material veto on true LLP decays. The fiducial volume considered for vertices in the analysis is defined by the material map, and requires that vertices have $L_{xy} < 300$ mm and $L_z < 300$ mm.
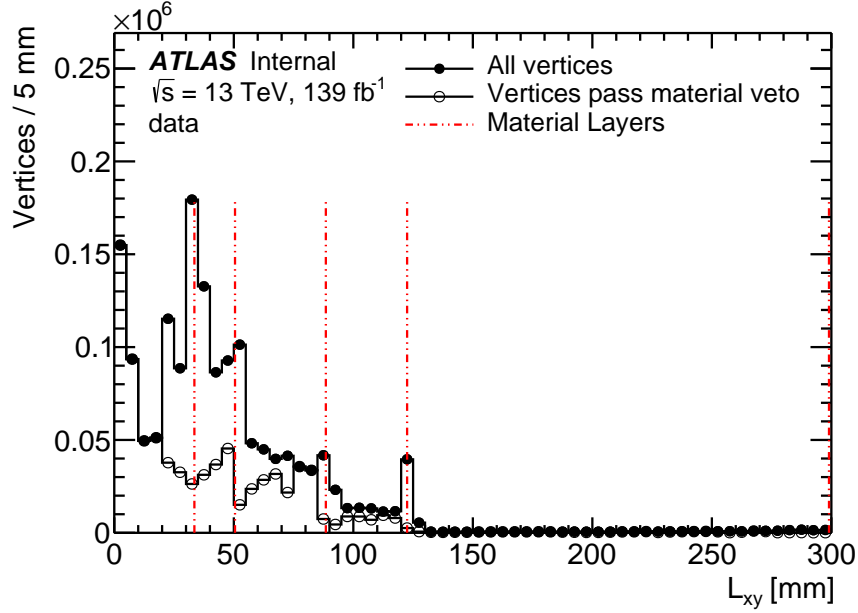
Figure 7.4: The radial distribution of secondary vertices in an inclusive data sample both with and without the material veto applied. The red lines indicate the position of the 4 pixel layers and first SCT layer.

Finally, to reduce the background contribution due to poorly fitted vertices, vertices are required to have $\chi^2/n_{\mathrm{DoF}} < 5$. The material veto, fiducial volume restrictions, and quality cut comprise the **vertex preselection** which is applied to all vertices considered in the analysis.

Signal vertex selection

After the removal of vertices originating from material interactions, the remaining background vertices are primarily comprised of QCD decays and combinatorial vertices. The primary discriminating variables between vertices originating from exotic decays and SM processes are the number of tracks associated to the vertex and the reconstructed mass.

Secondary vertices originating from SM processes such as K_S^0 decays and photon conversions tend to be 2-prong decays. Removing 2-track vertices eliminates the vast majority of vertices in data while only removing 20-30% of vertices in signal MC. Figure 7.6 shows the distribution of n_{trk} for all vertices in signal MC and a background-enriched data sample which pass the preselection. The vertices considered in this analysis are required to have $n_{\mathrm{trk}} > 2$.
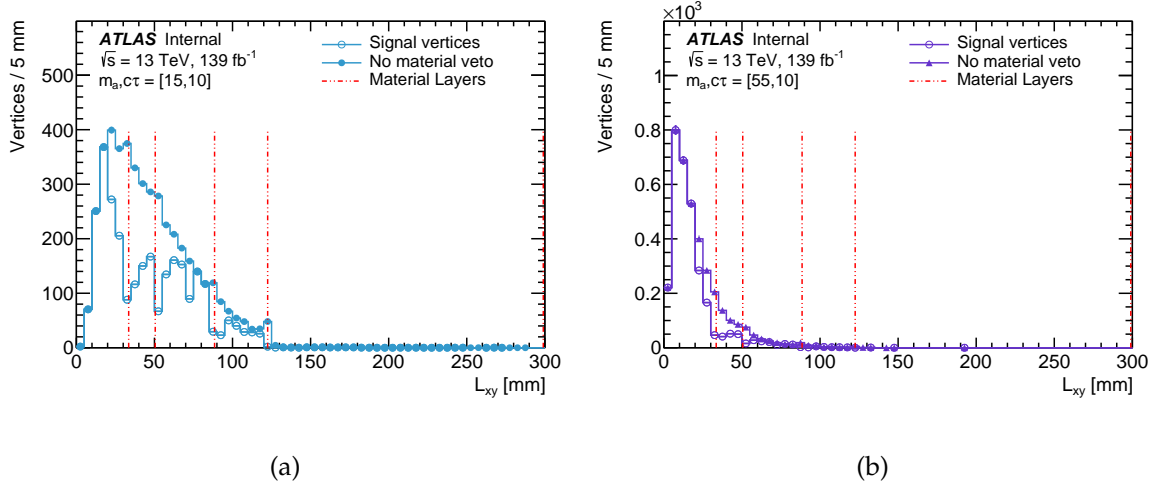
Figure 7.5: The L_{xy} distributions of signal with $m_a = 15$ GeV and $m_a = 55$ GeV both with and without the material veto applied.

Vertices with more than two tracks originate predominantly from **random crossings**. Random crossings refer to any 2-track vertex which is promoted to a higher track multiplicity by an unrelated track crossing within close enough proximity to the decay to be included in the vertex fit. Depending on the geometry of the random crossing with respect to the rest of the vertex, this can drastically increase the computed value of invariant mass. Figure 7.7 shows the distribution of the reconstructed vertex mass in signal MC and control region data. Due to the relatively low masses of the LLPs probed in this search in comparison to other searches for LLPs with displaced vertices, the reconstructed mass does not provide much separation between signal and background. Instead of placing a cut directly on the mass of the vertex, a novel discriminating variable has been developed which aims to exploit the geometry of the tracks in vertices formed from random crossings. Consider the diagram shown in Figure 7.8 which shows an example 4-track vertex formed from a random crossing of an unrelated track with a 3-track vertex originating from a low-mass metastable particle such as a B-hadron. These vertices are characterized by computing the quantity ΔR_{max}:

$$\Delta R_{\text{max}} = \max\left\{ \Delta R(\mathbf{T}_i, \sum_{j \neq i} \mathbf{T}_j) \right\}$$

where $\mathbf{T}_i$ is the four-vector of the ith track in the vertex. Vertices caused by a random crossing tend to have a large ΔR_{max} in comparison to signal vertices, as shown in Figure 7.9. By

(a)   (b)
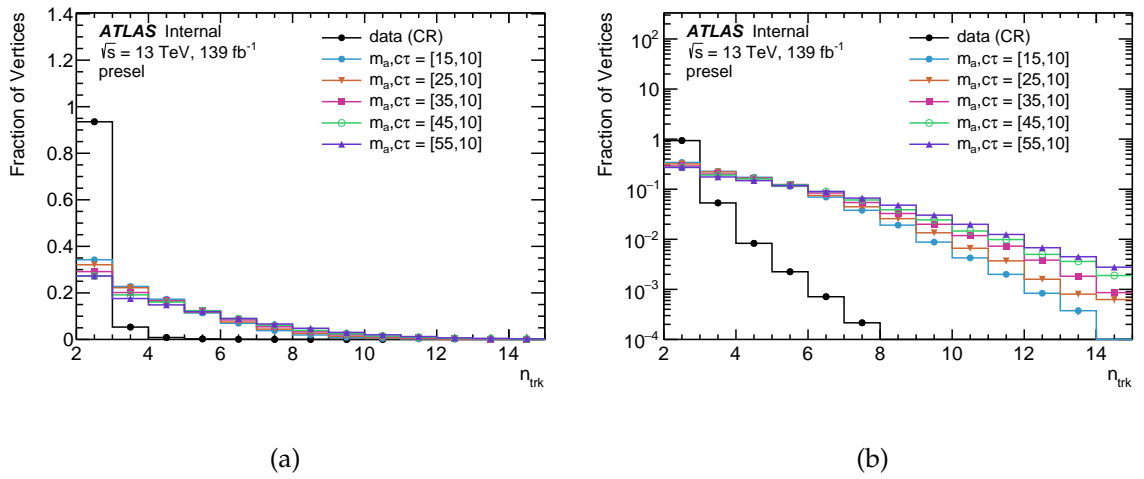
Figure 7.6: The (a) linear and (b) logarithmic distributions of the number of tracks per vertex in signal MC and control region data.

(a)   (b)
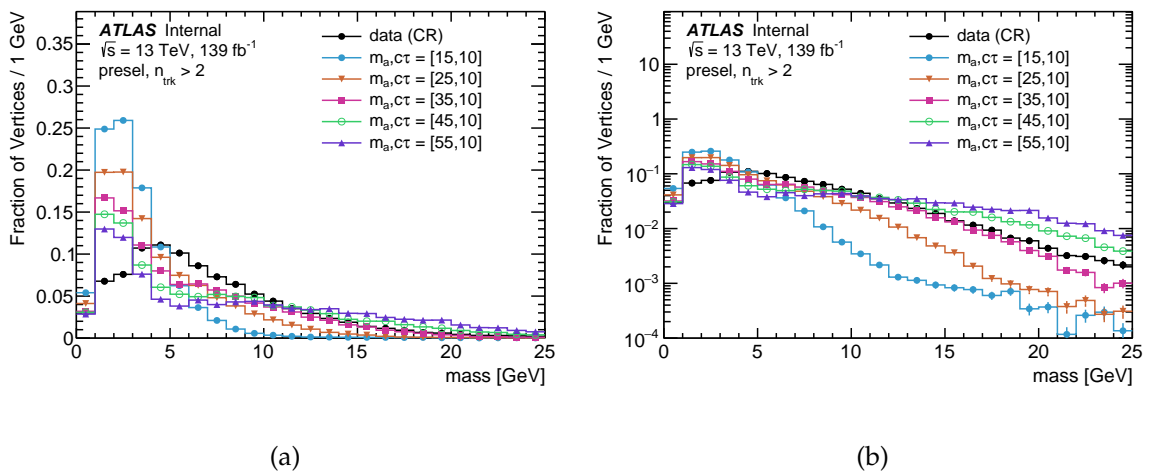
Figure 7.7: The (a) linear and (b) logarithmic distributions of the reconstructed vertex mass in signal MC and control region data. The vertices are required to pass the vertex preselection and have $n_{trk} > 2$.
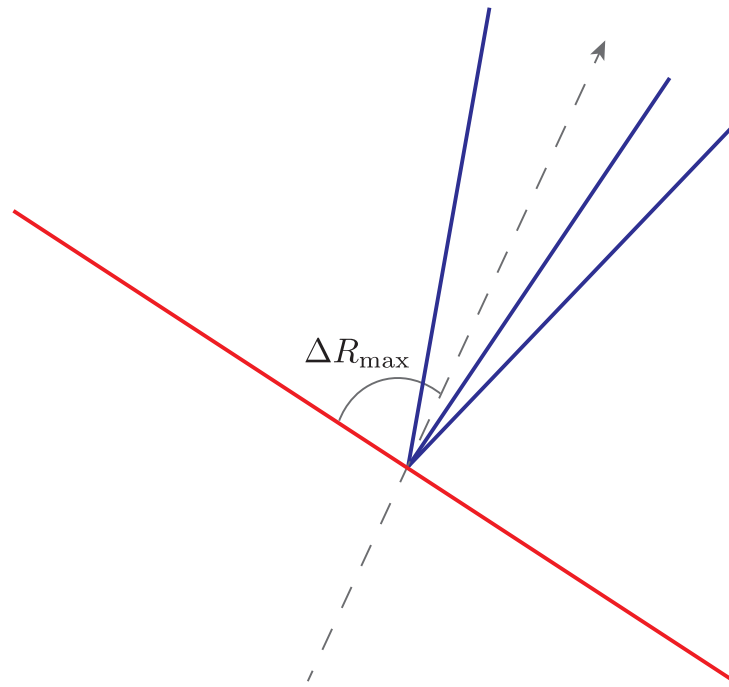
Figure 7.8: Schematic of a 4-track random crossing vertex. The blue tracks represent tracks originating from the decay of a metastable particle such as a B-hadron. The red track represents a track originating from an unrelated process that is spuriously associated to the vertex during reconstruction. The four-vector of the vertex without the inclusion of the random track is shown as a dotted grey line. The ΔR_{max} of this vertex is then given by the ΔR between this four-vector and the four-vector of the random track.
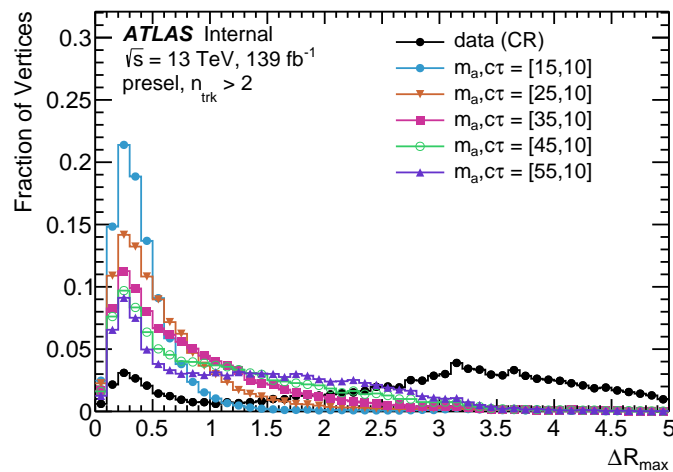
Figure 7.9: The distribution of ΔR_{max} in signal MC and control region data. The vertices are required to pass the vertex preselection and have $n_{\mathrm{trk}} > 2$.
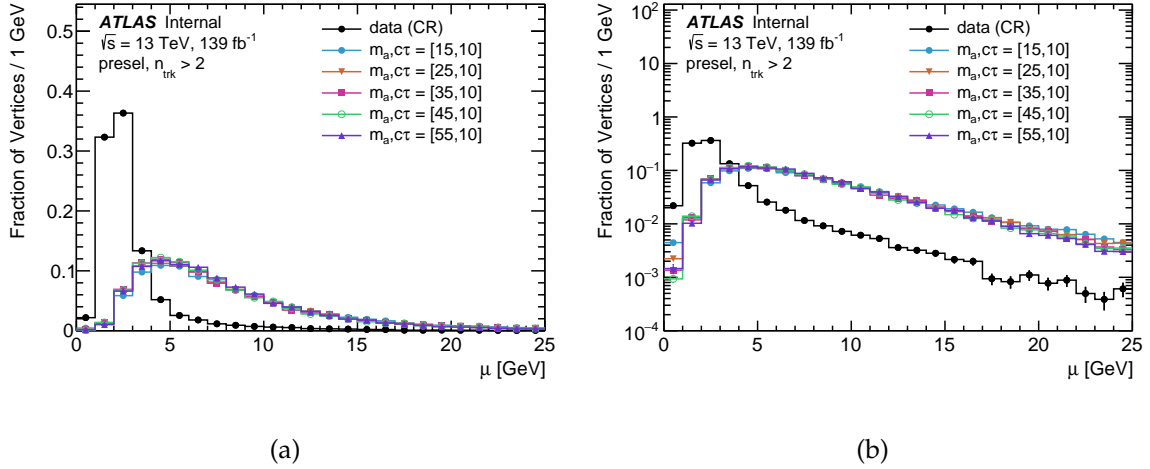
Figure 7.10: The (a) linear and (b) logarithmic distributions of the reduced reconstructed vertex mass in signal MC and control region data. The vertices are required to pass the vertex preselection and have $n_{\mathrm{trk}} > 2$.

dividing the reconstructed mass of the vertex by the quantity ΔR_{max} a modified mass observable is obtained. This variable, known as the **reduced mass** of the vertex, μ, provides much better discrimination power than the normal reconstructed vertex mass, as shown in Figure 7.10. In addition, the distribution of the reduced mass is largely independent of the mass of the LLP, allowing for a mass-agnostic discriminating variable. The vertices considered in this analysis are required to have $\mu > 3\,\mathrm{GeV}$.

To further reduce the contribution from QCD processes such as heavy-flavor decays, additional cuts are placed on the L_{xy} significance, defined as $L_{xy}/\sigma(L_{xy})$ as well as requiring that at least one track in the vertex has $d_0 > 3\,\mathrm{mm}$. These selections reduce the number of vertices originating from prompt SM decays while having a minimal impact on the signal selection efficiency. Finally, to facilitate the modeling of the background, the position of the vertex is required to be within $\Delta R < 0.6$ from the axis of one of the leading four jets. When multiple DVs are considered they must be matched to different jets. The full set of vertex selection criteria are shown in Table 7.2, and the impact of the various selections on the number of reconstructed vertices in signal with $c\tau_a = 100\,\mathrm{mm}$ is shown as a cutflow in Figure 7.11.

The selection efficiency for identifying true LLP decays in signal MC is shown as a function of L_{xy} in Figure 7.12. The identification efficiency is roughly 10-20% for LLPs

Selection type	Parameter	Value
Track cleaning	Max. $d_{0,\mathrm{SV}}$	0.8 mm
	Max. $z_{0,\mathrm{SV}}$	1.2 mm
	Max. $\sigma(d_{0,\mathrm{SV}})$	0.1 mm
	Max. $\sigma(z_{0,\mathrm{SV}})$	0.2 mm
Vertex preselection	Max χ^2/n_{DoF}	5
	Max. L_{xy}	300 mm
	Max. $|z|$	300 mm
	Material veto	True
Signal selection	Min. n_{trk}	3
	Min. $m/\Delta R_{\mathrm{max}}$	3 GeV
	Min. $L_{xy}/\sigma(L_{xy})$	100
	Min. $d_{0,\mathrm{max}}$	3 mm
	Max. ΔR_{jet}	0.6

Table 7.2: The full set of selections applied to vertices considered in the analysis.

decaying within the fiducial volume of the pixel detector, after which the decreased track resolution causes vertices to fail the MEDIUM WP.

7.1.3 Event categorization

The most discriminating variable between signal and background events is the number of displaced vertices present in the event. The **signal region (SR)** is defined by requiring events to pass the preselection described in Section 7.1.1, as well as the presence of at least two displaced vertices which pass the selections described in Section 7.1.2.

Selection	Value
Number of jets	≥ 2
Number of OSSF leptons	2
m_{ll}	$66 < m_{ll} < 116$ GeV
Number of DVs	≥ 2

Table 7.3: The full set of selections applied to the signal region after the trigger and filter requirements. The DVs are required to pass all of the selections listed in Table 7.2.

This search is conducted as a **blind** analysis, meaning that the data in regions expected to be populated by signal events are not revealed until after the experiment is complete. This prevents information which may influence the final results from biasing the analysis in any way. To define a region with minimal signal contamination, the selection on the number of displaced vertices in the event is inverted to define a **control region (CR)** that
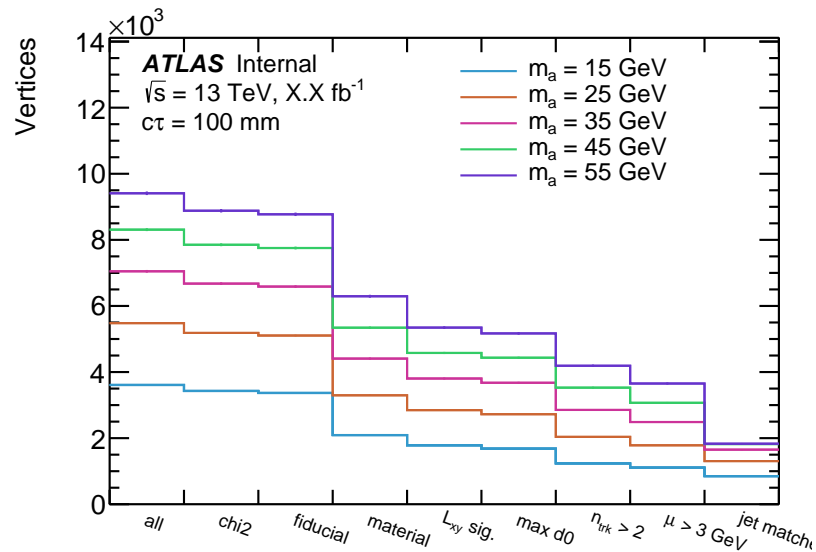
Figure 7.11: The per-vertex cutflow for all selections placed on vertices in signal MC with $c\tau_a = 100$ mm.
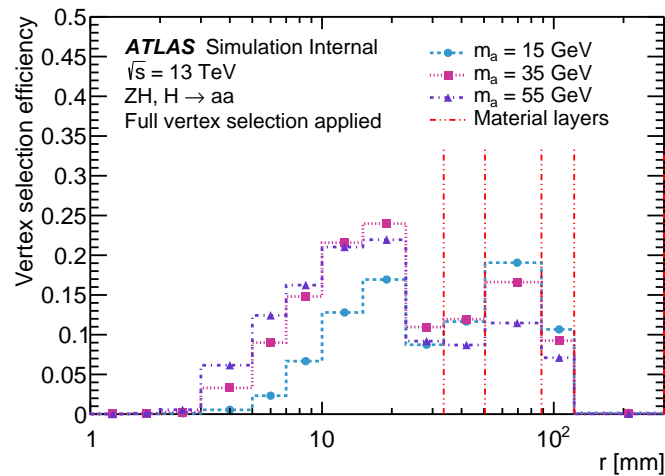
Figure 7.12: The fraction of a boson decays matched to reconstructed displaced vertices passing all vertex selections in signal MC. Truth LLP decay vertices are matched to reconstructed vertices using a p_T weighted track association as described in Section 5.2.2. The locations of the four pixel layers are shown as dashed red lines. The vertex selection efficiency drops significantly after the last pixel layer due to a loss of impact parameter resolution for tracks with zero pixel hits.

is used to estimate the background contribution from SM processes in the SR. Data in the signal region are not revealed until after the background estimate is derived with a corresponding systematic uncertainty. An additional signal-free region is used to validate the background estimate and will be described in Section 7.2.2.

7.1.4 Analysis cutflow

The full event selection applied to signal MC is shown as a cutflow in Figures 7.13 and 7.14 for the different values of $c\tau$. Samples are weighted to the Run 2 luminosity according to their cross sections and generated number of weighted events, so that the value of each bin represents the total expected signal yield passing that selection. The total expected yields

Sample			Selection							
m_a [GeV]	$c\tau$ [mm]	Yield	Init	Trigger	Filter	Leptons	Z	Jets	≥ 1 DV	≥ 2 DV
	10	Total	11371.6	6776.6	2950.5	1665.1	1606.0	1528.6	601.8	51.0
55	100	Total	11386.4	6770.2	3014.1	1737.8	1677.1	1590.2	411.9	23.7
	1000	Total	11409.2	6812.6	2735.8	1584.9	1525.9	1411.1	58.6	0.6
	10	Total	11361.7	6781.1	3082.4	1748.3	1690.9	1612.1	651.7	70.2
45	100	Total	11362.5	6747.2	3138.5	1812.2	1752.2	1669.5	376.7	20.9
	1000	Total	11372.6	6717.8	2747.1	1605.8	1549.8	1427.0	54.2	0.5
	10	Total	11406.3	6833.5	3187.6	1817.4	1760.6	1683.1	668.8	71.4
35	100	Total	11410.6	6804.4	3345.6	1911.9	1845.7	1747.1	339.3	21.1
	1000	Total	11438.0	6784.7	2760.2	1596.9	1544.5	1404.6	41.8	0.2
	10	Total	11435.8	6826.3	3315.1	1880.8	1822.4	1721.9	623.7	63.9
25	100	Total	11438.4	6807.4	3592.0	2072.7	2002.7	1879.4	282.8	11.4
	1000	Total	11434.5	6801.8	2639.6	1525.6	1472.2	1305.6	34.0	0.4
	10	Total	11434.3	6829.1	3659.9	2071.9	2002.4	1869.0	576.4	54.1
15	100	Total	11419.2	6804.0	3814.3	2196.8	2123.7	1985.8	194.5	4.6
	1000	Total	11404.4	6786.7	2224.3	1274.5	1228.2	1044.7	19.4	0.1

Table 7.4: The total expected yield for each signal point after each selection is applied, assuming $B(H \to aa \to b\bar{b}b\bar{b}) = 1$.

in the signal region (assuming $B(H \to aa \to b\bar{b}b\bar{b}) = 1$) are shown as a cutflow are shown for the full signal grid in Table 7.4. The fraction of weighted events passing each cut are shown for the full signal grid in Table 7.5.

(a)

(b)

(c)

(d)

(e)
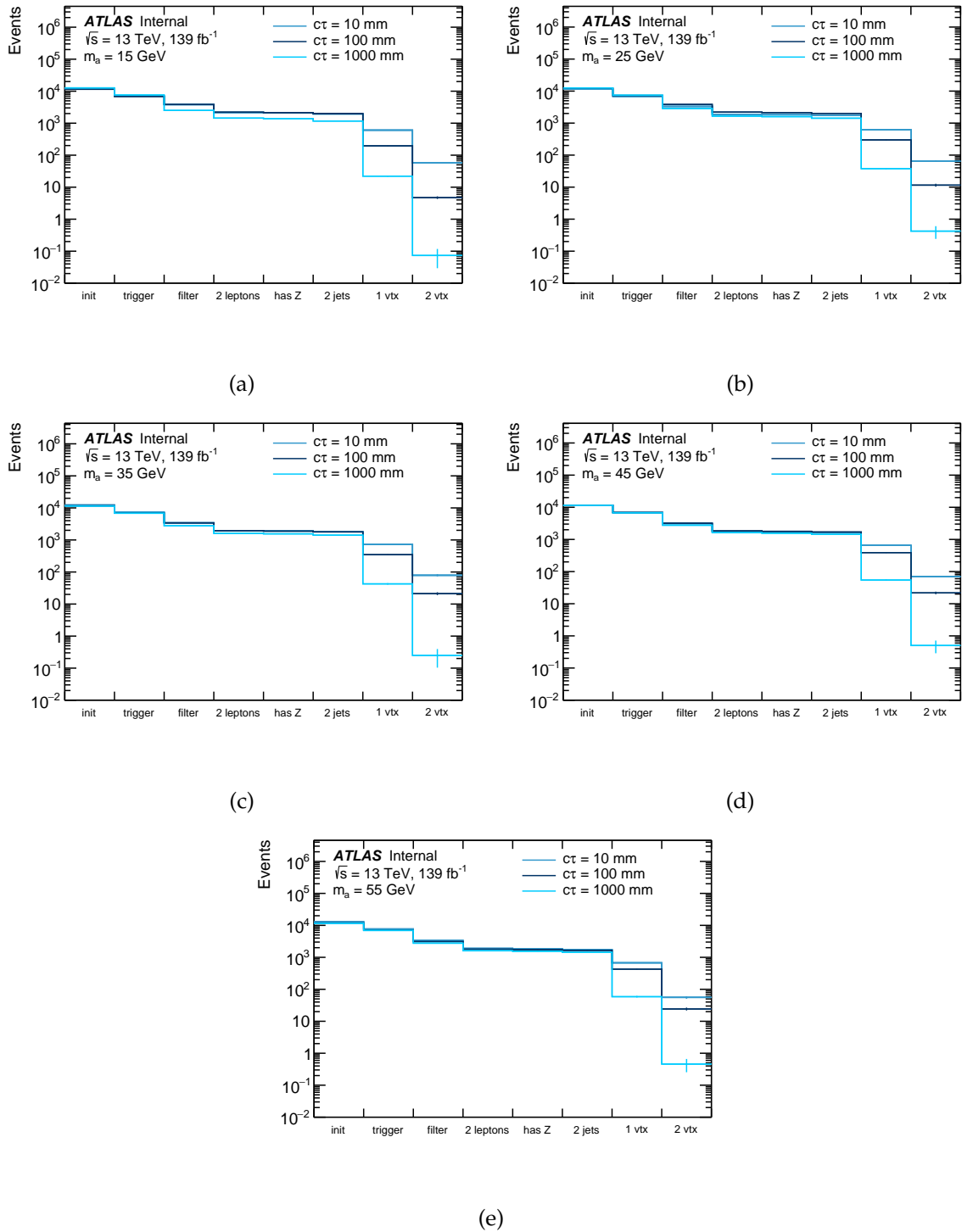
Figure 7.13: The weighted number of events passing each cut used in the event selection, for each signal mass point. Samples are weighted to the Run 2 luminosity according to their cross sections and generated number of weighted events.

(a)

(b)

(c)
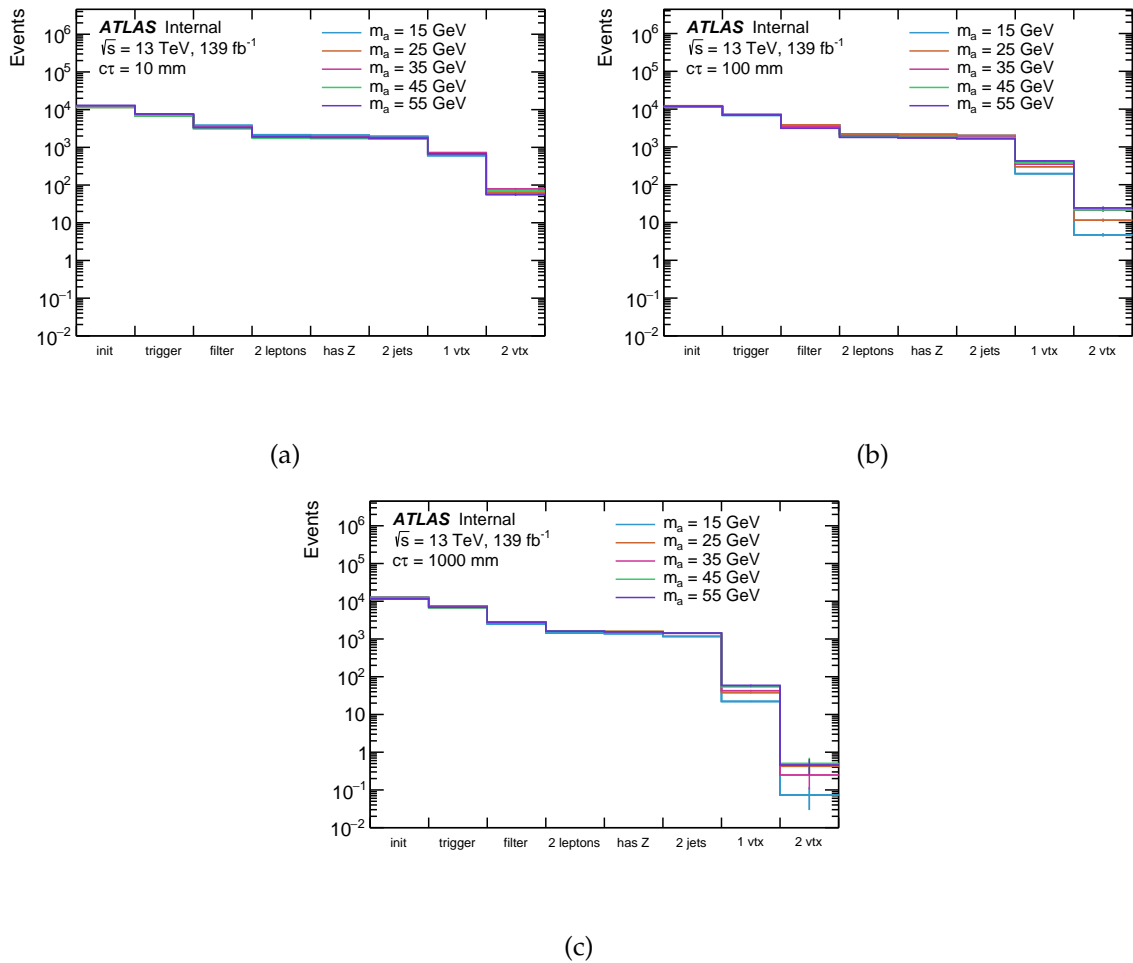
Figure 7.14: The weighted number of events passing each cut used in the event selection, for each generated value of $c\tau$. Samples are weighted to the Run 2 luminosity according to their cross sections and generated number of weighted events.

Sample			Selection							
m_a [GeV]	$c\tau$ [mm]	Efficiency	Init	Trigger	Filter	Leptons	Z	Jets	≥ 1 DV	≥ 2 DV
55	10	Total	1.0000	0.5949	0.2589	0.1457	0.1405	0.1336	0.0520	0.0044
		Relative	1.0000	0.5949	0.4353	0.5626	0.9646	0.9512	0.3894	0.0845
	100	Total	1.0000	0.5932	0.2640	0.1521	0.1468	0.1394	0.0359	0.0020
		Relative	1.0000	0.5932	0.4449	0.5762	0.9652	0.9497	0.2575	0.0567
	1000	Total	1.0000	0.5980	0.2401	0.1392	0.1340	0.1242	0.0051	0.0000
		Relative	1.0000	0.5980	0.4015	0.5797	0.9627	0.9269	0.0411	0.0096
45	10	Total	1.0000	0.5969	0.2720	0.1542	0.1492	0.1424	0.0573	0.0061
		Relative	1.0000	0.5969	0.4556	0.5670	0.9673	0.9543	0.4024	0.1069
	100	Total	1.0000	0.5940	0.2763	0.1595	0.1542	0.1470	0.0333	0.0018
		Relative	1.0000	0.5940	0.4651	0.5773	0.9669	0.9530	0.2268	0.0548
	1000	Total	1.0000	0.5908	0.2420	0.1415	0.1365	0.1257	0.0048	0.0000
		Relative	1.0000	0.5908	0.4096	0.5847	0.9650	0.9205	0.0379	0.0093
35	10	Total	1.0000	0.5983	0.2785	0.1586	0.1537	0.1468	0.0586	0.0064
		Relative	1.0000	0.5983	0.4656	0.5693	0.9694	0.9551	0.3994	0.1083
	100	Total	1.0000	0.5969	0.2940	0.1681	0.1623	0.1536	0.0299	0.0018
		Relative	1.0000	0.5969	0.4925	0.5718	0.9654	0.9465	0.1946	0.0614
	1000	Total	1.0000	0.5933	0.2417	0.1399	0.1353	0.1230	0.0036	0.0000
		Relative	1.0000	0.5933	0.4074	0.5788	0.9669	0.9091	0.0294	0.0046
25	10	Total	1.0000	0.5971	0.2897	0.1644	0.1593	0.1506	0.0545	0.0056
		Relative	1.0000	0.5971	0.4852	0.5673	0.9689	0.9457	0.3619	0.1024
	100	Total	1.0000	0.5928	0.3117	0.1796	0.1734	0.1633	0.0242	0.0009
		Relative	1.0000	0.5928	0.5259	0.5760	0.9657	0.9419	0.1480	0.0384
	1000	Total	1.0000	0.5918	0.2284	0.1316	0.1271	0.1131	0.0030	0.0000
		Relative	1.0000	0.5918	0.3859	0.5763	0.9656	0.8901	0.0263	0.0116
15	10	Total	1.0000	0.5987	0.3200	0.1813	0.1752	0.1631	0.0509	0.0048
		Relative	1.0000	0.5987	0.5344	0.5667	0.9664	0.9307	0.3118	0.0953
	100	Total	1.0000	0.5963	0.3345	0.1926	0.1862	0.1741	0.0171	0.0004
		Relative	1.0000	0.5963	0.5609	0.5759	0.9667	0.9353	0.0982	0.0235
	1000	Total	1.0000	0.5987	0.1983	0.1138	0.1096	0.0921	0.0017	0.0000
		Relative	1.0000	0.5987	0.3312	0.5738	0.9633	0.8404	0.0188	0.0033

Table 7.5: The total and relative efficiencies for each selection, for each signal point.

7.2 Background estimation

The probability that a given jet will contain a DV that passes the full signal vertex selection described in Section 7.1.2 is found to be highly correlated with several jet properties. The track multiplicity and density within a jet increase with the jet p_{T} [189], resulting in increased probability that a DV is reconstructed within the jet cone. Additionally, due to the lifetime of hadrons containing heavy flavor quarks, the probability also depends strongly on the flavor of the parton that initiated the jet. To estimate the number of background
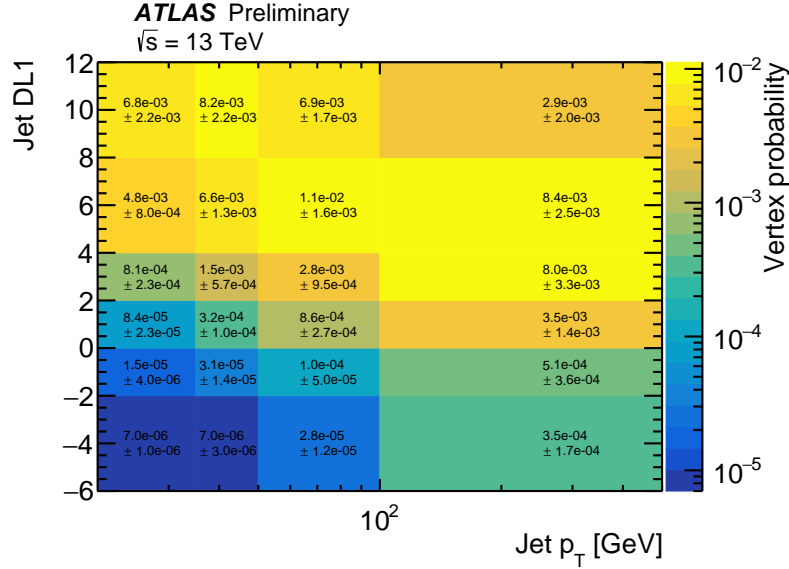
Figure 7.15: The per-jet DV probabilities as a function of jet p_T and DL1 b-tag score computed in the CR. The probabilities are computed by taking the ratio of jets that are matched to a DV within $\Delta R < 0.6$ to the inclusive jet collection in events with fewer than two DVs.

events that will pass the full signal selection, a *per-jet* vertex efficiency map is derived which parameterizes the probability that a given jet will contain a DV based on the jet p_T and DL1 b-tag score (Section 4.2.1). The map is computed by taking the ratio of jets which are matched to a DV passing the full signal vertex selection to the total number of jets in the preselected data. The probability that an event contains exactly one DV is then computed from a binomial distribution based on the leading four jets in the event:

$$P_{\text{event}}(n_{\text{DV}} = 1 | j_1, \ldots, j_4) = \sum_{i=1}^{4} P_{\text{jet}}(n_{\text{DV}} = 1 | j_i) \times \prod_{k \neq i} \left(1 - P_{\text{jet}}(n_{\text{DV}} = 1 | j_k)\right) \qquad (7.1)$$

where $P_{\text{jet}}(n_{\text{DV}} = 1 | j_i)$ is the probability for the ith jet in the event to contain a DV, given its p_T and DL1 score. The map used to predict the number of events in the signal region is shown in Figure 7.15. The numerator and denominator used to construct the efficiency map are shown in Figure 7.16.

To compute the number of events with at least 2 DVs, the compliment is used:

$$P_{\text{event}}(n_{\text{DV}} \geq 2) = 1 - P_{\text{event}}(n_{\text{DV}} = 1) - P_{\text{event}}(n_{\text{DV}} = 0) \qquad (7.2)$$
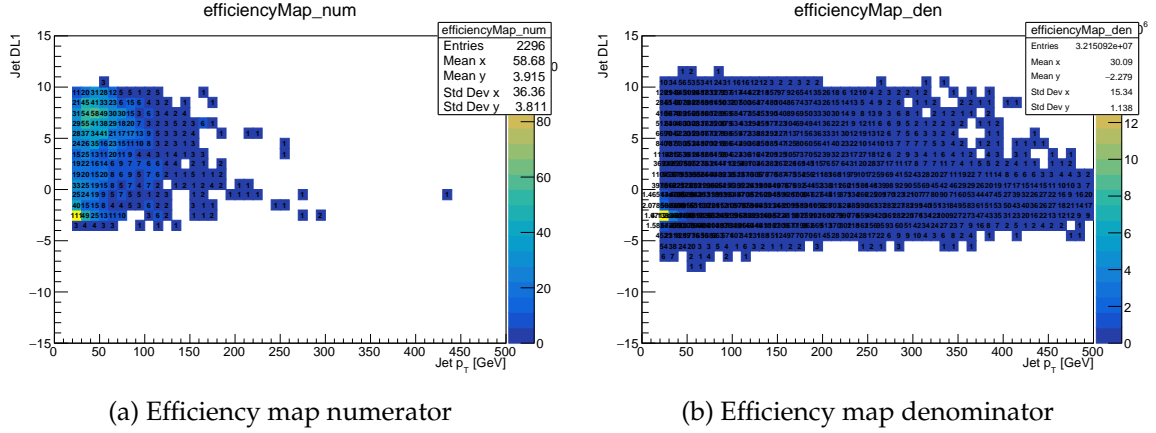
(a) Efficiency map numerator

(b) Efficiency map denominator

Figure 7.16: The (a) numerator and (b) denominator used to construct the efficiency map.

To compute the uncertainty on the background estimate, a toy method is used which performs $N = 100$ pseudo-experiments to propagate the statistical uncertainty on the values of the efficiency map to the final background estimate. The nominal efficiency map is varied bin-by-bin using a Gaussian of width given by the statistical uncertainty on the bin to create 100 statistically varied efficiency maps. The background estimate is then computed using both the nominal and statistically varied maps. This gives $N = 100$ different background estimates which are Gaussian distributed. The mean of this distribution is taken as the final background estimate, and the standard deviation is taken as the uncertainty. Using this strategy, we obtain an estimate of 1.30 ± 0.08 (stat) events in the signal region due to SM backgrounds.

7.2.1 Closure test

To ensure that the per-jet map sufficiently replicates per-event probabilities, a closure test is performed which compares the predicted and observed event-level distributions in the region with $n_{\mathrm{DV}} = 1$. Figure 7.18 shows the predicted and observed distributions for several event-level observables. Excellent agreement is observed for all variables, indicating that the per-jet method accurately captures the complete kinematics of the event. This method gives an estimate of **2283 ± 59** total events in the 1 DV region due to background. We observe **2297** events which is a deviation of 0.2σ away from the prediction.

(a) $p_{\mathrm{T},Z}$

(b) η_Z

(c) $\sum p_{\mathrm{T,jet}}$

(d) $\sum \mathrm{DL1}_{\mathrm{jet}}$
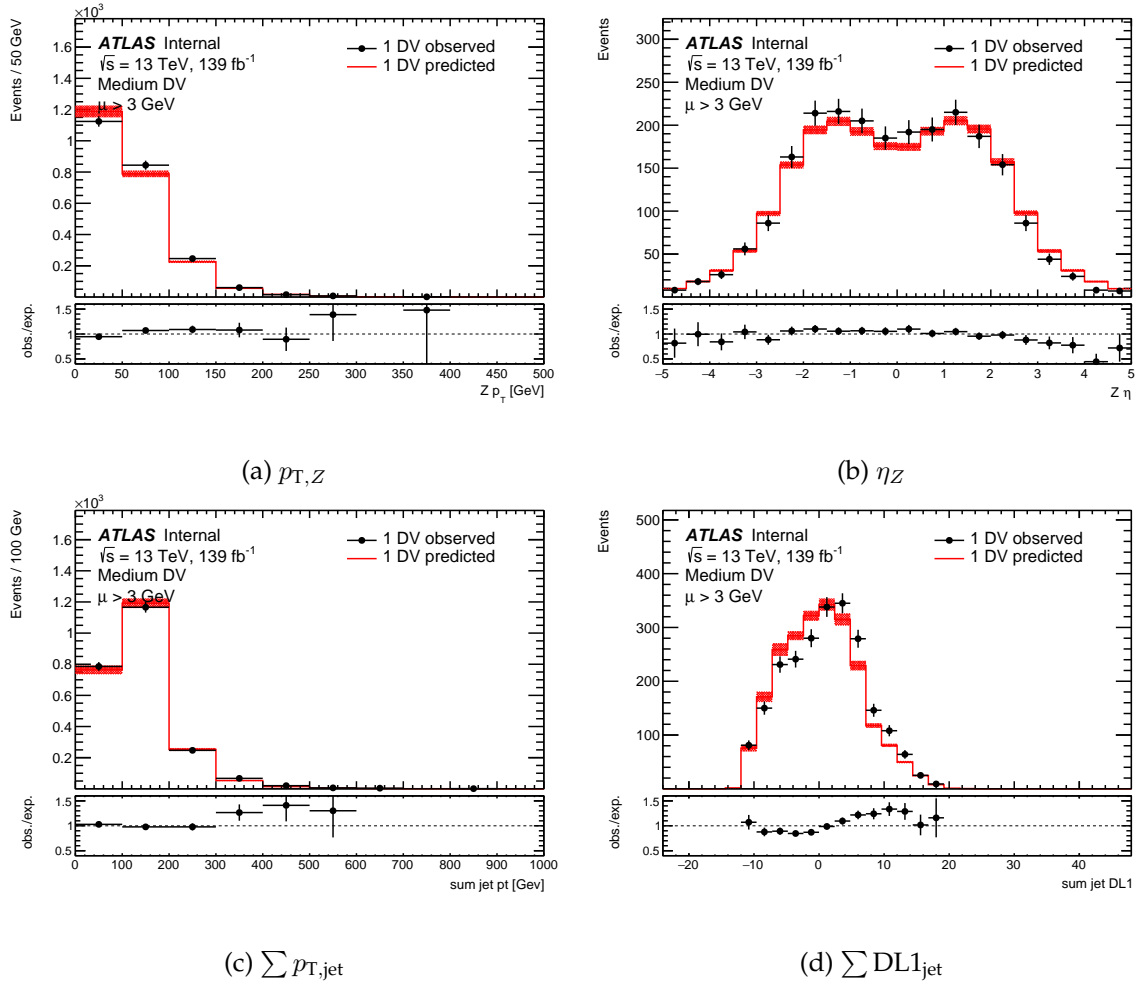
Figure 7.17: Predicted and observed event-level distributions with 1 DV.

(a) p_{T,j_0}

(b) p_{T,j_0}
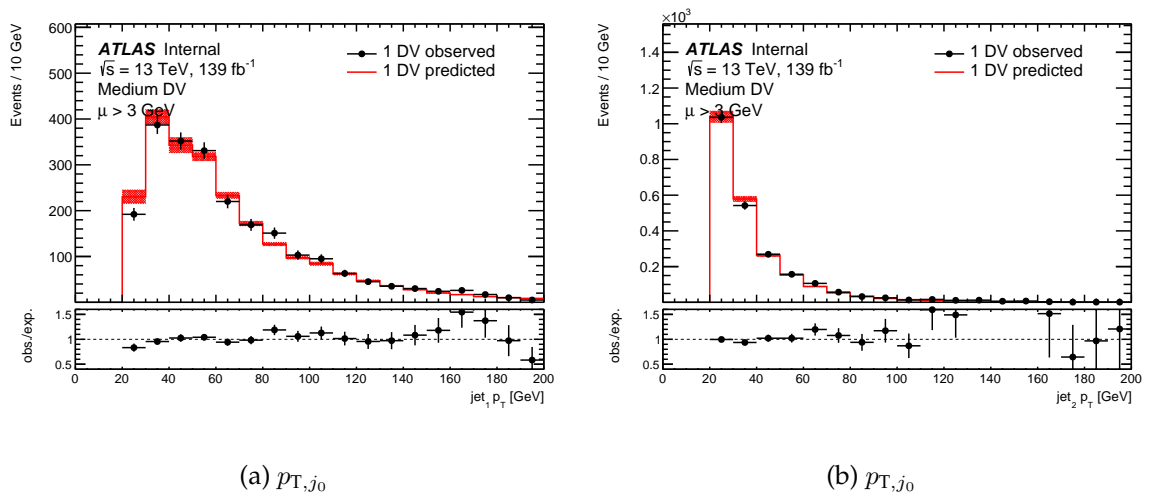
Figure 7.18: Predicted and observed event-level distributions with 1 DV.

7.2.2   Validation

This method for computing the background prediction relies on the assumption that the per-jet DV probabilities are unaffected by the presence of multiple DVs in an event. To test this assumption, events passing an orthogonal γ+jet selection are used which closely mimic the dominant Z+jet background in the signal region. This region, known as the **validation region (VR)**, requires events to pass a high p_T photon trigger, contain at least one photon with $p_T > 160$ GeV or two photons with $p_T > 60$ GeV, and at least two jets. Additionally, events containing charged leptons are vetoed in the VR to remove potential biases from signal. This selection results in a signal-free region with which to test the validity of the background modeling strategy. The parameterization of the per-jet DV probabilities in terms of p_T and DL1 allows for a robust validation of the method despite the different kinematic properties of the jets in this region with respect to the SR. By studying the predicted and observed number of events with at least two DVs in the VR, the core assumption of the background estimate may be tested and any systematic deviations may be taken into account as an additional uncertainty on the background estimate.

The per-jet DV probability is calculated using events in this VR with fewer than two DVs, and used to predict the number of events with at least two DVs. Using this method, 19.9 ± 0.4 events are predicted and 23 are observed, as shown in Figure 7.19, demonstrating that any jet-jet correlations are negligible or captured by the parameterization in terms of jet p_T and DL1. The distribution of the sum of the DL1 score of the leading four jets is shown in Figure 7.20 to demonstrate that per-event quantities are well modeled by the background estimation method.

The systematic uncertainty on the method used to obtain the background prediction is derived by comparing the number of predicted and observed events in the VR. Although the prediction and observation agree within uncertainties, due to the limited statistics available to test the background estimation method a conservative systematic uncertainty is assigned on the total expected number of background events in the SR which is equal to the statistical uncertainty on the observed number of events in the VR. This amounts to a 21% uncertainty, or ±0.27 events, on the final background estimate giving a prediction of 1.30 ± 0.08 (stat.) ± 0.27 (syst.) events.
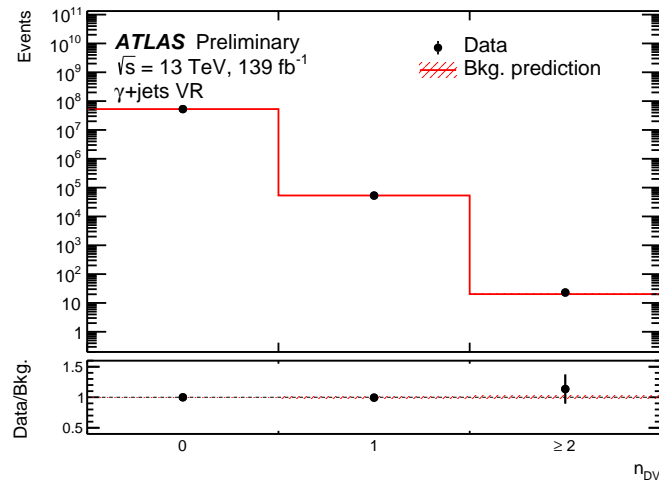
Figure 7.19: The predicted and observed number of events in the VR as a function of the number of DVs in the event. The first two bins are used to derive the background estimate and serve as a closure test. The number of events observed in the $n_{DV} \geq 2$ bin agrees with the prediction within statistical uncertainty.
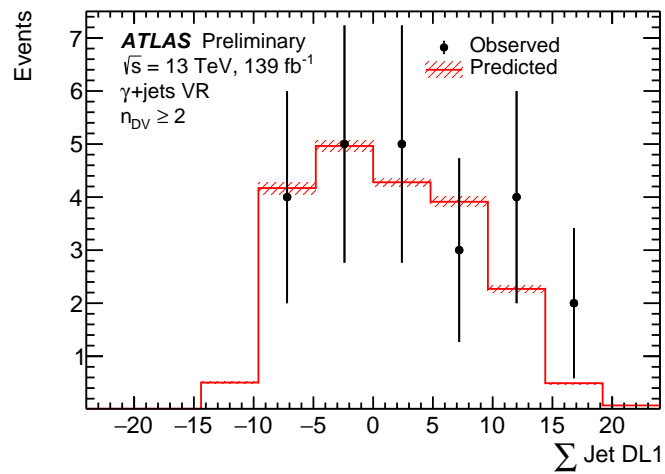
Figure 7.20: The predicted and observed number of events with at least two DVs in the γ+jet VR as a function of the sum of the DL1 discriminant values of the (up to) four leading jets. The shaded bands on the prediction represent the statistical uncertainty on the prediction.
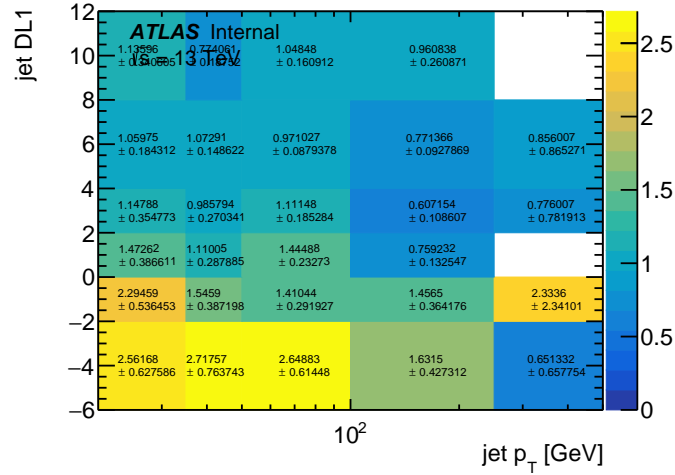
Figure 7.21: The ratio of the efficiency maps derived in the photon+filter selection to the Z selection

To ensure that the displaced jet filter used to collect the data for the Z region does not introduce an additional bias that is not present in the photon region, we mimic the filter by requiring that one of the leading two jets in the photon region passes the cuts on CHF and α_{max} described in Section 6.2.2. With these event selections the predicted number of events in the photon region is 2.2 events. We observe 2.0 events in this region, indicating that the displaced jet filter does not impact the background estimation method. Furthermore, when the additional selections are placed on the photon region, the discrepancy on the efficiency maps and between the photon and Z region is reduced, as shown in Figure 7.21. This translates to significantly improved agreement in the final background prediction obtained when using the photon and Z maps, as shown in Figure 7.22.

7.2.3 Signal injection test

To assess the impact of potential signal contamination in the 1 DV CR used to derive the efficiency map, injection tests are performed. First, we assume the presence of signal in the 1 DV Z region. A modified efficiency map is computed after subtracting the signal from the numerator and denominator used to create the map, assuming a 25% branching ratio of $H \rightarrow aa$. The ratio of the modified map to the nominal map is shown in Figure 7.23 for the 35 GeV scalar mass point with a lifetime of 10 cm. The number of signal and data jets used to compute the map are given in Table 7.6. The background prediction is then
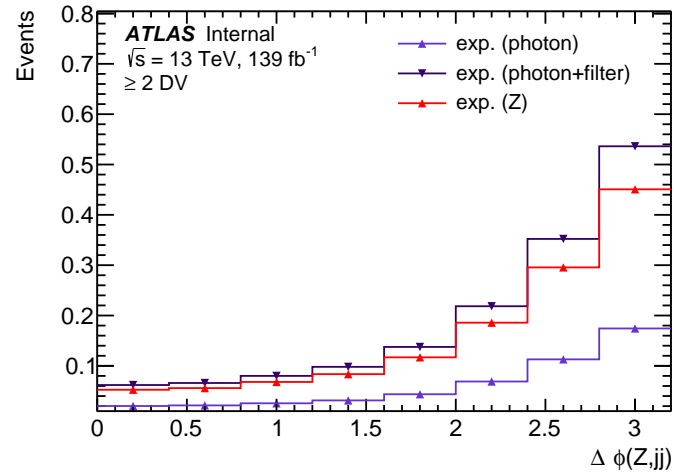
Figure 7.22: Background estimation with DV probability maps derived using either photon, photon+filter, or Z events.
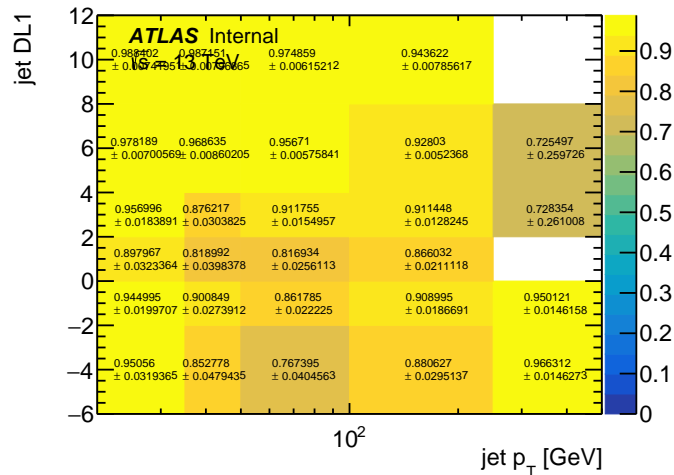
Figure 7.23: The modified efficiency map formed by subtracting signal.

Jet type	data	signal ($\mathcal{B}_{H \to aa} = 25\%$)
DV matched	2296	156
Inclusive	32150432	1457

Table 7.6: The number of jets used to compute the modified map. The numerator of the efficiency map is the first row (DV matched), and the denominator is the second (Inclusive)

(a) 1 DV (b) 2 DV
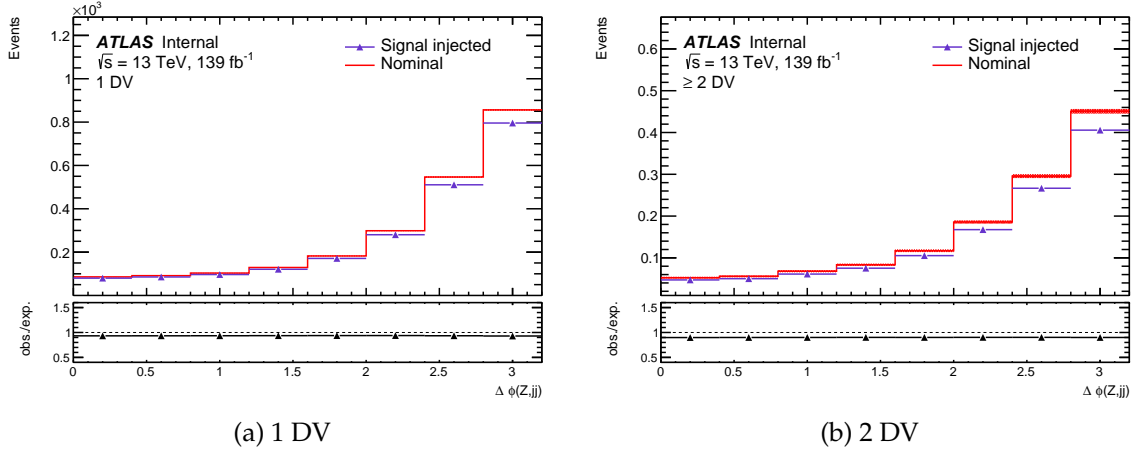
Figure 7.24: The predicted distribution of $|\Delta\Phi(Z, jj)|$ in the (a) 1DV and (b) ≥ 2 DV regions using the nominal and modified efficiency maps

computed using the modified map and compared to the nominal prediction. The predicted distributions of $|\Delta\Phi(Z, jj)|$ are shown in Figure 7.24. The number of predicted events in the 1 and 2 DV regions when using the two different maps is given in Table 7.7. Only

Region	Nominal	Modified	Observed
1 DV	2293	2140	2297
≥ 2 DV	1.30	1.18	-

Table 7.7: The number of predicted and observed events in the 1 and 2 DV regions when using the nominal and modified efficiency maps.

the baseline efficiency maps are used when computing the predicted background with no pseudoexperiments performed. Hence the predicted number of events for the nominal map in Table 7.7 is expected to differ slightly from the complete background prediction described in this Section. Overall the effect of subtracting the signal from the histograms used to compute the efficiency map has a roughly 10% effect, which is well within the total uncertainty on the background estimate. In comparison, under this signal hypothesis of a 25% branching ratio of $H \to aa$ we would expect 20 additional events in the signal region meaning that the presence of signal in the 1 DV region would not prevent a discovery.

This test was performed with for each generated value of m_a and $c\tau_a$. The results are summarized in Table 7.8

Sample		Value		
m_a [GeV]	$c\tau$ [mm]	Δ B	S	S/Δ B
	10	0.127	12.756	100.196
55	100	0.052	5.931	112.972
	1000	0.005	0.147	29.056
	10	0.124	17.551	141.901
45	100	0.045	5.237	116.101
	1000	0.005	0.130	25.572
	10	0.129	17.842	138.471
35	100	0.042	5.271	126.659
	1000	0.005	0.049	10.328
	10	0.118	15.947	135.570
25	100	0.035	2.842	81.966
	1000	0.002	0.095	38.924
	10	0.108	13.516	125.509
15	100	0.026	1.142	43.795
	1000	0.002	0.014	9.348

Table 7.8: Summary of the signal contamination tests.

7.3 Signal systematic uncertainties

The predicted number of signal events for each signal hypothesis is subject to experimental and theoretical sources of systematic error. These experimental uncertainties originate predominantly from differences in the modeling of physics objects and pileup between MC simulation and data. In this section, the various sources of systematic uncertainty on the total signal yield are described.

7.3.1 Uncertainties on standard objects

Experimental uncertainties originating from differences between data and simulation are considered for all physics objects used in the analysis. For standard objects, these include uncertainties on the reconstruction and identification efficiency, as well as energy calibrations.

Leptons

Efficiency scale factors are used to correct the modeling of electrons and muons in simulation with respect to data. These comprise electron identification and muon reconstruction scale factors as well as the scale factors applied to correct for differences in the trigger efficiencies between data and simulation. Each of these scale factors comes with a corresponding uncertainty which encompasses both statistical and systematic effects. For example, a breakdown of the relative sources of uncertainty on the efficiency scale factor for *Medium* muons is shown in Figure 7.25. To propagate these uncertainties to the final signal prediction, each lepton scale factor is varied up and down by one standard deviation, and the corresponding change in the expected number of signal events is taken as a systematic uncertainty.
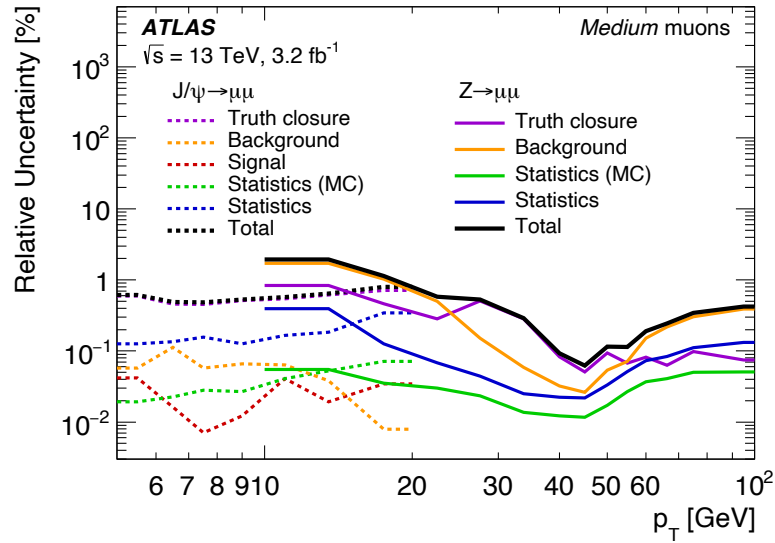
Figure 7.25: Total uncertainty in the efficiency scale factor for *Medium* muons as a function of the p_T of the muon in $Z \to \mu\mu$ and $J/\Psi \to \mu\mu$ events. Image taken from Ref [143].

The uncertainties associated with the correction factors applied to calibrate lepton energy scale and resolution must also be taken into consideration. To assess the impact of these uncertainties on the final signal yield, modified lepton containers are created for signal MC which correspond to up and down variations of groups of calibration parameters with respect to their nominal values. For each variation, the final signal yield is computed, and the sum in quadrature of all variations is taken as a systematic uncertainty on the

yield. For both electrons and muons, these variations are found to have a sub-percent level effect on the expected signal yield.

Jets

For jets, the uncertainties from the JES and JER calibrations are considered. Figure 7.26 shows the jet energy scale systematic uncertainty components, and Figure 7.27 shows the relative jet energy resolution as a function of p_T for fully calibrated jets along with the absolute uncertainty on the relative jet energy resolution. Similar to the uncertainties originating from the lepton calibrations, these uncertainties are propagated to the final signal yield by a set of varied jet containers which correspond to up and down variations of groups of calibration parameters. The quadrature sums of these variations for each JES and JER are taken as a systematic uncertainty on the final signal yield. The applicability
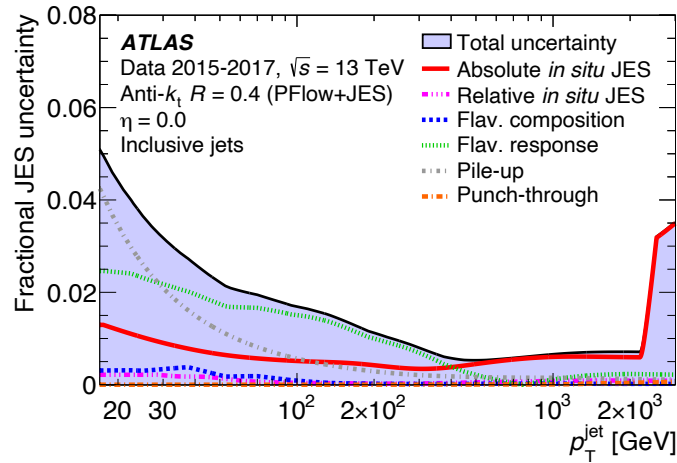
Figure 7.26: Fractional jet energy scale systematic uncertainty components for anti-kt $R = 0.4$ jets as a function of jet p_T at $\eta = 0$. The total uncertainty, determined as the quadrature sum of all components, is shown as a filled region topped by a solid black line. Image taken from Ref [138].

of the standard jet calibration scheme to the displaced jets considered in this analysis has been studied and found to be satisfactory [190], indicating that no additional uncertainties are needed to account for effects from jet displacement.
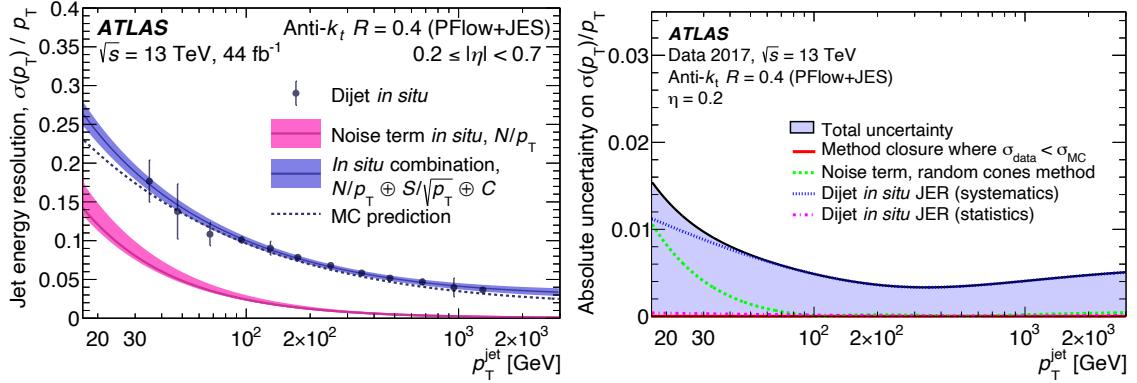
Figure 7.27: (left) The relative jet energy resolution as a function of p_T for fully calibrated PFlow+JES jets. The error bars on points indicate the total uncertainties on the derivation of the relative resolution in dijet events, adding in quadrature statistical and systematic components. The expectation from Monte Carlo simulation is compared with the relative resolution as evaluated in data through the combination of the dijet balance and random cone techniques. (right) Absolute uncertainty on the relative jet energy resolution as a function of jet p_T. Uncertainties from the two in situ measurements and from the data/MC simulation difference are shown separately. Image and caption taken from Ref [138].

7.3.2   Uncertainties on non-standard reconstruction

The dominant uncertainty is due to the difference in performance of both the standard and large radius tracking algorithms between data and MC. For standard tracking, this uncertainty is known to be around 2% [191]. To assess the systematic uncertainty of the ID vertex reconstruction efficiency due to the modeling of the large-radius tracking, the rates of displaced vertices consistent with $K_S^0 \to \pi^+\pi^-$ decays are compared between data and Z+jets simulation. The uncertainty is estimated by examining the variations between data and simulation in the K_S^0 yield.

From the preselected events, candidate K_S^0 vertices are identified by requiring that the vertices pass the vertex preselection, have exactly two tracks of opposite charge, and have an invariant mass in the region 450 to 550 MeV. The kinematic distributions of candidate K_S^0 vertices are compared between data and MC and are found to have good agreement within statistical uncertainties, as shown in Figure 7.28.

Tracks originating from a K_S^0 decay can be reconstructed by either the standard tracking or the LRT algorithm. The MC is normalized such that the number of K_S^0 vertices inside the beampipe ($L_{xy} < 23.5$ mm) is the same between data and simulation. This accounts

(a) $n_{\mathrm{trk,LRT}}$

(b) p_{T}

(c) m

(d) L_{xy}
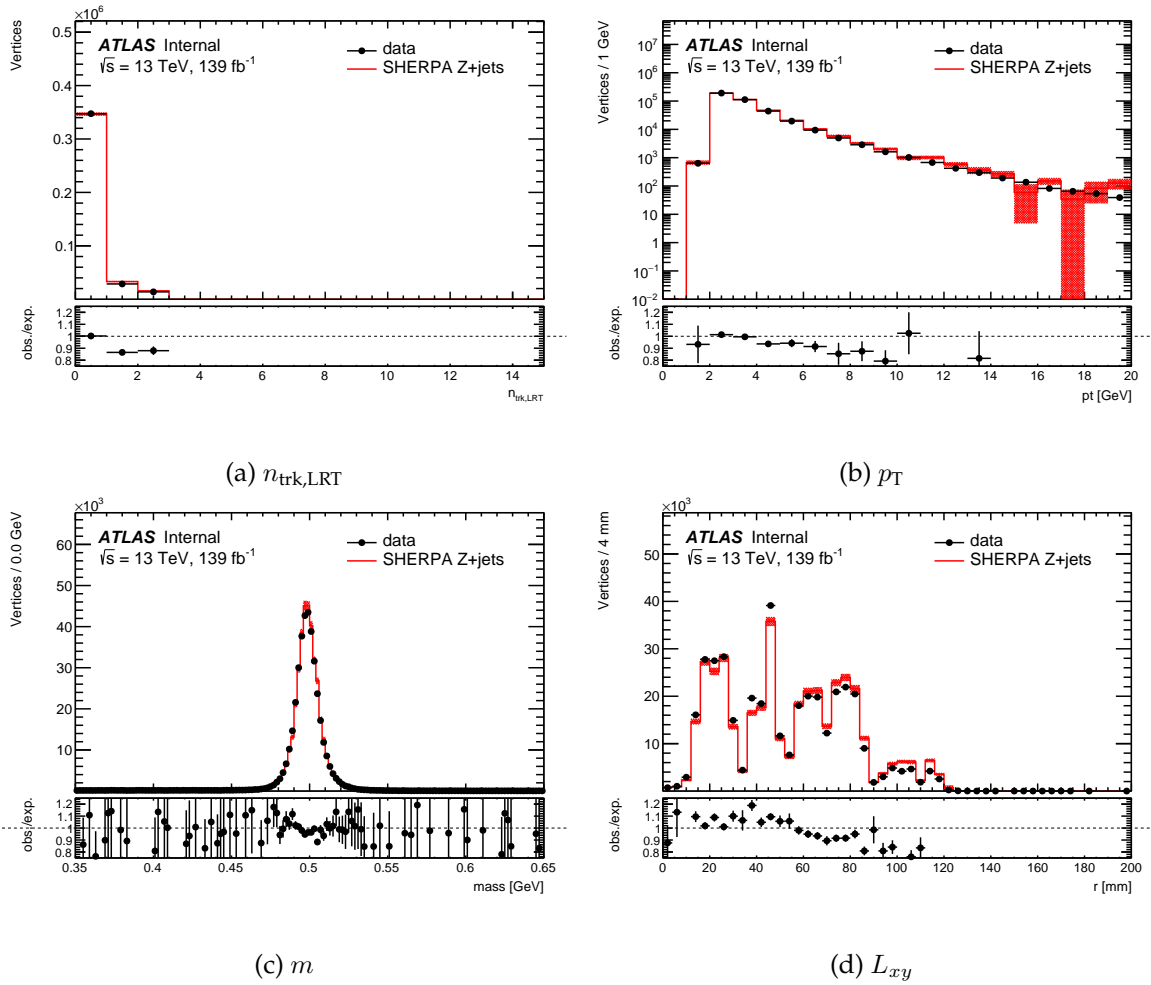
Figure 7.28: The kinematic distributions of candidate K_{S}^0 vertices in data and Z+jets MC.

(a) K_0^S yield

(b) Per-track uncertainty
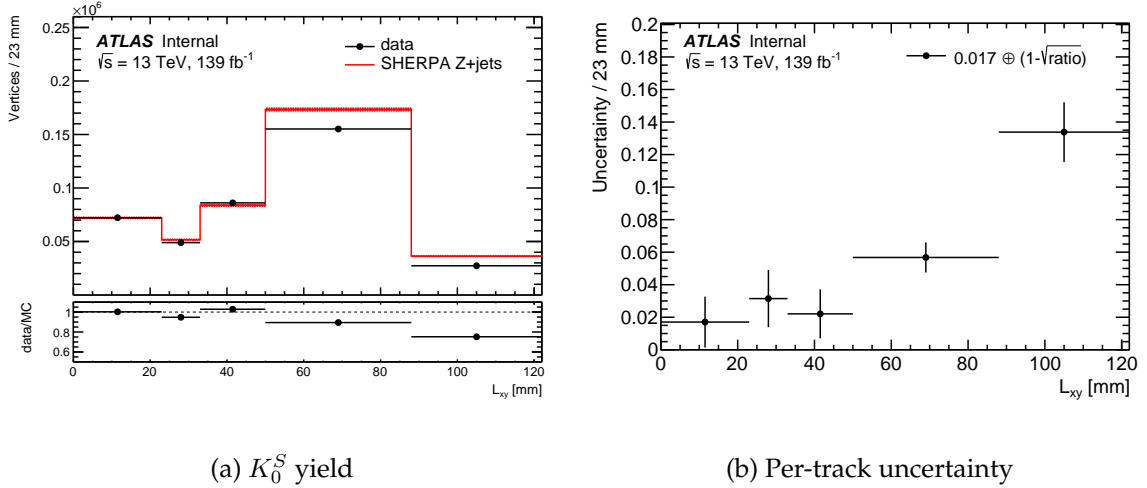
Figure 7.29: (a) The yield of candidate K_S^0 vertices as a function of L_{xy}. The MC is normalized such that the yield of candidate K_S^0 vertices inside the beampipe is equal to the yield in data. (b) The per-track uncertainty computed from the data/MC ratio.

for any differences that may exist between data and simulation in the total number of K_S^0 decays in a region where tracking uncertainties are well understood.

The vertex yields of K_S^0 are then compared between data and the normalized MC in 5 bins of L_{xy} ranging from 0 to the radius of the last pixel layer (122 mm). After this radius there are negligible statistics. The ratio quantifies the discrepancy between data and MC in the number of K_S^0 vertices reconstructed from tracks outside of the beampipe. To compute a per-track uncertainty, we take the square root of the deviation from unity (motivated by the fact that K_S^0 vertices are two-track vertices), which is then summed in quadrature with the 1.7% uncertainty on the standard tracking. The yields and per-track uncertainty are shown in Figure 7.29. To ensure that there is residual p_T dependence in the uncertainty, we reweight the K_0^S p_T distribution in MC such that the L_{xy} distributions agree between data and MC. As shown in Figure 7.30, the reweighted p_T distributions are in good agreement.

To propagate this uncertainty to the signal yield, tracks are randomly removed from reconstructed vertices with a probability given by the per-track uncertainty corresponding to the L_{xy} position of the vertex. The difference between the yield of vertices passing the full signal vertex selection is then compared between the nominal and modified vertex collections as a function of L_{xy}. To mitigate again statistical effects, the 10 mm, 100 mm, and 1000 mm samples are combined for each mass point. This is shown in Figure 7.31.
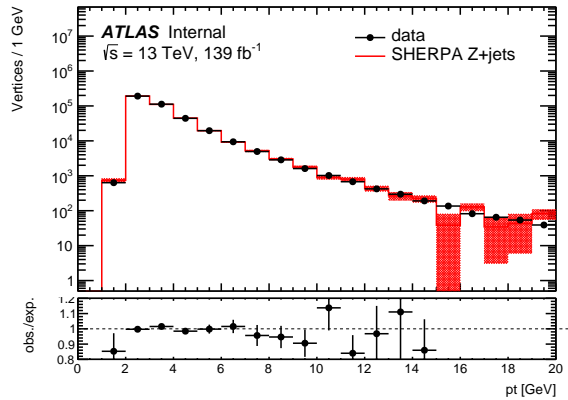
Figure 7.30: The reweighted p_T distributions
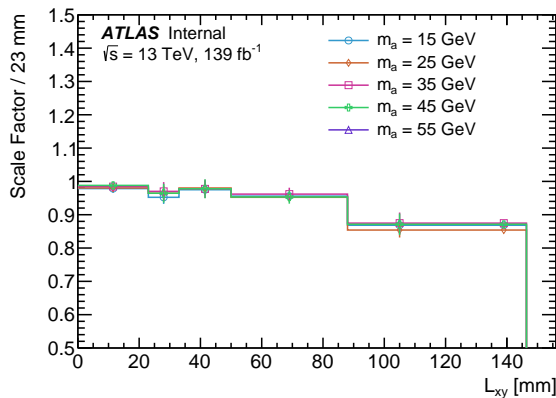
Figure 7.31: The per-vertex signal uncertainty computed by taking the ratio of the modified to the nominal vertex yields.

The decay position of the LLPs at truth level is then used to compute an scale factor for the reconstruction efficiency of each LLP. The scale factors corresponding to each LLP are multiplied together to obtain a per-event efficiency correction scale factor. The difference between the efficiency computed with the scale factors applied and the nominal selection efficiency is taken as the systematic uncertainty. This uncertainty is largest for small values of m_a and increases with the scalar proper lifetime up to a maximum value of 17%. This uncertainty is shown in Figure 7.32

An alternate approach was also tested in which tracks are removed in a fully correlated fashion, which effectively removed entire vertices with a probability given by the data/MC ratio in Figure 7.29. This method results in a considerably larger uncertainty, as shown in Figure 7.33. The statistical analysis described in Section 8.3 was found to be unaffected by this larger uncertainty. Because this approach will give an overestimate of the uncertainty
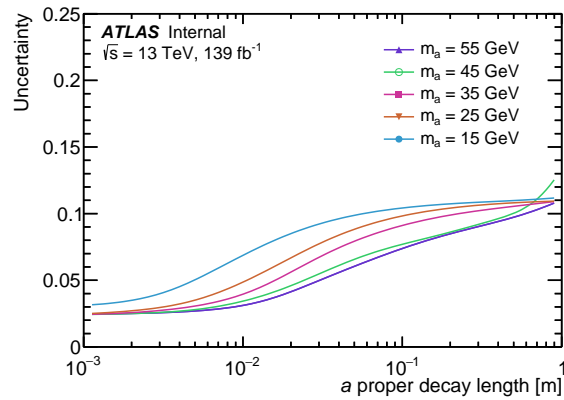
Figure 7.32: The vertex reconstruction uncertainty as a function of $c\tau$.
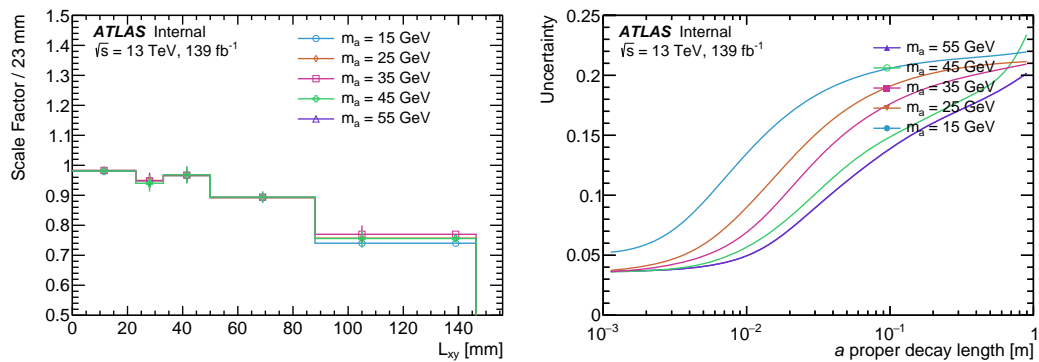
Figure 7.33: The vertex reconstruction uncertainty as a function of $c\tau$ when a fully correlated track removal is performed.

on the vertex reconstruction efficiency, it was chosen to not be adopted by the analysis.

Potential sources of uncertainty on the vertex selection are also investigated. In particular, due to the fact that the material veto is derived predominantly from data it is possible that simulated material interactions in signal MC will not be fully removed by this veto and artificially increase the signal acceptance. To quantify this effect, vertices passing the full signal selection are separated into two categories: vertices which are matched to a true LLP decay vertex, and vertices which are not matched to any true decay vertex. Simulated material interactions will fall into the second category. The vertices are then plotted as a function of L_{xy} to determine if there is any correlation between vertices that are not matched to any truth decay and the location of known detector elements. As shown in Figure 7.34, the fraction of vertices passing the full signal vertex selection that are not matched to a true LLP decay is very small, and there is no noticeable correlation between their position in L_{xy} and the densest material layers. Thus, from this we conclude that there is no systematic effect on the signal acceptance due to the material veto.
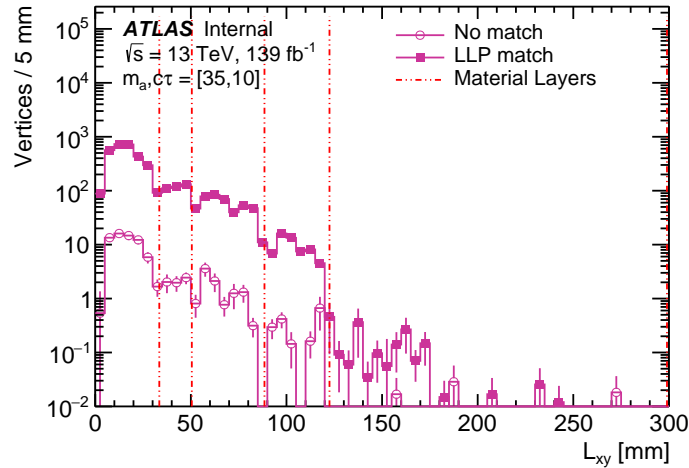
Figure 7.34: The L_{xy} distribution for vertices which pass the full signal selection.

7.3.3 Theory and signal modeling

An uncertainty of $\pm 4\%$ and $\pm 25\%$ is assumed for the total qqZH and ggZH, $H \rightarrow 2a \rightarrow 4b$ cross section, respectively [50]. These uncertainties include effects from varying the factorization and renormalization scales, the PDF and α_s. To determine the uncertainty due
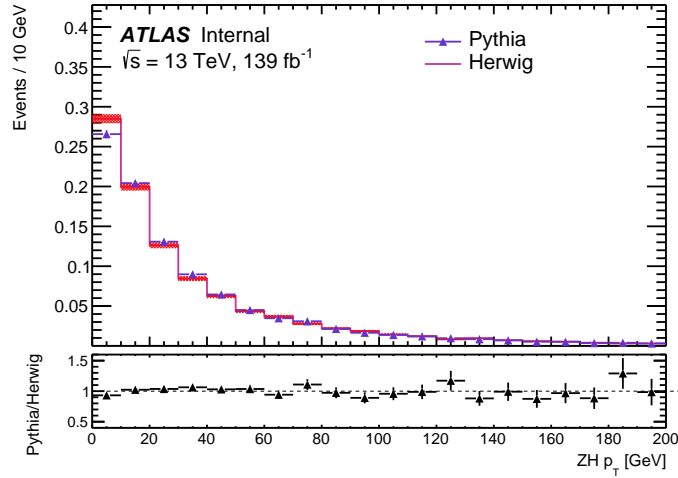
Figure 7.35: Comparison of the p_{T} spectra of the ZH system when considering Pythia8 or Herwig7 parton showers.

to the choice of parton shower, the nominal Pythia8 samples are compared to a reference Herwig7 sample of ZH production. The p_{T} of the ZH system is compared between the two samples as shown in Figure 7.35. To propagate the slight differences observed to the signal acceptance, the ratio of the unit-normalized distributions is used to derive per-event weights which are applied to the Pythia8 signal samples. The difference in acceptance after reweighting the p_{T} of the ZH system to the reference Herwig sample is found to be on the order of 0.5% and is included as and additional systematic uncertainty on the signal modeling.

7.3.4 Other sources of systematic error

Simulated events are reweighted such that the distribution of the average number of interactions per bunch crossing matches the distribution measured in data. The difference between predicted and measured inelastic cross-section [192], on which the measurement of interactions per bunch crossing depends, is propagated into simulation by a systematic variation of the reweighted distribution. Figure 7.36 shows the reweighted distributions of the mean number of interactions per bunch crossing ($\langle \mu \rangle$) in MC using both the nominal pileup weights, as well as the $\pm 1\sigma$ variations. The signal yields are then computed using each set of weights, and the largest difference from the nominal is taken as an additional systematic uncertainty for each sample.
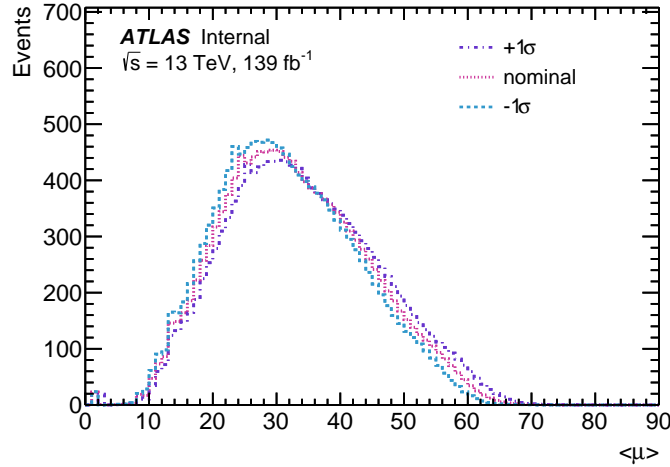
Figure 7.36: Distribution of the mean number of interactions per bunch crossing ($\langle\mu\rangle$) in MC using both the nominal pileup weights, as well as the $\pm1\sigma$ variations.

Uncertainties associated with the displaced-jet filter are considered. The dominant contribution to the uncertainty originates from the use of uncalibrated jets in the filter. This uncertainty is estimated by increasing the jet p_T criteria in the filter from 20 to 25 GeV and calculating the change in filter efficiency on simulated signal samples. The choice of 5 GeV is motivated by studying the difference in efficiency of the uncalibrated jet p_T selection as a function of calibrated jet p_T between data and simulation. This is shown in Figure 7.37 below.

Finally, the expected number of signal events is subject to the uncertainty on the total integrated luminosity of the data sample used, as described in Section 6.2. The uncertainty in the combined 2015–2018 integrated luminosity is 1.7% [193], obtained using the LUCID-2 detector [194] for the primary luminosity measurements.

7.3.5 Summary of uncertainties

A summary of the systematic uncertainties is given in Table 7.9. With the exception of the uncertainty on LRT and the displaced jet filter, the systematic uncertainties are not observed to vary significantly with m_a or $c\tau_a$ and are thus computed from the weighted average across samples.
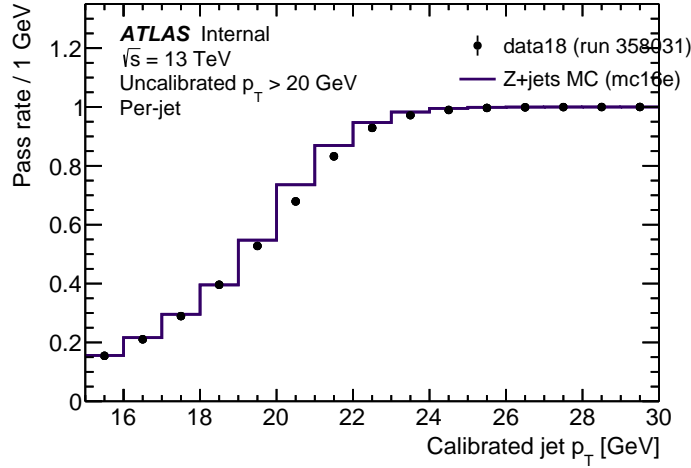
Figure 7.37: The fraction of jets passing a cut on uncalibrated p_T of 20 GeV, as a function of calibrated p_T for data and Z+jets simulation.

Source	Uncertainty (%)
Theory	4.7
Luminosity	1.7
Pileup reweighting	2.6
Electron identification	1.6
Electron calibration	0.4
Muon reconstruction	0.9
Muon calibration	0.4
Electron trigger	0.7
Muon trigger	1.3
Jet energy scale	1.4
Jet energy resolution	1.3
Filter	2.8-3.8
LRT	2.4-12
Total	7.4-14

Table 7.9: Summary of all systematic uncertainties considered in the analysis. The values in the table are percent uncertainties on the final signal yield. With the exception of the uncertainties on LRT and the displaced jet filter, no significant dependence on m_a or $c\tau_a$ is observed, so the quoted values are those derived from averaging over the different masses and lifetimes. The uncertainty on the displaced-jet filter was found to be uncorrelated with lifetime but increase with m_a, so the quoted values are derived from averaging over the different lifetimes and the range represents the minimum and maximum observed values corresponding to $m_a = 15$ GeV and $m_a = 55$ GeV. The range of values for the LRT and total uncertainties represent the minimum and maximum observed values across the five masses at $c\tau_a = 1$ mm and $c\tau_a = 1$ m.

Chapter 8

Results

The great tragedy of science–the slaying of a beautiful hypothesis by an ugly fact.

-Thomas Huxley

As described in Section 7.2.2, the method used to estimate the number of events in the SR from background has been shown to be robust, and a final background estimate and corresponding uncertainty have been derived. The analysis may then proceed to **unblind**, or reveal the data that populates the signal region. This chapter will describe the unblinded results and the methods used to interpret them. First, the unblinded signal region is shown in Section 8.1. Section 8.2 gives an overview of the theory behind the method used to interpret the observed data, and then in Section 8.3, this theory is applied to this search. The results are discussed and compared to the constraints set by previous searches at the LHC.

8.1   Unblinded results

As described in Section 7.2, the number of background events predicted in the SR is 1.30 ± 0.08 (stat.) ± 0.27 (syst.). The DV multiplicity for signal and data is shown in Figure 8.1 for the unblinded SR with $n_{\mathrm{DV}} \geq 2$. Zero events are observed in this region. Computing the 68% quantile on zero observed events gives an upper limit of 1.83 events, which is shown as an error bar on the third bin containing all events with $n_{\mathrm{DV}} \geq 2$. Thus, we may claim that the background prediction is in good agreement with the number of observed events in the signal region. Given that no excess of signal-like events is observed, we may place
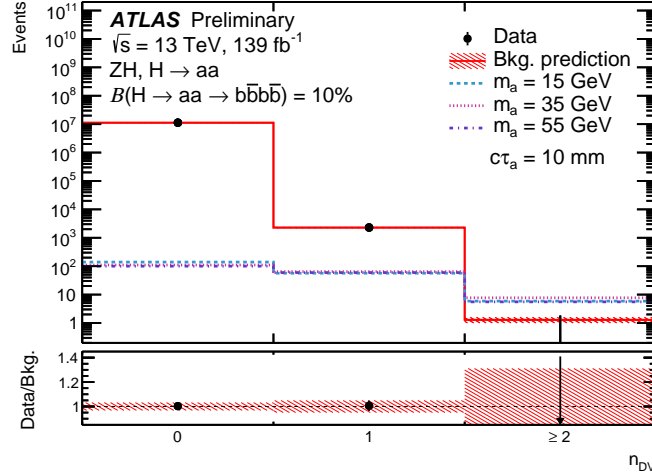
Figure 8.1: DV multiplicity among preselected events for signal (dashed lines), background prediction (solid line), and data (black points). The bins corresponding to $n_{DV} = 0$ and $n_{DV} = 1$ comprise the CR which is used to derive the background estimate. The third bin is the SR and contains all events with $n_{DV} \geq 2$. The shaded bands represent the combined statistical and systematic uncertainty on the prediction. Signal distributions are normalized assuming $\mathcal{B}(H \to aa \to b\bar{b}b\bar{b}) = 10\%$.

constraints on the branching ratio of Higgs decays to pairs of LLPs. The remainder of this chapter is dedicated to describing the procedure for setting these exclusion limits, and the final results we obtain after applying such a procedure to this search.

8.2   Statistics

After performing an analysis such as the one described in this thesis, a statistical analysis must be performed in order to interpret the results. This boils down to determining which of two **hypotheses** are most consistent with the observed data. Simply put, a hypothesis is a statement that is either true or false. For example "The Higgs boson decays to pairs of long lived scalars of mass 15 GeV and mean proper lifetime 10 mm with a 10% branching ratio". More formally, if $\mathbf{x}$ is the outcome of our experiment, a hypothesis H is a statement for the probability to find the data $\mathbf{x}$. We write $P(\mathbf{x}|H)$ for the probability to find data $\mathbf{x}$ under assumption of the hypothesis H. The first hypothesis, H_0, is called the **null hypothesis**. In high-energy physics terminology, this corresponds to the background-only (B) hypothesis. The second hypothesis, H_1, is called the **alternate hypothesis**. This corresponds to the signal-plus-background (S+B) hypothesis. Roughly speaking, claiming a

discovery is a statement that the observed data are incompatible with the background-only hypothesis.

In this section, we will describe the theory behind the statistical analysis used to interpret the results of the analysis presented in this thesis. Section 8.2.1 defines the likelihood function and describes how to build a statistical model to describe searches for new physics analysis. Section 8.2.2 then defines the concept of hypothesis testing and how test statistics are used to compute p-values. Finally 8.2.3 describes the procedure used to set limits on signal models when the background-only hypothesis can not be excluded. The theoretical discussion in this section is based primarily on that of Refs [195]–[197].

8.2.1 The likelihood function

To begin our discussion, let us introduce a concrete example. Consider a simple "counting experiment" in which the data $\mathbf{x}$ consists of a single number n_{obs}. Under the signal-plus-background hypothesis, the number of predicted events from our experiment may be written as

$$n_{\text{pred}} = \mu s + b \tag{8.1}$$

where s is the predicted signal yield, b is the predicted background yield, and μ is the **signal strength** which might represent the signal production cross-section or branching ratio. In the language of statistics, μ is the **parameter of interest (POI)** that differentiates our two hypotheses H_0 and H_1. The background-only hypothesis is obtained by letting $\mu = 0$.

The probability to observe n_{obs} events assuming our prediction is given by the Poisson distribution:

$$P(n|\mu) = \frac{(\mu s + b)^n}{n!} e^{-(\mu s + b)} \equiv Pois(n|\mu s + b) \tag{8.2}$$

This is an example of a **probability density function (PDF)**. More generally, a PDF is a function of the data $f(\mathbf{x})$ that satisfies

$$\int f(\mathbf{x})d\mathbf{x} = 1 \tag{8.3}$$

If our model depends on some parameter α, we often write the PDF as $f(x|\alpha)$, read "f of x given α". If we evaluate $f(x|\alpha)$ with the observed data and treat it as a function of α, we obtain the **likelihood function** $\mathcal{L}(\alpha)$. The likelihood function is the probability of the observed data, seen as a function of the model parameter(s). According to the **likelihood principle**, the likelihood function contains all the information from the experiment that is relevant to inferences about value of the model parameters. For the example in Equation 8.1, we have

$$\mathcal{L}(\mu) = Pois(n_{\text{obs}}|\mu s + b) \tag{8.4}$$

So far our likelihood $\mathcal{L}(\mu)$ assumes an idealized experiment with a single parameter μ which is not particularly representative of a true high-energy physics experiment. In order to incorporate the uncertainties on the number of signal and background events into our hypothesis test, we need to include a set of **nuisance parameters (NPs)**, θ into our model. The nuisance parameters will affect the number of predicted events in our counting experiment by modifying the expected signal and background yield:

$$n_{\text{pred}} = \mu s \theta_s + b \theta_b \tag{8.5}$$

The nuisance parameters each have their own PDF which must then be included in the likelihood function. For the NPs in the above example, the PDFs are usually assumed to be Gaussian with a width given by the corresponding uncertainty. For example, if our experiment has a 20% uncertainty on the number of predicted background events, the PDF describing θ_b will be a Gaussian with $\sigma_b = 0.2$. Our likelihood function then becomes

$$\mathcal{L}(\mu, \theta) = Pois(n_{\text{obs}}|\mu s \theta_s + b \theta_b) \cdot Gaus(\tilde{\theta}_s|\theta_s, \sigma_s) \cdot Gaus(\tilde{\theta}_b|\theta_b, \sigma_b) \tag{8.6}$$

where $\tilde{\theta}_s$ and $\tilde{\theta}_b$ are the **global observables** corresponding to our NPs. The nuisance parameter PDFs are often referred to as **constraints**. Generally speaking, a nuisance parameter is any parameter in the model other than the parameter of interest. The nuisance parameters affect the measurement, so we must account for them even though we are not interested in them directly.

We have now written down the full likelihood for a simple counting experiment with uncertainties on the predicted number of signal and background events. Although this is a simple model, it can be used to describe a wide range of realistic high-energy physics experiments, including the one presented in this thesis! We will see how the likelihood enters in to the actual statistical inference in the following sections.

8.2.2 Hypothesis tests

Armed with our likelihood function, we may now begin to test our two hypotheses. In frequentist statistics, we perform a **test** of H_0 by defining a subset of data space w called the **critical region** such that for some small value α, the probability of observing the data in that region is less than α. More compactly, the critical region satisfies

$$P(\mathbf{x} \in w | H_0) \leq \alpha. \tag{8.7}$$

Figure 8.2 shows schematically how the critical region is defined. A standard convention in high-energy physics is to let $\alpha = 0.05$. The **p-value** of a hypothesis H is the probability assuming H to have observed the data in the critical region. If the data are observed in w, or equivalently, the p-value of H_0 is found to be less or equal to α, then we conclude that the hypothesis H_0 is rejected. The p-value may be translated into an equivalent quantity called the **significance** Z, given by

$$Z = \Phi^{-1}(1 - p) \tag{8.8}$$

where Φ^{-1} is the inverse of the cumulative standard Gaussian distribution. A significance of $Z = 5$ is the gold-standard for claiming a discovery in high-energy physics, corresponding to a p-value of 2.9×10^{-7} for the background only hypothesis.

More concretely, in order to determine the critical region we need to define a **test statistic**. The test statistic may be thought of as a function q that maps the data $\mathbf{x}$ to a single real-valued number $q(\mathbf{x})$. This allows the critical region to be defined in terms of a single real-valued number q_α:

$$\alpha = P(q(\mathbf{x}) \geq q_\alpha | H_0) \tag{8.9}$$
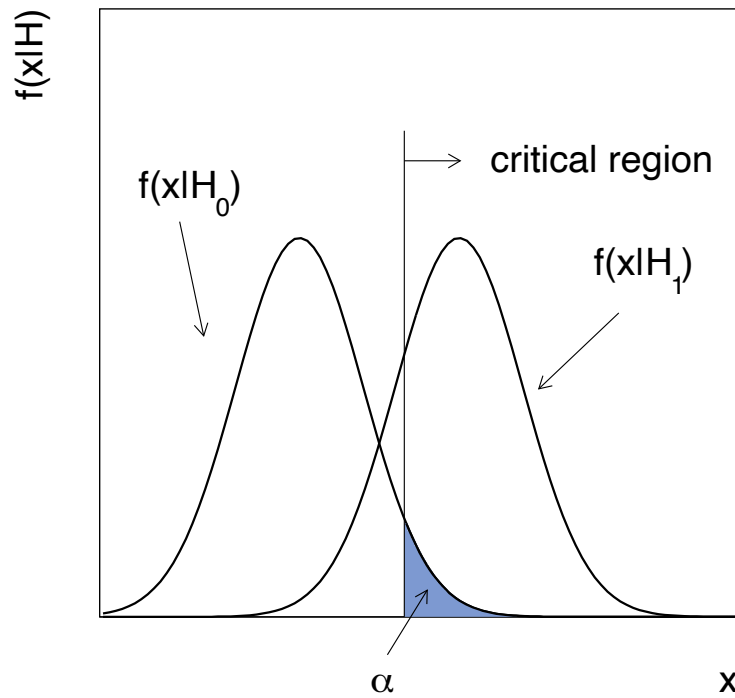
Figure 8.2: The critical region for a hypothesis test. Image taken from Ref [195].

The value α is called the **size** of the test, and it specifies the probability that the null hypothesis will be rejected when it is in fact true. Similarly, we may define β to be the probability that our test accepts the null hypothesis when the alternate is true

$$\beta = P(q(\mathbf{x}) < q_\alpha | H_1) \tag{8.10}$$

The quantity $1 - \beta$ is called the **power** of the test, and clearly represents the probability to *reject* the null hypothesis if the alternate is true.

The Neyman-Pearson lemma [198] states that if H_0 is the null hypothesis and H_1 is the alternate hypothesis, then the most powerful test statistic (assuming no systematics) is the likelihood ratio

$$\frac{\mathcal{L}(H_1)}{\mathcal{L}(H_0)} \tag{8.11}$$

The Neyman-Pearson lemma can be generalized to the case when systematics are included in our likelihood function by defining the **profile likelihood ratio**.

$$\lambda(\mu) = \frac{\mathcal{L}(\mu, \hat{\hat{\theta}}_\mu)}{\mathcal{L}(\hat{\mu}, \hat{\theta})} \tag{8.12}$$

Here, $\hat{\mu}$ and $\hat{\theta}$ are called the **maximum likelihood estimates (MLEs)** and are the values of the parameters that globally maximize the likelihood. The $\hat{\hat{\theta}}_\mu$ parameters in the numerator are called the **profiled** values of the nuisance parameters θ and are the values of θ that maximize $\mathcal{L}(\mu, \theta)$ *for the specified value of* μ. The profiled values of θ are also called the **conditional maximum likelihood estimates (CMLEs)**. The most commonly used test statistic for setting limits is the one-sided profile-likelihood test statistic, q_μ:

$$q_\mu = \begin{cases} -2\ln\lambda(\mu) & \hat{\mu} \leq \mu, \\ 0 & \hat{\mu} > \mu \end{cases} \tag{8.13}$$

In this thesis, it will be assumed that when referring to the test statistic, we are referring to the definition of q_μ in Equation 8.13.

8.2.3 Confidence intervals and the CL$_s$ Method

If our analysis is unable to reject the background-only hypothesis, we can still test various signal-plus-background hypotheses to determine whether or not they are compatible with the observed data. Consider a test of size α. The values of μ that are are not rejected define a **confidence interval** with a **confidence level** of CL $= 1 - \alpha$. In high energy physics, the standard convention is to let $\alpha = 0.05$ so that confidence intervals are reported with a confidence level of 95%. The highest value of μ that we do not reject is then called the **upper limit** of μ at 95% CL and will be denoted here as μ_{up}.

Given the test statistic, we may compute the p-values for the two hypotheses from their respective PDFs $f(q|H)$. For the signal plus background hypothesis H_1, we have

$$p_\mu = P(q_\mu \geq q_\mu^{\text{obs}} | \text{signal} + \text{background}) = \int_{q_\mu^{\text{obs}}}^\infty f(q_\mu | \mu, \hat{\theta}_\mu^{\text{obs}}) dq_\mu \tag{8.14}$$

For the null, background only hypothesis H_0, we have

$$1 - p_b = P(q_\mu \geq q_\mu^{\text{obs}}|\,\text{background-only}) = \int_{q_0^{\text{obs}}}^{\infty} f(q_\mu|0, \hat{\theta}_0^{\text{obs}})dq_\mu \qquad (8.15)$$

A standard frequentist 95% CL confidence interval is then obtained by solving for $p_\mu = 0.05$. Confidence levels derived in this way are often labeled $\text{CL}_{\text{s+b}}$. However, the $\text{CL}_{\text{s+b}}$ approach has undesirable pathologies. If the number of observed events fluctuates far below the expected background, the value of p_μ will be very small even for arbitrarily small signal sensitivities. Because the frequentist procedure will reject a signal hypothesis if the p-value is found to be less than $\alpha = 0.05$, we are bound to reject models to which we have little to no sensitivity. But if we have no sensitivity to a particular model, our measurement can not justify this exclusion! To avoid this pathology, several experiments at the LHC have adopted the **modified frequentist method** called CL_{s} [199]. The CL_{s} metric is defined as

$$\text{CL}_{\text{s}} = \frac{p_\mu}{1 - p_b} \qquad (8.16)$$

In the modified frequentist approach, downward fluctuations will lead to larger values of p_b, and hence larger values of CL_{s}, thereby preventing spurious exclusions.

The modified frequentist 95% CL upper limit on μ is obtained by solving for $\text{CL}_{\text{s}} = 0.5\%$. In order to compute the p-values in Equations 8.14 and 8.15, we must evaluate several complicated integrals. Under certain conditions, these integrals may be evaluated directly using the so-called asymptotic approximation [200]. However, in the scenario in which the number of background events is small (as is the case in this thesis) these approximations do not hold in general. Thus, the integrals must be performed numerically using "Toy" Monte Carlo techniques. In the Toy Monte Carlo approach, we generate **pseudoexperiments** in which the model parameters are sampled from the total PDF of the model to obtain the value of the test statistic. Figure 8.3 shows two example distributions of the profile likelihood test statistic generated using pseudoexperiments for the counting experiment we have been considering for $\mu = 0.1$ and $\mu = 0.05$. Here, we have let $s = 100$, $b = 10$, $\sigma_s = 0.1$, and $\sigma_b = 0.2$. The p-values may then be easily computed by numerically integrating the toy distributions using the observed value of the test statistic q_μ^{obs}. For
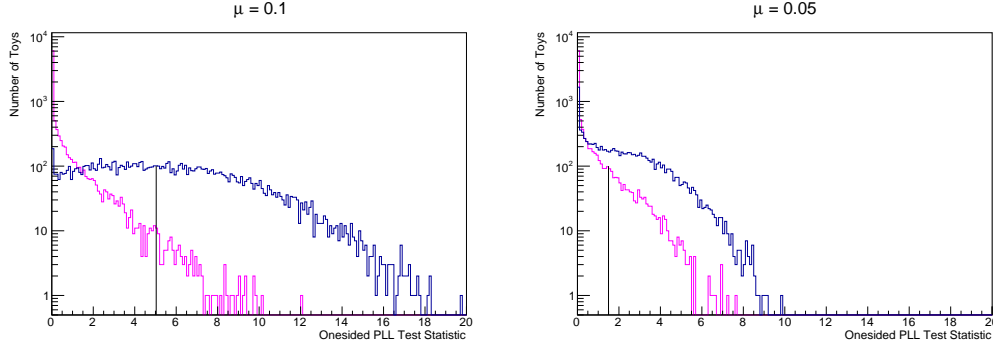
Figure 8.3: The distributions of the one-sided profile likelihood test statistic generated using toy Monte Carlo pseudoexperiments for $\mu = 0.1$ (left) and $\mu = 0.05$ (right). The alternate hypothesis is shown in pink, and the null hypothesis is shown in blue. The observed value of the test statistic is shown with a vertical black line.

$\mu = 0.1$, we have $n_{\mathrm{pred}} = \mu s + b = 20$ and $q_\mu^{\mathrm{obs}} = 5.0$. From Equations 8.14 and 8.15 we find $p_\mu = 0.014$ and $1 - p_b = 0.59$. Thus, $\mathrm{CL_s} = 0.024$, meaning that we may exclude the signal hypothesis with $\mu = 0.1$ at 95% CL. For $\mu = 0.05$, we have $n_{\mathrm{pred}} = \mu s + b = 15$ and $q_\mu^{\mathrm{obs}} = 1.5$. For this experiment we find $p_\mu = 0.12$, and $1 - p_b = 0.53$. Thus, $\mathrm{CL_s} = 0.23$, meaning that for our experiment does not have sufficient sensitivity to exclude this signal hypothesis.

By performing the above procedure for a range of values of μ, we may compute μ_{up} by finding the highest value of μ that we do not reject. Figure 8.4 shows the p-values for $\mathrm{CL_b}$, $\mathrm{CL_{s+b}}$, and $\mathrm{CL_s}$ for a range of values of μ computed for our simple counting experiment. Using this simple model, the computed upper limit on μ is 0.089. So far in this section, we have been describing how to compute the upper limits using the observed data. Figure 8.4 also shows the **expected limit** and its associated ± 1 and 2σ error bands. The expected limit is the upper limit we would expect to obtain if the background-only hypothesis is true. It is computed using the PDF $f(\mu_{\mathrm{up}}|0, \hat{\theta}_0^{\mathrm{obs}})$ by taking the median value of the upper limits obtained. A somewhat peculiar feature of the expected limit is that it depends on the profiled values of the nuisance parameters derived from the observed data, which has led some to pursue alternative approaches to limit setting [201][1]. The values of μ corresponding to $\pm 1\sigma$ deviations from the median are denoted $\mu_{\pm 1}$ and are computed

---

[1]In particular, the Bayesian approach makes use of our prior belief in the scale and description of the uncertainties on signal and background event yields, rather than fitting them to the observed data.
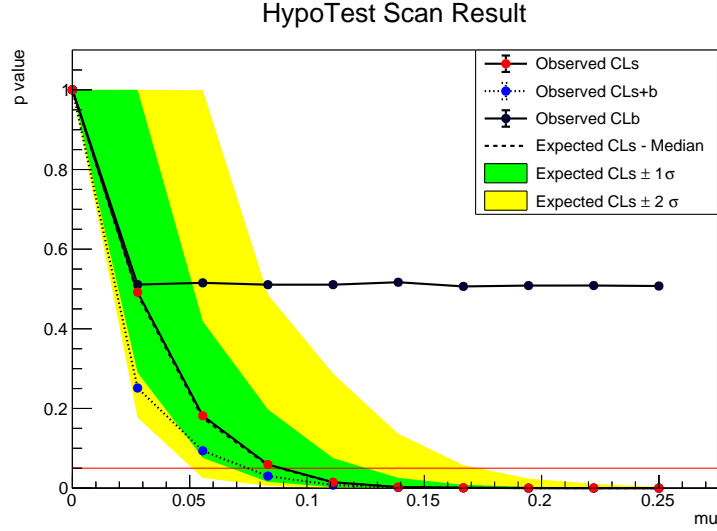
Figure 8.4: The CL_s scan for the counting experiment described in the text. The upper limit μ_{up} is obtained by finding the intersection between the CL_s curve and the red line at $p = 0.05$.

from

$$\int_0^{\mu_{\pm 1}} f(\mu_{up}|0, \hat{\theta}_0^{obs})d\mu_{up} = \Phi^{-1}(\pm 1) \tag{8.17}$$

where Φ^{-1} is the inverse of the cumulative distribution of the Gaussian. The $\pm 1\sigma$ errors are usually drawn as a dark green band around the median expected limit, as shown in Figure 8.4. The $\pm 2\sigma$ band is similarly computed from

$$\int_0^{\mu_{\pm 2}} f(\mu_{up}|0, \hat{\theta}_0^{obs})d\mu_{up} = \Phi^{-1}(\pm 2) \tag{8.18}$$

This band is usually drawn in yellow, giving the expected limit plot the characteristic "Brazilian flag" appearance.

We have now outlined the recipe needed to find the observed and expected limits for a given experiment. For completeness, this recipe is summarized below.

1. Construct the likelihood function $\mathcal{L}(\mu, \theta)$ where μ is the signal strength and θ is the set of nuisance parameters.

2. Construct the test statistic q_μ from the profile likelihood ratio

$$q_\mu = \begin{cases} -2\ln\lambda(\mu) & \hat{\mu} \le \mu, \\ 0 & \hat{\mu} > \mu \end{cases}$$

with

$$\lambda(\mu) = \frac{\mathcal{L}(\mu, \hat{\hat{\theta}}_\mu)}{\mathcal{L}(\hat{\mu}, \hat{\theta})}.$$

3. Compute the test statistic for the observed data q_μ^{obs}.

4. Generate pseudoexperiments to construct the PDF of q_μ under both signal-plus-background and background-only hypotheses.

5. From the generated distributions of q_μ, compute the p-values in Equations 8.14 and 8.15.

6. Determine the largest value of μ that satisfies

$$\text{CL}_{\text{s}} = \frac{p_\mu}{1 - p_b} < 0.05$$

This is the observed limit μ_{up}.

7. To derive the expected limit, take the median value of μ_{up} obtained through background-only toy MC pseudoexperiments and the PDF $f(\mu_{\text{up}}|0, \hat{\theta}_0^{\text{obs}})$.

8. Compute the ± 1 and $\pm 2\sigma$ error bands using the generated PDF for μ_{up}.

In the next section we will apply this machinery to the search for Higgs decays to LLPs.

8.3 Exclusion limits on $B(H \to aa \to b\bar{b}b\bar{b})$

We may now apply the recipe detailed above to the search presented in this thesis. In this section we will first derive the expected number of signal events as a function of $c\tau_a$ using a reweighting procedure. This allows us to compute exclusion curves of $B(H \to aa \to b\bar{b}b\bar{b})$ as a function of $c\tau_a$. The impact of systematic uncertainties on the final limits

are explored in a brief aside, and finally these results are then discussed and compared to existing constraints on $B(H \to aa \to b\bar{b}b\bar{b})$ set by previous searches at the LHC.

8.3.1   Lifetime reweighting

To extrapolate the signal efficiency to proper scalar lifetimes other than the generated values, a procedure known as **lifetime reweighting** is used which applies a weight to each event passing the analysis selection, which depends on the proper lifetimes of the LLPs in the event. To reweight from lifetime τ_1 to τ_2, the weight for the ith LLP is given by

$$w_i = \frac{\tau_1}{\tau_2} e^{-\left(\frac{1}{\tau_2} - \frac{1}{\tau_1}\right)t_i}$$

The total event weight is then simply the product of the weights for each LLP

$$w = w_1 w_2 = \left(\frac{\tau_1}{\tau_2}\right)^2 e^{-\left(\frac{1}{\tau_2} - \frac{1}{\tau_1}\right)(t_1 + t_2)}$$

For each mass point, events from all three generated lifetimes are used to mitigate against statistical dilution. In this procedure, a target lifetime sample is obtained by reweighting events from reference samples with lifetimes above and below the target lifetime. To reweight to lifetime τ_2 from reference samples with lifetimes τ_1 and τ_3 (where $\tau_1 < \tau_2 < \tau_3$) events from the τ_1 sample are used when the sum of the proper decay times t of the LLPs is less than the critical lifetime t_c, and events from the τ_3 sample are used when the sum of proper lifetimes is greater than the critical lifetime, where the critical lifetime is the point where the PDFs are equal:

$$t_c = \frac{2 \ln\left(\frac{\tau_3}{\tau_1}\right)}{\left(\frac{1}{\tau_1} - \frac{1}{\tau_3}\right)}$$

Figure 8.5 shows the exponential PDFs for the three generated values of $c\tau_a$ which shows how the critical lifetimes are computed. In each region, a partial efficiency is defined as

$$\epsilon_i = \frac{W_i}{N_i}$$
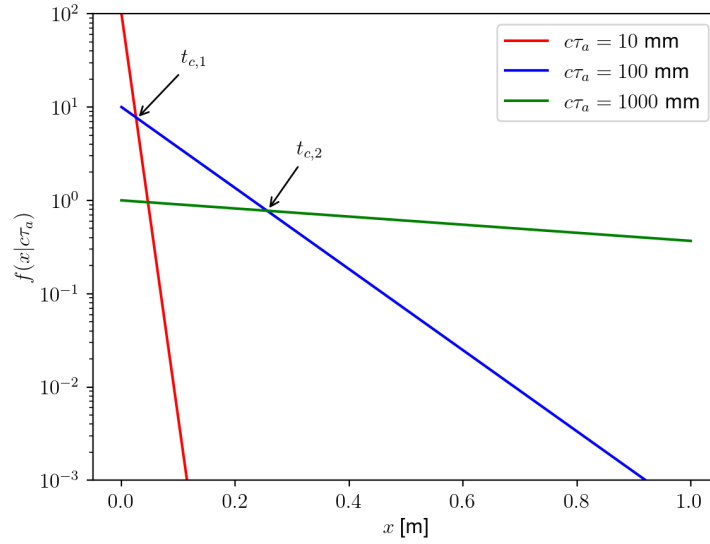
Figure 8.5: The exponential PDFs for the three generated values of $c\tau_a$. The critical lifetimes $t_{c,1}$ and $t_{c,2}$ are determined by finding the points at which the PDFs are equal.

where W_i is the sum of weights of the events passing the full analysis selection for the ith reference sample, and N_i is the number of entries in the ith reference sample. The weights are not included in the denominator as this has been shown to overestimate the efficiency when extrapolating to values of $c\tau$ larger than the generated mean proper lifetime. The overall efficiency is then computed by taking the sum of these partial efficiencies, as shown in Figure 8.6.

Applying the lifetime reweighting procedure to the full signal grid, we obtain the analysis selection efficiency as a function of $c\tau$ for each signal mass point. The efficiencies may then be scaled by the total ZH cross section and integrated luminosity to obtain the predicted number of signal events s. As shown in Figure 8.7, the selection efficiency peaks between $c\tau_a = 10$ and 20 mm, with expected signal yields of 50-75 events. To validate the extrapolated efficiency curves, we scale the curves by the total integrated luminosity multiplied by the ZH cross section to obtain the expected signal yield as a function of $c\tau$. The yields at 10, 100, and 1000 mm are then compared to the observed yields in the generated samples at each lifetime from Table 7.4. A comparison of the yields is shown in Table 8.1.
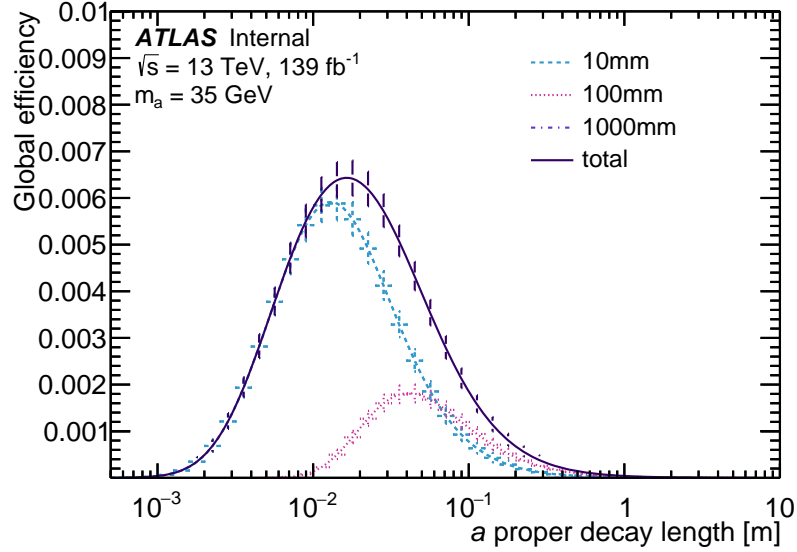
Figure 8.6: The partial and total efficiencies for $m_a = 35$ GeV.

8.3.2 Limits

As shown in Section 8.1, no excess of events over the predicted Standard Model background is observed. Thus, we are unable to exclude the background-only hypothesis or claim evidence of Higgs boson decays to long-lived scalar particles. Instead, we set exclusion limits on the branching ratio of the Higgs boson to pairs of long-lived scalars $B(H \rightarrow aa \rightarrow b\bar{b}b\bar{b})$.

After obtaining the number of predicted signal events as a function of $c\tau$, we may perform the CL_s procedure described in Section 8.2.3. We begin by establishing the probability model that will describe our experiment. The analysis is performed as a single bin counting experiment similar to the example described in Section 8.2.1. However unlike our simple example, this analysis considers several sources of systematic uncertainty on the number of expected signal events. Thus, rather than a single nuisance parameter associated to the signal prediction θ_s, we have a set of NPs $\theta_s = \{\theta_s^i\}$, one for each source of uncertainty described in Section 7.3. The likelihood function is then

$$\mathcal{L}(\mu, \theta) = Pois(n_{\text{obs}}|\mu s \theta_s + b \theta_b) \cdot \prod_i Gaus(\tilde{\theta}_s^i|\theta_s^i, \sigma_s^i) \cdot Gaus(\tilde{\theta}_b|\theta_b, \sigma_b) \qquad (8.19)$$

In our model, μ represents the branching ratio $B(H \rightarrow aa \rightarrow b\bar{b}b\bar{b})$. A value of $\mu = 1$ means
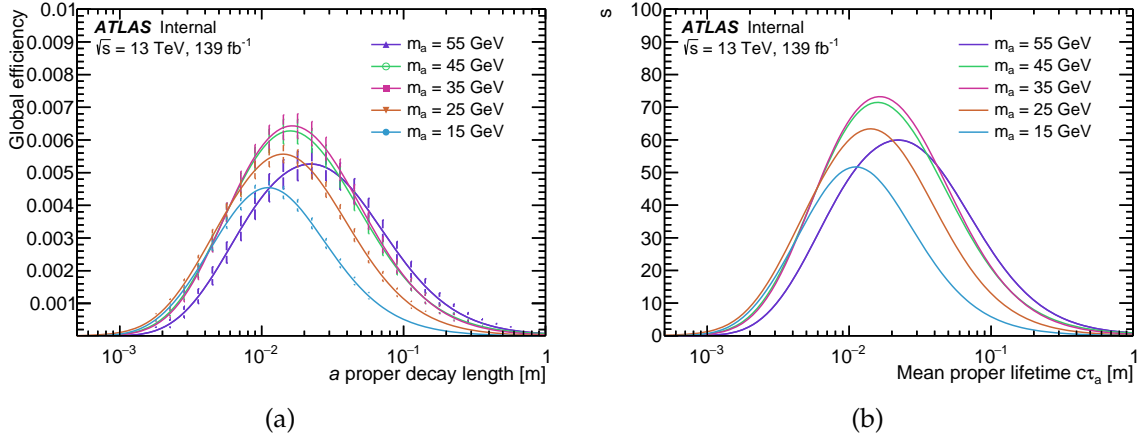
Figure 8.7: (a) The global selection efficiency curves and (b) the number of predicted signal events s as a function of $c\tau_a$ for each signal mass point.

that the Higgs boson decays to pairs of long-lived scalars 100% of the time. A value of $\mu = 0$ corresponds to the background only hypothesis in which the Higgs boson has no coupling to LLPs.

Upper limits at 95% CL are derived for each signal mass hypothesis at a range of values of $c\tau_a$ from 10^{-4} to 10 m using the observed dataset $n_{\mathrm{obs}} = 0$ the background prediction $b = 1.3$, and the value of s taken from the scaled efficiency curve in Figure 8.7. For each value of m_a and $c\tau_a$, we follow the prescription described at the end of Section 8.2.3 to compute μ_{up}. Twenty-five values of μ are considered in the $\mathrm{CL_s}$ scan. For each hypothesis, we generate 25 000 pseudoexperiments for the alternative hypothesis and 12 500 pseudo-experiments for the null hypothesis to compute the PDF of the test statistic. Figure 8.8 shows the generated pseudoexperiments at each point in the $\mathrm{CL_s}$ scan for $m_a = 35$ GeV and $c\tau_a = 10$ mm. From the generated distributions, the p-values for $\mathrm{CL_{s+b}}$, $\mathrm{CL_b}$, and $\mathrm{CL_s}$ are computed. This allows us to compute the observed upper limit μ_{up} as well as the expected limit and corresponding ± 1 and $\pm 2\sigma$ error bands, as shown in Figure 8.9 for $m_a = 35$ GeV and $c\tau_a = 10$ mm.

After performing the $\mathrm{CL_s}$ prescription across the full range of masses and scalar proper lifetimes, we obtain the final exclusion limits on the branching ratio $B(H \to aa \to b\bar{b}b\bar{b})$, as shown in Figure 8.10. A discussion of these results will be given in Section 8.3.4 after a brief *intermezzo* to investigate the impact of systematic uncertainties in the analysis.

Sample		Selection	
m_a [GeV]	$c\tau$ [mm]	Generated	Extrapolated
	10	51.0 ± 4.4	$50.4^{+5.8}_{-5.4}$
55	100	23.7 ± 2.4	$26.2^{+2.8}_{-2.6}$
	1000	0.6 ± 0.3	$1.0^{+0.5}_{-0.4}$
	10	70.2 ± 3.4	$67.2^{+4.8}_{-4.6}$
45	100	20.9 ± 1.9	$22.8^{+2.2}_{-2.1}$
	1000	0.6 ± 0.2	$0.8^{+0.3}_{-0.3}$
	10	71.4 ± 4.3	$70.4^{+4.7}_{-4.5}$
35	100	21.1 ± 2.2	$23.4^{+2.2}_{-2.1}$
	1000	0.2 ± 0.2	$0.5^{+0.3}_{-0.2}$
	10	63.9 ± 2.9	$65.7^{+3.3}_{-3.2}$
25	100	11.4 ± 1.2	$14.5^{+1.2}_{-1.2}$
	1000	0.4 ± 0.2	$0.3^{+0.1}_{-0.1}$
	10	54.1 ± 2.4	$52.7^{+2.2}_{-2.2}$
15	100	4.6 ± 0.4	$6.8^{+0.5}_{-0.5}$
	1000	0.1 ± 0.0	$0.1^{+0.1}_{-0.0}$

Table 8.1: The total expected yield for each signal point after each selection is applied, assuming $B(H \to aa \to b\bar{b}b\bar{b}) = 1$.

8.3.3 Better than zero?

In most cases, there are several ways to improve the sensitivity of a physics analysis. First and most obviously, would be to modify the analysis strategy to improve $S/\sqrt{B}$. However, assuming that the analysis has been sufficiently optimized, this may or many not be feasible. The other possibility is to collect more data using the same analysis methodology. This will increase the expected signal and background yields correspondingly, but increase $S/\sqrt{B}$ giving rise to a more sensitive analysis. The third and final way is to increase the precision of the analysis predictions, i.e. reducing the systematic uncertainties. In the presence of a systematic uncertainty on σ_b on the background prediction, the sensitivity of the analysis may be approximated as $S/\sqrt{B(1 + \sigma_b^2 B)}$ for large S and B. In the limit of infinite luminosity, this becomes $\frac{S}{\sigma_b B}$, significantly reducing the significance of the observation if σ_b is sufficiently large.

To understand the limitations of the current analysis, it is necessary to determine whether or not the systematic uncertainties on the signal and background prediction have a significant impact on the sensitivity of the analysis. To assess the impact of the systematics on the final exclusion limits, we perform the CL$_s$ method with all nuisance parameters set to
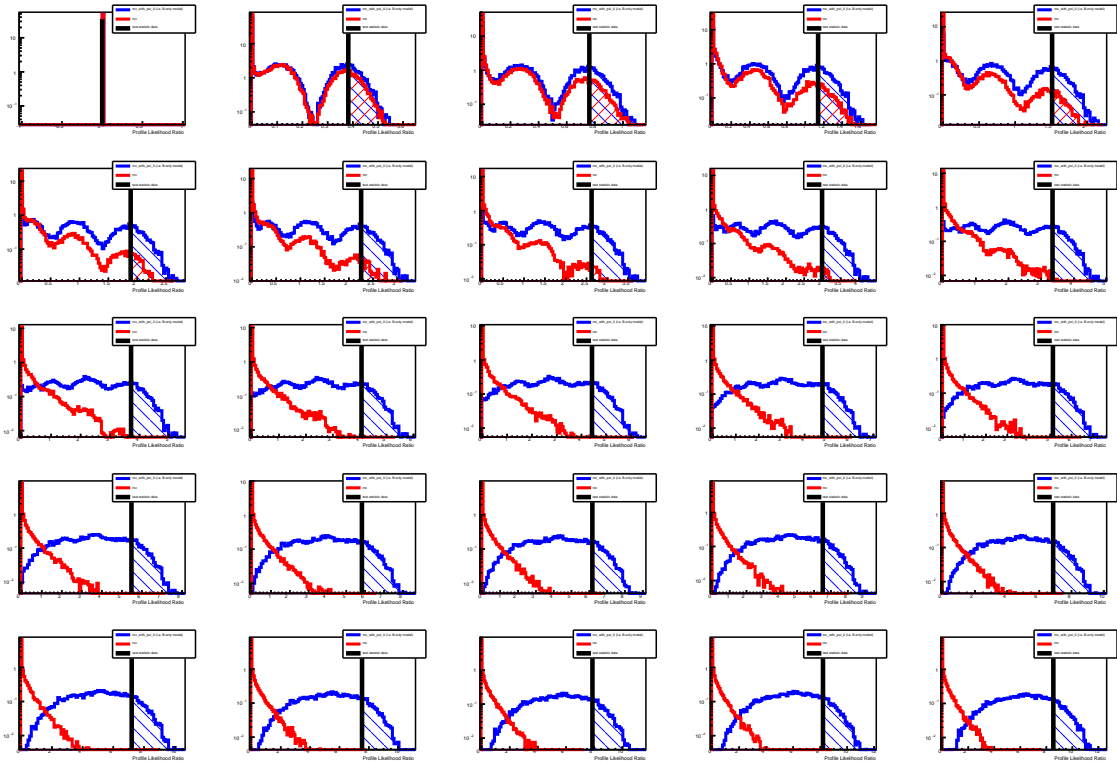
Figure 8.8: The distribution of the profile-likelihood test statistic for various values of μ for $m_a = 35$ GeV and $c\tau_a = 10$ mm. The signal-plus-background hypothesis is shown in red, and the background-only hypothesis is shown in blue. The observed value of the test statistic is drawn as a black line, and the integral used to compute the p-values is shown as a shaded area.
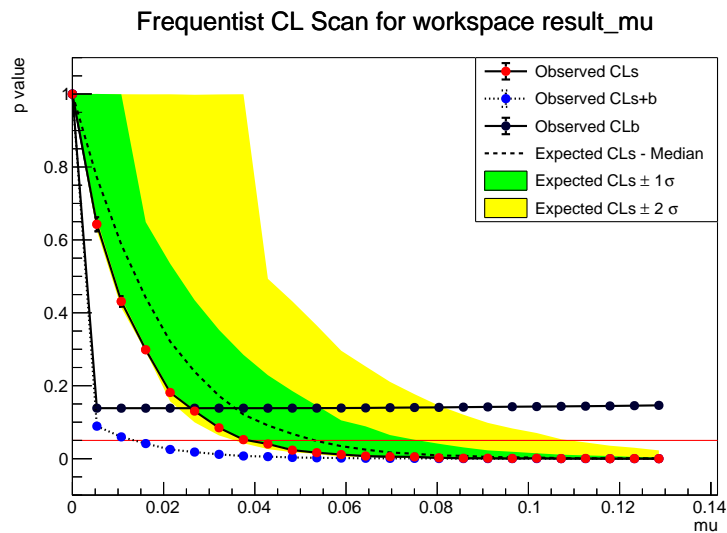
Figure 8.9: The 95% CL upper limits on μ for $m_a = 35$ GeV and $c\tau_a = 10$ mm.

(a) $m_a = 15$ GeV

(b) $m_a = 25$ GeV

(c) $m_a = 35$ GeV
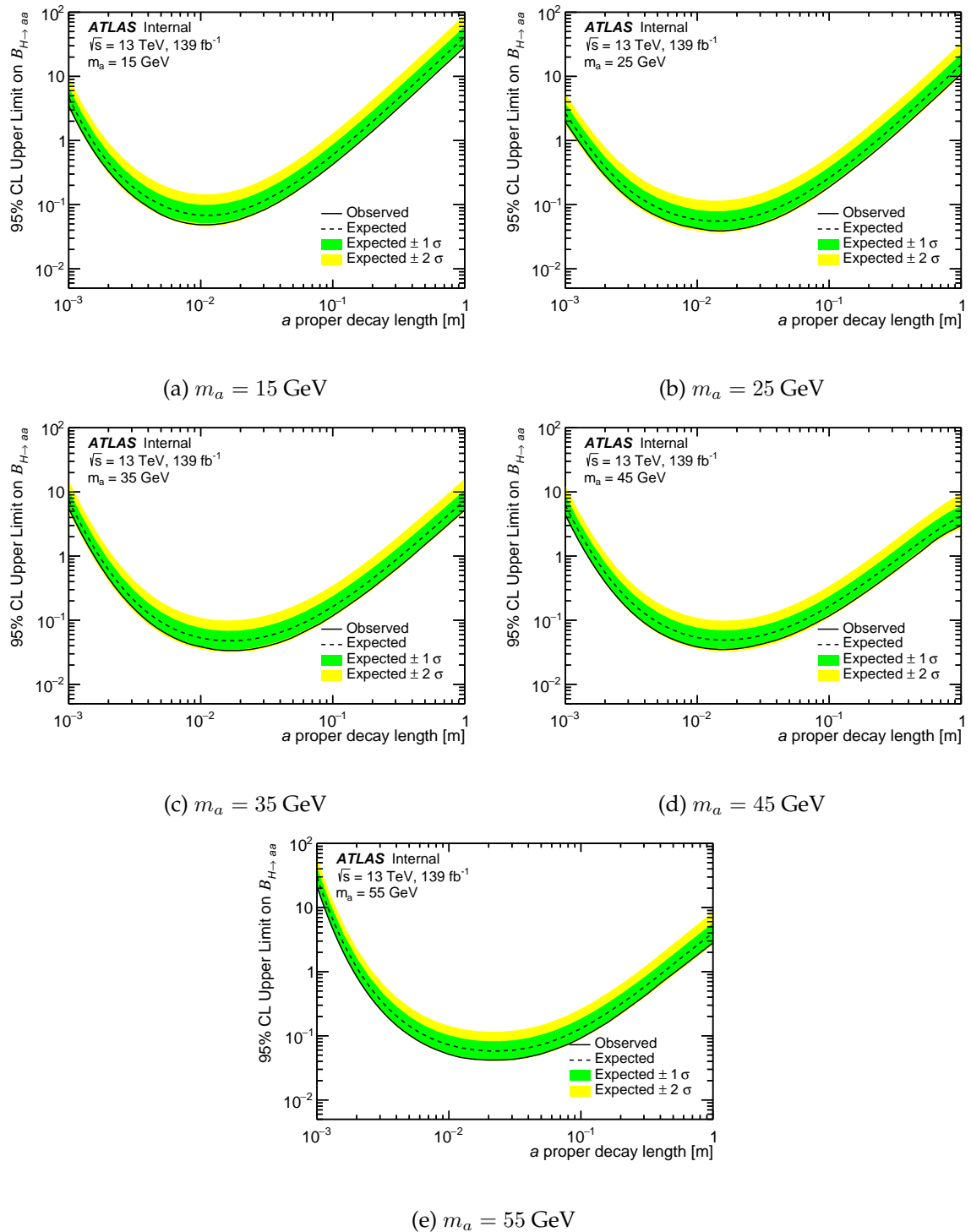
(d) $m_a = 45$ GeV

(e) $m_a = 55$ GeV

Figure 8.10: Expected and observed exclusion limits on $B_{H \to aa}$ for (a) $m_a = 15$ GeV, (b) $m_a = 25$ GeV, (c) $m_a = 35$ GeV, (d) $m_a = 45$ GeV, and (e) $m_a = 55$ GeV with $\pm 1\sigma$ and $\pm 2\sigma$ error bands.
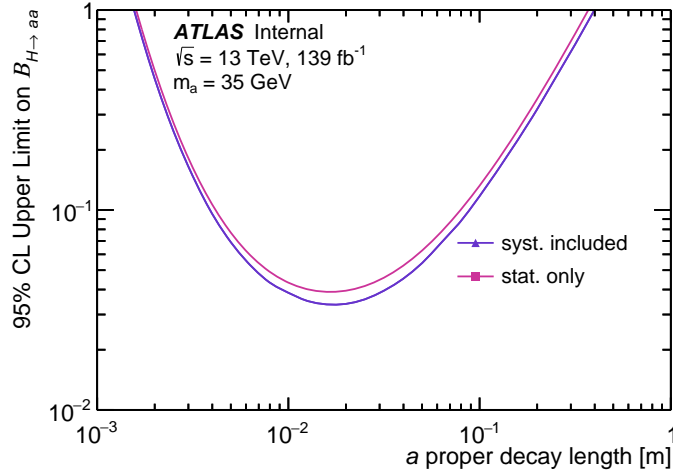
Figure 8.11: Comparison of the exclusion curves with and without systematics applied.
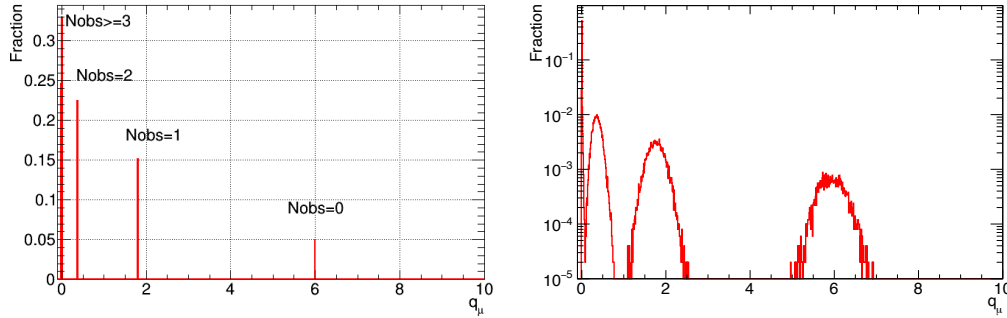
Figure 8.12: Normalized distribution of the one-sided profile likelihood test statistic q_μ for $\mu = 3$ with no systematic uncertainty (left) and with a systematic uncertainty on the signal efficiency of $\sigma_s = 0.05$ (right). Image taken from Ref [202].

their nominal constant values. In most situations, uncertainty on the predicted number of signal and background events decreases the sensitivity of an analysis and therefore gives rise to weaker limits. However as shown in Figure 8.11, the limits derived with systematics included are slightly stronger than when all nuisance parameters are constant! This somewhat peculiar result is an example of the **better than zero problem** [202].

To explore this problem further, let us further simplify the example counting experiment used previously in Section 8.2.1 to the situation in which $b = 0$, and there is only one nuisance parameter in our model, θ. Figure 8.12 shows the distribution of pseudoexperiments generated under the alternate hypothesis with $\mu = 3$ both with and without a systematic uncertainty on the signal efficiency for this scenario. In both cases, 5% of the alternate hypothesis resides in the final peak, but the uncertainty on the signal efficiency
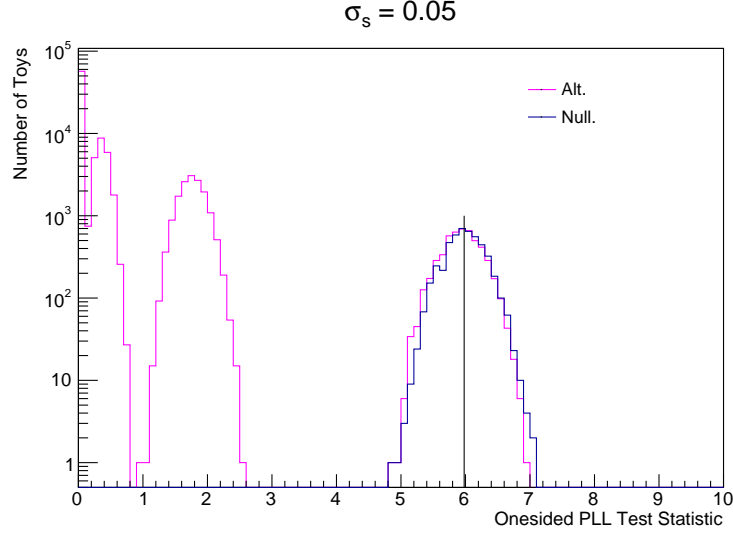
Figure 8.13: Distribution of the one-sided profile likelihood test statistic for a hypothesis test with $\mu = 3$, where $\sigma_s = 0.05$. The solid black vertical line indicates the observed value of the test statistic for an observation of 0 events.

smooths out the overall distribution symmetrically about the center of each peak. The p-value for this example is given by

$$
\begin{aligned}
p_\mu &= Pois(n_{\text{obs}} = 0|\mu s \theta) \cdot Gaus(\tilde{\theta} > \tilde{\theta}^{\text{obs}}|\theta, \sigma_s) \\
&= e^{-\mu s \theta} \cdot \Phi\left(\frac{\theta - \tilde{\theta}^{\text{obs}}}{\sigma_s}\right)
\end{aligned}
$$

where θ is the assumed true value of the nuisance parameter when generating the pseudoexperiments. The CMLE of the nuisance parameter θ is given by

$$
\hat{\theta}_\mu^{\text{obs}} = \tilde{\theta}^{\text{obs}} - \mu s \sigma_s^2. \tag{8.20}
$$

Thus, the toys are generated at a slightly shifted value of θ relative to the observed value, with the shift depending on the uncertainty of the signal yield. In the background-only hypothesis, the shift in the distribution is not present because $\mu = 0$. Figure 8.12 shows the distributions of the test statistic for both the null and alternate hypotheses, with the final peaks corresponding to $n_{\text{obs}} = 0$ being clearly shifted from one another. The location of the observed value of the test statistic corresponds to the central value of the background-only distribution, giving a CL_b p-value of 0.5. The shift in the distribution for the alternate

hypotheses implies that the $\mathrm{CL_{s+b}}$ p-value will be slightly less than 0.025, corresponding to a lower $\mathrm{CL_s}$ limit than would be computed from the unshifted distribution!

For this simple model, we can quantify this effect by solving for the p-values exactly. The $\mathrm{CL_{s+b}}$ and $\mathrm{CL_b}$ p-values are given by

$$p_\mu = e^{-\mu s \tilde{\theta}^{\mathrm{obs}}} \cdot e^{\mu^2 s^2 \sigma_{\tilde{s}}^2} \Phi(-\mu s \sigma_s), \quad p_b = \Phi(0) = 0.5 \tag{8.21}$$

and thus the 95% CL upper limit is obtained by solving (note $\tilde{\theta}^{\mathrm{obs}} = 1$)

$$0.05 = 2 e^{\mu^2 s^2 \sigma_{\tilde{s}}^2 - \mu s} \Phi(-\mu s \sigma_S) \tag{8.22}$$

Numerical solutions to this equation are given in Table 8.2 for several values of σ_s. Hence,

σ_s	95% CL upper limit on $s\mu$
0	2.996
0.05	2.894
0.10	2.824
0.20	2.757
0.25	2.759
0.30	2.786

Table 8.2: Upper limits for difference values of uncertainty on the signal yield. The lowest lowest limit is obtained for an uncertainty of approximately 20%. Values taken from Ref [202].

in the case of zero background, the introduction of a systematic uncertainty on the signal prediction actually leads to a stronger limit than in the absence of all uncertainties.

Let us now explore what is happening in the hypothesis testing for the search for Higgs boson decays to LLPs. Although we are no longer able to easily solve for the p-values exactly, we can still investigate what happens to the distributions of the test statistic when we either enable or disable the nuisance parameters in our fit. We will use the values of the model parameters corresponding to $m_a = 35\,\mathrm{GeV}$ and $c\tau_a = 10\,\mathrm{mm}$. Figure 8.14 shows the distributions of the test statistic for the case in which no systematics considered as well as only considering systematic uncertainties on the background estimate. Here we have set μ equal to the value μ_{up} computed with no systematics. In both cases, we observe that the final peak is a delta function similar to what was observed in Figure 8.12. As shown in
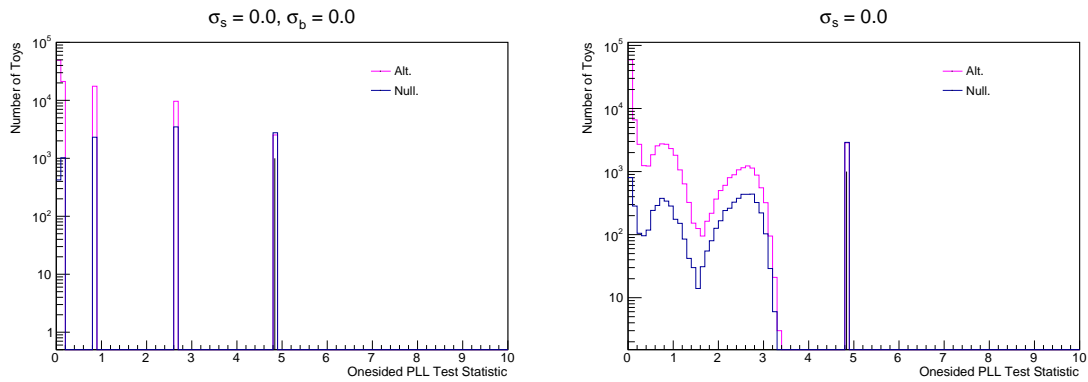
Figure 8.14: Distribution of the one-sided profile likelihood test statistic for $m_a = 35$ GeV and $c\tau_a = 10$ mm with no systematics (left) and only the systematic uncertainty on the background prediction (right).The solid black vertical line indicates the observed value of the test statistic for an observation of 0 events.
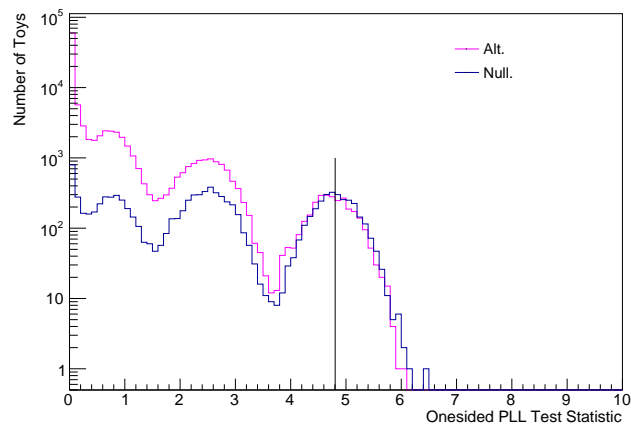
Figure 8.15: Distribution of the one-sided profile likelihood test statistic for $m_a = 35$ GeV and $c\tau_a = 10$ mm with all systematic uncertainties included. The solid black vertical line indicates the observed value of the test statistic for an observation of 0 events.
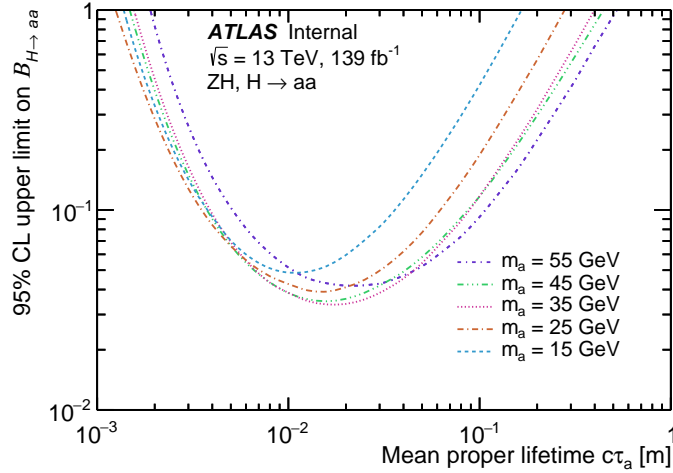
Figure 8.16: The observed limits for all signal mass points as a function of $c\tau$ of the a boson.

Figure 8.15, when we introduce systematic uncertainties on the signal prediction, the same shift in the distribution for the alternate hypotheses relative to the null hypothesis is observed as in Figure 8.13. Thus, the same "better than zero" phenomenon is observed with nonzero background prediction and uncertainty on the background yield. Quantitatively, including the systematic uncertainties in the model gives improved limits on the order of a few percent. From this we conclude that systematic uncertainties are not a limiting factor in the sensitivity of this analysis. Hence, to improve upon the sensitivity, either more data or a more highly optimized analysis strategy is needed.

8.3.4   Summary of results

Now that we have computed 95% CL upper limits on $B(H \rightarrow aa \rightarrow b\bar{b}b\bar{b})$ for a range of masses m_a and lifetimes $c\tau_a$, we move to a discussion of how to interpret these results and their significance. The observed limits from Figure 8.10 are shown together on one canvas in Figure 8.16. We observe that this search has excluded $B(H \rightarrow aa \rightarrow b\bar{b}b\bar{b}) > 10\%$ for LLP mean proper lifetimes $c\tau_a$ as small as 4 mm and as large as 110 mm. For $m_a = 35$ GeV, $B(H \rightarrow aa \rightarrow b\bar{b}b\bar{b}) \gtrsim 3\%$ is excluded for $c\tau = 20$ mm. The excluded ranges of $c\tau$ are shown in Table 8.3 for several branching ratio hypotheses, and Figure 8.17 shows the exclusion in the 2-dimensional space of m_a vs. $c\tau_a$.
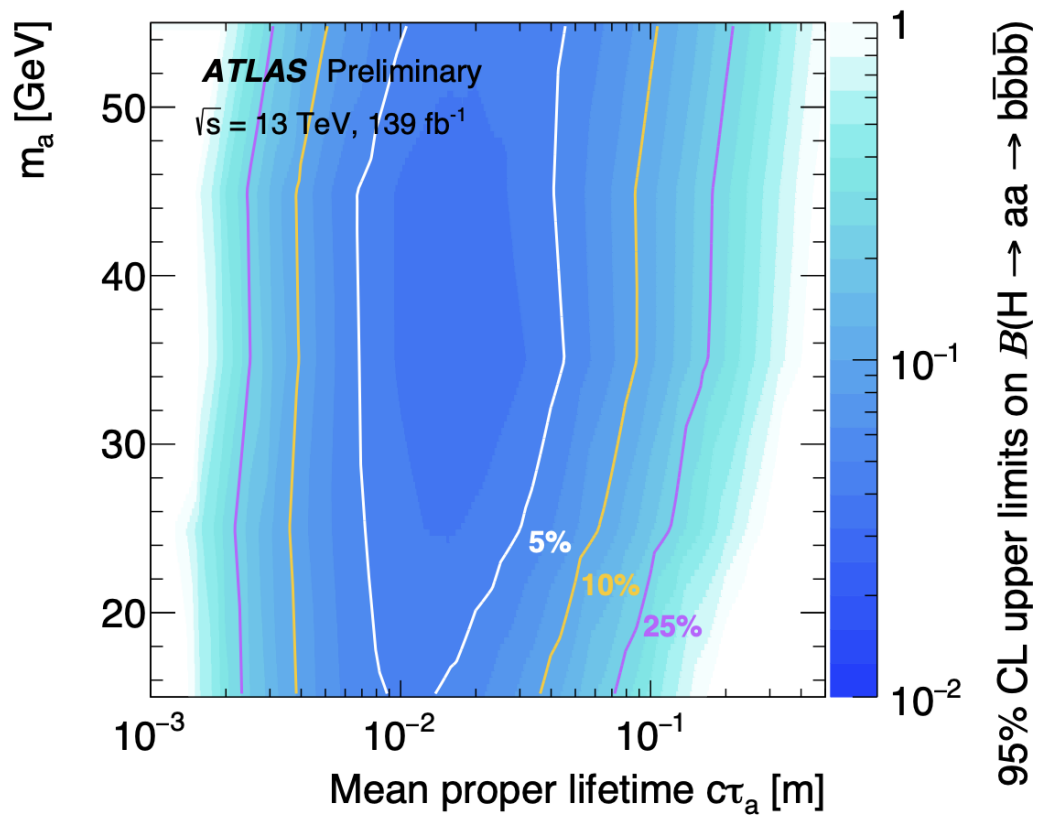
Figure 8.17: Observed 95% CL exclusion limits on $\mathcal{B}(H \to aa \to b\bar{b}b\bar{b})$ shown as a function of both m_a and proper lifetime $c\tau_a$. Contours are included which show the area of excluded values for several branching ratio hypotheses.

m_a	$B(H \rightarrow aa \rightarrow b\bar{b}b\bar{b})$	Excluded $c\tau$ range [m]
	100%	0.0019 - 0.5248
55	50%	0.0024 - 0.3388
	25%	0.0031 - 0.2163
	10%	0.0052 - 0.1072
	100%	0.0015 - 0.4467
45	50%	0.0019 - 0.2851
	25%	0.0025 - 0.1778
	10%	0.0038 - 0.0871
	100%	0.0016 - 0.3981
35	50%	0.0020 - 0.2630
	25%	0.0025 - 0.1698
	10%	0.0039 - 0.0881
	100%	0.0013 - 0.2786
25	50%	0.0016 - 0.1862
	25%	0.0022 - 0.1202
	10%	0.0036 - 0.0624
	100%	0.0014 - 0.1660
15	50%	0.0018 - 0.1109
	25%	0.0023 - 0.0716
	10%	0.0038 - 0.0359

Table 8.3: Ranges of proper lifetimes excluded at 95% CL for each benchmark sample shown for several values of $B(H \rightarrow aa \rightarrow b\bar{b}b\bar{b})$.

In comparison to the previous searches for Higgs decays to LLPs described in Section 2.6, these are among the most stringent limits placed on $B(H \rightarrow aa \rightarrow b\bar{b}b\bar{b})$ thus far at the LHC. For scalars with $m_a < 40$ GeV, these results represent the strongest existing constraints on $B(H \rightarrow aa \rightarrow b\bar{b}b\bar{b})$ in this lifetime regime. Although for scalar masses above 40 GeV this search is not as sensitive as the search for displaced jets performed by the CMS experiment [90], among ATLAS searches, the region $c\tau_a < 100$ mm was mostly unconstrained prior to this search regardless of the scalar mass. Figure 8.18 shows a new version of Figure 2.10 which has been updated to include the results of this search in the summary of current exclusion limits set by ATLAS. The limits derived from this search fill the gap in exclusion left by the previous searches which targeted lifetimes $c\tau_a < 1$ mm and $c\tau_a > 1$ m. Despite not being as sensitive as the searches which probed LLP lifetimes $c\tau_a > 1$ m, this search provides the complementarity needed to begin to exclude a significantly wider range of LLP lifetimes.
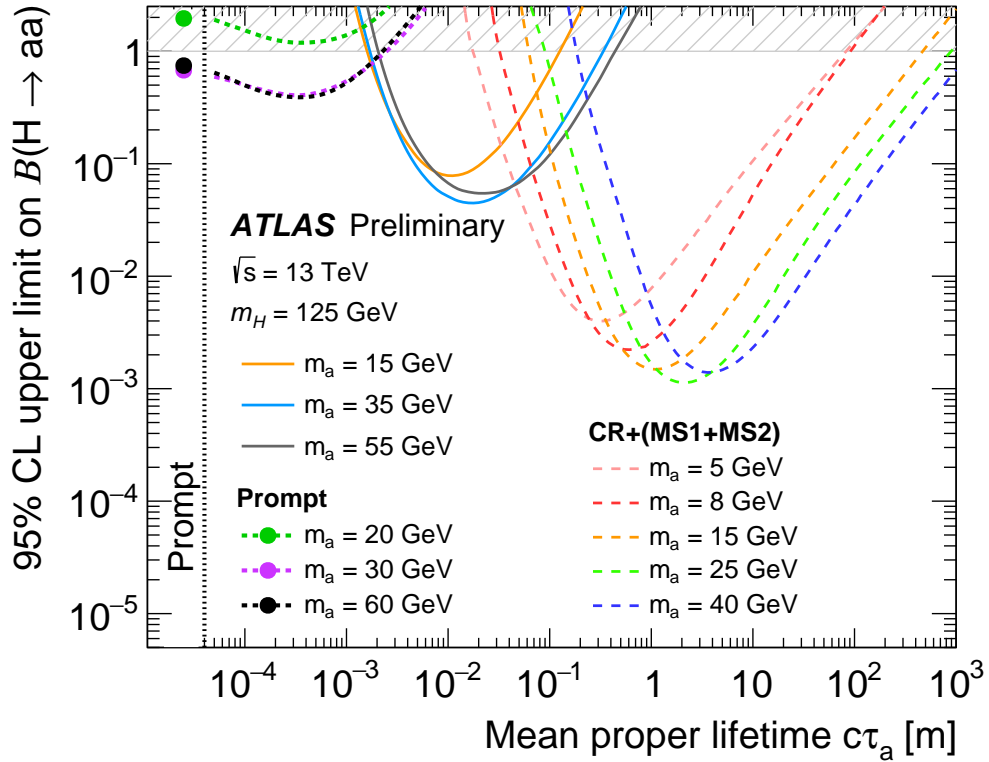
Figure 8.18: Summary of current observed limits on decays of the Higgs boson to pairs of long-lived a bosons as a function of proper lifetime $c\tau_a$, obtained by the ATLAS experiment. The limits shown include the results from a search optimized for prompt decays (JHEP 10 (2018) 031), the inner detector DV-based search presented here, and the combined results of two searches for displaced jets in the ATLAS calorimeter (CR) and muon spectrometer (MS1+MS2) (Eur. Phys. J. C 79 (2019) 481). The a bosons are allowed to decay inclusively to all kinematically-allowed final states, with mass-dependent a boson branching ratios. For $m_a > 25$ GeV, the branching ratios to $b\bar{b}$, $c\bar{c}$, and $\tau^+\tau^-$ are approximately constant and given by 85%, 5%, and 8%, respectively. The prompt and inner detector DV-based results assume negligible signal efficiency for decays other than $a \rightarrow b\bar{b}$.

Chapter 9

Conclusion

And once the storm is over you won't remember how you made it through, how you managed to survive. You won't even be sure, in fact, whether the storm is really over. But one thing is certain. When you come out of the storm you won't be the same person who walked in. That's what this storm's all about.

-Haruki Murakami, *Kafka on the Shore*

This thesis has described a novel search for exotic decays of the Higgs boson to pairs of displaced vertices in the ATLAS inner detector. Although no evidence for BSM physics was observed, the limits derived through the statistical interpretation presented in Chapter 8 represent the strongest existing constraints on the branching ratio of the Higgs boson to pairs of long-lived scalars with $m_a < 40$ GeV in the lifetime region $1 < c\tau_a < 100$ mm. Branching ratios of greater than 10% are excluded in this regime for a wide range of scalar masses m_a. In order to probe branching ratios less than 1%, considerable improvements to the analysis strategy must be made. Including the $W^\pm H$ production mode would give an immediate improvement of roughly a factor of 5 in terms of total signal cross section due to the larger $\sigma \times B(V \to \ell\ell)$ of WH with respect to ZH production modes [50]. However, the WH channel will suffer from larger backgrounds due to the additional contribution from the $t\bar{t}$ process. Thus, further studies will need to be performed to assess the actual improvement gained by including this additional channel. Being a zero background search already, the only way to improve the sensitivity of the ZH channel is to increase the signal selection efficiency. The most obvious way to accomplish this would be to only require the
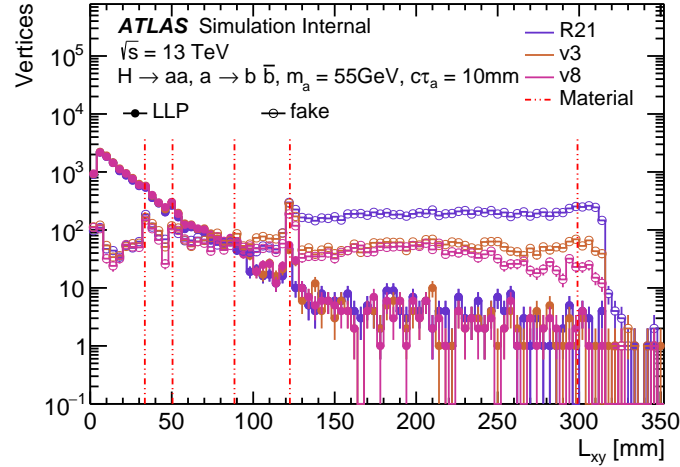
Figure 9.1: The radial distribution of truth-matched LLP vertices and fake vertices for three different versions of the LRT algorithm. "R21" is the version of the algorithm used in this thesis, while "v8" is the final configuration of the algorithm that will be used in Run III. "v3" is an intermediate configuration that was being considered but was superseded by the v8. Material layers are shown as red dashed lines.

presence of one DV. However, with the current analysis selections the single DV channel has prohibitively large background, so future developments will need to be made to the both the reconstruction algorithms and analysis-level selections in order to achieve the background rejection necessary to pursue a single DV channel.

Thankfully, the LRT algorithm has been reoptimized to significantly decrease the number of fake tracks, and therefore the number of fake vertices reconstructed. Figure 9.1 shows the radial distribution of vertices reconstructed in a simulated sample of $H \to aa \to 4b$ production for three different versions of the LRT algorithm. "R21" is the version of the algorithm used in this thesis, while "v8" is the final configuration of the algorithm that will be used in Run III The filled-in markers represent vertices that are matched to true LLP decays, while the hollow markers represent fake vertices that are not matched to any truth particle. The number of fake vertices reconstructed *in signal MC* is reduced by an order of magnitude with a negligible impact on the LLP vertex reconstruction efficiency. Further studies need to be performed to quantify the reduction in fake vertices reconstructed in data, but the reduction in background is expected to be substantial. With this updated configuration and the addition of the WH channel, we expect to be able to significantly improve the analysis sensitivity in future searches.

While writing this thesis, tantalizing hints of new physics have been presented by the LHCb Collaboration [203] and the Muon $g - 2$ experiment at Fermilab [204]. All eyes are thus once again on the ATLAS and CMS experiments to find direct evidence for new particles that could be causing these discrepancies between theoretical prediction and experimental observations. As described in Section 2.5, there is strong reason to believe that the most promising avenue for discovery of BSM physics is by searching for exotic Higgs decays to challenging detector signatures that have been overlooked by traditional ATLAS searches. Despite not finding evidence of new physics, this novel search has laid the groundwork for future research to scrutinize the Higgs sector more closely using different final states. The current theory space is extremely vast and there are myriad scenarios in which the Higgs boson can serve as a mediator between the SM and new physics. The possible detector signatures are numerous, from long-lived scenarios such as displaced vertices and emerging jets, to challenging prompt signatures like semi-visible jets and soft unclustered energy patterns (SUEP). The improved LRT algorithm will open the door for many such searches, and the interest from the experimental and theoretical community in these searches is growing quickly. We hope that this search will be the first in an exhaustive search program for exotic Higgs decays with challenging detector signatures that exploit the associated production mode to trigger.

We live to search another day.

Bibliography

[1] ATLAS Collaboration, "Observation of a new particle in the search for the Standard Model Higgs boson with the ATLAS detector at the LHC," *Phys. Lett. B*, vol. 716, p. 1, 2012. DOI: `10.1016/j.physletb.2012.08.020`. arXiv: `1207.7214 [hep-ex]` (cit. on pp. 1, 4, 30).

[2] CMS Collaboration, "Observation of a new boson at a mass of 125 GeV with the CMS experiment at the LHC," *Phys. Lett. B*, vol. 716, p. 30, 2012. DOI: `10.1016/j.physletb.2012.08.021`. arXiv: `1207.7235 [hep-ex]` (cit. on pp. 1, 4, 30).

[3] "Search for exotic decays of the Higgs boson to long-lived particles in pp collisions at $\sqrt{s} = 13$ TeV using displaced vertices in the ATLAS inner detector," CERN, Geneva, Tech. Rep. ATLAS-CONF-2021-005, Mar. 2021. [Online]. Available: `http://cds.cern.ch/record/2759209` (cit. on p. 2).

[4] S. Argyropoulos, "Probing the dark sector with b-quarks with the ATLAS detector," CERN, Geneva, Tech. Rep. ATL-COM-PHYS-2021-072, Mar. 2021, 21 March 2021. [Online]. Available: `https://cds.cern.ch/record/2753603` (cit. on p. 2).

[5] J. J. Thomson, "Cathode rays," *Phil. Mag. Ser. 5*, vol. 44, pp. 293–316, 1897. DOI: `10.1080/14786449708621070` (cit. on p. 4).

[6] E. Noether, "Invariante variationsprobleme," ger, *Nachrichten von der Gesellschaft der Wissenschaften zu Göttingen, Mathematisch-Physikalische Klasse*, vol. 1918, pp. 235–257, 1918. [Online]. Available: `http://eudml.org/doc/59024` (cit. on p. 8).

[7] A. Einstein, "Zur Elektrodynamik bewegter Körper," *Annalen der Physik*, vol. 322, no. 10, pp. 891–921, Jan. 1905. DOI: `10.1002/andp.19053221004` (cit. on p. 9).

[8]   C. N. Yang and R. L. Mills, "Conservation of isotopic spin and isotopic gauge invariance," *Phys. Rev.*, vol. 96, pp. 191–195, 1 Oct. 1954. DOI: `10.1103/PhysRev.96.191` (cit. on p. 10).

[9]   P. A. M. Dirac, "The quantum theory of the emission and absorption of radiation," *Proceedings of the Royal Society of London. Series A, Containing Papers of a Mathematical and Physical Character*, vol. 114, no. 767, pp. 243–265, 1927. DOI: `10.1098/rspa.1927.0039` (cit. on p. 13).

[10] P. A. M. Dirac, "The quantum theory of the electron," *Proceedings of the Royal Society of London. Series A, Containing Papers of a Mathematical and Physical Character*, vol. 117, no. 778, pp. 610–624, 1928. DOI: `10.1098/rspa.1928.0023` (cit. on p. 13).

[11] S. Tomonaga, "On a Relativistically Invariant Formulation of the Quantum Theory of Wave Fields," *Progress of Theoretical Physics*, vol. 1, no. 2, pp. 27–42, Aug. 1946, ISSN: 0033-068X. DOI: `10.1143/PTP.1.27` (cit. on p. 13).

[12] R. P. Feynman, "Space-time approach to quantum electrodynamics," *Phys. Rev.*, vol. 76, pp. 769–789, 6 Sep. 1949. DOI: `10.1103/PhysRev.76.769` (cit. on p. 13).

[13] R. P. Feynman, "The theory of positrons," *Phys. Rev.*, vol. 76, pp. 749–759, 6 Sep. 1949. DOI: `10.1103/PhysRev.76.749` (cit. on p. 13).

[14] R. P. Feynman, "Mathematical formulation of the quantum theory of electromagnetic interaction," *Phys. Rev.*, vol. 80, pp. 440–457, 3 Nov. 1950. DOI: `10.1103/PhysRev.80.440` (cit. on p. 13).

[15] J. Schwinger, "On quantum-electrodynamics and the magnetic moment of the electron," *Phys. Rev.*, vol. 73, pp. 416–417, 4 Feb. 1948. DOI: `10.1103/PhysRev.73.416` (cit. on p. 13).

[16] J. Schwinger, "Quantum electrodynamics. i. a covariant formulation," *Phys. Rev.*, vol. 74, pp. 1439–1461, 10 Nov. 1948. DOI: `10.1103/PhysRev.74.1439` (cit. on p. 13).

[17] F. J. Dyson, "The radiation theories of tomonaga, schwinger, and feynman," *Phys. Rev.*, vol. 75, pp. 486–502, 3 Feb. 1949. DOI: `10.1103/PhysRev.75.486` (cit. on p. 13).

[18] M. Gell-Mann, "The Eightfold Way: A Theory of strong interaction symmetry," Mar. 1961. DOI: `10.2172/4008239` (cit. on p. 14).

[19] Y. Ne'eman, "Derivation of strong interactions from a gauge invariance," *Nucl. Phys.*, vol. 26, R. Ruffini and Y. Verbin, Eds., pp. 222–229, 1961. DOI: `10.1016/0029-5582(61)90134-1` (cit. on p. 14).

[20] W. Heisenberg, "Über den Bau der Atomkerne. I," *Zeitschrift fur Physik*, vol. 77, no. 1-2, pp. 1–11, Jan. 1932. DOI: `10.1007/BF01342433` (cit. on p. 14).

[21] M. Gell-Mann, "A Schematic Model of Baryons and Mesons," *Phys. Lett.*, vol. 8, pp. 214–215, 1964. DOI: `10.1016/S0031-9163(64)92001-3` (cit. on p. 14).

[22] G. Zweig, "An SU(3) model for strong interaction symmetry and its breaking. Version 2," in *DEVELOPMENTS IN THE QUARK THEORY OF HADRONS. VOL. 1. 1964 - 1978*, D. B. Lichtenberg and S. P. Rosen, Eds. Feb. 1964 (cit. on p. 14).

[23] G. Zweig, "An SU(3) model for strong interaction symmetry and its breaking. Version 1," Jan. 1964 (cit. on p. 14).

[24] J. D. Bjorken, "Asymptotic sum rules at infinite momentum," *Phys. Rev.*, vol. 179, pp. 1547–1553, 5 Mar. 1969. DOI: `10.1103/PhysRev.179.1547`. [Online]. Available: `https://link.aps.org/doi/10.1103/PhysRev.179.1547` (cit. on p. 15).

[25] O. W. Greenberg, "Spin and unitary-spin independence in a paraquark model of baryons and mesons," *Phys. Rev. Lett.*, vol. 13, pp. 598–602, 20 Nov. 1964. DOI: `10.1103/PhysRevLett.13.598` (cit. on p. 15).

[26] M. Y. Han and Y. Nambu, "Three-triplet model with double su(3) symmetry," *Phys. Rev.*, vol. 139, B1006–B1010, 4B Aug. 1965. DOI: `10.1103/PhysRev.139.B1006` (cit. on p. 15).

[27]   H. Fritzsch, M. Gell-Mann, and H. Leutwyler, "Advantages of the color octet gluon picture," *Physics Letters B*, vol. 47, no. 4, pp. 365–368, 1973, ISSN: 0370-2693. DOI: `https://doi.org/10.1016/0370-2693(73)90625-4` (cit. on p. 15).

[28]   D. J. Gross and F. Wilczek, "Ultraviolet behavior of non-abelian gauge theories," *Phys. Rev. Lett.*, vol. 30, pp. 1343–1346, 26 Jun. 1973. DOI: `10.1103/PhysRevLett.30.1343`. [Online]. Available: `https://link.aps.org/doi/10.1103/PhysRevLett.30.1343` (cit. on p. 16).

[29]   H. D. Politzer, "Reliable perturbative results for strong interactions?" *Phys. Rev. Lett.*, vol. 30, pp. 1346–1349, 26 Jun. 1973. DOI: `10.1103/PhysRevLett.30.1346`. [Online]. Available: `https://link.aps.org/doi/10.1103/PhysRevLett.30.1346` (cit. on p. 16).

[30]   A. Deur, S. J. Brodsky, and G. F. de Téramond, "The qcd running coupling," *Progress in Particle and Nuclear Physics*, vol. 90, pp. 1–74, Sep. 2016, ISSN: 0146-6410. DOI: `10.1016/j.ppnp.2016.04.003`. [Online]. Available: `http://dx.doi.org/10.1016/j.ppnp.2016.04.003` (cit. on p. 17).

[31]   Heather Russell, CC BY-NC 4.0, "Formation of jets (hadronization)," (cit. on p. 18).

[32]   S. S. Gershtein and Y. B. Zeldovich, "Meson corrections in the theory of beta decay," *Zh. Eksp. Teor. Fiz.*, vol. 29, Y. A. Trutnev, Ed., pp. 698–699, 1955 (cit. on p. 19).

[33]   C. S. Wu, E. Ambler, R. W. Hayward, D. D. Hoppes, and R. P. Hudson, "Experimental test of parity conservation in beta decay," *Phys. Rev.*, vol. 105, pp. 1413–1415, 4 Feb. 1957. DOI: `10.1103/PhysRev.105.1413`. [Online]. Available: `https://link.aps.org/doi/10.1103/PhysRev.105.1413` (cit. on p. 19).

[34]   R. P. Feynman and M. Gell-Mann, "Theory of Fermi interaction," *Phys. Rev.*, vol. 109, L. M. Brown, Ed., pp. 193–198, 1958. DOI: `10.1103/PhysRev.109.193` (cit. on p. 19).

[35]   S. Weinberg, "The Making of the Standard Model," *Eur. Phys. J. C*, vol. 34, no. hep-ph/0401010, 5–13. 21 p., streaming video, 2003. [Online]. Available: `https://cds.cern.ch/record/799984` (cit. on p. 19).

[36] S. L. Glashow, "Partial-symmetries of weak interactions," *Nuclear Physics*, vol. 22, no. 4, pp. 579–588, 1961, ISSN: 0029-5582. DOI: `https://doi.org/10.1016/0029-5582(61)90469-2` (cit. on p. 19).

[37] S. Weinberg, "A model of leptons," *Phys. Rev. Lett.*, vol. 19, pp. 1264–1266, 21 Nov. 1967. DOI: `10.1103/PhysRevLett.19.1264`. [Online]. Available: `https://link.aps.org/doi/10.1103/PhysRevLett.19.1264` (cit. on p. 19).

[38] A. Salam, "Weak and Electromagnetic Interactions," *Conf. Proc. C*, vol. 680519, pp. 367–377, 1968. DOI: `10.1142/9789812795915_0034` (cit. on p. 19).

[39] P. W. Higgs, "Broken symmetries and the masses of gauge bosons," *Phys. Rev. Lett.*, vol. 13, pp. 508–509, 16 Oct. 1964. DOI: `10.1103/PhysRevLett.13.508`. [Online]. Available: `https://link.aps.org/doi/10.1103/PhysRevLett.13.508` (cit. on p. 23).

[40] F. Englert and R. Brout, "Broken symmetry and the mass of gauge vector mesons," *Phys. Rev. Lett.*, vol. 13, pp. 321–323, 9 Aug. 1964. DOI: `10.1103/PhysRevLett.13.321`. [Online]. Available: `https://link.aps.org/doi/10.1103/PhysRevLett.13.321` (cit. on p. 23).

[41] G. S. Guralnik, C. R. Hagen, and T. W. B. Kibble, "Global conservation laws and massless particles," *Phys. Rev. Lett.*, vol. 13, pp. 585–587, 20 Nov. 1964. DOI: `10.1103/PhysRevLett.13.585`. [Online]. Available: `https://link.aps.org/doi/10.1103/PhysRevLett.13.585` (cit. on p. 23).

[42] J. Goldstone, "Field Theories with Superconductor Solutions," *Nuovo Cim.*, vol. 19, pp. 154–164, 1961. DOI: `10.1007/BF02812722` (cit. on p. 25).

[43] F. Hasert *et al.*, "Observation of neutrino-like interactions without muon or electron in the gargamelle neutrino experiment," *Physics Letters B*, vol. 46, no. 1, pp. 138–140, 1973, ISSN: 0370-2693. DOI: `https://doi.org/10.1016/0370-2693(73)90499-1`. [Online]. Available: `http://www.sciencedirect.com/science/article/pii/0370269373904991` (cit. on p. 30).

[44] M. Banner *et al.*, "Observation of Single Isolated Electrons of High Transverse Momentum in Events with Missing Transverse Energy at the CERN anti-p p Collider," *Phys. Lett. B*, vol. 122, pp. 476–485, 1983. DOI: `10.1016/0370-2693(83)91605-2` (cit. on p. 30).

[45] G. Arnison *et al.*, "Experimental Observation of Isolated Large Transverse Energy Electrons with Associated Missing Energy at s**(1/2) = 540-GeV," *Phys. Lett. B*, vol. 122, pp. 103–116, 1983. DOI: `10.1016/0370-2693(83)91177-2` (cit. on p. 30).

[46] P. Bagnaia *et al.*, "Evidence for $Z^0 \to e^+e^-$ at the CERN $\bar{p}p$ Collider," *Phys. Lett. B*, vol. 129, pp. 130–140, 1983. DOI: `10.1016/0370-2693(83)90744-X` (cit. on p. 30).

[47] G. Arnison *et al.*, "Experimental Observation of Lepton Pairs of Invariant Mass Around 95-GeV/c**2 at the CERN SPS Collider," *Phys. Lett. B*, vol. 126, pp. 398–410, 1983. DOI: `10.1016/0370-2693(83)90188-0` (cit. on p. 30).

[48] J. P. Ellis, "Ti k z-feynman: Feynman diagrams with ti k z," *Computer Physics Communications*, vol. 210, pp. 103–123, Jan. 2017, ISSN: 0010-4655. DOI: `10.1016/j.cpc.2016.08.019`. [Online]. Available: `http://dx.doi.org/10.1016/j.cpc.2016.08.019` (cit. on pp. 31, 32, 36, 41, 137).

[49] M. Tanabashi *et al.*, "Review of particle physics," *Phys. Rev. D*, vol. 98, p. 030 001, 3 Aug. 2018. DOI: `10.1103/PhysRevD.98.030001`. [Online]. Available: `https://link.aps.org/doi/10.1103/PhysRevD.98.030001` (cit. on p. 31).

[50] D. de Florian *et al.*, "Handbook of LHC Higgs Cross Sections: 4. Deciphering the Nature of the Higgs Sector," 2016. DOI: `10.23731/CYRM-2017-002`. arXiv: `1610.07922 [hep-ph]` (cit. on pp. 32, 180, 210).

[51] ATLAS Collaboration, "Summary plots from the ATLAS Standard Model physics group," (cit. on p. 34).

[52] ATLAS Collaboration, "Combined measurements of Higgs boson production and decay using up to $80\,\text{fb}^{-1}$ of proton–proton collision data at $\sqrt{s} = 13\,\text{TeV}$ collected with the ATLAS experiment," *Phys. Rev. D*, vol. 101, p. 012 002, 2020. DOI: `10.`

`1103/PhysRevD.101.012002`. arXiv: `1909.02845 [hep-ex]` (cit. on pp. 35, 56).

[53] ATLAS Collaboration, "Summary plots from the ATLAS Higgs physics group," (cit. on p. 35).

[54] V. Trimble, "Existence and nature of dark matter in the universe," *Annual Review of Astronomy and Astrophysics*, vol. 25, no. 1, pp. 425–472, 1987. DOI: `10.1146/annurev.aa.25.090187.002233` (cit. on p. 37).

[55] G. Bertone, D. Hooper, and J. Silk, "Particle dark matter: Evidence, candidates and constraints," *Physics Reports*, vol. 405, no. 5-6, pp. 279–390, Jan. 2005, ISSN: 0370-1573. DOI: `10.1016/j.physrep.2004.08.031`. [Online]. Available: `http://dx.doi.org/10.1016/j.physrep.2004.08.031` (cit. on p. 37).

[56] J. L. Feng, "Dark matter candidates from particle physics and methods of detection," *Annual Review of Astronomy and Astrophysics*, vol. 48, no. 1, pp. 495–545, 2010. DOI: `10.1146/annurev-astro-082708-101659` (cit. on p. 37).

[57] K. G. Begeman, A. H. Broeils, and R. H. Sanders, "Extended rotation curves of spiral galaxies: Dark haloes and modified dynamics," *Mon. Not. Roy. Astron. Soc.*, vol. 249, p. 523, 1991 (cit. on p. 37).

[58] H. Georgi and S. L. Glashow, "Unity of all elementary-particle forces," *Phys. Rev. Lett.*, vol. 32, pp. 438–441, 8 Feb. 1974. DOI: `10.1103/PhysRevLett.32.438`. [Online]. Available: `https://link.aps.org/doi/10.1103/PhysRevLett.32.438` (cit. on p. 39).

[59] S. Coleman and J. Mandula, "All possible symmetries of the s matrix," *Phys. Rev.*, vol. 159, pp. 1251–1256, 5 Jul. 1967. DOI: `10.1103/PhysRev.159.1251` (cit. on p. 40).

[60] Y. A. Golfand and E. P. Likhtman, "Extension of the Algebra of Poincare Group Generators and Violation of p Invariance," *JETP Lett.*, vol. 13, pp. 323–326, 1971 (cit. on p. 40).

[61]   D. V. Volkov and V. P. Akulov, "Is the Neutrino a Goldstone Particle?" *Phys. Lett. B*, vol. 46, pp. 109–110, 1973. DOI: `10.1016/0370-2693(73)90490-5` (cit. on p. 40).

[62]   J. Wess and B. Zumino, "Supergauge Transformations in Four-Dimensions," *Nucl. Phys. B*, vol. 70, A. Salam and E. Sezgin, Eds., pp. 39–50, 1974. DOI: `10.1016/0550-3213(74)90355-1` (cit. on p. 40).

[63]   J. Wess and B. Zumino, "Supergauge invariant extension of quantum electrodynamics," *Nucl. Phys. B*, vol. 78, p. 1, 1974. DOI: `10.1016/0550-3213(74)90112-6` (cit. on p. 40).

[64]   S. Ferrara and B. Zumino, "Supergauge invariant Yang-Mills theories," *Nucl. Phys. B*, vol. 79, p. 413, 1974. DOI: `10.1016/0550-3213(74)90559-8` (cit. on p. 40).

[65]   A. Salam and J. A. Strathdee, "Supersymmetry and Nonabelian Gauges," *Phys. Lett. B*, vol. 51, pp. 353–355, 1974. DOI: `10.1016/0370-2693(74)90226-3` (cit. on p. 40).

[66]   R. Haag, J. T. Lopuszanski, and M. Sohnius, "All Possible Generators of Supersymmetries of the s Matrix," *Nucl. Phys. B*, vol. 88, p. 257, 1975. DOI: `10.1016/0550-3213(75)90279-5` (cit. on p. 41).

[67]   M. Drees, "An Introduction to Supersymmetry," Seoul Univ. Asia-Pacific Cent. Theor. Phys., Tech. Rep., Nov. 1996. [Online]. Available: `https://cds.cern.ch/record/315597/` (cit. on p. 42).

[68]   I. J. R. Aitchison, *Supersymmetry in Particle Physics. An Elementary Introduction*. Cambridge: Cambridge University Press, 2007, ISBN: 978-0-511-61925-0. DOI: `10.1017/CBO9780511619250` (cit. on p. 42).

[69]   G. Burdman, Z. Chacko, H.-S. Goh, and R. Harnik, "Folded supersymmetry and the lep paradox," *Journal of High Energy Physics*, vol. 2007, no. 02, pp. 009–009, Feb. 2007, ISSN: 1029-8479. DOI: `10.1088/1126-6708/2007/02/009`. [Online]. Available: `http://dx.doi.org/10.1088/1126-6708/2007/02/009` (cit. on p. 43).

[70] T. Cohen, N. Craig, H. K. Lou, and D. Pinner, "Folded supersymmetry with a twist," *Journal of High Energy Physics*, vol. 2016, no. 3, Mar. 2016, ISSN: 1029-8479. DOI: `10.1007/jhep03(2016)196`. [Online]. Available: `http://dx.doi.org/10.1007/JHEP03(2016)196` (cit. on p. 43).

[71] P. A. Zyla *et al.*, "Review of Particle Physics," *Progress of Theoretical and Experimental Physics*, vol. 2020, no. 8, Aug. 2020, 083C01, ISSN: 2050-3911. DOI: `10.1093/ptep/ptaa104`. eprint: `https://academic.oup.com/ptep/article-pdf/2020/8/083C01/34673722/ptaa104.pdf`. [Online]. Available: `https://doi.org/10.1093/ptep/ptaa104` (cit. on p. 44).

[72] Z. Chacko, H.-S. Goh, and R. Harnik, "Natural electroweak breaking from a mirror symmetry," *Physical Review Letters*, vol. 96, no. 23, Jun. 2006, ISSN: 1079-7114. DOI: `10.1103/physrevlett.96.231802`. arXiv: `hep-ph/0506256`. [Online]. Available: `http://dx.doi.org/10.1103/PhysRevLett.96.231802` (cit. on p. 44).

[73] H. Cai, H.-C. Cheng, and J. Terning, "A quirky little higgs model," *Journal of High Energy Physics*, vol. 2009, no. 05, pp. 045–045, May 2009, ISSN: 1029-8479. DOI: `10.1088/1126-6708/2009/05/045`. [Online]. Available: `http://dx.doi.org/10.1088/1126-6708/2009/05/045` (cit. on p. 45).

[74] C. J. Morningstar and M. Peardon, "Glueball spectrum from an anisotropic lattice study," *Physical Review D*, vol. 60, no. 3, Jul. 1999, ISSN: 1089-4918. DOI: `10.1103/physrevd.60.034509`. [Online]. Available: `http://dx.doi.org/10.1103/PhysRevD.60.034509` (cit. on p. 46).

[75] D. Curtin and C. B. Verhaaren, "Discovering uncolored naturalness in exotic higgs decays," *Journal of High Energy Physics*, vol. 2015, no. 12, pp. 1–36, Dec. 2015, ISSN: 1029-8479. DOI: `10.1007/jhep12(2015)072`. [Online]. Available: `http://dx.doi.org/10.1007/JHEP12(2015)072` (cit. on pp. 46–48).

[76] J. Juknevich, "Pure-glue hidden valleys through the higgs portal," *Journal of High Energy Physics*, vol. 2010, Nov. 2009. DOI: `10.1007/JHEP08(2010)121` (cit. on p. 47).

[77]   Heather Russell, CC BY-NC 4.0, "LLP overview," (cit. on p. 50).

[78]   J. Alimena, J. Beacham, M. Borsato, Y. Cheng, X. C. Vidal, G. Cottin, D. Curtin, A. De Roeck, N. Desai, J. A. Evans, and et al., "Searching for long-lived particles beyond the standard model at the large hadron collider," *Journal of Physics G: Nuclear and Particle Physics*, vol. 47, no. 9, p. 090 501, Sep. 2020, ISSN: 1361-6471. DOI: `10.1088/ 1361-6471/ab4574`. [Online]. Available: `http://dx.doi.org/10.1088/ 1361-6471/ab4574` (cit. on p. 51).

[79]   Heather Russell, CC BY-NC 4.0, "Collimated hadronic ID decay," (cit. on p. 52).

[80]   Heather Russell, CC BY-NC 4.0, "Non-collimated hadronic ID decay," (cit. on p. 52).

[81]   M. J. Strassler, K. Zurek, "Echoes of a hidden valley at hadron colliders," *Phys. Lett. B*, vol. 651, p. 374, 2007. DOI: `10.1016/j.physletb.2007.06.055`. arXiv: `hep-ph/0604261` (cit. on p. 53).

[82]   M. J. Strassler, K. M. Zurek, "Discovering the Higgs through highly-displaced vertices," *Phys. Lett. B*, vol. 661, pp. 263–267, 2008. DOI: `10.1016/j.physletb.2008.02.008`. arXiv: `hep-ph/0605193 [hep-ph]` (cit. on p. 54).

[83]   D. Curtin *et al.*, "Exotic decays of the 125 gev higgs boson," *Physical Review D*, vol. 90, no. 7, Oct. 2014, ISSN: 1550-2368. DOI: `10.1103/physrevd.90.075004`. [Online]. Available: `http://dx.doi.org/10.1103/PhysRevD.90.075004` (cit. on p. 56).

[84]   CMS Collaboration, "Combined measurements of Higgs boson couplings in proton–proton collisions at $\sqrt{s} = 13\,\text{TeV}$," *Eur. Phys. J. C*, vol. 79, p. 421, 2019. DOI: `10.1140/epjc/s10052-019-6909-y`. arXiv: `1809.10733 [hep-ex]` (cit. on p. 56).

[85]   ATLAS Collaboration, "Triggers for displaced decays of long-lived neutral particles in the ATLAS detector," *JINST*, vol. 8, P07015, 2013. DOI: `10.1088/1748-0221/ 8/07/P07015`. arXiv: `1305.2284 [hep-ex]` (cit. on p. 56).

[86]   ATLAS Collaboration, "Search for long-lived neutral particles in pp collisions at $\sqrt{s} = 13\,\text{TeV}$ that decay into displaced hadronic jets in the ATLAS calorimeter,"

Eur. Phys. J. C, vol. 79, p. 481, 2019. DOI: `10.1140/epjc/s10052-019-6962-6`. arXiv: `1902.03094 [hep-ex]` (cit. on pp. 56, 58).

[87] ATLAS Collaboration, "Search for long-lived particles produced in pp collisions at $\sqrt{s} = 13\,\text{TeV}$ that decay into displaced hadronic jets in the ATLAS muon spectrometer," *Phys. Rev. D*, vol. 99, p. 052 005, 2019. DOI: `10.1103/PhysRevD.99.052005`. arXiv: `1811.07370 [hep-ex]` (cit. on p. 57).

[88] ATLAS Collaboration, "Search for long-lived neutral particles produced in pp collisions at $\sqrt{s} = 13\,\text{TeV}$ decaying into displaced hadronic jets in the ATLAS inner detector and muon spectrometer," *Phys. Rev. D*, vol. 101, p. 052 013, 2020. DOI: `10.1103/PhysRevD.101.052013`. arXiv: `1911.12575 [hep-ex]` (cit. on p. 57).

[89] LHCb Collaboration, "Updated search for long-lived particles decaying to jet pairs. Updated search for long-lived particles decaying to jet pairs," *Eur. Phys. J. C*, vol. 77, no. LHCB-PAPER-2016-065. 12, 812. 23 p, May 2017. DOI: `10.1140/epjc/s10052-017-5178-x` (cit. on p. 57).

[90] CMS Collaboration, "Search for long-lived particles using displaced jets in proton-proton collisions at $\sqrt{s} = 13$ TeV," 2020. arXiv: `2012.01581 [hep-ex]` (cit. on pp. 57, 208).

[91] ATLAS Collaboration, "Search for the Higgs boson produced in association with a vector boson and decaying into two spin-zero particles in the $H \rightarrow aa \rightarrow 4b$ channel in pp collisions at $\sqrt{s} = 13\,\text{TeV}$ with the ATLAS detector," *JHEP*, vol. 10, p. 031, 2018. DOI: `10.1007/JHEP10(2018)031`. arXiv: `1806.07355 [hep-ex]` (cit. on p. 57).

[92] ATLAS Collaboration, "Search for Higgs boson decays into two new low-mass spin-0 particles in the $4b$ channel with the ATLAS detector using pp collisions at $\sqrt{s} = 13\,\text{TeV}$," 2020. arXiv: `2005.12236 [hep-ex]` (cit. on p. 57).

[93] L. Evans and P. Bryant, "LHC machine," *Journal of Instrumentation*, vol. 3, no. 08, S08001–S08001, Aug. 2008. DOI: `10.1088/1748-0221/3/08/s08001`. [Online]. Available: `https://doi.org/10.1088/1748-0221/3/08/s08001` (cit. on pp. 61, 64).

[94]   *LEP design report*. Geneva: CERN, 1983, By the LEP Injector Study Group. [Online].
       Available: `https://cds.cern.ch/record/98881` (cit. on p. 61).

[95]   *LEP design report*. Geneva: CERN, 1984, Copies shelved as reports in LEP, PS and
       SPS libraries. [Online]. Available: `https://cds.cern.ch/record/102083`
       (cit. on p. 61).

[96]   ATLAS Collaboration, "The ATLAS Experiment at the CERN Large Hadron Col-
       lider," *JINST*, vol. 3, S08003, 2008. DOI: `10.1088/1748-0221/3/08/S08003`
       (cit. on pp. 61, 70, 76, 79, 80, 82, 83).

[97]   CMS Collaboration, "The CMS experiment at the CERN LHC," *JINST*, vol. 3, S08004,
       2008. DOI: `10.1088/1748-0221/3/08/S08004` (cit. on p. 61).

[98]   LHCb Collaboration, "The LHCb Detector at the LHC," *JINST*, vol. 3, S08005, 2008.
       DOI: `10.1088/1748-0221/3/08/S08005` (cit. on p. 61).

[99]   ALICE Collaboration, "The ALICE experiment at the CERN LHC," *JINST*, vol. 3,
       S08002, 2008. DOI: `10.1088/1748-0221/3/08/S08002` (cit. on p. 61).

[100] C. Service graphique, "Overall view of the LHC. Vue d'ensemble du LHC," Jun.
       2014, General Photo. [Online]. Available: `https://cds.cern.ch/record/1708849` (cit. on p. 62).

[101] M. Benedikt, P. Collier, V. Mertens, J. Poole, and K. Schindl, *LHC Design Report*,
       ser. CERN Yellow Reports: Monographs. Geneva: CERN, 2004. DOI: `10.5170/CERN-2004-003-V-3` (cit. on p. 61).

[102] R. Scrivens, M. Kronberger, D. Küchler, J. Lettry, C. Mastrostefano, O. Midttun, M.
       O'Neil, H. Pereira, and C. Schmitzer, "Overview of the status and developments on
       primary ion sources at CERN*," 4 p, Sep. 2011 (cit. on p. 61).

[103] J. Haffner, "The CERN accelerator complex. Complexe des accélérateurs du CERN,"
       Oct. 2013, General Photo. [Online]. Available: `http://cds.cern.ch/record/1621894` (cit. on p. 63).

[104]   D. Boussard and T. P. R. Linnecar, "The LHC Superconducting RF System," CERN, Geneva, Tech. Rep. LHC-Project-Report-316. CERN-LHC-Project-Report-316, Dec. 1999. [Online]. Available: `https://cds.cern.ch/record/410377` (cit. on p. 63).

[105]   O. S. Brüning, P. Collier, P. Lebrun, S. Myers, R. Ostojic, J. Poole, and P. Proudlock, *LHC Design Report*, ser. CERN Yellow Reports: Monographs. Geneva: CERN, 2004. DOI: `10.5170/CERN-2004-003-V-1` (cit. on p. 64).

[106]   A. Team, "Diagram of an LHC dipole magnet. Schéma d'un aimant dipôle du LHC," Jun. 1999, [Online]. Available: `https://cds.cern.ch/record/40524` (cit. on p. 65).

[107]   S. Baird, "Accelerators for pedestrians; rev. version," CERN, Geneva, Tech. Rep. AB-Note-2007-014. CERN-AB-Note-2007-014. PS-OP-Note-95-17-Rev-2. CERN-PS-OP-Note-95-17-Rev-2, Feb. 2007. [Online]. Available: `http://cds.cern.ch/record/1017689` (cit. on p. 66).

[108]   B. G. Taylor, "Timing distribution at the LHC," 2002. DOI: `10.5170/CERN-2002-003.63`. [Online]. Available: `https://cds.cern.ch/record/592719` (cit. on p. 67).

[109]   P. Grafström and W. Kozanecki, "Luminosity determination at proton colliders," *Progress in Particle and Nuclear Physics*, vol. 81, pp. 97–148, 2015, ISSN: 0146-6410. DOI: `https://doi.org/10.1016/j.ppnp.2014.11.002`. [Online]. Available: `http://www.sciencedirect.com/science/article/pii/S0146641014000878` (cit. on p. 67).

[110]   ATLAS Collaboration, "Luminosity Public Results Run 2," [Online]. Available: `https://twiki.cern.ch/twiki/bin/view/AtlasPublic/LuminosityPublicResultsRun2` (cit. on pp. 68, 69).

[111]   A. Yamamoto *et al.*, "Progress in atlas central solenoid magnet," *IEEE Transactions on Applied Superconductivity*, vol. 10, no. 1, pp. 353–356, 2000. DOI: `10.1109/77.828246` (cit. on p. 70).

[112] ATLAS Collaboration, "ATLAS Magnet System: Magnet Project Technical Design Report, Volume 1," ATLAS-TDR-6; CERN-LHCC-97-018, 1997. [Online]. Available: `https://cds.cern.ch/record/338080` (cit. on p. 71).

[113] ATLAS Collaboration, "Study of the material of the ATLAS inner detector for Run 2 of the LHC," *JINST*, vol. 12, P12009, 2017. DOI: `10.1088/1748-0221/12/12/P12009`. arXiv: `1707.02826 [hep-ex]` (cit. on pp. 73, 74, 151, 152).

[114] ATLAS Collaboration, "ATLAS pixel detector electronics and sensors," *Journal of Instrumentation*, vol. 3, no. 07, P07007–P07007, Jul. 2008. DOI: `10.1088/1748-0221/3/07/p07007`. [Online]. Available: `https://doi.org/10.1088/1748-0221/3/07/p07007` (cit. on p. 73).

[115] ATLAS Collaboration, "ATLAS Calorimeter Performance: Technical Design Report," ATLAS-TDR-1; CERN-LHCC-96-040, 1996. [Online]. Available: `https://cds.cern.ch/record/331059` (cit. on p. 77).

[116] ATLAS Collaboration, "Topological cell clustering in the ATLAS calorimeters and its performance in LHC Run 1," *Eur. Phys. J. C*, vol. 77, p. 490, 2017. DOI: `10.1140/epjc/s10052-017-5004-5`. arXiv: `1603.02934 [hep-ex]` (cit. on pp. 78, 97).

[117] ATLAS Collaboration, "ATLAS Liquid Argon Calorimeter: Technical Design Report," ATLAS-TDR-2; CERN-LHCC-96-041, 1996. [Online]. Available: `https://cds.cern.ch/record/331061` (cit. on p. 77).

[118] ATLAS Collaboration, "ATLAS Tile Calorimeter: Technical Design Report," ATLAS-TDR-3; CERN-LHCC-96-042, 1996. [Online]. Available: `https://cds.cern.ch/record/331062` (cit. on p. 79).

[119] ATLAS Collaboration, "ATLAS Muon Spectrometer: Technical Design Report," CERN, ATLAS-TDR-10; CERN-LHCC-97-022, 1997. [Online]. Available: `https://cds.cern.ch/record/331068` (cit. on pp. 81, 84, 86).

[120] F. Bauer *et al.*, "Construction and test of mdt chambers for the atlas muon spectrometer," *Nuclear Instruments and Methods in Physics Research Section A: Accelerators, Spectrometers, Detectors and Associated Equipment*, vol. 461, no. 1, pp. 17–20, 2001, 8th Pisa Meeting on Advanced Detectors, ISSN: 0168-9002. DOI: `https://doi.`

org/10.1016/S0168-9002(00)01156-6. [Online]. Available: http://www.sciencedirect.com/science/article/pii/S0168900200011566 (cit. on p. 81).

[121] T. Argyropoulos *et al.*, "Cathode strip chambers in atlas : Installation, commissioning and in situ performance," in *2008 IEEE Nuclear Science Symposium Conference Record*, 2008, pp. 2819–2824. DOI: 10.1109/NSSMIC.2008.4774958 (cit. on p. 81).

[122] G. Aielli *et al.*, "The rpc first level muon trigger in the barrel of the atlas experiment," *Nuclear Physics B - Proceedings Supplements*, vol. 158, pp. 11–15, 2006, Proceedings of the 8th International Workshop on Resistive Plate Chambers and Related Detectors, ISSN: 0920-5632. DOI: https://doi.org/10.1016/j.nuclphysbps.2006.07.031. [Online]. Available: http://www.sciencedirect.com/science/article/pii/S0920563206004178 (cit. on p. 81).

[123] S. Majewski, G. Charpak, A. Breskin, and G. Mikenberg, "A thin multiwire chamber operating in the high multiplication mode," *Nuclear Instruments and Methods in Physics Research*, vol. 217, no. 1, pp. 265–271, 1983, ISSN: 0167-5087. DOI: https://doi.org/10.1016/0167-5087(83)90146-1. [Online]. Available: http://www.sciencedirect.com/science/article/pii/0167508783901461 (cit. on p. 81).

[124] Y. Arai *et al.*, "Atlas muon drift tube electronics," *Journal of Instrumentation*, vol. 3, no. 09, P09001–P09001, Sep. 2008. DOI: 10.1088/1748-0221/3/09/p09001. [Online]. Available: https://doi.org/10.1088/1748-0221/3/09/p09001 (cit. on p. 84).

[125] P. Branchini, F. Ceradini, S. Di Luise, M. Iodice, and F. Petrucci, "Global time fit for tracking in an array of drift cells: The drift tubes of the atlas experiment," *IEEE Transactions on Nuclear Science*, vol. 55, no. 1, pp. 620–627, 2008. DOI: 10.1109/TNS.2007.914020 (cit. on p. 84).

[126] ATLAS Collaboration, "Performance of the ATLAS trigger system in 2015," *Eur. Phys. J. C*, vol. 77, p. 317, 2017. DOI: `10.1140/epjc/s10052-017-4852-3`. arXiv: `1611.09661 [hep-ex]` (cit. on p. 87).

[127] J. Pequenao and P. Schaffner, "How ATLAS detects particles: diagram of particle paths in the detector," Jan. 2013, [Online]. Available: `https://cds.cern.ch/record/1505342` (cit. on p. 89).

[128] ATLAS Collaboration, "Event Displays from Run 2 physics analyses," (cit. on p. 90).

[129] ATLAS Collaboration, "Performance of the ATLAS track reconstruction algorithms in dense environments in LHC Run 2," *Eur. Phys. J. C*, vol. 77, p. 673, 2017. DOI: `10.1140/epjc/s10052-017-5225-7`. arXiv: `1704.07983 [hep-ex]` (cit. on pp. 91, 93).

[130] ATLAS Collaboration, *Performance of the ATLAS Silicon Pattern Recognition Algorithm in Data and Simulation at $\sqrt{s} = 7\,TeV$*, ATLAS-CONF-2010-072, 2010. [Online]. Available: `https://cds.cern.ch/record/1281363` (cit. on pp. 91, 92).

[131] R. Frühwirth, "Application of Kalman filtering to track and vertex fitting," *Nucl. Instrum. Methods Phys. Res., A*, vol. 262, no. HEPHY-PUB-503, 444. 19 p, Jun. 1987. [Online]. Available: `https://cds.cern.ch/record/178627` (cit. on p. 92).

[132] ATLAS Collaboration, *Performance of the reconstruction of large impact parameter tracks in the inner detector of ATLAS*, ATL-PHYS-PUB-2017-014, 2017. [Online]. Available: `https://cds.cern.ch/record/2275635` (cit. on pp. 94, 116–119).

[133] K. Choi, "Tracking and Vertexing with the ATLAS Inner Detector in the LHC Run-2," CERN, Geneva, Tech. Rep. ATL-PHYS-PROC-2017-075, Jun. 2017. DOI: `10.1007/978-981-13-1316-5_75`. [Online]. Available: `https://cds.cern.ch/record/2271033` (cit. on p. 95).

[134] ATLAS Collaboration, "Reconstruction of primary vertices at the ATLAS experiment in Run 1 proton–proton collisions at the LHC," *Eur. Phys. J. C*, vol. 77, p. 332, 2017. DOI: `10.1140/epjc/s10052-017-4887-5`. arXiv: `1611.10235 [hep-ex]` (cit. on p. 95).

[135] K. Grimm, S. Boutle, D. Casper, B. Hooberman, B. Gui, G. Lee, J. Maurer, A. Morley, S. Pagan Griso, B. Petersen, K. Prokofiev, L. Shan, D. Shope, A. Wharton, B. Whitmore, and M. Zhang, "Primary vertex reconstruction at the ATLAS experiment," CERN, Geneva, Tech. Rep. ATL-SOFT-PROC-2017-051. 4, Feb. 2017. DOI: `10.1088/1742-6596/898/4/042056`. [Online]. Available: `https://cds.cern.ch/record/2253428` (cit. on pp. 95, 96).

[136] ATLAS Collaboration, "Jet reconstruction and performance using particle flow with the ATLAS Detector," *Eur. Phys. J. C*, vol. 77, p. 466, 2017. DOI: `10.1140/epjc/s10052-017-5031-2`. arXiv: `1703.10485 [hep-ex]` (cit. on p. 98).

[137] M. Cacciari, G. P. Salam, and G. Soyez, "The anti-k_t jet clustering algorithm," *JHEP*, vol. 04, p. 063, 2008. DOI: `10.1088/1126-6708/2008/04/063`. arXiv: `0802.1189 [hep-ph]` (cit. on pp. 98, 99).

[138] ATLAS Collaboration, "Jet energy scale and resolution measured in proton–proton collisions at $\sqrt{s} = 13$ TeV with the ATLAS detector," 2020. arXiv: `2007.02645 [hep-ex]` (cit. on pp. 100, 102, 174, 175).

[139] M. Cacciari, G. P. Salam, and G. Soyez, "The catchment area of jets," *Journal of High Energy Physics*, vol. 2008, no. 04, pp. 005–005, Apr. 2008, ISSN: 1029-8479. DOI: `10.1088/1126-6708/2008/04/005`. [Online]. Available: `http://dx.doi.org/10.1088/1126-6708/2008/04/005` (cit. on p. 100).

[140] ATLAS Collaboration, "Jet energy scale measurements and their systematic uncertainties in proton–proton collisions at $\sqrt{s} = 13$ TeV with the ATLAS detector," *Phys. Rev. D*, vol. 96, p. 072 002, 2017. DOI: `10.1103/PhysRevD.96.072002`. arXiv: `1703.09665 [hep-ex]` (cit. on pp. 101, 103).

[141] ATLAS Collaboration, "ATLAS b-jet identification performance and efficiency measurement with $t\bar{t}$ events in pp collisions at $\sqrt{s} = 13$ TeV," *Eur. Phys. J. C*, vol. 79, p. 970, 2019. DOI: `10.1140/epjc/s10052-019-7450-8`. arXiv: `1907.05120 [hep-ex]` (cit. on p. 102).

[142] ATLAS Collaboration, *Optimisation and performance studies of the ATLAS b-tagging algorithms for the 2017-18 LHC run*, ATL-PHYS-PUB-2017-013, 2017. [Online]. Available: `https://cds.cern.ch/record/2273281` (cit. on p. 102).

[143] ATLAS Collaboration, "Muon reconstruction performance of the ATLAS detector in proton–proton collision data at $\sqrt{s} = 13\,\text{TeV}$," *Eur. Phys. J. C*, vol. 76, p. 292, 2016. DOI: `10.1140/epjc/s10052-016-4120-y`. arXiv: `1603.05598 [hep-ex]` (cit. on pp. 103, 105–108, 173).

[144] ATLAS Collaboration, "Electron reconstruction and identification in the ATLAS experiment using the 2015 and 2016 LHC proton–proton collision data at $\sqrt{s} = 13\,\text{TeV}$," *Eur. Phys. J. C*, vol. 79, p. 639, 2019. DOI: `10.1140/epjc/s10052-019-7140-6`. arXiv: `1902.04655 [hep-ex]` (cit. on pp. 108–110).

[145] ATLAS Collaboration, "Electron and photon performance measurements with the ATLAS detector using the 2015–2017 LHC proton–proton collision data," *JINST*, vol. 14, P12006, 2019. DOI: `10.1088/1748-0221/14/12/P12006`. arXiv: `1908.00005 [hep-ex]` (cit. on pp. 108, 111–114).

[146] ATLAS Collaboration, *Improved electron reconstruction in ATLAS using the Gaussian Sum Filter-based model for bremsstrahlung*, ATLAS-CONF-2012-047, 2012. [Online]. Available: `https://cds.cern.ch/record/1449796` (cit. on p. 109).

[147] ATLAS Collaboration, "Electron and photon energy calibration with the ATLAS detector using LHC Run 1 data," *Eur. Phys. J. C*, vol. 74, p. 3071, 2014. DOI: `10.1140/epjc/s10052-014-3071-4`. arXiv: `1407.5063 [hep-ex]` (cit. on p. 111).

[148] ATLAS Collaboration, "Electron and photon energy calibration with the ATLAS detector using 2015–2016 LHC proton–proton collision data," *JINST*, vol. 14, P03017, 2019. DOI: `10.1088/1748-0221/14/03/P03017`. arXiv: `1812.03848 [hep-ex]` (cit. on p. 111).

[149] ATLAS Collaboration, *Performance of vertex reconstruction algorithms for detection of new long-lived particle decays within the ATLAS inner detector*, ATL-PHYS-PUB-2019-013, 2019. [Online]. Available: `https://cds.cern.ch/record/2669425` (cit. on pp. 120, 122–124, 126, 127).

[150] V. Kostyukhin, "VKalVrt - package for vertex reconstruction in ATLAS.," CERN, Geneva, Tech. Rep. ATL-PHYS-2003-031, Aug. 2003, revised version number 1 submitted on 2003-09-24 11:10:53. [Online]. Available: `https://cds.cern.ch/record/685551` (cit. on p. 121).

[151] S. Höche, "Introduction to parton-shower event generators," in *Theoretical Advanced Study Institute in Elementary Particle Physics: Journeys Through the Precision Frontier: Amplitudes for Colliders*, 2015, pp. 235–295. DOI: `10.1142/9789814678766_0005`. arXiv: `1411.4085 [hep-ph]` (cit. on p. 131).

[152] L. A. Harland-Lang, A. D. Martin, P. Motylinski, and R. S. Thorne, "Parton distributions in the lhc era: Mmht 2014 pdfs," *The European Physical Journal C*, vol. 75, no. 5, May 2015, ISSN: 1434-6052. DOI: `10.1140/epjc/s10052-015-3397-6`. [Online]. Available: `http://dx.doi.org/10.1140/epjc/s10052-015-3397-6` (cit. on p. 132).

[153] R. D. Ball *et al.*, "Parton distributions for the LHC run II," *JHEP*, vol. 04, p. 040, 2015. DOI: `10.1007/JHEP04(2015)040`. arXiv: `1410.8849 [hep-ph]` (cit. on pp. 132, 140).

[154] S. Dulat, T.-J. Hou, J. Gao, M. Guzzi, J. Huston, P. Nadolsky, J. Pumplin, C. Schmidt, D. Stump, and C. P. Yuan, "New parton distribution functions from a global analysis of quantum chromodynamics," *Phys. Rev. D*, vol. 93, no. 3, p. 033 006, 2016. DOI: `10.1103/PhysRevD.93.033006`. arXiv: `1506.07443 [hep-ph]` (cit. on p. 132).

[155] J. Alwall, M. Herquet, F. Maltoni, O. Mattelaer, and T. Stelzer, "MadGraph 5 : Going Beyond," *JHEP*, vol. 06, p. 128, 2011. DOI: `10.1007/JHEP06(2011)128`. arXiv: `1106.0522 [hep-ph]` (cit. on p. 132).

[156] S. Alioli, P. Nason, C. Oleari, and E. Re, "A general framework for implementing NLO calculations in shower Monte Carlo programs: the POWHEG BOX," *JHEP*, vol. 06, p. 043, 2010. DOI: `10.1007/JHEP06(2010)043`. arXiv: `1002.2581 [hep-ph]` (cit. on pp. 132, 136).

[157] B. R. Webber, "Fragmentation and hadronization," *Int. J. Mod. Phys. A*, vol. A15S1, no. supp01b, pp. 577–606, 2000. DOI: `10.1142/S0217751X00005334` (cit. on pp. 133, 135).

[158] T. Sjöstrand, S. Ask, J. R. Christiansen, R. Corke, N. Desai, P. Ilten, S. Mrenna, S. Prestel, C. O. Rasmussen, and P. Z. Skands, "An introduction to PYTHIA 8.2," *Comput. Phys. Commun.*, vol. 191, p. 159, 2015. DOI: `10.1016/j.cpc.2015.01.024`. arXiv: `1410.3012 [hep-ph]` (cit. on pp. 133, 136).

[159] J. Bellm *et al.*, "Herwig 7.0/Herwig++ 3.0 release note," *Eur. Phys. J. C*, vol. 76, no. 4, p. 196, 2016. DOI: `10.1140/epjc/s10052-016-4018-8`. arXiv: `1512.01178 [hep-ph]` (cit. on p. 133).

[160] B. Andersson, G. Gustafson, G. Ingelman, and T. Sjästrand, "Parton fragmentation and string dynamics," *Physics Reports*, vol. 97, no. 2, pp. 31–145, 1983, ISSN: 0370-1573. DOI: `https://doi.org/10.1016/0370-1573(83)90080-7`. [Online]. Available: `https://www.sciencedirect.com/science/article/pii/0370157383900807` (cit. on p. 133).

[161] B. Webber, "A qcd model for jet fragmentation including soft gluon interference," *Nuclear Physics B*, vol. 238, no. 3, pp. 492–528, 1984, ISSN: 0550-3213. DOI: `https://doi.org/10.1016/0550-3213(84)90333-X` (cit. on p. 134).

[162] D. Amati and G. Veneziano, "Preconfinement as a Property of Perturbative QCD," *Phys. Lett. B*, vol. 83, pp. 87–92, 1979. DOI: `10.1016/0370-2693(79)90896-7` (cit. on p. 134).

[163] ATLAS Collaboration, "Measurement of the underlying event in jet events from 7 TeV proton–proton collisions with the ATLAS detector," *Eur. Phys. J. C*, vol. 74, p. 2965, 2014. DOI: `10.1140/epjc/s10052-014-2965-5`. arXiv: `1406.0392 [hep-ex]` (cit. on p. 134).

[164] S. Agostinelli *et al.*, "GEANT4 – A SIMULATION TOOLKIT," *Nucl. Instrum. Meth. A*, vol. 506, p. 250, 2003. DOI: `10.1016/S0168-9002(03)01368-8` (cit. on p. 135).

[165]   P. Nason and C. Oleari, "NLO Higgs boson production via vector-boson fusion matched with shower in POWHEG," *JHEP*, vol. 02, p. 037, 2010. DOI: `10.1007/JHEP02(2010)037`. arXiv: `0911.5299 [hep-ph]` (cit. on p. 136).

[166]   P. Nason, "A new method for combining NLO QCD with shower Monte Carlo algorithms," *JHEP*, vol. 11, p. 040, 2004. DOI: `10.1088/1126-6708/2004/11/040`. arXiv: `hep-ph/0409146` (cit. on p. 136).

[167]   S. Frixione, P. Nason, and C. Oleari, "Matching NLO QCD computations with parton shower simulations: the POWHEG method," *JHEP*, vol. 11, p. 070, 2007. DOI: `10.1088/1126-6708/2007/11/070`. arXiv: `0709.2092 [hep-ph]` (cit. on p. 136).

[168]   G. Cullen, N. Greiner, G. Heinrich, G. Luisoni, P. Mastrolia, G. Ossola, T. Reiter, and F. Tramontano, "Automated One-Loop Calculations with GoSam," *Eur. Phys. J. C*, vol. 72, p. 1889, 2012. DOI: `10.1140/epjc/s10052-012-1889-1`. arXiv: `1111.2034 [hep-ph]` (cit. on p. 136).

[169]   J. Butterworth *et al.*, "PDF4LHC recommendations for LHC Run II," *J. Phys. G*, vol. 43, p. 023 001, 2016. DOI: `10.1088/0954-3899/43/2/023001`. arXiv: `1510.03865 [hep-ph]` (cit. on p. 136).

[170]   M. L. Ciccolini, S. Dittmaier, and M. Krämer, "Electroweak radiative corrections to associated WH and ZH production at hadron colliders," *Phys. Rev. D*, vol. 68, p. 073 003, 2003. DOI: `10.1103/PhysRevD.68.073003`. arXiv: `hep-ph/0306234 [hep-ph]` (cit. on p. 136).

[171]   O. Brein, A. Djouadi, and R. Harlander, "NNLO QCD corrections to the Higgs-strahlung processes at hadron colliders," *Phys. Lett. B*, vol. 579, pp. 149–156, 2004. DOI: `10.1016/j.physletb.2003.10.112`. arXiv: `hep-ph/0307206` (cit. on p. 136).

[172]   O. Brein, R. Harlander, M. Wiesemann, and T. Zirke, "Top-Quark Mediated Effects in Hadronic Higgs-Strahlung," *Eur. Phys. J. C*, vol. 72, p. 1868, 2012. DOI: `10.1140/epjc/s10052-012-1868-6`. arXiv: `1111.0761 [hep-ph]` (cit. on p. 136).

[173] L. Altenkamp, S. Dittmaier, R. V. Harlander, H. Rzehak, and T. J. E. Zirke, "Gluon-induced Higgs-strahlung at next-to-leading order QCD," *JHEP*, vol. 02, p. 078, 2013. DOI: `10.1007/JHEP02(2013)078`. arXiv: `1211.5015 [hep-ph]` (cit. on p. 136).

[174] A. Denner, S. Dittmaier, S. Kallweit, and A. Mück, "HAWK 2.0: A Monte Carlo program for Higgs production in vector-boson fusion and Higgs strahlung at hadron colliders," *Comput. Phys. Commun.*, vol. 195, pp. 161–171, 2015. DOI: `10.1016/j.cpc.2015.04.021`. arXiv: `1412.5390 [hep-ph]` (cit. on p. 136).

[175] O. Brein, R. V. Harlander, and T. J. E. Zirke, "vh@nnlo – Higgs Strahlung at hadron colliders," *Comput. Phys. Commun.*, vol. 184, pp. 998–1003, 2013. DOI: `10.1016/j.cpc.2012.11.002`. arXiv: `1210.5347 [hep-ph]` (cit. on p. 136).

[176] R. V. Harlander, A. Kulesza, V. Theeuwes, and T. Zirke, "Soft gluon resummation for gluon-induced Higgs Strahlung," *JHEP*, vol. 11, p. 082, 2014. DOI: `10.1007/JHEP11(2014)082`. arXiv: `1410.0217 [hep-ph]` (cit. on p. 136).

[177] ATLAS Collaboration, "Measurement of the Z/γ^* boson transverse momentum distribution in pp collisions at $\sqrt{s} = 7\,\text{TeV}$ with the ATLAS detector," *JHEP*, vol. 09, p. 145, 2014. DOI: `10.1007/JHEP09(2014)145`. arXiv: `1406.3660 [hep-ex]` (cit. on p. 136).

[178] T. Gleisberg, S. Höche, F. Krauss, M. Schönherr, S. Schumann, F. Siegert, and W. J., "Event generation with SHERPA 1.1," *JHEP*, vol. 02, p. 007, 2009. DOI: `10.1088/1126-6708/2009/02/007`. arXiv: `0811.4622 [hep-ph]` (cit. on p. 139).

[179] T. Gleisberg and S. Höche, "Comix, a new matrix element generator," *JHEP*, vol. 12, p. 039, 2008. DOI: `10.1088/1126-6708/2008/12/039`. arXiv: `0808.3674 [hep-ph]` (cit. on p. 139).

[180] F. Cascioli, P. Maierhöfer, and S. Pozzorini, "Scattering Amplitudes with Open Loops," *Phys. Rev. Lett.*, vol. 108, p. 111 601, 2012. DOI: `10.1103/PhysRevLett.108.111601`. arXiv: `1111.5206 [hep-ph]` (cit. on p. 139).

[181] S. Schumann and F. Krauss, "A parton shower algorithm based on Catani–Seymour dipole factorisation," *JHEP*, vol. 03, p. 038, 2008. DOI: `10.1088/1126-6708/2008/03/038`. arXiv: `0709.1027 [hep-ph]` (cit. on p. 139).

[182]   S. Höche, F. Krauss, M. Schönherr, and F. Siegert, "QCD matrix elements + parton showers. The NLO case," *JHEP*, vol. 04, p. 027, 2013. DOI: `10.1007/JHEP04(2013)027`. arXiv: `1207.5030 [hep-ph]` (cit. on p. 139).

[183]   K. Melnikov and F. Petriello, "Electroweak gauge boson production at hadron colliders through $\mathcal{O}(\alpha_s^2)$," *Phys. Rev. D*, vol. 74, p. 114 017, 2006. DOI: `10.1103/PhysRevD.74.114017`. arXiv: `hep-ph/0609070` (cit. on p. 140).

[184]   ATLAS Collaboration, "ATLAS data quality operations and performance for 2015–2018 data-taking," *JINST*, vol. 15, P04003, 2020. DOI: `10.1088/1748-0221/15/04/P04003`. arXiv: `1911.04632 [physics.ins-det]` (cit. on p. 140).

[185]   ATLAS Collaboration, "Performance of electron and photon triggers in ATLAS during LHC Run 2," *Eur. Phys. J. C*, vol. 80, p. 47, 2020. DOI: `10.1140/epjc/s10052-019-7500-2`. arXiv: `1909.00761 [hep-ex]` (cit. on p. 142).

[186]   ATLAS Collaboration, "Performance of the ATLAS muon triggers in Run 2," 2020. arXiv: `2004.13447 [hep-ex]` (cit. on p. 142).

[187]   CMS Collaboration, "Search for new long-lived particles at $\sqrt{s} = 13\,\text{TeV}$," *Phys. Lett. B*, vol. 780, p. 432, 2018. DOI: `10.1016/j.physletb.2018.03.019`. arXiv: `1711.09120 [hep-ex]` (cit. on p. 143).

[188]   ATLAS Collaboration, "Search for long-lived, massive particles in events with displaced vertices and missing transverse momentum in $\sqrt{s} = 13\,\text{TeV}$ pp collisions with the ATLAS detector," *Phys. Rev. D*, vol. 97, p. 052 012, 2018. DOI: `10.1103/PhysRevD.97.052012`. arXiv: `1710.04901 [hep-ex]` (cit. on p. 151).

[189]   ATLAS Collaboration, "Measurement of the charged-particle multiplicity inside jets from $\sqrt{s} = 8\,\text{TeV}$ pp collisions with the ATLAS detector," *Eur. Phys. J. C*, vol. 76, p. 322, 2016. DOI: `10.1140/epjc/s10052-016-4126-5`. arXiv: `1602.00988 [hep-ex]` (cit. on p. 163).

[190]   ATLAS Collaboration, *Transverse momentum response and reconstruction efficiency for jets from displaced decays in the ATLAS detector*, ATL-PHYS-PUB-2019-025, 2019. [Online]. Available: `https://cds.cern.ch/record/2682843` (cit. on p. 174).

[191] ATLAS Collaboration, *Early Inner Detector Tracking Performance in the 2015 Data at* $\sqrt{s} = 13$ *TeV*, ATL-PHYS-PUB-2015-051, 2015. [Online]. Available: `https://cds.cern.ch/record/2110140` (cit. on p. 175).

[192] ATLAS Collaboration, "Measurement of the Inelastic Proton–Proton Cross Section at $\sqrt{s} = 13$ TeV with the ATLAS Detector at the LHC," *Phys. Rev. Lett.*, vol. 117, p. 182 002, 2016. DOI: `10.1103/PhysRevLett.117.182002`. arXiv: `1606.02625 [hep-ex]` (cit. on p. 181).

[193] ATLAS Collaboration, *Luminosity determination in pp collisions at* $\sqrt{s} = 13$ *TeV using the ATLAS detector at the LHC*, ATLAS-CONF-2019-021, 2019. [Online]. Available: `https://cds.cern.ch/record/2677054` (cit. on p. 182).

[194] G. Avoni *et al.*, "The new LUCID-2 detector for luminosity measurement and monitoring in ATLAS," *Journal of Instrumentation*, vol. 13, no. 07, P07017–P07017, Jul. 2018. DOI: `10.1088/1748-0221/13/07/p07017` (cit. on p. 182).

[195] G. Cowan, "Statistics for searches at the lhc," 2013. arXiv: `hep-ex/1307.2487` (cit. on pp. 186, 189).

[196] K. Cranmer, "Practical statistics for the lhc," 2015. arXiv: `physics.data-an/1503.07622` (cit. on p. 186).

[197] E. Gross, "LHC Statistics for Pedestrians," 2008. DOI: `10.5170/CERN-2008-001.205`. [Online]. Available: `https://cds.cern.ch/record/1099994` (cit. on p. 186).

[198] J. Neyman and E. S. Pearson, "On the problem of the most efficient tests of statistical hypotheses," *Philosophical Transactions of the Royal Society of London. Series A, Containing Papers of a Mathematical or Physical Character*, vol. 231, pp. 289–337, 1933, ISSN: 02643952. [Online]. Available: `http://www.jstor.org/stable/91247` (cit. on p. 189).

[199] A. L. Read, "Presentation of search results: the CL_S technique," *J. Phys. G*, vol. 28, p. 2693, 2002. DOI: `10.1088/0954-3899/28/10/313` (cit. on p. 191).

[200] G. Cowan, K. Cranmer, E. Gross, and O. Vitells, "Asymptotic formulae for likelihood-based tests of new physics," *The European Physical Journal C*, vol. 71, no. 2, Feb. 2011, ISSN: 1434-6052. DOI: `10.1140/epjc/s10052-011-1554-0`. [Online]. Available: `http://dx.doi.org/10.1140/epjc/s10052-011-1554-0` (cit. on p. 191).

[201] ATLAS Collaboration, *Procedure for the LHC Higgs boson search combination in summer 2011*, ATL-PHYS-PUB-2011-011, 2011. [Online]. Available: `https://cds.cern.ch/record/1375842` (cit. on p. 192).

[202] K. Bjoerke, W. Buttinger, D. Casadei, K. Cranmer, E. Gross, B. Malaescu, A. L. Read, G. Redlinger, and O. Vitells, "Summary of and Recommendations for the "Better than Zero" Problem," CERN, Geneva, Tech. Rep. ATL-COM-GEN-2017-009, Aug. 2017. [Online]. Available: `https://cds.cern.ch/record/2280679` (cit. on pp. 202, 204).

[203] L. Collaboration, *Test of lepton universality in beauty-quark decays*, 2021. arXiv: `2103.11769 [hep-ex]` (cit. on p. 212).

[204] T. Albahri *et al.*, "Measurement of the anomalous precession frequency of the muon in the fermilab muon $g - 2$ experiment," *Physical Review D*, vol. 103, no. 7, Apr. 2021, ISSN: 2470-0029. DOI: `10.1103/physrevd.103.072002`. [Online]. Available: `http://dx.doi.org/10.1103/PhysRevD.103.072002` (cit. on p. 212).